Investigation into early interneuron circuits of the mouse visual cortex



Filippo Ghezzi

University College Oxford
University of Oxford

A thesis submitted for the degree of

Doctor of Philosophy

Trinity Term 2022

Abstract

GABAergic interneurons play critical roles during cortical development in mammals, by maintaining excitatory-inhibitory balance and controlling emergent activity. In the mouse barrel cortex (S1BF), somatostatin-expressing (SST+) interneurons establish early, transient synaptic connections with thalamo-recipient excitatory neurons in cortical layer (L)4, while they receive transient thalamic inputs. This immature feed-forward inhibitory motif by SST+ cells acts as a scaffold for the mature S1BF neuronal networks and regulates developmental plasticity mechanisms. Given this critical role, it is conceivable transient networks by SST+ interneurons are a general feature of the developing mammalian cortex; however, there is limited knowledge on early networks and functions of SST+ interneurons in other brain regions. To explore this issue, the current thesis explores the primary visual cortex (V1) of the mouse, to study the degree of similarity between GABAergic interneuron networks and functions across sensory areas over early postnatal development. *In vitro* electrophysiology and optical techniques were used to map input/output connectivity patterns of SST+ interneurons in V1 to show they are only engaged in feedback inhibitory motifs with local excitatory neurons. Differences at the neuronal network level between V1 and S1BF relates to distinct functions played by SST+ interneurons across the developing brain. *In vivo* electrophysiology, together with optogenetics and chemogenetics, revealed SST+ interneurons in V1 regulate spontaneous activity but have minor impacts on early sensory activity before the onset of active perception. Circuit mapping experiments onto L6 excitatory neurons extended the concept of different early GABAergic networks between V1 and S1BF to the output layer of the cerebral cortex. Although canonical cortical circuits permeate the adult mammalian cortex, their developmental trajectories differ between similar primary sensory areas. GABAergic interneurons have been associated with neurodevelopmental disorders; it is, hence, pivotal to consider their developmental networks and functions to gain an understanding of the mechanisms underlying these disorders.

Statement of authorship

This thesis is submitted to the Department of Physiology, Anatomy and Genetics, University of Oxford, in fulfilment of the requirements for the degree of Doctor of Philosophy. This thesis is entirely my own work and describes research that I directly performed and/or supervised. All experiments described in the three experimental chapters are my own work, with the exception stated below:

- Dataset to investigate intrinsic electrophysiological properties of excitatory and inhibitory neurons (Sections 3.2 and 3.3) includes 51 recordings obtained by Mr. M. Shah-Ostrowski, undergraduate student, as part of his FHS lab project. I acted as his day-to-day supervisor throughout his project.
- *In vitro* circuit mapping data of GABAergic connectivity onto pyramidal neurons (Section 3.4) and connectivity of SST+ interneurons (Section 3.5) include 75 recordings previously performed by Dr. J. Stacey. They were included in the full dataset to provide a comprehensive analysis.
- Thalamic connectivity data (Section 3.7) includes 33 recordings obtained by Mr. M. Shah-Ostrowski, undergraduate student, as part of his FHS lab project. I acted as his day-to-day supervisor throughout his project.
- *In vitro* experiments in Chapter 5 (Sections 5.2 and 5.3) include 117 recordings obtained by Mr. Luca Discepolo, MSc student, as part of his MSc lab project and Erasmus Traineeship Programme. I acted as his day-to-day supervisor throughout his project.

Funding

The work described in this thesis was funded by the Wellcome Trust.

Word count: 48.724

Table of Contents

CHAPTER 1 - INTRODUCTION 6

1.1 – ROLE OF GABAERGIC INTERNEURONS DURING EARLY POSTNATAL DEVELOPMENT 7

1.1.1 – Somatostatin-expressing interneurons establish transient GABAergic networks during early postnatal development in the mouse *9*

1.1.2 – Parvalbumin-expressing interneurons regulate the transition between "critical" developmental periods *11*

1.2 – DEVELOPMENT OF PRIMARY VISUAL CORTEX NETWORK AND FUNCTION IN THE MOUSE 12

1.2.1 – Development of the visual system during the precritical period *13*

1.2.2 – Developing networks of the primary visual cortex *21*

1.3 – THESIS OUTLINE 22

CHAPTER 2 – MATERIALS AND METHODS 24

2.1 – ANIMAL MODELS 24

2.2 – *IN VITRO* ELECTROPHYSIOLOGY 24

2.2.1 – Intrinsic electrophysiological properties *25*

2.2.2 – Laser-scanning photostimulation *26*

2.2.3 – In vitro optogenetics *31*

2.2.4 – Morphological reconstruction *33*

2.3 – IMMUNOHISTOCHEMISTRY 33

2.4 – *IN VIVO* ELECTROPHYSIOLOGY 35

2.4.1 – Surgical and recording procedures *35*

2.4.2 – Analysis of in vivo electrophysiology data *36*

2.5 – CHEMOGENETIC EXPERIMENTS 39

2.6 – STATISTICS 40

CHAPTER 3 – GABAERGIC INTENEURON NETWORKS IN POSTNATAL MOUSE V1 41

3.1 – INTRODUCTION 41

3.2 – CHARACTERISATION OF V1 PYRAMIDAL NEURONS ELECTROPHYSIOLOGICAL PROPERTIES OVER EARLY POSTNATAL DEVELOPMENT 41

3.2.1 – Electrophysiological and morphological properties of V1 layer 4 pyramidal neurons *41*

3.2.2 – Electrophysiological properties of V1 supragranular and infragranular pyramidal neurons *44*

3.3 – CHARACTERISATION OF V1 GABAERGIC INTERNEURONS ELECTROPHYSIOLOGICAL PROPERTIES OVER EARLY POSTNATAL DEVELOPMENT 47

3.3.1 – Immunohistological characterisation of Lhx6-eGFP; SSTCre; Ai9 animals *47*

3.3.2 – Electrophysiological and morphological properties of L4 fast-spiking interneurons in V1 49
3.3.3 – Electrophysiological properties of SSTCre+ interneurons in V1 52
3.4 – GABAergic networks of V1 pyramidal neurons through early development 54
3.5 – Networks of V1 SST+ interneurons through early development 61
3.5.1 – GABAergic connectivity from SST+ interneurons onto L4 pyramidal neurons in V1 ... 61
3.5.2 – Excitatory connectivity networks of infragranular SST+ interneurons in V1 64
3.6 – Development of dis-inhibitory interneuron networks in developing V1 66
3.6.1 – Establishing an optogenetic strategy to identify PV+ interneurons during early postnatal development 66
3.6.2 – Development of SST+ interneuron connectivity onto L4 FS interneurons in V1 69
3.7 – Development of thalamocortical connectivity in the developing V1 75
3.7.1 – Development of thalamocortical connectivity onto pyramidal neurons in V1 77
3.7.2 – Development of thalamocortical connectivity onto GABAergic interneurons in V1 80
3.7.3 – Development of fast feed-forward inhibition in V1 L4 83
3.8 – Development of dis-inhibitory interneuron networks in S1BF 85
3.8.1 – Characterisation of S1BF L4 neurons intrinsic electrophysiological properties. 85
3.8.2 – Development of SST+ interneuron connectivity onto L4 FS interneurons in S1BF 88
3.9 – Summary of results 93
3.10 – Tables 95

CHAPTER 4 – FUNCTION OF GABAERGIC INTERNEURONS IN THE DEVELOPING V1 100

4.1 – Introduction 100
4.2 – Characterisation of spontaneous and sensory-evoked activity in developing V1 in anaesthetised mice 100
4.3 – Optogenetic strategy for interneurons tagging in the developing V1 105
4.4 – Involvement of cortical neurons in spontaneous and sensory-evoked activity in V1 during development 110
4.4.1 – Involvement of RS neurons in spontaneous and sensory-evoked activity in V1 110
4.4.1 – Involvement of GABAergic interneurons in spontaneous and sensory-evoked activity in V1 115
4.5 – Impact of optogenetic activation of GABAergic interneurons on spontaneous and sensory-evoked activity in the developing V1 120
4.5.1 – Impact of optogenetic activation of GABAergic interneurons on spontaneous activity 120
4.5.2 – Impact of optogenetic activation of GABAergic interneurons on sensory-evoked activity 126
4.6 – Impact of chemogenetic inhibition of SST+ interneurons on *in vivo* activity 129

4.6.1 – Impact of chemogenetic inhibition of SST+ interneurons on spontaneous and sensory-evoked activity in the developing V1 ..... *131*
4.6.2 – Impact of chemogenetic inhibition of SST+ interneurons on spontaneous and sensory-evoked activity in the developing S1BF *135*
4.7 – EFFECTS OF URETHANE ANAESTHESIA ON *IN VIVO* V1 SU ACTIVITY 137
4.8 – SUMMARY OF RESULTS 140

CHAPTER 5 – NETWORKS AND FUNCTIONS OF L6 NEURONS IN THE DEVELOPING MOUSE BRAIN **143**

5.1 – INTRODUCTION 143
5.2 – GABAERGIC NETWORKS OF L6 PYRAMIDAL NEURONS IN PRIMARY SENSORY AREAS OVER EARLY POSTNATAL DEVELOPMENT 144
5.2.1 – GABAergic networks of L6 pyramidal neurons in V1 ..... *144*
5.2.2 – GABAergic networks of L6 pyramidal neurons in S1BF *149*
5.2.3 – Distribution of GABAergic interneurons in V1 and S1BF over early postnatal development *153*
5.3 – GABAERGIC NETWORKS OF L6 CORTICOTHALAMIC AND CORTICOCORTICAL PYRAMIDAL NEURONS IN V1 155
5.4 – INVOLVEMENT OF L6 NEURONS IN SPONTANEOUS AND SENSORY-EVOKED ACTIVITY IN V1 *IN VIVO* 160
5.5 – SUMMARY OF RESULTS 169

CHAPTER 6 - DISCUSSION **174**

6.1 – FEEDBACK AND FEED-FORWARD GABAERGIC NETWORKS BY SOMATOSTATIN INTERNEURONS ACROSS PRIMARY SENSORY AREAS 174
6.2 – PARVALBUMIN INTERNEURONS ESTABLISH THE CANONICAL FEED-FORWARD INHIBITORY MOTIF AT THE TIME OF EYE OPENING IN V1 179
6.3 – A ROLE FOR DIS-INHIBITORY NETWORKS IN STATE-DEPENDENT CONTROL OF SENSORY PROCESSING BEFORE ACTIVE PERCEPTION 180
6.4 – A TRANSLAMINAR GABAERGIC NETWORK BETWEEN SUPRAGRANULAR CORTICAL INTERNEURONS AND L6 PYRAMIDAL NEURONS 183
6.5 – CONCLUSION 185

REFERENCES **187**

Chapter 1

Introduction

The mammalian cerebral cortex is one of the higher achievements of evolution. It supports critical functions for animals and humans like sensory perception, execution of behaviours, learning and memory. All these functions are possible thanks to intricate neuronal networks which, at the highest level of classification, are composed of two main cellular components: glutamatergic excitatory projections neurons and GABAergic inhibitory interneurons. During the process of nervous system development, neurons that populate the cortex have the complex task of finding their place within the cortical network, by establishing synaptic connections with other cell types (Greig et al., 2013). This task becomes even more complex when considering the staggering level of neuronal diversity within excitatory and inhibitory cell classes (Tasic et al., 2018), each likely playing a different role in the mature and developing neuronal networks. Understanding how networks are assembled is a fundamental question for neuroscience. This allows gaining more knowledge on rules that govern neuronal functions in the mature network; in essence, understanding how the brain works by looking at how it is built. On the other hand, knowledge as to how neuronal networks are established might pave the way to understanding mechanisms underlying disorders of the nervous system, such as neurodevelopmental diseases (Marín, 2012).

While neuronal networks are assembled during neocortical development, a general rule that applies is that there must be a balance between excitatory and inhibitory drive, often referred to as E/I balance. Indeed, impairment in the inhibitory side of the balance often leads to abnormalities and pathologies that affect humans. Experimental works in the last few years, however, inspired a transversally different view on the role of inhibition for circuit development, whereby they are dispensable at its earliest stages (Kirmse and Zhang, 2022).

This thesis aimed at addressing the overarching question: *what are the roles and functions of GABAergic interneurons in developing cortical networks?* The model systems used to address that question are the primary sensory cortices of the mouse, which are ideally suited as we have good understanding of their mature networks (Harris and Shepherd, 2015). Primary sensory cortices have the advantage that their "primary" role is to interpret sensory information from the periphery, which can be experimentally controlled and assessed. Throughout the thesis, I will provide a continuous comparison between the primary somatosensory cortex and the primary visual cortex (V1), to also investigate the level as to which developmental rules generalise across similar brain areas. In the next sections, I will briefly review the current knowledge on the role of GABAergic interneurons during cortical development in the mouse, by focusing on previous experiments mostly performed in the primary somatosensory barrel cortex (S1BF). I will then summarise the timeline of early postnatal development of V1.

1.1 – Role of GABAergic interneurons during early postnatal development

During cortical development, excitatory projection neurons originate locally in the dorsal telencephalon from progenitor cells and populate the six-layered cerebral cortex in an inside-out fashion (Greig et al., 2013) . Conversely, GABAergic interneurons, which include one fifth of the total number of cortical cells, originate in the ventral telencephalon, in regions termed ganglionic eminences. They follow complex migratory routes to reach their destination brain region where they integrate with local excitatory neurons (Lim et al., 2018). At the most basic level, GABAergic interneurons can be classified into three main classes, based on the expression of parvalbumin (PV+), somatostatin (SST+) or the serotonin ionotropic receptor (5-HT_3R+), the latter including vasoactive intestinal peptide-expressing (VIP+) interneurons (Rudy et al., 2011a) . These subtypes originate at various times during cortical development, with SST+ interneurons being the earliest to populate the developing cortex (Miyoshi et al., 2007), hence being ideally suited to provide GABAergic signalling early in life (Butt et al., 2017). At the end of the migration route, GABAergic interneurons

establish synapses with locally born excitatory pyramidal neurons, thus providing inhibitory signalling to balance the nascent excitatory drive (Kirmse and Zhang, 2022). Locally born excitatory cells assemble into a canonical cortical circuit, well-known for primary sensory areas, whereby inputs from the periphery are relayed from the primary sensory thalamus to excitatory neurons in cortical layer (L)4, which in turn project to superficial layers, L2/3. Excitatory projections neurons in L2/3 are responsible for lateral communication between cortical areas, besides projecting to L5 and L6 pyramidal cells which provide outputs to sub-cortical structures (Harris and Shepherd, 2015).

Besides this classification into three subtypes, recent transcriptomic endeavours identified up to sixty-one distinct subtypes of GABAergic interneurons (Tasic et al., 2018; Gouwens et al., 2019). Unlike excitatory cells that shows an area-specific distribution, interneurons subtypes are homogeneously distributed across distinct brain areas, pointing to the existence of canonical inhibitory motifs in the brain (Tasic et al., 2018). In line with this, PV+ expressing interneurons have been shown to provide “blanket” inhibitory activity to the surrounding excitatory pyramidal neurons, regardless of the brain area (Packer and Yuste, 2011). Moreover, they show conserved roles in higher-order brain functions such as learning and memory, across multiple brain structures (Khan et al., 2018; Geiller et al., 2021). The view of stereotyped canonical interneurons networks in the mammalian brain is challenged by recent evidence that revealed the existence of differences among brain areas with similar functions. For example, SST+ interneurons in the thalamo-recipient L4 differs in morphology between primary visual and somatosensory cortices, in line with variability observed for L4 excitatory neurons (Scala et al., 2019). Differences between these two areas extend to interneuron subtypes interpreting top-down projections from other cortical areas (Shen et al., 2020). The extent to which inhibitory motifs described in adult animals translate to developing cortical networks is still largely unknown. The diversity between GABAergic interneuron subtypes allows them to provide flexible functions to a rapidly changing network such as the one that characterises developing sensory areas. In the next

sections, I will briefly focus on roles proposed for the two main interneuron subclasses – PV+ and SST+ interneurons – in cortical development.

1.1.1 – Somatostatin-expressing interneurons establish transient GABAergic networks during early postnatal development in the mouse

GABAergic interneurons characterised by the expression of the neuropeptide SST are the earliest to populate the developing cortex (Miyoshi et al., 2007) and are thus ideally suited to provide GABAergic signalling during early life (Butt et al., 2017). SST+ interneurons in the hippocampus have been shown to function as hub cells, coordinating neuronal activity and guiding synaptic integration (Bonifazi et al., 2009; Picardo et al., 2011). At cortical level, the role of SST+ interneurons have been explored primarily in the mouse primary somatosensory cortex responsible for receiving information from the whiskers, termed barrel cortex (S1BF; Staiger and Petersen, 2021). In this area, SST+ interneurons establish functional synapses with excitatory neurons from the first postnatal week of development (Anastasiades et al., 2016), before the appearance of canonical inhibitory motifs by PV+ interneurons (Daw et al., 2007). This period of S1BF development corresponds with the critical period for L4 plasticity when connections between thalamic inputs and L4 thalamo-recipient spiny stellate neurons (SSNs) are established (Crair and Malenka, 1995; Erzurumlu and Gaspar, 2012). At the same time, thalamic inputs target a population of SST+ interneurons in L5b which, in turn, establish reciprocal connectivity with L4 SSNs (Marques-Smith et al., 2016). This network, termed the L5b-L4 loop is rapidly removed after the end of the critical period for plasticity (after P8), when SST+ interneurons are also disengaged from direct thalamic inputs (Marques-Smith et al., 2016; Tuncdemir et al., 2016). By receiving thalamic inputs and projecting to L4 SSNs, this network architecture resembles an immature feed-forward inhibitory motif, that, in mature networks, ultimately involve PV+ interneurons (Cruikshank et al., 2007). During the first postnatal week in S1BF, fast feed-forward inhibition through PV+ interneurons is not functional, and its onset again correspond with the end of the critical period of L4 plasticity (Daw et al., 2007). Critically,

ablation of SST+ interneurons during this period lead to abnormal thalamic connection onto PV+ interneuron (Tuncdemir et al., 2016). This evidence points to a critical role played by SST+ interneurons during the critical period for plasticity in S1BF, when transient circuits support the establishment of the mature network architecture. In line with this, recent experiments showed that conditional ablation of SST+ interneurons lead to impairments in the pattern of spontaneous activity and short-term synaptic plasticity *in vivo* (Baruchin et al., 2021).

All these experiments points to a key role played by SST+ interneurons in S1BF where transient networks function as a scaffold onto which the next stage of network architecture is built. *In vitro* circuit mapping experiments further revealed the level of flexibility of SST+ interneurons in S1BF. Before they innervate L4 SSNs (Marques-Smith et al., 2016), L5b SST interneurons establish transient networks with the prototypical “transient” structure of cortical development, namely the subplate (Ghezzi et al., 2021). Classically, subplate neurons are referred to as a transient cell type that populates the deepest layer of the developing cortex and are ascribed key functions for cortical development (Kanold and Luhmann, 2010). Indeed, they are the first cortical cells to receive thalamic connection and, in turn, project to L4 thalamo-recipient cells (Zhao et al., 2009). Experiments from our lab recently revealed that subplate neurons that are targeted by thalamic inputs, also receive GABAergic inputs from L5b SST+ interneurons in the first 4 postnatal days (Ghezzi et al., 2021).

Finally, after the transient connection between L5b SST+ interneurons and L4 SSNs is removed, around P8, L5b SST+ interneurons projections switch onto supragranular pyramidal neurons, in the days that precede onset of active exploration (Anastasiades et al., 2016). This period corresponds to a moment where plasticity rules in supragranular excitatory neurons changes, allowing for the strengthening of L4 to L2/3 excitatory projections (Wen and Barth, 2011). It appears SST+ interneurons in S1BF, at least those located in L5b, flexibly change their synaptic target over the first two weeks of development,

targeting the site where synaptic plasticity is maximal (subplate neurons first, followed by L4 and L2/3 excitatory neuron in sequence).

1.1.2 – Parvalbumin-expressing interneurons regulate the transition between "critical" developmental periods

PV+ interneurons are the most abundant group of GABAergic interneurons in the cortex and include diverse morphological cell types characterize by fast-spiking properties (Gouwens et al., 2019). Fewer studies focused on the role of PV+ interneuron in early postnatal development due to the late expression of the PV peptide (around P14; del Rio et al., 1994), which limits experiments of circuit dissection, given the unavailability of the specific Cre transgenic mouse line. A large body of literature investigated the role of this interneuron class at later developmental stages, during the critical period for binocular plasticity in V1 (Hensch, 2005). Together with studies performed in early S1BF, PV+ interneurons are thought to regulate the transitions between "critical" developmental periods. For example, in S1BF, L4 PV+ interneurons are integrated in the thalamocortical network at the same time when they establish strong synaptic connections with local excitatory cells, thus establishing the canonical feed-forward inhibitory motif (Daw et al., 2007). All these events occur around the end of the first postnatal week and limit the window of opportunity for classical Hebbian plasticity onto L4 SSNs, thus closing the critical period (Minlebaev et al., 2011). *In vivo* electrophysiological recordings in V1, suggest this transition might be delayed up until eye opening, driven by the late maturation of the feed-forward inhibitory motif by PV+ interneurons (Colonnese, 2014).

In V1, PV+ interneurons are critical regulator of the critical period for binocular plasticity as demonstrated by a variety of studies employing monocular deprivation to trigger this process (Fagiolini et al., 2004; Hensch, 2005). During this period, corresponding to the fourth postnatal week (P21-P28), pyramidal neurons in extragranular layers are particularly sensitive to synaptic plasticity (Trachtenberg et al., 2000), which, in normal conditions, has the objective of matching binocular inputs between thalamocortical and intracortical

connections (Gu and Cang, 2016). The pattern of connectivity between PV+ FS interneurons and excitatory pyramidal neurons is permissive for synaptic plasticity to occur (Kuhlman et al., 2013). Over the course of this period PV+ interneurons undergo changes at the morphological (Chattopadhyaya et al., 2004) and functional level (Yazaki-Sugiyama et al., 2009; Kuhlman et al., 2011), that culminates with the closure of the critical period. Thus, in analogy with the establishment of the feed-forward inhibitory motif for the closure of the early critical period for thalamocortical plasticity, changes in PV+ interneuron networks and functions limit plasticity later in development. Recent experiments however, also highlighted key roles for dis-inhibition of PV+ interneurons by SST+ interneurons in the development of binocular responses (Yaeger et al., 2019) suggesting reciprocal connectivity between different interneuron subclasses are critical during cortical network development.

1.2 – Development of primary visual cortex network and function in the mouse

Studies on the development of the visual system date back to the work of Hubel and Wiesel on the discovery of ocular dominance plasticity (Wiesel and Hubel, 1963) and it is now one of the most well-known brain structures. Its sensory organ, the retina, converts photons into electrical activity and relays visual information to two subcortical structures, the superior colliculus (SC) and the dorso lateral geniculate nucleus (dLGN) of the thalamus (Seabrook et al., 2017). While the former is implicated in a range of networks with sub-cortical structured and higher-order visual cortices, the dLGN is the main gateway for visual information to reach V1. Since the work of Hubel and Wiesel, a large body of literature on the development of the visual system focused on a period that, in mice and rats, starts around the third postnatal week. This period is defined as “critical” for plasticity mechanisms to occur and establish appropriate binocularity (Hensch, 2005; Gu and Cang, 2016). Before that, molecular and functional mechanisms contribute to establish basic features used by the visual system to translate the external world into perception. This thesis will focus on the first three postnatal week, a period termed “precritical” (Feller and Scanziani, 2005), by

investigating how functional properties and neuronal networks at the level of V1 changes over this timeframe and especially around the time of eye opening which, in mice and rats, occur around P14.

1.2.1 – Development of the visual system during the precritical period

In vivo recordings in non-anaesthetised neonatal rats and mice showed that the first two weeks after birth are characterized by dramatic changes in the spontaneous and sensory evoked electrical activity. Observations that visual cortical neurons immediately after eye opening already possess response features typical of adult animals (Rochefort et al., 2011; Ko et al., 2013; Hoy and Niell, 2015; Gu and Cang, 2016), suggest that activity occurring prior to this developmental milestone is important in driving key aspects of network development. A common feature of immature sensory and motor systems is their ability to generate spontaneous synchronous activity. Several lines of evidence point to a significant role for such spontaneous activity in the initial stages of neuronal network wiring (Kirkby et al., 2013), since they provide an ideal substrate for developmental plasticity to occur (Butts and Kanold, 2010). In support of this notion, alterations to such pattern of spontaneous activity can have long-lasting implications on neuronal networks and functions (Huberman et al., 2008). In the rat visual system, *in vivo* activity during the first three postnatal weeks can be divided into three distinct stages (Colonnese et al., 2010). The first period (P0–P7) is termed *physiological blindness of immaturity*, followed by the *bursting period* (P8–P11) and the *acuity period* (>P12). In the mouse, the bursting period lasts two days longer, and terminate in correspondence of eye opening, around P14 (Shen and Colonnese, 2016).

Physiological blindness of immaturity: P0 – P7

During the first postnatal week, the visual system is not responsive to sensory stimulation (Shen and Colonnese, 2016) and hence its activity is dominated by prolonged period of network silence intermitted by brief bursts of activity initiated in the retina, termed retinal waves (Blankenship and Feller, 2010). Experimental manipulation of these spontaneous

events has been extensively used to understand the relative contribution of emergent activity versus molecular cues in driving the early maturation of visual cortical maps. Long-lasting research question in developmental neuroscience, still partially unresolved, is whether activity in the visual system is permissive or instructive for map formation (Crair, 1999).

Retinal waves originate in the retina, where retinal ganglion cells (RGCs) spontaneously fire bursts of action potentials that are transmitted to neighbouring cells and sweep the retinal surface as depolarizing waves (Huberman et al., 2008; Blankenship and Feller, 2010). In rodents prior to birth, retinal waves are dependent on gap junctions while and are termed phase I retinal waves; their function for network development and visual map formation is still largely unknown. Phase II retinal waves occur from birth to the end of the first week (P7-P8) and are dependent on cholinergic neurotransmission in the retina. Finally, phase III retinal waves occur during the second postnatal week in mice, prior to eye opening (~P14) and they are dependent upon glutamatergic neurotransmission (Kerschensteiner, 2016). A large body of research focused on retinal waves, trying to establish their contribution to visual map formation and the development of early networks in the visual system. These studies explore subcortical nodes in the visual system, specifically the dLGN and the SC, focusing on two low-order readouts for visual map formations: retinotopic arrangements and eye-specific segregation. More recently, following observations that retinal waves are relayed up the hierarchy of the visual system to V1 and higher-order visual areas (Ackman et al., 2012; Gribizis et al., 2019), the focus of the research field expanded to the cortex, where cortical network and activity undergo dramatic changes in the period preceding eye opening (Shen and Colonnese, 2016; Colonnese et al., 2017). This would allow gain an understanding as to how higher-order receptive field properties that characterizes visual cortical neurons, such as orientation and direction selectivity, are established during development.

Phase II retinal waves occurring during the first postnatal week in the mouse, are now thought to be instructive, and not simply permissive, to establish retinotopic maps and eye-specific segregations of RGC fibres, in cooperation with a variety of molecular mechanisms like axon guidance molecules. The dependency of phase II retinal waves on cholinergic neurotransmission made these spontaneous activity events a target for pharmacological and genetical interventions. Moreover, the disappearance of cholinergic retinal waves during the second postnatal week, also allowed investigating the specific role of spontaneous activity during the first week of postnatal development, a period where RGCs do not respond to light.

Pharmacological (Penn et al., 1998) and genetic (McLaughlin et al., 2003) abolishment of cholinergic retinal waves induced defects in the refinement of retinal projections in the SC (McLaughlin et al., 2003; Chandrasekaran et al., 2005) and thalamocortical innervation of V1 (Cang et al., 2005). In addition, functional techniques showed impairment of gross functional maps in both cortex (Cang et al., 2005) and SC (Mrsic-Flogel et al., 2005) as well as defects in synaptic plasticity mechanisms at the retinocollicular synapse (Shah and Crair, 2008). Recent experiments with more refined genetic strategies provided experimental proof of an instructive role for cholinergic retinal waves for both retinotopic map refinement and eye-specific segregation. In particular, the pattern of local correlated activity between neighbouring RGCs was shown to determine refinement of gross retinotopic projections in both dLGN and SC (Xu et al., 2011, 2015, 2016a; Burbridge et al., 2014) whereas overall level of activity is important for eye-specific segregation by promoting competition between the two eyes (Zhang et al., 2012; Burbridge et al., 2014; Xu et al., 2015, 2016a).

At the level of the thalamocortical system, retinal waves trigger spindle bursts, spindle-like shaped oscillatory activities (10-30 Hz) lasting for few seconds and occurring once every 1-2 minutes (Hanganu et al., 2006) nested within slower oscillations (Colonnese and Khazipov, 2010). Spindle bursts are first originated in the visual thalamus, thanks to the interaction between excitatory thalamic relay cells and the inhibitory thalamic reticular

nucleus (TRN; also called nucleus reticularis thalami, nRT; Murata and Colonnese, 2016). At the cortical level, spindle bursts entrain cortical V1 neurons in the same oscillatory activity (Colonnese et al., 2010, 2017; Shen and Colonnese, 2016); however, despite the thalamic origin, corticothalamic feedback is critical already at this stage to sustain spindle-bursts and amplify retinogeniculate activity (Murata and Colonnese, 2016). It is currently unknown how activity during spindle bursts impact the developing cortical networks at the level of V1.

Bursting period: P8 – P14

Around P8, immature cortical responses to visual stimuli can be recorded within the thalamo-recipient L4 with only minor differences between rats (Colonnese et al., 2010) and mice (Shen and Colonnese, 2016). Spontaneous retinal waves are still present and dependent on glutamatergic neurotransmission (phase III) from retinal bipolar cells to RGCs (Kerschensteiner, 2016). The contribution of glutamatergic retinal waves to visual map formation is less understood; since they coexist with early visually evoked activities generated through the closed eyelids (Krug et al., 2001; Akerman et al., 2002; Shen and Colonnese, 2016), it is also contentious what is the relative role of spontaneous and sensory-evoked activity for maturation of connectivity in the visual system. Current knowledge suggests retinotopic refinement and eye-specific segregation are largely in place once cholinergic waves disappear and alterations of correlated activity among RGCs between P10 and P13 only led to subtle alterations of retinogeniculate projections refinement (Blankenship et al., 2011). Moreover, defects induced by genetic or pharmacological elimination of cholinergic waves cannot be fully rescued by phase III waves activity (Chandrasekaran et al., 2005; McLaughlin et al., 2003; Zhang et al., 2012), strengthening the idea of a “critical period” for visual map formation restricted to the first postnatal week.

Recent evidence, however, highlighted the importance of phase III glutamatergic waves and shed light on their relationship with the earliest form of sensory-evoked activity. Indeed,

in *in vitro* retinal preparations from P10-P13 mice, light flashes can trigger retinal waves whereas no sensory-induced activity could be evoked in retinal preparations from P6-P8 mice (Tiriac et al., 2018). Moreover, dark rearing for 1 week prior to eye opening led to alterations in retinogeniculate refinement (Tiriac et al., 2018). Although this study is in apparent disagreement with other studies showing maturation of properties of the visual system to occur similarly in dark-reared and light-reared animals (Hooks and Chen, 2006; Rochefort et al., 2011; Hagihara et al., 2015), it also points to early sensory-evoked activity having an impact on the maturation of the visual system. Elegant electrophysiological network mapping studies of the retina during the period of glutamatergic retinal waves, pointed to another possible function for such emergent activity. It was shown ON and OFF bipolar cells, activated by light stimuli turning on or off respectively, are progressively recruited during retinal waves. Specifically, ON bipolar cells fire one second before OFF bipolar cells (Kerschensteiner and Wong, 2008), whose are hyperpolarized when ON bipolar cells are entrained in bursts (Akrouh and Kerschensteiner, 2013). For this reason, it was proposed that glutamatergic retinal waves may promote ON/OFF segregation at the level of the LGN and they could contribute to the formation of orientation selective receptive field in V1 (Kerschensteiner, 2016).

In agreement with the light-dependency of glutamatergic retinal waves, cortical responses to visual stimulation before eye opening are characterized by long-latency, sustained multi-unit activity (MUA) firing, with appearance of sensory-evoked oscillatory activity (Shen and Colonnese, 2016). In the rat, a faster, initial oscillatory response in the gamma frequency (termed early gamma oscillation, EGOs; Minlebaev et al., 2011) is followed by a second oscillatory activity resembling spindle burst (termed delta brushes; Colonnese et al., 2010). Although MUA firing is primarily initiated in L4, it rapidly engages all cortical layers in a highly synchronous fashion. In the mouse, V1 responses are characterized exclusively by beta-band oscillations (i.e., delta brushes) while early gamma oscillations are not evoked. However, a rapid initial response to visual stimuli resembling mature visual evoked potential

can already be recorded from around P10 (Shen and Colonnese, 2016). At single cell level, visual stimulation often leads to the appearance of plateau potentials in V1 neurons, made possible by the presence of only weak, long-latency, intracortical feedback inhibition (Colonnese, 2014).

Retinal waves and spindle-bursts (or their sensory-evoked counterpart, delta brushes) have been proposed to create ideal windows for developmental synaptic plasticity to occur, to establish the first-level, coarse maps between the sensory periphery and the primary cortex (Butts and Kanold, 2010). During such plasticity windows, the peripheral information (being spontaneous or evoked) is dramatically amplified (Colonnese et al., 2010, 2017), leading to multiple replays through oscillations (Minlebaev et al., 2011). Transmission of retinal waves from the retinal to the dLGN and SC agrees with a burst-time-dependent plasticity where sustained postsynaptic depolarization within dLGN neurons is coupled with spiking of presynaptic RGCs to strengthen retinogeniculate synapses (Butts et al., 2007; Shah and Crair, 2008). Conversely, spindle-bursts in the thalamocortical network are more suited to trigger classical Hebbian spike-time-dependent plasticity (STDP; Butts and Kanold, 2010). Replay of sensory input during sustained oscillations has the role of opening multiple windows for synapse strengthening trough STDP rules (Minlebaev et al., 2011). It is noteworthy, however, that within periods of sustained activity, correlation between individual V1 cortical neurons is lower than expected by chance, questioning the STDP model (Colonnese et al., 2017). Whether a similar burst-based plasticity rule or another form of non-Hebbian plasticity is enacted within the thalamocortical loop is still unclear.

Beside activity originated in the retina, whether spontaneous or light-induced retinal waves, cortical activity before eye opening become less dependent on peripheral drive (Gribizis et al., 2019) and can sustain retinal-independent activity in the form of calcium events that entrain a large fraction of cortical neurons (Siegel et al., 2012). Computational models suggest that, while retinal-dependent activity support synaptic plasticity, cortex-dependent

activity provides homeostatic plasticity mechanism to regulate synaptic strength (Wosniack et al., 2021).

Acuity period: after eye opening

Over the few days preceding eye opening (at P14), there is a progressive maturation of the visual response with reduction of the long latency slow component and appearance of the mature visual-evoked potential responses, characterized by short latency and short duration. Remarkably, the transition between the bursting period and acuity period occurs in a brief time that, in mice, correspond with eye opening (P14; Shen and Colonnese, 2016) whereas in the rat occurs two days earlier (P12; Colonnese et al., 2010). This critical developmental milestone is accompanied by numerous other changes including (1) increase in continuity of baseline spontaneous activity (Shen and Colonnese, 2016; Colonnese et al., 2017); (2) increased cortical firing activity during movement (Murata and Colonnese, 2018); (3) maturation of cortical inhibition that abolishes plateau potentials (Colonnese, 2014); (4) sparsification of supragranular neuron responses to visual stimuli (Rochefort et al., 2009); (5) and onset of inhibitory effect of the corticothalamic network between V1 and dLGN (Murata and Colonnese, 2016).

Despite this extensive knowledge, it is complex to determine the causality between all these factors. On one hand, maturation of state-dependency and neuromodulatory networks might play a key role. On the other hand, the maturation of the visual evoked potential observed at thalamic and cortical level might involve maturation of retinal activity, development of neuronal networks within the thalamus, or corticothalamic feedback (Murata and Colonnese, 2016). At cortical level, short responses to visual stimulation are primarily achieved thanks to the maturation of feed-forward inhibition. *In vivo* patch-clamp recordings in awake neonatal rats showed that visual stimulation recruits GABAergic postsynaptic currents on L4 excitatory neurons during the bursting period. However, they undergo a dramatic reduction in latency as soon as visual-evoked potential is observed,

suggesting that maturation of feed-forward inhibition occurs at comparable time course (Colonnese, 2014). As in other sensory systems, maturation of cortical feed-forward inhibition rapidly contrasts excitatory currents on cortical neurons (Cruikshank et al., 2007; Daw et al., 2007), thus effectively suppressing amplification of thalamic responses. Remarkably, Colonnese (2014) also suggested that feedback inhibition is functional before the feed-forward motif, implying specific forms of inhibitory networks move through distinct developmental trajectories. A cardinal role for feed-forward inhibition in this context is plausible, given its well-known importance for determining the timeline of the critical period for ocular dominance plasticity (Hensch, 2005).

Immediately following eye opening, individual neurons in V1 already display several features that characterise adult cortical neurons such as receptive field structure (Ko et al., 2013), orientation and direction selectivity (Rochefort et al., 2011), spatial frequency preference, and linearity of responses (e.g., presence of simple and complex cells; Hoy and Niell, 2015) but also matching of binocular thalamic inputs (Gu and Cang, 2016). This might suggest that spontaneous and sensory-evoked activity occurring prior to eye opening and described in the previous paragraph might impact the correct development of the neuronal networks underlying those response features. The period between eye opening and the onset of the critical period for ocular dominance plasticity (onset around P21; Hensch, 2005) is still highly dynamic. *In vivo* electrophysiology and two-photon Ca^{2+} imaging showed that response features such as orientation and direction selectivity undergo significant maturation in the 5-7 days following eye opening (Rochefort et al., 2011; Hoy and Niell, 2015), together with intracortical connectivity (Ko et al., 2013; Miao et al., 2016) and binocular responses (Smith and Trachtenberg, 2007). Around the same time, research has shown changes at the level of GABAergic interneurons, including selectivity of PV+ cells to visual stimuli (Kuhlman et al., 2011) and impact of neuromodulatory activity onto SST+ interneurons (Yaeger et al., 2019).

1.2.2 – Developing networks of the primary visual cortex

Despite the large body of evidence accumulated concerning changes in V1 around the time of eye opening at the system level, there is still relatively little knowledge on the underlying neuronal cortical network. Investigation of neuronal networks at each developmental stage is critical to fully understand the complex changes occurring at the higher level as well as to provide opportunities to affect the network through external interventions. A key aspect of developing networks, at least at the level of the cerebral cortex, is the presence of transient connectivity motifs that are readily eliminated once their role is no longer necessary (Butt et al., 2017; Kanold and Luhmann, 2010). However, whereas the presence of transient developmental networks has been extensively studied in other primary sensory areas, only a minority of studies investigated this issue in visual cortex around the time of eye opening.

The most well-known transient network established during early postnatal development in V1 involves subplate neurons. The subplate is a transient structure located between the developing cortical plate and the white matter, populated by a heterogeneous population of neurons showing advanced maturation compared to any other cortical neurons already during the earlier postnatal days (Kanold and Luhmann, 2010). Subplate neurons are the main recipient of excitatory thalamocortical connections prior to the innervation of the thalamo-recipient L4 and they are thought to establish a transient excitatory network with L4 excitatory neurons (Zhao et al., 2009; Wess et al., 2017). Through this connection they are critical for the maturation of thalamocortical connectivity onto L4 neurons, by promoting developmental plasticity mechanisms. The importance of SPNs for early postnatal development has been demonstrated in several primary sensory areas, including V1.

While subplate neurons may be important in visual cortex to lie the foundation of the thalamocortical connectivity and retinotopy during early postnatal development, only few other studies focused on V1 networks around the time of eye opening. Guan et al. (2017) demonstrated that, in L2/3, eye opening leads to rearrangement of inhibitory connectivity

onto pyramidal neurons. Connectivity from SST+ interneurons to pyramidal neurons undergoes a reduction in strength when compared to the period preceding eye opening. Conversely, PV+ interneurons undergo a change in the opposite direction, with increased strength of connectivity onto pyramidal neurons observed after eye opening. The unaffected connectivity from SST+ to PV+ interneurons effectively led SST+ interneurons to switch from an inhibitory role prior to eye opening to a disinhibitory role (via inhibition of PV+ cells) afterwards, with implications for synaptic plasticity (Yaeger et al., 2019). Before eye opening, the inhibitory effect of SST+ interneurons in V1 limits the participation of excitatory neurons to retinal-driven calcium events as well as their lateral spatial spread (Leighton et al., 2021). This study is in line with similar experiments performed in S1BF, demonstrating that GABAergic interneurons restrict correlated activity within assemblies of neurons (Duan et al., 2020; Modol et al., 2020).

1.3 – Thesis outline

The overarching aim of this thesis is to deepen our understanding of the neuronal networks and function of cortical GABAergic interneurons during early postnatal development in the mouse. Detailed knowledge regarding the role of spontaneous and sensory-evoked neuronal activity requires insights on the underlying neuronal network that generate, propagate, or regulate it. Conversely, knowledge of the network architecture paves the way for technological tools to interrogate the role of specific cell types or connections for a given network function. Throughout the thesis, I will focus on the earliest GABAergic interneurons that populate the neonatal cortex, those deriving from the medial ganglionic eminence (namely, SST+ and PV+ interneurons). Their network and functions will be compared between two primary sensory areas, V1 and S1BF. The specific aim of each experimental chapter of the thesis are summarised below.

Chapter 3 aims at providing a comprehensive description of the developing neuronal networks in V1. I employed a combination of *in vitro* electrophysiology and optical techniques to describe connectivity between genetically defined GABAergic interneurons

and excitatory cells at different ages. Specifically, after an initial electrophysiological and morphological characterisation of pyramidal neurons and GABAergic interneurons, I will focus on describing the timeline of GABAergic innervation of excitatory neurons throughout cortical layers. I will next focus on SST+ interneurons, to reveal whether they establish similar reciprocal connectivity patterns with excitatory neurons compared to S1BF. Subsequently, I will investigate the timeline for the establishment of the dis-inhibitory network between SST+ and PV+ interneurons in both V1 and S1BF. Finally, I will provide the first characterisation, to the best of my knowledge, on the development of functional thalamocortical innervation of pyramidal cells and GABAergic interneurons in V1.

Chapter 4 will tackle questions related to the function of GABAergic interneurons during early spontaneous and sensory-evoked activity in V1. By taking advantage of *in vivo* electrophysiology and optogenetics, I will tag genetically defined GABAergic interneurons to understand their involvement in spontaneous spindle bursts (the corresponding cortical activity to retinal waves) and early sensory-evoked activity. Through optogenetic and chemogenetic interventions to activate or inhibit SST+ interneurons, I will provide insights as to their role in regulating cortical activity.

Research thus far, including the previous two chapter, focused on the input layers of the cortex, L4. ***Chapter 5*** will focus on one of the output neurons in primary sensory areas, namely L6 pyramidal neurons. Inspired by findings reported in the previous chapters, I will investigate the development of GABAergic networks onto L6 pyramidal neurons, by comparing V1 and S1BF. Next, I will target a specific subpopulation of corticothalamic L6 pyramidal neurons for *in vitro* circuit mapping and *in vivo* electrophysiological experiments, to provide insights as to how cortical output cells are integrated in the developing network.

Chapter 2

Materials and methods

2.1 – Animal models

All experiments were approved by the University of Oxford ethical review committee and performed in accordance with Home Office personal (I77C5C5C5) and project (P861F9BB7) licenses under the UK Animals (Scientific Procedures) 1986 Act. The following mouse lines were used *SST-ires-Cre* (*Sst*$^{tm2.1(cre)Zjh}$*/J*), *Lhx6-eGFP* (*Tg(Lhx6-EGFP)BP221Gsat*), *Ai32*(*Gt(ROSA)26Sor*$^{tm32(CAG-COP4*H134R/EYFP)Hze}$*/J), Ai9* (Cg-*Gt(ROSA)26Sor*$^{tm9(CAG-tdTomato)Hze}$/J), *Lpar1-eGFP* (*Tg(Lpar1-EGFP)GX193Gsat*), *Nkx2-1-Cre* (*Tg(Nkx2-1-cre)2Sand/J*), *Ntsr1Cre-GN220* (*Tg(Ntsr1-cre)GN220Gsat*), *P2X2R* (*R26::P2x2r-EGFP*), and *Olig3-Cre* (*Olig3*$^{tm1(cre)Ynka}$). Experimental double or triple transgenic neonatal mice of either sex were obtained by targeted breeding pairs and used between postnatal day (P)5 and P18. For all experiments, data was split into 3 developmental windows: P5-P8, P9-P13, and P14-P18.

2.2 – *In vitro* electrophysiology

Neonatal mice were anaesthetised with 4% isoflurane (in 100% O_2) prior to decapitation followed by rapid dissection of the cerebral cortex in cold carbogenated (95% O_2 + 5% CO_2) cutting artificial cerebrospinal fluid (ACSF) of the following composition (in mM): 72 sucrose, 83 NaCl, 2.5 KCl, 26 $NaHCO_3$, 1 NaH_2PO_4, 3.3 $MgSO_4$, 0.5 $CaCl_2$, 10 glucose (300-310 mOsm; all chemicals were purchased from Sigma unless otherwise stated). Coronal cortical slices were cut in cold cutting ACSF using a vibratome (Vibratome 3000 Plus, The Vibratome Company or VT1200, Leica) and allowed to recover in cutting ACSF maintained at 34°C for 30 min and then at room temperature (RT) for a minimum of 30 min. Selected slices for recordings were moved to a recording chamber superfused with recording ACSF at RT of the following composition (in mM): 119 NaCl, 2.5 KCl, 26 $NaHCO_3$, 1.3 NaH_2PO_4, 1.3 $MgSO_4$, 2.5 $CaCl_2$, 10 glucose (300-310 mOsm).

Target neurons for *in vitro* electrophysiological recordings (pyramidal cells, eGFP-expressing interneurons, or tdTomato-expressing cells) were visualized through infrared (IR)-differential interference contrast (DIC) microscopy using a 40X objective. Layer location of the recorded cell was confirmed through IR-DIC at 10X or 4X magnification: layer boundaries could be distinguished according to darkness differences in the image. Whole-cell patch-clamp recordings were performed using a Multiclamp 700B amplifier and a Digidata 1440A digitizer (Molecular Devices, US). Target neurons were patched with borosilicate glass micropipettes (Harvard Apparatus, UK; 6-9 MΩ resistance), forged using a PC-100 puller (Narishige, Japan). For GABAergic connectivity experiments, recording pipettes were filled with a Cs-based intracellular solution of the following composition (in mM): 100 gluconic acid, 0.2 EGTA, 5 MgCl2, 40 HEPES, 2 Mg-ATP, 0.3 Li-GTP (pH 7.2 using CsOH; 270-280 mOsm). When recording intrinsic properties or glutamatergic connectivity, pipettes were filled with a K-based intracellular solution of the following composition (in mM): 128 KGluconate, 10 HEPES, 4 NaCl, 5 Mg-ATP, 1 Li-GTP, 0.5 $CaCl_2$ (pH 7.2 using KOH; 270-280 mOsm). For loose-seal cell-attached recordings, pipettes were filled with recording ACSF. To allow for morphological reconstruction of the recorded neurons, the internal solution was supplemented with Biocytin (0.3%). All recordings were sampled at 20 kHz. Cell input resistance (R_{in}) was measured using a brief (50 ms) negative voltage pulse (10 mV) from holding potential (V_h) of −60 mV. Access resistance (R_a) was monitored during recording and not compensated; recordings were discarded if R_a increase more than 20% of its initial value.

2.2.1 – Intrinsic electrophysiological properties

To investigate intrinsic electrophysiological properties, patched neurons were recorded in current-clamp configuration and held at their resting membrane potential (RMP). Negative and positive current steps (500 ms) of increasing amplitude (multiples of 5, 10, 20 pA, depending on cell type and developmental age) from RMP were employed and the voltage traces recorded. Intrinsic electrophysiological data were analysed through a custom-made

script written in Python (Jupyter Lab v1.0.2) to extract 11 electrophysiological features, with similar methods to Scala et al. (2019). Passive features investigated were R_{in}, RMP, membrane time constant (Tau), rheobase, and hyperpolarisation-induced voltage sag. Active properties extracted from the data were maximum firing frequency (Max Firing), adaptation Index, action potential (AP) threshold, AP half-width, AP height, and AP afterhyperpolarizing potential (AHP). R_{in} was calculated as the regression slope of the steady-state membrane voltage vs. the current injected during hyperpolarising steps. RMP was calculated as the median value of baseline voltage over all recorded sweeps before current injection. Membrane Tau was obtained from a mono exponential fit to the voltage obtained during a small negative current step. The voltage sag was measured as the difference between instantaneous and steady-state voltage during a hyperpolarising current step that allowed the voltage to drop close to −100 mV. The rheobase was set as the current value that elicited only one spike. Max Firing was obtained from the maximum number of spikes elicited during any of the depolarizing current steps. The adaptation index was defined as the ratio between the second and the first inter spike interval, for current sweeps that elicited half maximal firing frequency. AP features (threshold, half-width, height, and AHP) were calculated from the very first spike fired by each neuron. Of these 11 features, a subset of 8 was selected (all except for adaptation index, voltage sag, and AP AHP which displayed large within-group variability) to compute a cell maturity index which describes the relative maturation of individually recorded cells compared to cells recorded in the last developmental window. Cell maturity index was defined as the average ratio between individual values of each electrophysiological feature and the mean value for that feature for cells in each group recorded at P14-P18.

2.2.2 – Laser-scanning photostimulation

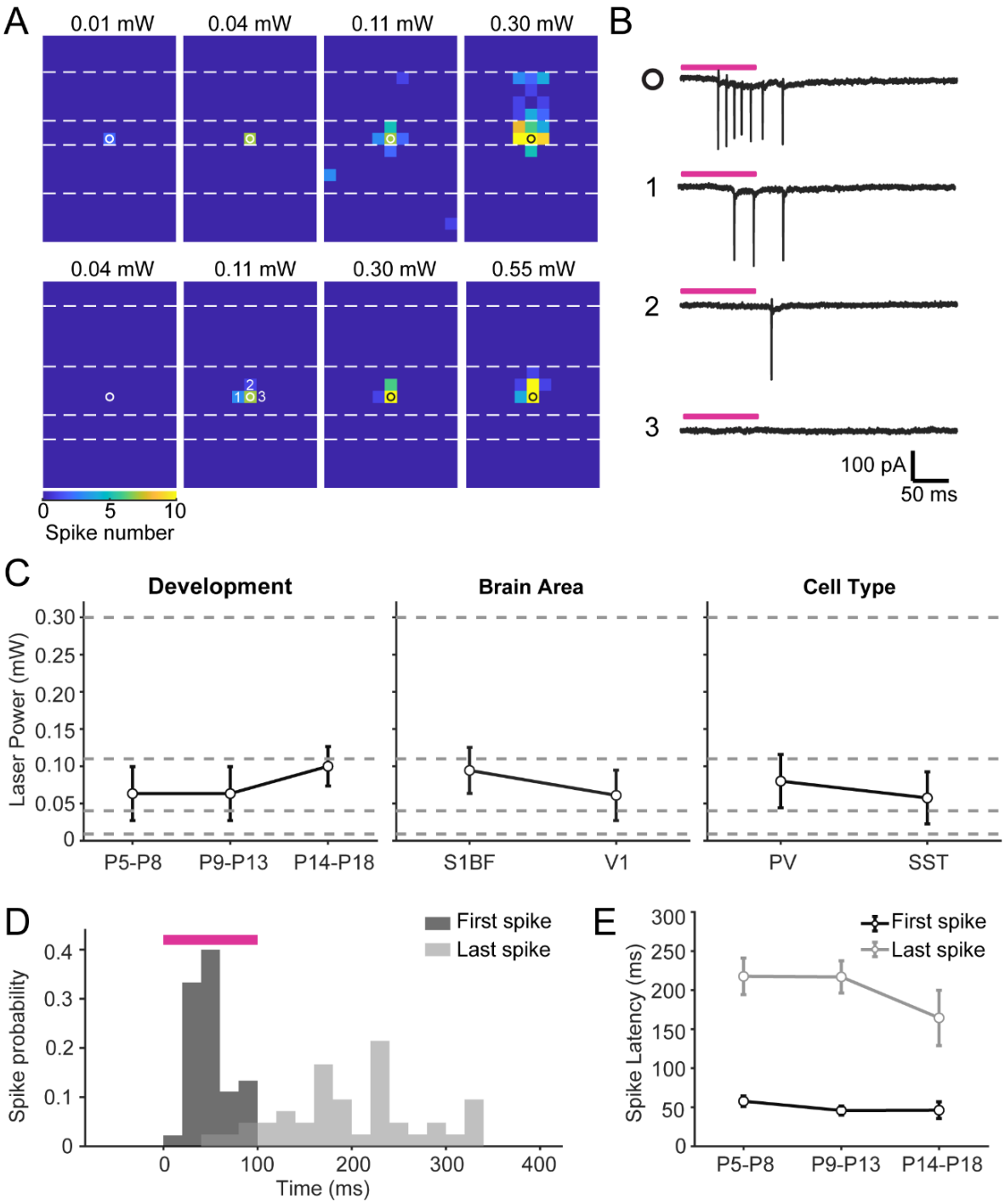
Laser-scanning photostimulation (LSPS) was performed as previously described (Anastasiades and Butt, 2012; Anastasiades et al., 2018); this technique allows stimulation of a portion of presynaptic neurons (~50 µm area) to the recorded cell and their localization

within the cortical column. Prior to photostimulation, slices were maintained for a minimum of 6 min in high-divalent cation (HDC) ACSF of the same composition of the recording ACSF but with higher concentration (4 mM) of $MgCl_2$ and $CaCl_2$ and supplemented with MNI-caged glutamate (200 µM; Tocris Bioscience, UK) or DMNPE-caged ATP (200 µM; Tocris Bioscience). Ultraviolet (UV) laser pulses (355 nm; DPSL-355/30, Rapp OptoElectronic, Germany) were directed to the slices through a galvanometer scanner system (UGA-42; Rapp OptoElectronic) and focused through a 10X dry objective. LSPS grid was characterized by 11x17 spots stimulated in a pseudorandom sequence and spaced ~50 µm; long duration (100 ms) laser pulses were administered at 1-2 Hz frequency. To record the whole extent of the cortical thickness, LSPS grid was moved and for each grid position a minimum of 3 sequences were administered and current traces recorded. For GABAergic connectivity experiments, laser-evoked inhibitory postsynaptic currents were recorded by clamping the cell near the reversal potential for glutamate (~0 mV; corrected for liquid junction potential of 13 mV for the Cs-based intracellular solution). For glutamatergic connectivity experiments, laser-evoked excitatory postsynaptic currents (EPSCs) were recorded by clamping the cell near RMP (V_h = −60 mV).

Analysis of LSPS data was performed with a customized MATLAB (R2020a, MathWorks) toolbox personally developed. Analysis of this dataset requires the definition of a putative window for monosynaptic connectivity following the laser stimulus. For glutamatergic connectivity mapping, this window was set according to previously published data, obtained in mouse at comparable ages (40 – 337 ms; Anastasiades and Butt, 2012). For GABAergic connectivity mapping, control experiments were performed to determine the putative monosynaptic window for analysis as well as to calibrate the power of the laser used for further experiments. Lhx6-eGFP+ interneurons in layers 2-5 (n = 19) of visual and somatosensory cortices were targeted for loose-seal cell-attached electrophysiological recordings. Application of the standard LSPS protocol at multiple laser power levels triggered spiking activity in the recorded cell (**Fig. 2.1B**) used to build cell spiking maps (**Fig. 2.1A**). Optimal laser power was selected as the one capable of triggering robust firing

of the cell when the laser was fired in its exact location and weak or no spiking activity when the laser was fired at neighbouring locations in the map (0.04 mW in the upper example cell in **Fig. 2.1A** and 0.11 mW in the lower example cell). While minor differences between optimal laser power for cells in distinct brain areas were observed (**Fig. 2.1C**), for all LSPS experiments described in this thesis laser power was usually set to 0.11 mW. At these optimal laser settings, an average of 6.4 ± 4.2 (standard deviation, SD) action potentials were fired when the laser targeted the position of the cell against 2.0 ± 1.4 (SD) when the laser was targeted 50 µm away. Analysis of spike times at the optimal laser power (**Fig. 2.1D**) also allowed to determine the putative monosynaptic window for analysis of LSPS data. The lower boundary of the putative monosynaptic window was chosen as the average first spike latency at each developmental window (**Fig. 2.1E**) whereas the upper boundary was chosen as 100 ms longer than the average last spike latency (P5-P8: 57 – 317 ms; P9-P13: 45 – 317 ms; P14-P18: 46 – 264 ms; all values are referred to the onset of the laser stimulus).

Fig. 2.1 (next page). Laser calibration and monosynaptic window for laser-scanning photostimulation experiments. (A) Heatmaps representing the number of spikes fired by a recorded Lhx6+ interneuron in loose-seal cell-attached configuration during laser-scanning photostimulation (LSPS) and glutamate uncaging, at different ultraviolet (UV) laser power levels. Top, representative cell recorded in primary visual cortex (V1); bottom, representative cell recorded in primary somatosensory barrel cortex (S1BF).
(B). Representative traces from the cell shown in A (bottom); purple lines indicate timing of the UV laser pulse, numbers (0-3) indicate distinct positions in the map (indicated in A bottom as well).
(C) Error bar plot (mean ± standard deviation, SD) of optimal laser power for triggering spiking in Lhx6-eGFP+ interneurons at different developmental stages (left), different brain areas (middle), and for different interneuron subtypes (putative parvalbumin-expressing, PV+; somatostatin-expressing, SST+). There are statistically significant effects of the factor "*Brain Area*" (3-way analysis of variance (ANOVA): $F(1,13) = 16.0$, $p = 0.001$) but not "*Development*" ($F(2,13) = 2.5$, $p = 0.12$) or "*Cell Type*" ($F(3,13) = 2.9$, $p = 0.08$).
(D) Histogram of spike probability vs. latency from laser onset (set at 0; laser pulse indicated by purple line), for the first spike (dark grey) and last spike (light grey) triggered by optimal laser stimulation on the position of the cell for Lhx6+ interneurons.
(E) Error bar plot (mean ± SD) of the average first and last spike latency from laser onset at different developmental window, used to determine the putative monosynaptic window.



For GABAergic connectivity mapping, laser evoked inhibitory postsynaptic currents (IPSCs) were identified as outward events occurring within the monosynaptic window previously determined (**Fig. 2.2B**). Within this monosynaptic window, whenever the current traces crossed a threshold set at 6 times the SD of the baseline current, the area under the curve (AUC) was measured as a proxy of the strength of the connectivity. For glutamatergic maps, all EPSCs in the trace were identified with the template search event detection algorithm

implemented in Clampfit (v10.7, Molecular Devices). Only EPSCs falling within the monosynaptic window were selected and their amplitude summed in each pixel of the LSPS grid. Multiple maps were then averaged, layer boundaries were manually determined using the DIC image acquired under 10X magnification (**Fig. 2.2A**) and the final heatmap was generated (**Fig. 2.2C**). Normalized connectivity maps were obtained by dividing value in each spot by the sum of all pixels. Columnar profiles were obtained by summing all values for each line in individual heatmaps; layer distribution of inputs was calculated by summing all inputs occurring in all pixels belonging to a given cortical layer. Total inputs were obtained by summing values in each pixel of the map. Average maps per groups were obtained by aligning each individual map to the L4-L5 boundary and averaging corresponding pixel values.

Cluster analysis of LSPS maps was performed by grouping all maps into a single observation/feature matrix, where each map is represented by a row and corresponding location in the map are organized in the same column. Dimensionality reduction was performed with a truncated singular value decomposition (SVD) of the matrix to obtain the first 6 singular vectors and values, used to build a reduced matrix. K-means clustering was then applied to the reduced matrix, varying the number of clusters (K) from 2 to 10; 1.000 iterations of the K-means clustering algorithm were repeated for each K and the optimal K was found as the one yielding the higher mean silhouette value. For representation purposes, the original matrix was decomposed with a principal component analysis (PCA) and the first two principal components plotted.

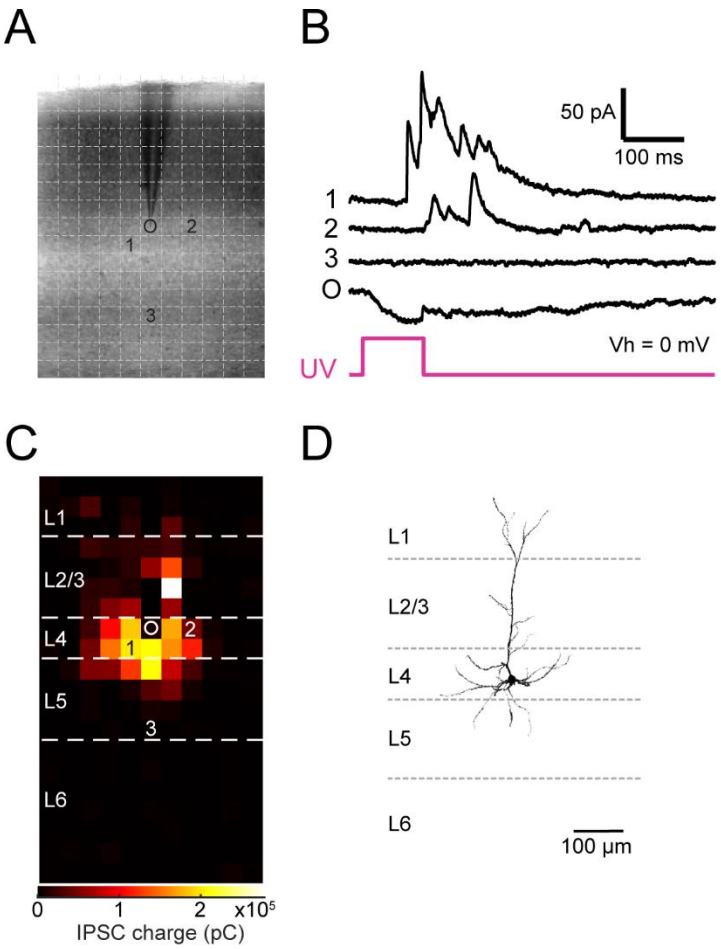


Fig. 2.2. Mapping cortical GABAergic networks with LSPS and glutamate uncaging. (A) Differential interference contrast (DIC) image (10X) of a V1 cortical slice with a pyramidal cell in layer (L)4 patched. Superimposed dashed lines indicate the grid for LSPS experiments.
(B) Representative current traces (holding potential, V_h = 0 mV) of inhibitory postsynaptic currents (IPSCs) obtained by stimulating pixel locations (0-3) in the grid in A with a pulse of UV laser (indicated by purple line).
(C) Heatmap of GABAergic connectivity obtained from traces shown in B (see corresponding pixel locations indicated by numbers 0-3). White circle indicates location of the cell in the map. Dashed horizontal lines indicate approximate layer boundaries determined from the DIC picture in A.
(D) Morphological reconstruction of the dendrite of the L4 pyramidal neuron shown in A-C.

2.2.3 – In vitro *optogenetics*

In vitro optogenetics experiments were performed using a 470 nm light emitting diode (LED; Thorlabs Inc., US or CoolLed, UK); blue light was administered on the slice through a 40X objective to trigger neurotransmitter release from the synaptic terminals of Cre-expressing cell axons. Light-evoked IPSC were recorded voltage-clamping the target cell near the reversal potential for glutamate (V_h = 0 mV) whereas EPSCs were recorded near RMP (V_h = −60 mV). Brief (1 or 10 ms) LED pulses were used to trigger synaptic events in the recorded cell; an inter-stimulus interval of 20-50 s was used to allow for channelrhodopsin-

2 (ChR2) recovery. Different LED power intensity were employed to determine power-dependent responses of recorded neurons. When studying GABAergic connectivity, a minimum of 6 trials were recorded for each LED power intensity value. For thalamic input experiments, the minimal stimulation power value was found by increasing the LED power in consecutive sweeps; a minimum of 6 trials were then recorded at the minimal stimulation power level.

Analysis of *in vitro* optogenetics data were carried out with customized scripts in Python. Light-evoked synaptic events were identified when the LED stimulus induced a deflection in current larger than 9 times the SD of the baseline. A large monosynaptic window (0 – 50 ms from LED stimulus onset) was used to account for possible developmental effects on ChR2 and study all kinds of responses triggered by the stimulus. For events within the monosynaptic detection window, synaptic event features were measured, such as peak amplitude, onset latency (obtained by linear regression fit between the value at 20 and 80% of the peak amplitude), onset jitter (standard deviation of the latency), and decay time constant (tau; monoexponential fit to the decay phase of the synaptic event). Percentage of synaptic events occurrence was calculated throughout all trials at each combination of LED power intensity or minimal stimulation LED power. A neuron was considered responsive if synaptic events occurred in at least 33% of the trials at maximal (or minimal for thalamic input experiments) LED power level. For thalamocortical input experiments, relative latency for cells other than L4 pyramidal neurons was calculated by subtracting the latency of a synaptic event to the average obtained from a L4 pyramidal cells patched within the same slice. In a subset of experiments, the following chemical compounds were used to affect optogenetically-evoked synaptic events (all purchased from Tocris Bioscience): Bicuculline methiodide (10 µM), Tetrodotoxin citrate (TTX, 1 µM) and 4-aminopyridine (4-AP, 50 µM). Drugs were incubated for a minimum of 10 min before applying the optogenetic protocol.

2.2.4 – Morphological reconstruction

Following electrophysiological experiments, slices containing biocytin-filled cells were fixed in 4% paraformaldehyde (PFA; in phosphate-buffered saline, PBS) overnight at 4˚C. Slices were then rinsed in PBS and incubated into 0.05% PBST containing Streptavidin-Alexa568 or Streptavidin-Alexa488 (1:500, Molecular Probes, US) for 48-72h at 4˚C. Finally, slices were washed in PBS and mounted on histology slides with Fluoromount (Sigma) mounting medium. Slices were imaged through an Olympus FV1200 confocal microscope equipped with a 10X dry objective. Z-stack images were acquired to maximize imaging of all neuronal processes to allow offline morphological reconstruction. Image analysis was performed with Fiji-ImageJ software (NIH, US): morphological reconstruction was manually performed using the Simple Neurite Tracer plugin (Arshadi et al., 2021). Axonal and dendritic arbours were reconstructed separately; throughout the experimental ***Chapters***, pyramidal neurons morphology reconstructions show only the dendritic arbour whereas interneuron morphology reconstructions show the axon.

2.3 – Immunohistochemistry

Experimental mice for immunohistochemistry were terminally anaesthetized with pentobarbital (90mg/kg) and transcardially perfused with 4% PFA in PBS. Dissected brains were incubated in PFA for 24h at 4°C and cryoprotected in 20% sucrose for a minimum of 24h at 4°C. Whole brains were embedded into OCT (VWR, US) or 4% agarose gel (Sigma), to be further cut through distinct methods. Brains embedded in OCT were frozen on dry ice and stored at −80°C until sectioned into ~16 µm-thick slices through a cryostat; slices were mounted on histology slides and stored at −20°C. Brain embedded in agarose were immediately cut into 50 µm-thick slices through a vibratome (Leica VT1000S) and stored in PBS until treated for immunohistochemistry.

For immunohistochemistry slices were selected to contain S1BF or V1 and washed in PBS (3x10 minutes, min). Slices were incubated in blocking solution (PBST 0.25%, Natural Goat Serum (NGS) 5%) for 1 hour (h) at RT followed by incubation in primary antibody solution

overnight at 4°C. After that, slices were washed in PBS (3x10 min) and incubated in secondary antibody solution for 2h at RT. Finally, slices were washed in PSB (3x10 min), counterstained with 4′,6-diamidino-2-phenylindole (DAPI, ThermoFisher Scientific; diluted 1:1000 in PBS) and mounted with Fluoromount (Sigma). The primary antibodies (diluted in blocking solution) used were the following: chicken anti-GFP (1:500; Abcam, ab13970), rabbit anti-dsRed (1:1000; LivingColors, 632496), mouse anti-PV (1:500; Millipore, MAB1572). The secondary antibody (diluted in blocking solution) used were the following: goat anti-chicken Alexa488 (1:1000; Abcam, ab150169), goat anti-rabbit Alexa546 (1:1000; Invitrogen, A11035), and goat anti-mouse Alexa633 (1:500; Invitrogen, A21070).

Slices treated for immunohistochemistry were imaged at a confocal microscope Olympus FV3000 with a 10x dry objective to capture the whole extent of the cortical thickness. For representation purposes, images were taken at 4x or 40x dry objectives to obtain lower and higher magnification of specific regions of interest. For each animal, 3 fields of view from each brain area were imaged and analysed through semi-automated scripts written in Fiji. Automatic detection of cell expressing a given fluorescent marker (e.g., Lhx6-eGFP) was performed through a machine learning-based segmentation algorithm implemented in Fiji (Trainable Weka Segmentation plugin; Arganda-Carreras et al., 2017). A subset of images (training sample) was used to train a random forest model to classify pixels as belonging to either a cell body or the background. The trained models displayed >99% accuracy when tested on a subset of test images (excluded from the training sample). The model was then employed to perform automatic pixel segmentation of the remaining images and classify cell bodies vs. background. Segmented images were further processed with a customised script in Fiji to build region of interests (ROIs) corresponding to the boundaries of the cell bodies identified. Finally, layer boundaries were manually selected based on the DAPI profile. Data related to cell bodies and layer boundaries were imported in MATLAB to automatically detect overlapping cell bodies in distinct channels and assign cell bodies to a given cortical layer. Two ROIs corresponding to cell bodies in different channels were considered overlapping if the centroid of one ROI was included in the other ROI. Cell

numbers were used to calculate cell density, by dividing the former by the volume of tissue in each layer.

2.4 – *In vivo* electrophysiology

2.4.1 – Surgical and recording procedures

In vivo electrophysiology experiments were performed on neonatal mice under urethane anaesthesia (0.5–1.0 g/kg) or in awake head-fixed animals. For the former, as soon as animals lost their tail and pedal reflexes, they were head-fixed in a stereotaxic apparatus and a small craniotomy was opened over V1 (2.2–2.5 mm lateral and 0.5–0.7 mm rostral to lambda) or S1BF (2.7–3.2 mm lateral and 2.4–2.8 mm rostral to lambda). For awake head-fixed experiments, mice were anaesthetised with isoflurane (in O_2; 5% for induction, 2-3% for maintenance) and placed on a heating pad. The skin over the skull was then removed, the skull cleaned with 3% H_20_2 and a head-fixation apparatus was made, using dental cement and two light plastic tubes. Finally, a craniotomy was opened over V1, and the animal was head-fixed in the same stereotaxic apparatus and allowed to recover from isoflurane anaesthesia. Within the stereotaxic apparatus, mice were placed on a heating pad to provide thermoregulation. Recordings were performed with a single shank, 32-channel multi-electrode array (A1x32-Poly2–5mm-50s-177 or A1x32-Poly3-10mm-50-177; NeuroNexus, US) or corresponding optoelectrodes, slowly inserted (~1 µm/s) perpendicular to the brain surface at a depth of ~800 µm using a micromanipulator (SOLO-50, Sutter Instruments, US). After 30 min interval to allow for tissue recovery, data were acquired at 30 kHz with an OpenEphys acquisition board. Recordings lasted for approximately 60 min and consisted of one 20-min baseline session followed by optogenetic tagging and sensory stimulation sessions.

Visual stimuli were administered on the contralateral eye and consisted of a 100 ms-long white LED light stimulus (C503C-WAN, Cree, UK) every 15-30 seconds administered through input-output board (National Instruments, UK).

Whisker stimulation was obtained by inserting the contralateral whiskers into a glass cannula connected to a piezoelectric unit (Thorlabs, US), in turn controlled by piezoelectric amplifier (E-650 Piezo Amplifier; PI; Germany). Two stimuli were applied at 500 ms inter-stimulus interval, known to trigger short-term plasticity in the developing S1BF (Baruchin et al., 2021); 50 sets of this whisker stimulation protocol were applied every 15-30 s.

Optogenetic spike-tagging was performed through a fibre-coupled blue (472 nm) laser, positioned close to the craniotomy or connected to an optoelectrode. Long duration (50 ms) laser pulses were employed to account for reduced excitability of ChR2 during early postnatal development. One optogenetic session, characterized by 100 laser pulses delivered at 0.1 Hz frequency, was conducted immediately before the sensory stimulation session.

2.4.2 – Analysis of in vivo *electrophysiology data*

Automatic spike sorting was performed with Kilosort2 (Pachitariu et al., 2016), and manually refined in Phy2 (Rossant et al., 2016) to classify single unit (SU) activity from multi-unit activity (MUA) and noise clusters. Generally, the minimum criteria for a cluster to be considered a SU was to be characterised by less than 0.2% of refractory period violations (±1 ms). Spike waveforms were extracted from the raw data through a customised Phy plugin and waveform half-width and trough to peak latency were measured. SUs were classified into regular-spiking (RS) or fast-spiking (FS) based on an arbitrary spike trough to peak latency cut-off value of 0.75 ms (for V1 data), with units falling below this number classified as FS units.

Analysis of *in vivo* electrophysiology data was performed with customised MATLAB scripts. Local field potential (LFP) was obtained by low-pass filtering (150 Hz) the raw signal. The initial 20-min baseline recording was used to extract features of spontaneous activity. The power spectral density (PSD) of the data (between 1–50 Hz) was obtained from the entirety of the 20-min recording session through the Welch's method. Raw PSD was normalised by multiplying each value for the corresponding frequency and dividing by the mean PSD

power. Spontaneous MUA or SU activity was obtained as the average number of spikes fired over the course of the 20-min recording session.

For spike-LFP coupling, LFP signal was bandpass filtered (10-30 Hz), and the phase of the beta (β) oscillation estimated using the Hilbert transform. Phase values at the time of each SU spike were collected and a statistical test was used to evaluate whether they occurred in a specific phase of the oscillation (Rayleigh's test for nonuniformity; Berens, 2009). Strength of the spike-LFP coupling for SU was measured by calculating a pairwise phase-consistency (PPC) value as previously reported (Vinck et al., 2010) which is more robust that classical vector length method when dealing with small number of spikes (Chen et al., 2017; Veit et al., 2017).

Spindle bursts (SBs) were detected during the 20-min spontaneous activity recording in the best L4 channel (see below) as previously described (Baruchin et al., 2021). In brief, raw LFP signal was bandpass filtered in the β frequency (10-30 Hz), and the envelope of the signal was estimated as the real part of its Hilbert transform. SBs events were defined as portions of the envelope signal larger than 2 times its SD, characterised by at least 3 cycles in the filtered LFP signal, and with a duration longer than 100 ms. SB event onset, offset and duration were obtained and used to evaluate entrainment of SU activity with SB events. SU spike probability within SB events was obtained as the ratio between the number of spikes occurring within predefined events over the total number of spikes fired over the 20-min baseline recording. To evaluate the statistical significance of SU spike firing within SB events, inter-spike intervals (ISIs) for each SU were shuffled 1.000 times and the probability of spike to occur within SB events calculated as before. A SU was deemed entrained by SBs if the real spike probability was larger than the shuffled probability in at least 99% of cases.

For the analysis of responses to visual stimulation, LFP signals were first used to build a current-source density (CSD), employed to identify L4 as the earliest sink following the visual stimulus. Amplitude and latency of the LFP deflection in every channel were measured and the best L4 channel was selected as the channel within L4 with the largest

negative LFP deflection. Each SU was then assigned to a cortical layer (L2/3, L4 or L5/6) and their peri-stimulus time histogram (PSTH) following visual stimulation obtained (bin size of 3 ms, smoothing of 15 ms) from the trial-wise spike times (raster plots). Spike times in the raster plots were also used to evaluate whether a SU was responsive to visual stimulation, by comparing total number of spikes occurring within response windows to number of spikes fired during baseline. For the fast phase of the visual stimulation (0-200 ms after stimulus onset), two response windows were defined (0-100 ms and 100-200 ms) and compared with a window of equal length immediately before the stimulus (−100 ms-0). An analysis of variance (ANOVA) or Kruskal-Wallis test (if the spike number data were not normally distributed) on the trial-by-trial number of spikes within these windows was used to determine whether a SU was responsive during the fast phase of the visual stimulation (with p-value, $p \leq 0.05$). SU spiking reliability during this phase was estimated with the Fano factor, defined as the ratio between the variance and the mean number of spikes in all trials. For the slow phase of the visual stimulation (400-4000 ms from stimulus onset), the total number of spikes occurring within this window was compared with a baseline window of equal length immediately preceding the stimulus onset; a Wilcoxon signed rank test was used to evaluate whether each SU was responsive during the slow phase of the visual stimulation. Peak SU activity (for every SUs) and MUA (for every channel) during the fast phase of the visual stimulation were stored and used for further comparison; similarly peak MUA or average SU activity during the slow phase of the visual stimulation were measured.

Responsive units to whisker stimulation were evaluated in a 100 ms window following each whisker stimulus and compared with an equal length baseline window immediately preceding the stimulus.

Similar statistical methods were employed to evaluate optogenetically-tagged SU, by comparing the trial-by-trial total number of spikes during the optogenetic stimulus (50 ms) and spike number in a baseline window before the stimulus. Additionally, to be classified

as optically tagged SU, they had to fire at least one spike during the optogenetic stimulus in at least 20% of the trials.

For optogenetics experiments, SU firing change during the first 100 ms of the stimulus was measured as the $\log_2$ of the ratio between firing rate during this window and a baseline window of 100 ms before the stimulus. Similarly, SU firing change during the rebound from optogenetic stimulation was obtained as the $\log_2$ of the ratio between the firing in the 100 ms following stimulus offset and firing rate during a baseline window.

2.5 – Chemogenetic experiments

For chemogenetic experiments, *SSTCre*^{HET} pups at P0 were separated from the dam and anaesthetised with isoflurane (in O_2; 3% induction for 3 minutes; 1.5% maintenance) according to a recently published method (Ho et al., 2020). Once a pup lost high righting reflex and displayed reduced motility, it was moved to a 3D printed custom-made stereotaxic frame and a small volume of virus (50 nL x 3 cycles; rate: 0.23 nL/s; delay: 3 s) was rapidly injected (Nanoject III, Drummond) in the right V1 (0.1 mm posterior and 1.5 mm lateral to lambda, depth of 0.4-0.7 mm) or S1BF (1.4 mm anterior and 1.4 mm lateral to lambda, depth of 0.4-0.7 mm). The following viruses were used: AAV8-KORD (pAAV-hSyn-dF-HA-KORD-IRES-mCitrine; Addgene, US: 65417-AAV8) and AAV1-GFP (pAAV-CAG-GFP; Addgene: 37825-AAV1.T).

Mice injected with viral vectors were then used for *in vivo* electrophysiological recordings as described before. In this case, a 20-min baseline was followed by a sensory stimulation session (50 trials of single visual stimulations or paired whisker stimulations). After that, the designer drug Salvinorin B (SalB; Tocris; 1 mg/kg, 0.1 mg/ml in saline with 1% dimethyl sulfoxide, DMSO) was injected intraperitoneally to activate KORD. After 20 min, a second 20-min baseline recording was obtained followed by another sensory stimulation session. For control experiments, SalB solution was intraperitoneally injected in animals previously infected with a GFP virus; in other cases, saline (with 1% DMSO) was injected in animals previously infected with the KORD virus.

At the end of the recording, mice were terminally anaesthetised with isoflurane (4% in O_2) and their brain rapidly dissected and incubated in PFA for 24-72h at 4°C. A few brains were treated for immunohistochemistry, while the remaining were sliced into 50 µm-thick slices, mounted on histology slides, and imaged at confocal microscopy. Animals that did not display clear fluorescent signal (mCitrine for KORD injected animals and GFP for the remaining animals) in the injected brain area were excluded from the analysis.

2.6 – Statistics

Results are expressed as mean ± standard error of the mean (SEM) unless otherwise indicated; n corresponds to either the number of cells recorded (*in vitro* electrophysiology), the number of animals recorded (*in vivo* electrophysiology) or the number of slices images (immunohistochemistry) for each independent experiment. Statistical analysis was carried out in MATLAB or R. The Shapiro-Wilk test was initially run on each independent dataset to distinguish parametric and non-parametric data. Two groups were then compared with appropriate two sample statistical tests for parametric (unpaired or paired Student's t-test) or non-parametric data (Wilcoxon signed rank or Wilcoxon rank sum tests). Multiple groups were compared with ANOVA or Kruskal-Wallis tests, for parametric and non-parametric data, respectively. Factors used for each analysis are indicated in the text and their statistics reported. Multiple comparison tests used were the Tukey's test for parametric data and Dunn's test with Benjamini-Hochberg correction for non-parametric data.

Chapter 3

GABAergic interneuron networks in postnatal mouse V1

3.1 – Introduction

Our characterisation of developing primary visual cortex (V1) cortical networks start with an analysis of electrophysiological and morphological properties of excitatory pyramidal neurons and two of the major classes of GABAergic interneurons, notably somatostatin-expressing (SST+) and parvalbumin-expressing (PV+) interneurons (Rudy et al., 2011b). I will describe the development of GABAergic connectivity onto V1 pyramidal neurons across cortical layers, with a special focus on connectivity established between SST+ interneurons and excitatory neurons. Through optogenetics and transgenic mouse lines, I probed the development of dis-inhibitory network between SST+ and PV+ interneurons. Finally, I will provide the first description regarding the maturation of thalamic inputs onto excitatory pyramidal neurons and GABAergic interneurons in V1. To ease the description of developmental trajectories of neuronal networks, the data presented in all Chapters are grouped into three developmental windows: postnatal day (P)5-P8, P9-P13 and P14-P18.

3.2 – Characterisation of V1 pyramidal neurons electrophysiological properties over early postnatal development

3.2.1 – Electrophysiological and morphological properties of V1 layer 4 pyramidal neurons

To understand the developmental timeline of cortical neurons in V1, I first characterised electrophysiological and morphological features of thalamo-recipient layer (L)4 pyramidal neurons. Neurons in acute cortical slices of V1 were targeted for whole-cell patch-clamp electrophysiological recordings in current-clamp configuration and their electrophysiological intrinsic profile recorded during depolarising and hyperpolarising current step injections. Electrophysiological properties of neurons recorded between P5-P8 (**Fig. 3.1A**) were

characterised by high input resistance, slow membrane time constant, broad, and short action potentials, and inability to sustain high firing frequencies, typically associated with immature neurons. Neurons recorded between P9-P13 (**Fig. 3.1B**) and P14-P18 (**Fig. 3.1C**) showed progressively more mature electrophysiological properties, both in term of passive membrane properties, spike features, and suprathreshold firing patterns. Regardless of the developmental differences, all recorded L4 neurons (n = 86) showed stereotyped electrophysiological features, characterised by regular-spiking profile with little spike adaptation during supra-threshold firing.

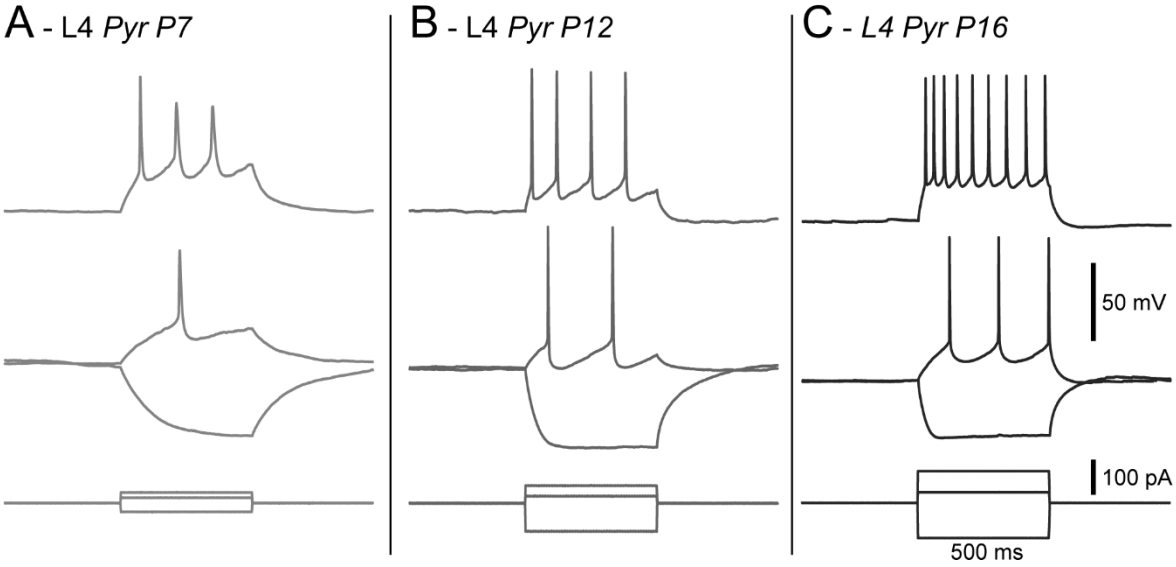


Fig. 3.1. Electrophysiological properties of primary visual cortex (V1) layer (L)4 pyramidal neurons (Pyr). (A) Current-clamp recordings of a representative L4 Pyr in V1 at postnatal day (P)7 during current steps application; recorded traces show electrophysiological profiles for a negative current step, a positive current step close to rheobase (bottom) and a positive current step close to maximum firing rate (top).
(B, C) Current clamp recordings of representative P12 (B) and P16 (C) L4 Pyr in V1 as described in A.

Quantification of passive (**Fig. 3.2A-E**) and active (**Fig. 3.2F-K**) electrophysiological properties (**Table 2**; see end of chapter) revealed significant changes in the development of L4 neurons over the time windows investigated. As a comprehensive measure, I computed a cell maturity index value taking into account all investigated electrophysiological properties (see *Methods* for details), relative to the average P14-P18 window (scored as 1.0). This analysis (**Fig. 3.2L**) revealed the progressive development of L4 pyramidal cell intrinsic properties during the second and third postnatal weeks.

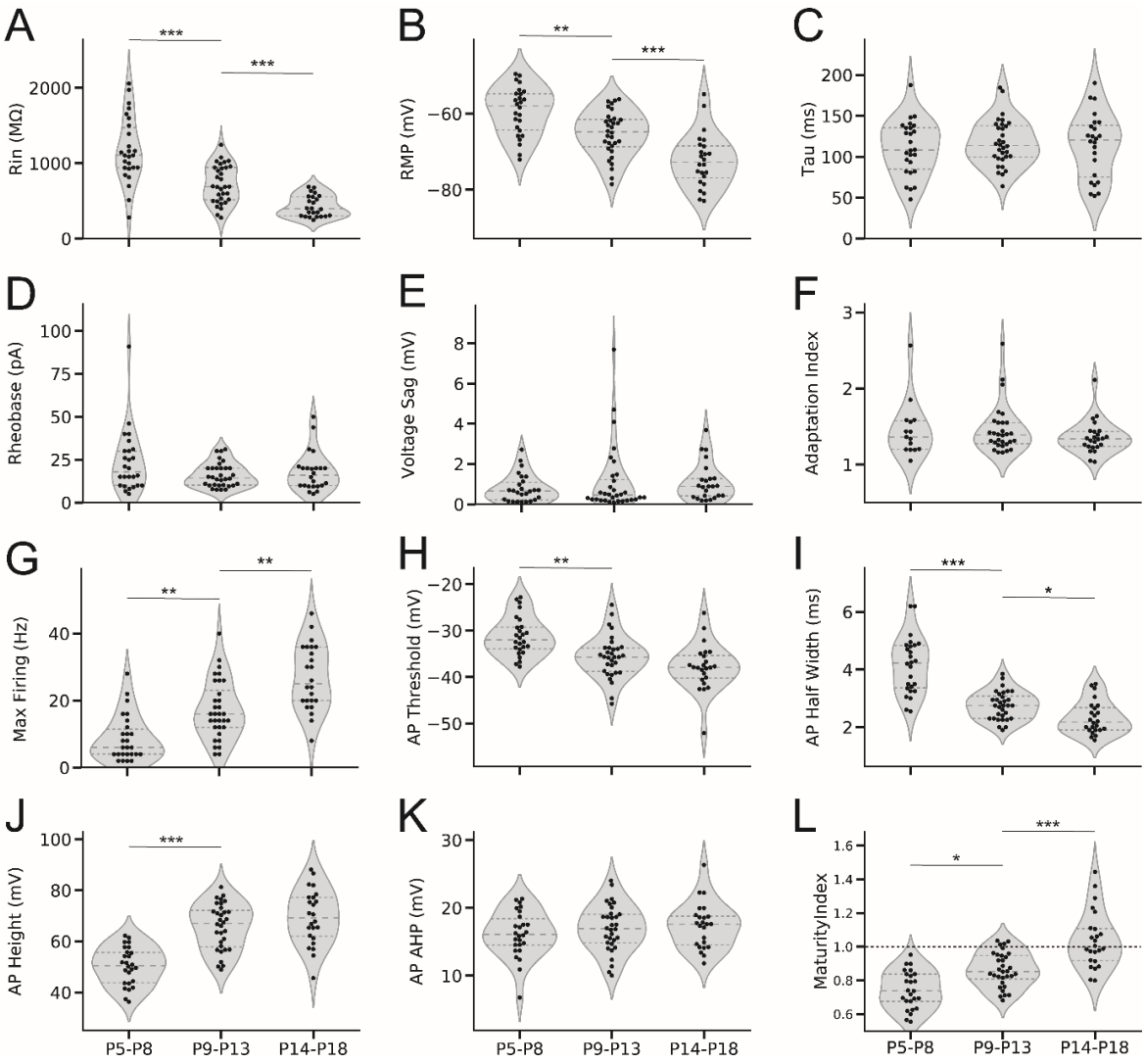


Fig. 3.2. Quantification of V1 L4 Pyr passive and active intrinsic electrophysiological properties. (A-L) Violin plots of cell input resistance (Rin; A), resting membrane potential (RMP; B), membrane time constant (Tau; C), rheobase (D), voltage sag (E), adaptation index (F), maximum firing rate (Max firing; G), action potential (AP) threshold (H), AP half-width (I), AP height (J), AP after-hyperpolarizing potential (AHP, K), and maturity index (L) for L4 Pyr in V1 at different developmental stages (P5-P8, P9-P13, and P14-P18). Individual points show values from individual recorded cells (P5-P8, n = 25; P9-P13, n = 35; P14-P18, n = 26), dashed line shows the median of the distribution, dotted lines show the 1st and 3rd quartile of the distribution. There is a statistically significant effect of "*Development*" for the following features: Rin (Kruskal-Wallis test: X^2 (2) = 50.3, $p \leq 0.001$), RMP (One-way analysis of variance (ANOVA): F (2,83) = 26.7, $p \leq 0.001$), Max firing (Kruskal-Wallis test: X^2 (2) = 35.6, $p \leq 0.001$), AP threshold (One-way ANOVA: F (2,83) = 13.6, $p \leq 0.001$), AP half-width (Kruskal-Wallis test: X^2 (2) = 43.1, $p \leq 0.001$), AP height (One-way ANOVA: F (2,83) = 34.8, $p \leq 0.001$) and cell maturity index (One-way ANOVA: F (2,83) = 48.1, $p \leq 0.001$). Asterisks in the plots show statistically significant differences between groups, when tested with post-hoc analysis corrected for multiple comparisons (Tukey's test for parametric data and Dunn's test with Benjamini-Hochberg correction for non-parametric data), according to the following notation: * $p \leq 0.05$, ** $p \leq 0.01$, and *** $p \leq 0.001$.

In parallel with the electrophysiological properties, morphological features of L4 pyramidal neurons undergo similar development over the course of the first three postnatal weeks. Representative morphological reconstructions of the dendritic arbour of L4 pyramidal

neurons are shown in **Fig. 3.3A-C** for cells recorded at P7, P13, and P15, respectively. These examples show how the main apical dendrite increases in length in line with the expansion of the cortex while the basal dendritic arbour increases in complexity and size.

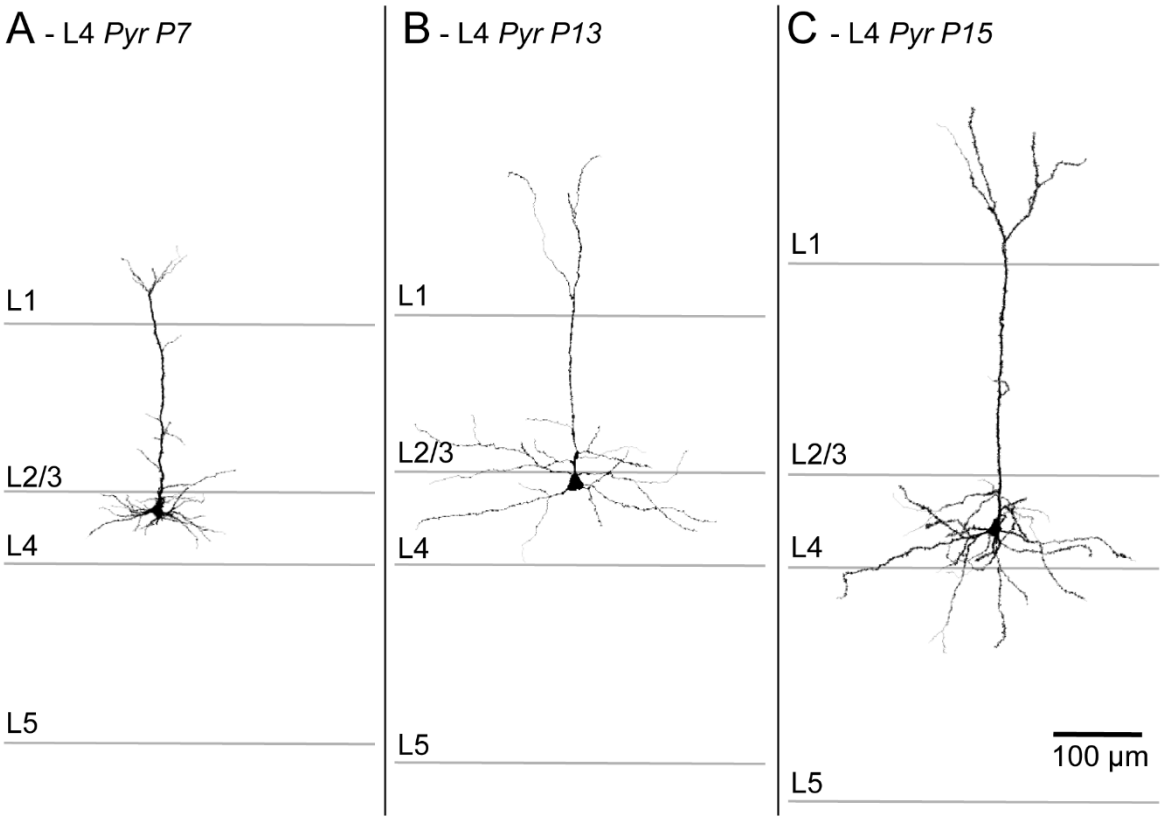


Fig. 3.3. Morphological properties of V1 L4 Pyr over postnatal development. (A-C) Morphological reconstructions of the dendrites of L4 Pyr in V1 recorded at P7 (A), P13 (B), and P15 (C).

3.2.2 – Electrophysiological properties of V1 supragranular and infragranular pyramidal neurons

Pyramidal cells populate the layers of neocortex in an inside-out manner during embryonic development (Greig et al., 2013). To examine if this has consequence for the development of intrinsic properties of other pyramidal neurons, I expanded the analysis of intrinsic electrophysiological properties to excitatory neurons in other layers. Similar to L4 neurons, those recorded in L2/3 (n = 17) resembled an electrophysiologically homogeneous population, characterised by regular-spiking profile with little adaptation (see **Fig. 3.4A**). Quantitative analysis of passive and active electrophysiological features revealed

maturation over the course of the developmental stages investigated (**Table 1**) with the cell maturity index (**Fig. 3.4D**, left) significantly increasing between P9-P13 and P14-P18. Unlike granular and supragranular pyramidal neurons, infragranular cells were more diverse in terms of electrophysiological profile. After eye opening, both L5 and L6 pyramidal cells could be characterised as either bursting or regular-spiking cells (**Fig. 3.4B** and **Fig. 3.4C**). While the latter were similar to pyramidal cells recorded in L2-L4, bursting cell displayed a doublet of spikes fired at rheobase/threshold current injection, a response that evolved into a highly adapting firing profile at suprathreshold current steps. Intrinsic bursting was not observed prior to eye opening, when all recorded L5 and L6 cells displayed regular-spiking electrophysiological profiles (**Fig. 3.4B** and **Fig. 3.4C**). Quantitative analysis of the electrophysiological features of L5 (n = 19) and L6 (n = 20) cells is shown in **Table 3** and **Table 4**, respectively, with several physiological properties of these cells showing significant changes over development. The cell maturity index of L5 cells showed similar developmental progression to L4 (**Fig. 3.4D**, middle), whereas L6 cells rapidly matured between the first two development time windows under investigation (**Fig. 3.4D**, right).

Overall, analysis of electrophysiological properties of pyramidal neurons in V1 reveals a maturation of intrinsic features over the first three postnatal week of development in the mouse, which follows the inside-out development of the cortex.

Fig. 3.4 (next page). Characterisation of V1 infragranular and supragranular pyramidal neurons intrinsic electrophysiological properties. (A) Representative morphological reconstruction of the dendrites of a P6 L2/3 V1 Pyr (left) and current-clamp recordings of representative L2/3 Pyr cells at P7 (i), P11 (ii), P18 (iii), and P15 (iiii) during current steps application; recorded traces show electrophysiological profiles for a negative current step, a positive current step close to rheobase (bottom) and a positive current step close to maximum firing rate (top).
(B, C) Morphological reconstructions of dendrites and current clamp recordings of representative P7 L5 (B) and P8 L6 (C) Pyr cells at different ages as described in A. For the later developmental window, representative traces for L5 and L6 bursting cells and regular-spiking cells are shown in (iii) and (iiii), respectively.

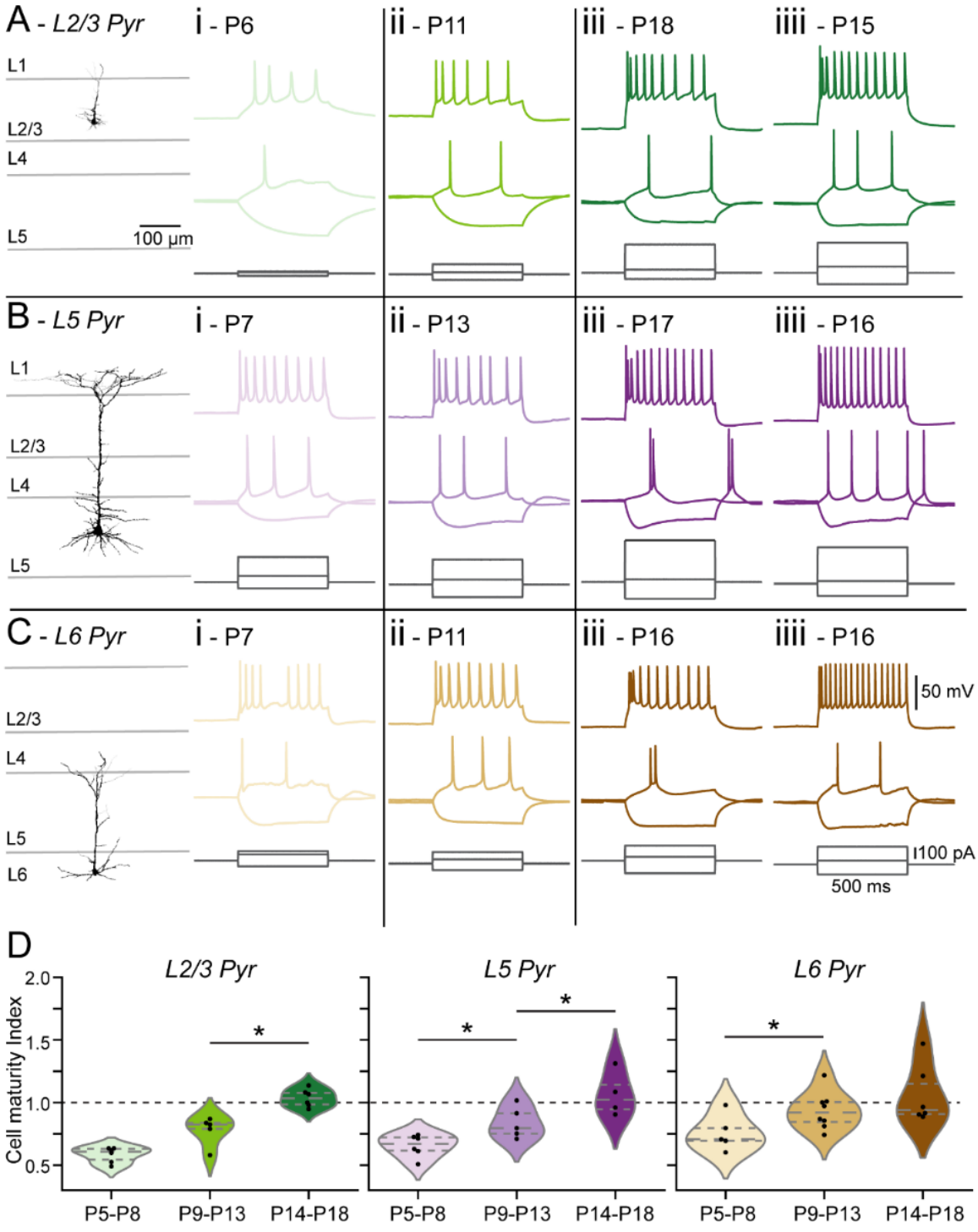


Fig. 3.4 (continue). (D) Violin plot of cell maturity index values for L2/3 (left), L5 (middle) and L6 (right) Pyr cells in V1 at different developmental stages (P5-P8, P9-P13, and P14-P18). Individual points show values from individual recorded cells (L2/3: P5-P8, n = 6; P9-P13, n = 5; P14-P18, n = 6; L5: P5-P8, n = 6; P9-P13, n = 7; P14-P18, n = 6; L6: P5-P8, n = 5; P9-P13, n = 9; P14-P18, n = 6). There is a statistically significant effect of "*Development*" on cell maturity index for L2/3 (Kruskal-Wallis test: X^2 (2) = 12.4, $p \leq 0.01$), L5 (One-way ANOVA: F (2,16) = 11.2, $p \leq 0.001$), and L6 Pyr (Kruskal-Wallis test: X^2 (2) = 8.23, $p \leq 0.05$). Asterisks in the plots show statistically significant differences between groups, when tested with post-hoc analysis corrected for multiple comparisons (Tukey's test for parametric data and Dunn's test with Benjamini-Hochberg correction for non-parametric data), according to the following notation: * $p \leq 0.05$.

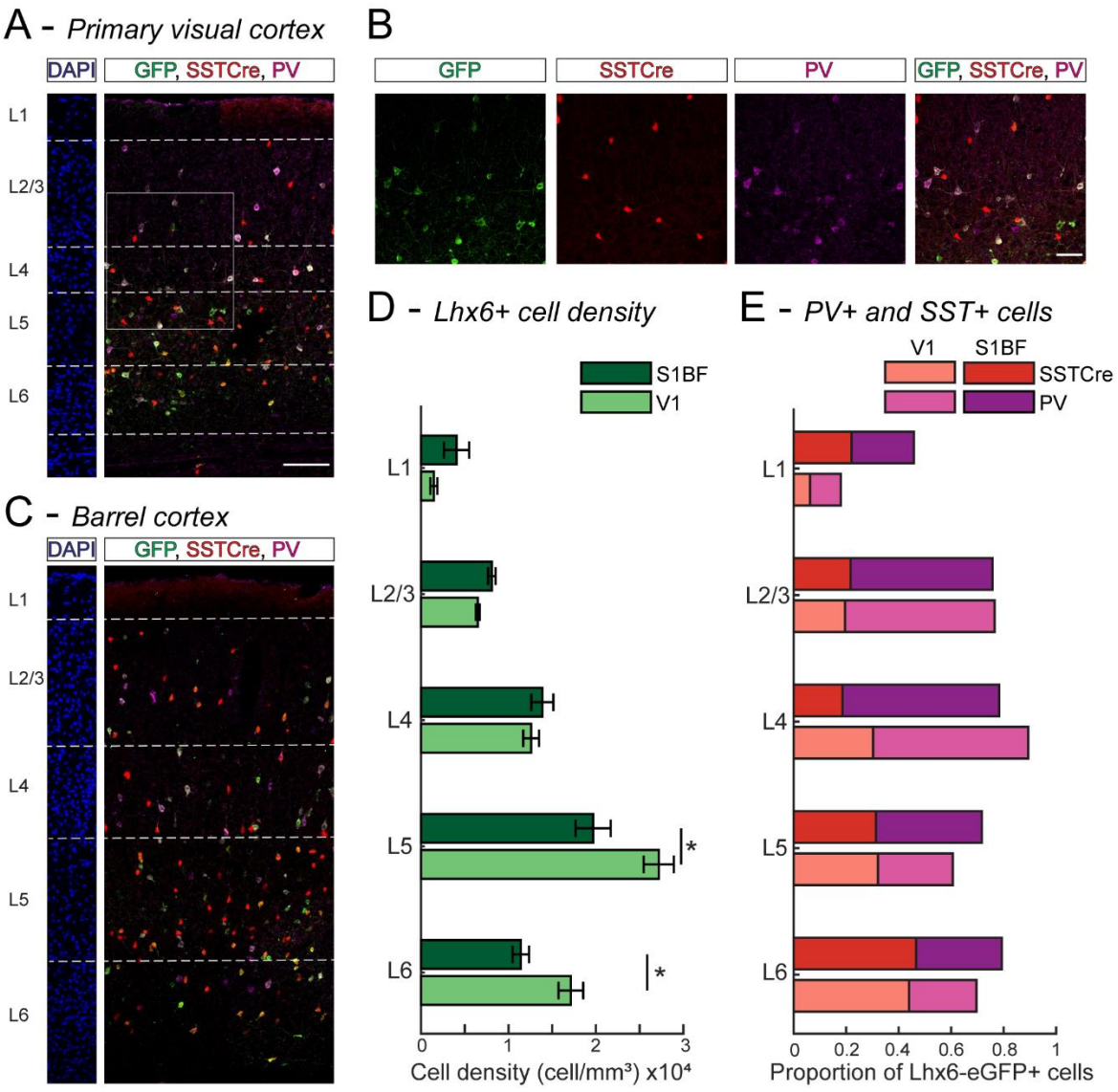
3.3 – Characterisation of V1 GABAergic interneurons electrophysiological properties over early postnatal development

3.3.1 – Immunohistological characterisation of Lhx6-eGFP; SSTCre; Ai9 animals

To target GABAergic interneurons in developing V1, I took advantage of several transgenic mouse lines to both identify distinct GABAergic interneurons via expression of fluorescent markers and subsequently manipulating their activity using conditional expression of chemo- and optogenetic actuators. As the subtypes captured with the various lines has not been characterised in early V1, I first set out to define these populations. The *Lhx6-eGFP* line labels interneurons derived from the Nkx2-1-espressing medial ganglionic eminence (MGE; Du et al., 2008). The MGE give rise to the two most abundant populations of cortical GABAergic interneurons in the adult cortex, namely PV+ and SST+ cortical interneurons. *Lhx6-eGFP* mice were crossed with *Ai9* mice (to allow Cre-dependent expression of tdTomato) and their offspring further crossed with *SSTCre* mice, where Cre recombinase is under the control of the SST promoter (Taniguchi et al., 2011). *Lhx6-eGFP; SSTCre; Ai9* mice would enable the identification of both immature, putative PV+ interneurons (eGFP only) and SST+ cells (both eGFP and tdTomato).

I first performed immunohistochemistry to characterise interneuron diversity captured in our *Lhx6-eGFP; SSTCre; Ai9* line. I stained coronal brain slices (≈16-20 µm) from P21 animals containing either V1 or S1BF with antibodies against eGFP, tdTomato, and PV, obtained confocal images of these brain regions (**Fig. 3.5A, B** for V1 and **Fig. 3.5C** for S1BF), and analysed cells expressing combinations of these markers. MGE-derived Lhx6-eGFP+ cells were primarily located in granular and infragranular layers in both V1 and S1BF, with the highest density found in L5 for both brain areas, albeit a higher density of cells in L5 and L6 of V1 compared with S1BF (**Fig. 3.5D**). The majority of Lhx6-eGFP+ cells also expressed either PV or tdTomato (i.e., SSTCre+ neurons; **Fig. 3.5E**), again in line with previous reports of MGE-derived neurons. However, the proportion of Lhx6-eGFP+ cells that either

expressed PV or SSTCre varied depending on the layer – in a manner independent of sensory area – with a larger proportion of PV+ cells found in L2/3 and L4, equal proportions of SSTCre+ and PV+ cells in L5 and more SSTCre+ cells than PV+ cells in L6. Of the total population of SSTCre+ neurons, 34 ± 8 % (standard deviation, SD) also expressed eGFP while of the total PV-expressing population, 57 ± 12 % of cells also expressed eGFP. As previously reported (Hu et al., 2013), a fraction (5.7 ± 0.2 %) of cells expressed both SSTCre and PV, beside Lhx6-eGFP. Thus, the *Lhx6-eGFP* transgenic line captures both SSTCre+ and PV+ interneurons and can be used in conjunction with the *SSTCre* transgenic line to isolate these two interneuron subtypes.



3.3.2 – Electrophysiological and morphological properties of L4 fast-spiking interneurons in V1

Lhx6+ interneurons in V1 L4 were then targeted for whole-cell patch-clamp experiments in current-clamp configuration to study the development of intrinsic electrophysiological properties. Lhx6+ interneurons were characterised by two distinct spiking profiles, as shown in **Fig. 3.6** and **Fig. 3.8**. The majority of Lhx6+ cells (31/37, corresponding to 84%) were characterised by narrow action potential waveform and sustained firing at high frequency with negligible spike time adaptation (**Fig. 3.6** and **Table 5**), features of classical fast-spiking (FS) cells. The remaining (6/37, 16%) displayed firing characteristics of non-fast spiking (NFS) interneurons (**Fig. 3.8**), characterised by broader spike waveform and lower maximum firing frequency than FS interneurons (although narrower waveform and higher firing frequency than pyramidal neurons; see **Table 6**). Out of the 6 Lhx6+ NFS interneurons, 4 also expressed tdTomato, confirming their identity as SSTCre+ interneuron. I also recorded from SSTCre+ cell expressing tdTomato across granular and infragranular layers of V1. Most of these cells (41/42, 98%) were classified as NFS interneurons with only 1 out of 42 (2%) classified as FS interneuron.

Fig. 3.5 (previous page): Characterisation of the *Lhx6-EGFP;SSTCre;Ai9* mouse line. (A) Representative confocal image (10X) of a V1 slice obtained from a *Lhx6-EGFP;SSTCre;Ai9* mouse at P21, stained with antibodies against GFP (green), tdTomato (for SSTCre, red), and parvalbumin (PV, magenta); DAPI profile (blue) is shown on the left and used to determine layer boundaries (dashed lines). Scale bar = 100 µm.
(B) High magnification confocal image (40X) showing the region identified by the rectangle in A. Scale bar = 50 µm.
(C) Same as in A but for a slice containing the primary somatosensory barrel cortex (S1BF).
(D) Bar plot (error bar indicate the standard error of the mean, SEM) of Lhx6-eGFP cell density in each layer for V1 (light green; n = 15 images from 5 animals) and S1BF (dark green; n = 15 images from 5 animals). There is a statistically significant effect of the factor "*Layers"* on Lhx6-eGFP cell density (Two-way ANOVA: $F(3,84) = 22.7$, $p \leq 0.001$).
(E) Bar plot showing the proportion of Lhx6-eGFP cells labelled with either tdTomato (SSTCre, red) or PV (magenta) for V1 (light colours) or S1BF (dark colours). There is a statistically significant effect of the factor "*Layers"* on SSTCre+ cell proportion (Two-way ANOVA: $F(3,84) = 33.8$, $p \leq 0.001$) and PV+ cell proportion (Two-way ANOVA: $F(3,84) = 25.05$, $p \leq 0.001$). Asterisks in the plots show statistically significant differences between groups, when tested with post-hoc analysis corrected for multiple comparisons (Estimated marginal means method; *emmeans* function in R), according to the following notation: * $p \leq 0.05$.

Our ability to discriminate immature PV+, FS interneurons allowed us to assess the development of their intrinsic properties at early postnatal ages in V1 (**Fig. 3.6**). Recordings obtained after eye opening revealed FS interneurons with previously reported, stereotypical features (e.g., narrow action potential waveform and sustained firing at high frequency; **Fig. 3.6C**). Prior to eye opening, these cells showed immature spiking profiles, with lower firing frequency and broader action potential waveform (**Fig. 3.6A, B**). Quantification of intrinsic electrophysiological properties for FS interneurons (n = 35; **Table 5** and **Fig. 3.6D-E)** indicate several features progressively mature over early development, with the cell maturity index significantly increasing around the time of eye opening (**Fig. 3.6F**).

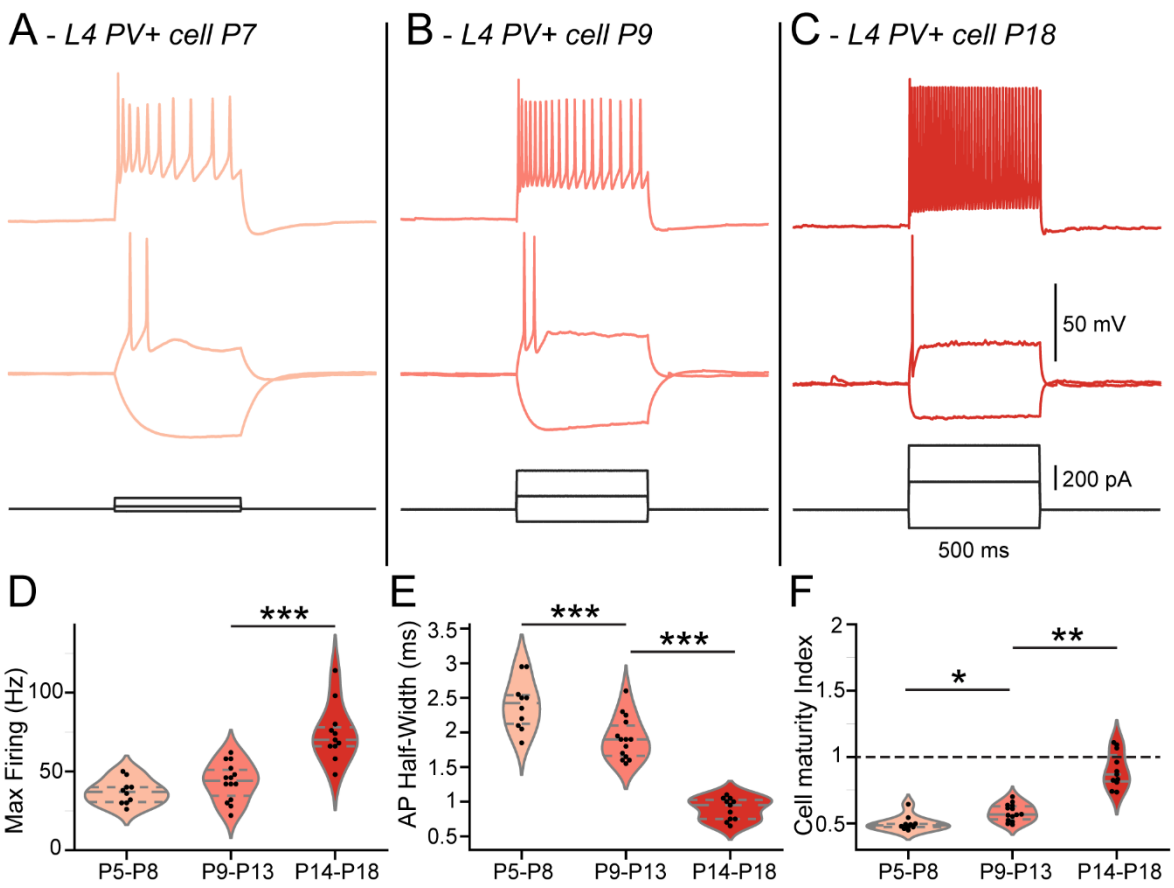


Fig. 3.6. Electrophysiological characterization of L4 fast-spiking (FS) parvalbumin-expressing (PV+) interneurons in V1. (A) Representative current-clamp recordings of L4 PV+ interneurons at P7 during current steps application; recorded traces show electrophysiological profiles for a negative current step, a positive current step close to rheobase (bottom) and a positive current step close to maximum firing rate (top).
(B, C) Current clamp recordings of representative L4 PV+ interneurons recorded at P9 (B) and P18 (C) as described in A.

Morphological reconstructions from recorded Lhx6+ PV+ interneurons (**Fig. 3.7**) also point to progressive maturation during the first three postnatal week. PV+ cells in L4 obtained from animals at P9-P13 and P14-P18 display classical features of V1 FS basket cells including dense axonal ramification within L4 and extending to L5 (**Fig. 3.7B, C**). At P5-P8, Lhx6+ PV+ interneurons are characterised by distinct morphologies, characterised by long axonal processes, often spanning many cortical layer (**Fig. 3.7A**).

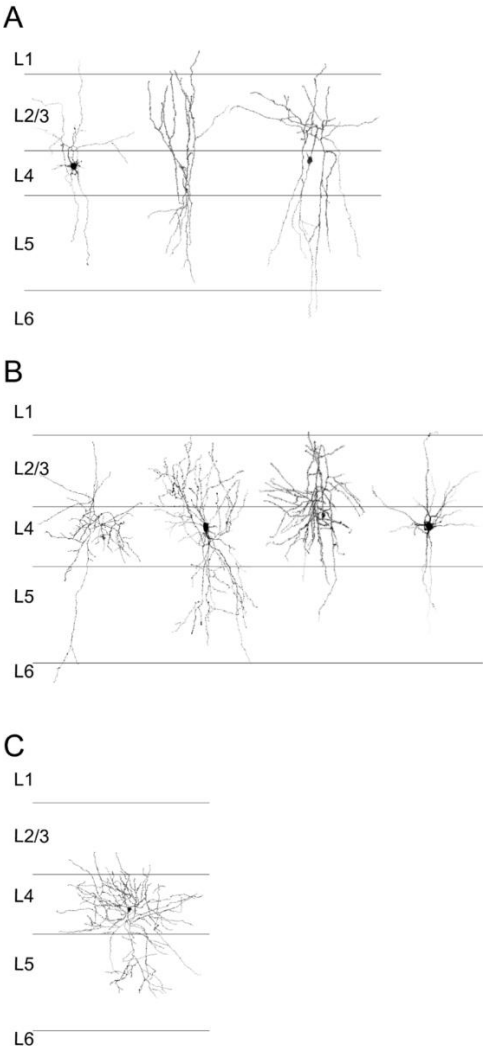


Fig. 3.7: Cell morphology of L4 PV+ interneurons in V1. (A) Representative morphological reconstructions of the axonal arbours of L4 PV+ interneurons in V1 at P5-P8.
(B) Same as in A but for cells recorded at P9-P13.
(C) Same as in A but for a cell recorded at P14-P18.

Fig. 3.6 (continue from previous page). (D) Violin plot for maximum firing rate at different developmental ages (P5-P8, n = 10; P9-P13, n = 14; P14-P18, n = 11) showing statistically significant effect of "*Development*" (One-way ANOVA: $F(2,32) = 24.2$, $p \leq 0.001$).
(E) Violin plot for AP half-width at different developmental ages, showing statistically significant effect of "*Development*" (One-way ANOVA: $F(2,32) = 74.6$, $p \leq 0.001$).
(F) Violin plot for cell maturity index at different developmental ages, showing statistically significant effect of "*Development*" (Kruskal-Wallis test: $X^2(2) = 26.2$, $p \leq 0.001$). Asterisks in the plots show statistically significant differences between groups, when tested with post-hoc analysis corrected for multiple comparisons (Tukey's test for parametric data and Dunn's test with Benjamini-Hochberg correction for non-parametric data), according to the following notation: * $p \leq 0.05$, ** $p \leq 0.01$, and *** $p \leq 0.001$.

3.3.3 – Electrophysiological properties of SSTCre+ interneurons in V1

I next characterised intrinsic properties of SSTCre+ interneurons in granular and infragranular layers of V1. Unlike FS cells, SSTCre+ interneurons (**Fig. 3.8**) exhibited diverse firing patterns and could be classified into classical NFS (**Fig. 3.8A**) and rebound intrinsic bursting (rIB; **Fig. 3.8B**), with the latter fired a burst of two or more action potentials on release from a hyperpolarising current step. SSTCre+ interneurons with rIB profiles were recorded across all developmental windows (see **Fig. 3.8B(i)** and **Fig. 3.8B(ii)** for a P8 and P9 cell, respectively). I also recorded intrinsic electrophysiological profiles from eGFP+ interneurons labelled using the *Lpar-eGFP* transgenic line, previously shown to delineate a subset of L5 SST+ interneurons (Marques-Smith et al., 2016). Consistent with findings from S1BF, V1 Lpar1-SST+ interneurons (**Fig. 3.8C**) are NFS SST+ interneurons. Quantification of electrophysiological properties of SST+ interneurons irrespective of their subtype (n = 57) show they undergo progressive maturation during the first three postnatal week of development, as shown for maximum firing frequency (**Fig. 3.8D**) and AP half-width (**Fig. 3.8E**; see **Table 6**). Analysis of the cell maturity index only shows significant increase between the P5-P8 and P9-P13 developmental windows (**Fig. 3.8F**), suggesting maturation of SSTCre+ interneurons is largely completed by the time of eye opening.

Overall, I successfully employed a combinatorial genetic approach to target both SSTCre+ and PV+ interneurons during early postnatal development in the mouse. Lhx6+ SSTCre− cells show histological, electrophysiological, and morphological features of classical FS PV+ interneurons and thus will be henceforth referred to as PV+ interneurons. Analysis of electrophysiological properties of PV+ and SSTCre+ interneurons highlights that the latter attain mature electrophysiological properties prior to eye opening whereas PV+ interneurons properties mature only after the time of eye opening.

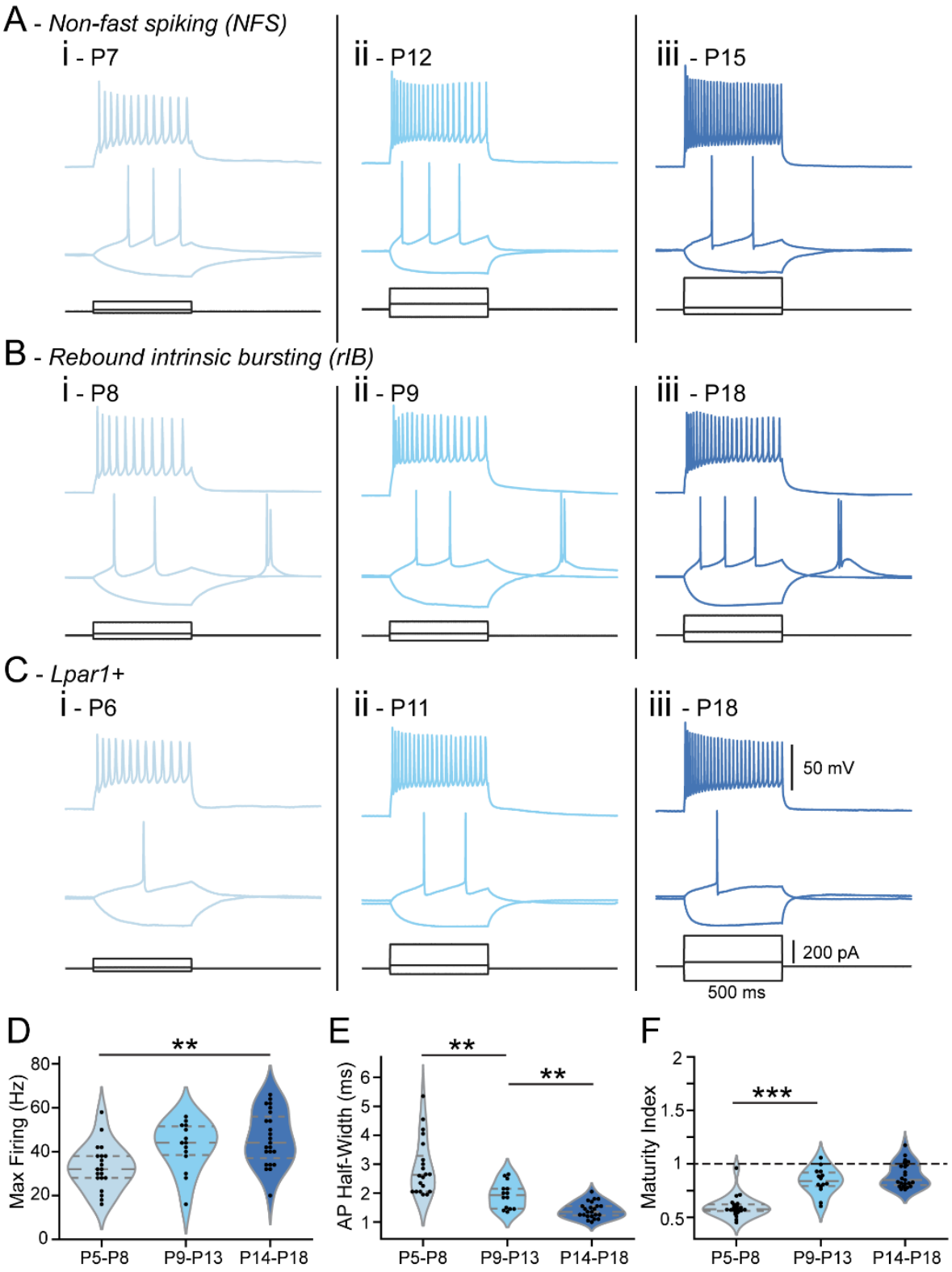


Fig. 3.8. Electrophysiological characterization of SST+ interneurons in V1. (A) Current-clamp traces for SST+ cells displaying non-fast spiking (NFS) electrophysiological profiles, recorded at P7 (i), P12 (ii), and P15 (iii).
(B) Current-clamp traces for SST+ cells displaying rebound intrinsic bursting (rIB) electrophysiological profiles, recorded at P8 (i), P9 (ii), and P18 (iii).

Fig. 3.8 (continue from previous page). (C) Current-clamp traces for Lpar+ SST+ interneurons displaying NFS electrophysiological profiles, recorded at P6 (i), P11 (ii), and P18 (iii).
(D) Violin plot for maximum firing rate at different developmental ages (P5-P8, n = 20; P9-P13, n = 14; P14-P18, n = 23), showing statistically significant effect of "*Development*" (One-way ANOVA: $F(2,54) = 7.1$, $p \leq 0.01$).
(E) Violin plot for AP half-width at different developmental ages, showing statistically significant effect of "*Development*" (Kruskal-Wallis test: $X^2(2) = 35.8$, $p \leq 0.001$).
(F) Violin plot for cell maturity index at different developmental ages, showing statistically significant effect of "*Development*" (One-way ANOVA: $F(2,54) = 38.2$, $p \leq 0.01$). Asterisks in the plot show statistically significant differences between groups, when tested with post-hoc test corrected for multiple comparisons (Tukey's test for parametric data and Dunn's test with Benjamini-Hochberg correction for non-parametric data), according to the following notation: ** $p \leq 0.01$ and *** $p \leq 0.001$.

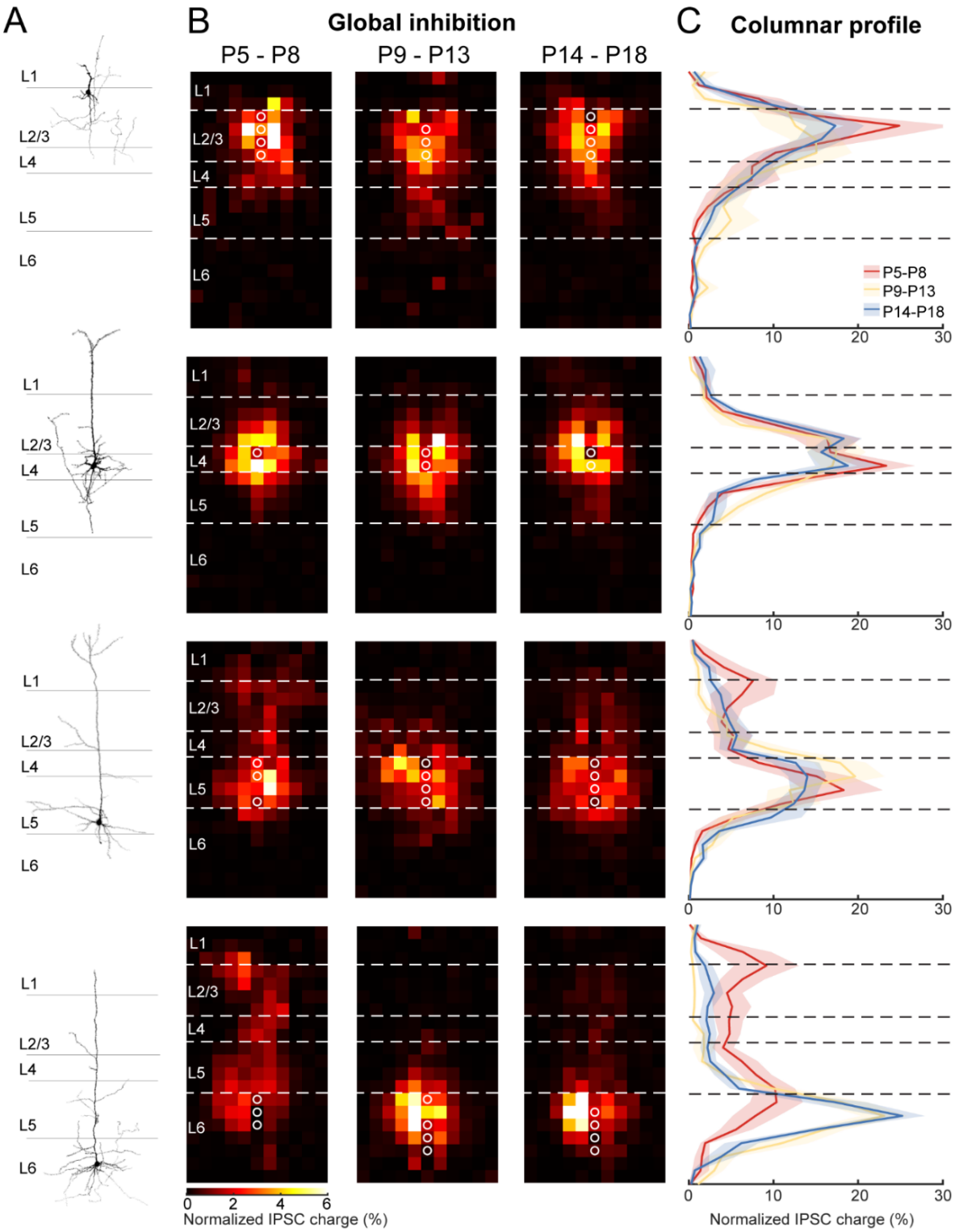
3.4 – GABAergic networks of V1 pyramidal neurons through early development

Circuit mapping experiments previously performed in our lab demonstrated the existence of a translaminar, reciprocal network between L5b SST+ interneurons and L4 excitatory neurons that is established between P5 and P8 in the mouse S1BF (Anastasiades et al., 2016; Marques-Smith et al., 2016). This network is thought to promote maturation of thalamo-cortical connectivity onto L4 spiny stellate neurons (SSNs) as well as to support appropriate wiring of PV+ interneurons to establish the canonical feed-forward inhibitory motif (Tuncdemir et al., 2016). Given this critical role for network maturation in S1BF, I wanted to understand whether such transient network is conserved across primary sensory areas of the mouse. However, to date, there are no studies focusing on connectivity between pyramidal neurons and GABAergic interneurons in V1 at comparable developmental stages.

Laser-scanning photostimulation (LSPS) and glutamate uncaging were used to map the presynaptic location of GABAergic inputs onto pyramidal neurons across cortical layers in monocular V1 (**Fig. 3.9**). Pyramidal neurons (n = 126) were recorded across the depth of cortex (L2/3, L4, L5, or L6) with the distance to pial surface calculated from a low-magnification micrograph (**Fig. 3.10A**). The layer location and morphological identity of the pyramidal neurons was confirmed by biocytin filling and post-hoc histological analysis (**Fig. 3.9A**). Heatmaps of the average, normalized GABAergic input onto V1 pyramidal cells through development (**Fig. 3.9B**) revealed that local, mostly intralaminar connectivity is the

dominant pattern, irrespective of layer, through early postnatal development. The only exceptions to this connectivity logic were L5 and L6 pyramidal neurons between P5-P8 (see **Fig. 3.9B**, third and bottom row, left column), receiving translaminar GABAergic inputs from supragranular layers besides local input. In contrast to equivalent cells in S1BF (Marques-Smith et al., 2016), V1 L4 excitatory neurons (**Fig. 3.9B**, second row), only ever received local GABAergic inputs from within L4 and its immediate vicinity. Columnar profiles (**Fig. 3.9C**) and normalised layer input plots (**Fig. 3.10C**) confirm the local pattern of GABAergic connectivity for L2/3 and L4 neurons at each developmental stage as well as the substantial GABAergic connectivity from supragranular layers onto infragranular pyramidal neurons. Finally, analysis of total GABAergic input (**Fig. 3.10B**) points to a developmental increase in the strength of GABAergic connectivity, especially for L4 pyramidal neurons at P5-P8 vs. P9-P13.

Fig. 3.9 (next page). Development of GABAergic connectivity onto V1 pyramidal neurons. (A) Representative morphological reconstruction of L2/3 (top row), L4 (second row), L5 (third row), and L6 (bottom row) Pyr in V1.
(B) Average normalised global GABAergic connectivity maps for Pyr cells in V1 obtained with laser-scanning photostimulation (LSPS) of caged glutamate. Individual maps are grouped by cell layer assignment (L2/3, top row; L4, second row; L5, third row; and L6, bottom row) and developmental window (P5-P8, first column; P9-P13, second column; P14-P18, last column). The heatmaps shown are average of individual maps in each group (L2/3: P5-P8, n = 11; P9-P13, n = 7; P14-P18, n = 10; L4: P5-P8, n = 18; P9-P13, n = 10; P14-P18, n = 9; L5: P5-P8, n = 10; P9-P13, n = 10; P14-P18, n = 11; L6: P5-P8, n = 12; P9-P13, n = 9; P14-P18, n = 9). Circles in the average map indicate approximate location of the recorded neurons in each group; dashed lines indicate approximate layer boundaries.
(C) Columnar GABAergic connectivity profile for L2/3 (top row), L4 (second row), L5 (third row), and L6 (bottom row) Pyr in V1, colour-coded for developmental window (P5-P8, red; P9-P13, yellow; P14-P18, blue). Solid line indicates average normalised connectivity; shaded area shows the SEM.


A
B
Global inhibition
C
Columnar profile
P5 - P8
P9 - P13
P14 - P18
L1
L2/3
L4
L5
L6
P5-P8
P9-P13
P14-P18
0
10
20
30
0
2
4
6
Normalized IPSC charge (%)
Normalized IPSC charge (%)

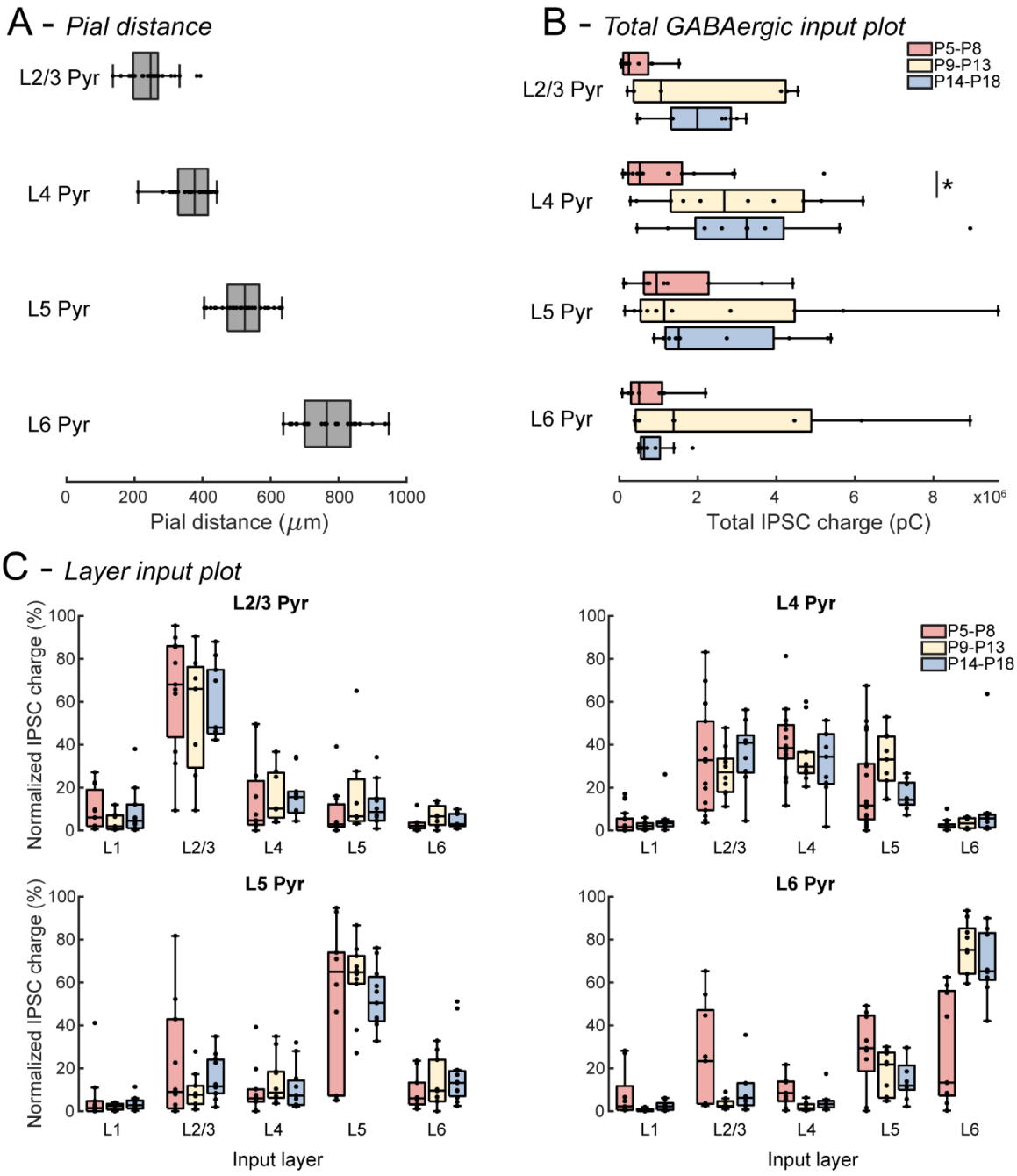


Fig. 3.10. Quantification of GABAergic connectivity onto V1 Pyr over development. (A) Box plot for pial distance of each recorded cell grouped by arbitrary layer assignment (L2/3, L4, L5, or L6).

(B) Box plot of raw total GABAergic inputs for each cell recorded during LSPS experiments, grouped by layer assignment and developmental window (P5-P8, red; P9-P13, yellow; P14-P18, blue). There is a statistically significant effect of the factors "*Development*" (Two-way ANOVA: $F(2,120) = 10.3$, $p \leq 0.001$) but not "*Cell Layer*".

(C) Box plot of normalised GABAergic inputs from each layer (Input layer) onto L2/3 (top left), L4 (top right), L5 (bottom left), and L6 (bottom right) Pyr in V1, grouped by developmental window (colour coded as in B). Number of recorded cells in each group is described in Fig. 3.10. Asterisks in the plot show statistically significant differences between groups, when tested with post-hoc Tukey's test corrected for multiple comparisons, according to the following notation: * $p \leq 0.05$.

Whereas average heatmaps shown in **Fig. 3.9B** provide an immediate interpretation of the connectivity of large neuronal populations, they may hide individual differences within a heterogeneous population. To better represent individual differences between recordings, the columnar profile (**Fig. 3.9C**) of each individual recorded cell was plotted as a developmental heatmap after sorting the recordings by age (**Fig. 3.11**). While individual L2/3 (**Fig. 3.11A**) and L4 (**Fig. 3.11B**) pyramidal neurons shows insignificant variation from the canonical local GABAergic connectivity logic, it is evident individual differences exist between L5 and L6 pyramidal neurons recorded in the P5-P8 window. Indeed, individual cells are characterized by either local, intralaminar connectivity or by translaminar GABAergic inputs (see **Fig. 3.11C, D**).

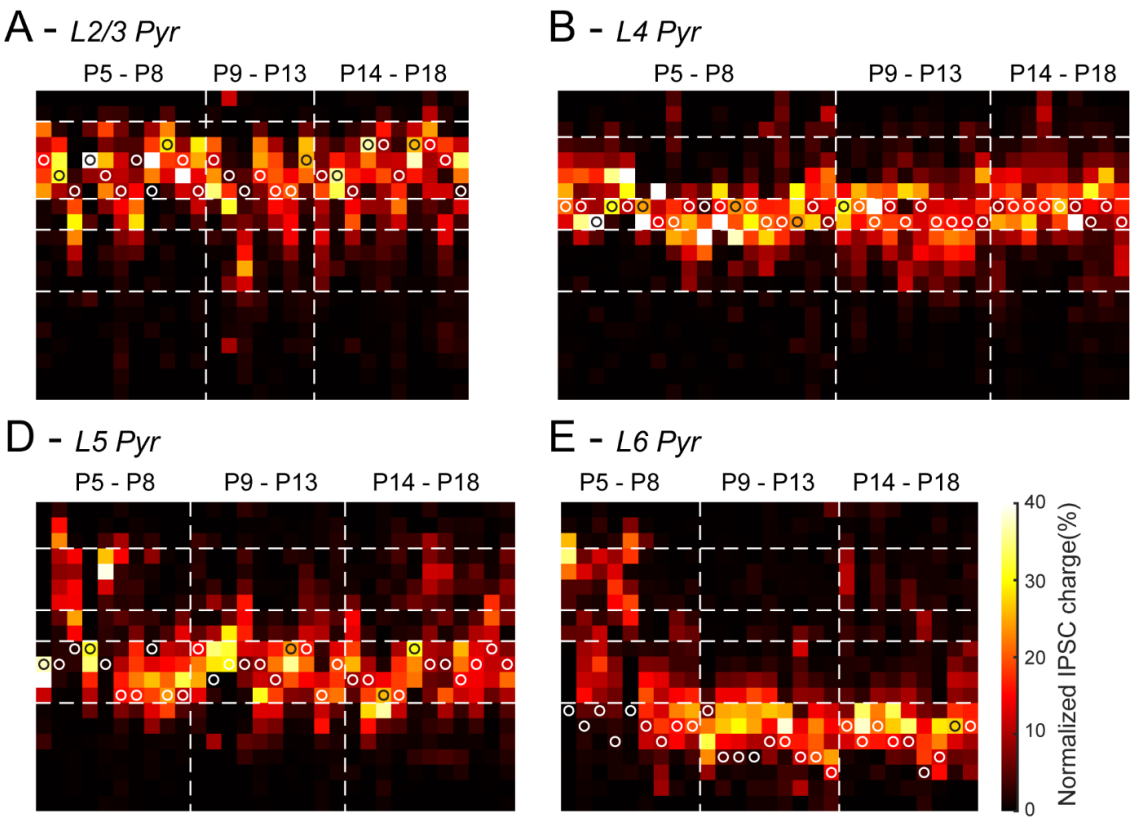


Fig. 3.11. Individual variability of V1 Pyr GABAergic connectivity maps. (A) Developmental GABAergic connectivity map for L2/3 Pyr in V1. Each column in the map shows the normalised GABAergic connectivity map obtained from an individual cell, collapsed along its rows to obtain a linear columnar profile. Columns (i.e., individual cells) are sorted by age while vertical dashed lines indicate the transition between developmental windows (P5-P8, P9-P13, and P14-P18). Horizontal lines indicate layer boundaries, and white or black circles indicate the location of the cell recorded in the linear map.
(B-D) Same as in A but for L4 (B), L5 (C), and L6 (D) Pyr in V1.

To better explore individual differences in the GABAergic connectivity profile of V1 pyramidal cells, all recorded maps were pooled together (**Fig. 3.12A**) to perform dimensionality reduction followed by K-means clustering (see *Method* section for details). Iterating the K-means clustering algorithm across different number of clusters (K) showed these data to be better characterized by 4 clusters (**Fig. 3.12B, C**). Principal component analysis (PCA) was then employed to represent the data in a bidimensional space. Cluster labels (**Fig. 3.12D**) show good correspondence with layer location of the recorded cells (**Fig. 3.12E**). As such, cells belonging to clusters 2 to 4 approximately correspond to L4, L5 and L6 cells and are hence characterized by local GABAergic inputs from within their layer and the immediate vicinity (**Fig. 3.12F**). Conversely, while cluster 1 mainly contains L2/3 cells, it also includes a small number of early L5 and L6 cells that deviate from the canonical intralaminar connectivity.

Overall, these results demonstrate that GABAergic connectivity onto V1 pyramidal neurons during early postnatal development is in line with connectivity logic reported in adult animals (Kätzel et al., 2011; Xu et al., 2016b), i.e., characterised by local, mostly intralaminar GABAergic inputs. This result highlights a critical difference between S1BF and V1, with the former characterised by substantial translaminar GABAergic inputs from L5b interneurons onto L4 excitatory SSNs (during the first postnatal week; Marques-Smith et al., 2016) and L2/3 pyramidal neurons (during the second postnatal week; Anastasiades et al., 2016). Moreover, infragranular pyramidal neurons in V1 during the first postnatal week deviate from the canonical intralaminar motif and receive substantial GABAergic inputs from supragranular interneurons. The remaining sections of ***Chapter 3*** will expand onto the findings related to connectivity of V1 L4 neurons, while ***Chapter 5*** will focus on infragranular pyramidal neurons.

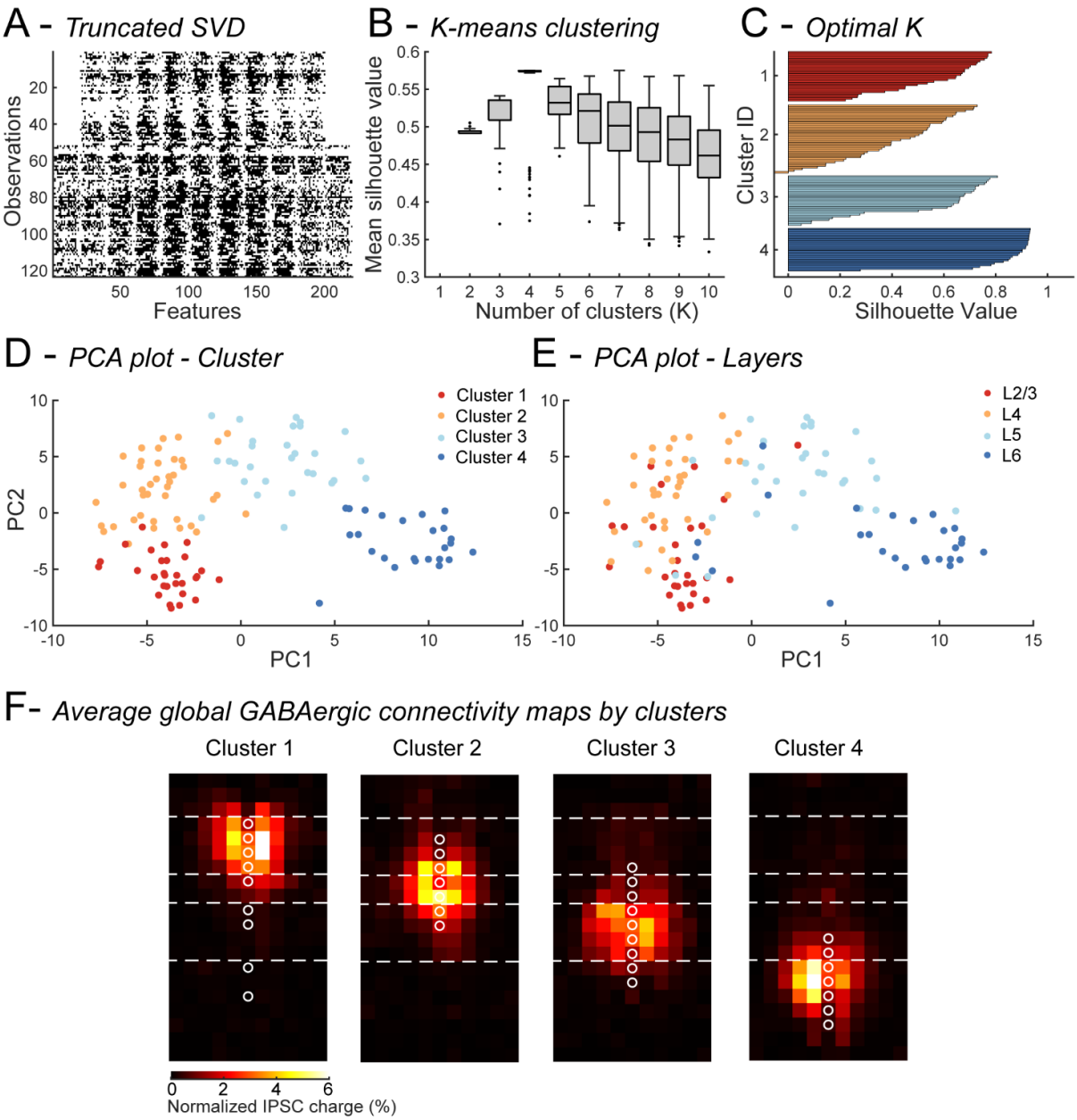


Fig. 3.12. Cluster analysis of GABAergic connectivity maps of V1 pyramidal neurons. (A) Feature-observation plot of individual recorded GABAergic connectivity maps. Each row (observation) represents an individual map and each column (feature) represent a specific pixel location in the map. Black pixels indicate non-zero values in the individual map, whereas white pixels indicate zero values.
(B) Box plot of average silhouette values obtained by K-means clustering at different number of clusters (k; from 2 to 10).
(C) Silhouette plot for optimal cluster number as shown in B (K = 4).
(D, E) Scatter plots of the first two principal components (PC) obtained by principal component analysis (PCA) of the GABAergic connectivity map dataset, colour-coded by clusters obtained through K-means clustering (D) or by arbitrary layer assignment (E; L2/3, red; L4, yellow; L5, light blue; L6, dark blue).
(F) Average normalised global GABAergic connectivity maps for Pyr cells in V1, grouped by clusters obtained through K-means clustering. White or black circles indicate approximate location of the cell recorded.

3.5 – Networks of V1 SST+ interneurons through early development

3.5.1 – GABAergic connectivity from SST+ interneurons onto L4 pyramidal neurons in V1

Global GABAergic connectivity onto early postnatal L4 pyramidal neurons shows they are characterised by local connections received from interneurons mostly located within L4 itself (**Fig. 3.9**). Conversely, L4 SSNs in S1BF are characterised by substantial GABAergic input from SST+ interneurons located in L5b (Marques-Smith et al., 2016). In cortex, PV+ FS interneurons are densely connected with local pyramidal neurons (Packer and Yuste, 2011) and provide the strongest inhibitory drive (Pfeffer et al., 2013). It is hence possible our global GABAergic map might also be biased towards inputs from this interneuron class.

To rule out the presence of GABAergic connectivity from L5 SST+ interneurons, I exploited an optogenetic strategy to specifically map GABAergic inputs from SSTCre+ interneurons. I conditionally expressed the P2X2 receptor in *SSTCre* animals and then used UV laser uncaging of ATP to stimulate SSTCre+ interneurons, while simultaneously recording from L4 pyramidal neurons in V1 voltage-clamped at 0 mV (n = 31; **Fig. 3.13**). Average normalised maps of SST+ interneuron input onto L4 pyramidal neurons at different developmental windows (**Fig. 3.13A**) replicate the finding obtained with global GABAergic connectivity mapping (**Fig. 3.10B**, second row), suggesting that SST+ interneuron input is local and not translaminar, in contrast to S1BF. This data is confirmed by the columnar profile of GABAergic connectivity (**Fig. 3.13B**) and normalised layer input plot (**Fig. 3.13D**). Developmental maps in **Fig. 3.13C** also highlight the lack of heterogeneity among recorded L4 pyramidal neurons.

Comparison of total columnar GABAergic connectivity onto L4 pyramidal neurons (data in **Fig. 3.9** and **Fig. 3.10**) with SST-specific connectivity (**Fig. 3.13**) revealed a significant increase in total GABAergic input over the time window studied, an increase not observed for SST+ interneurons input alone (**Fig. 3.14A**). Analysis of the columnar profiles (**Fig. 3.14B**) revealed similar distributions at the P5-P8 and P14-P18 time windows but a

discrepancy at P9-P13, where SST-specific inputs are clustered near the L4-L5 boundary. Such discrepancy is confirmed by larger kurtosis values obtained from SST-specific columnar profiles than values obtained from global GABAergic columnar profiles at P9-P13 (see **Fig. 3.14C**).

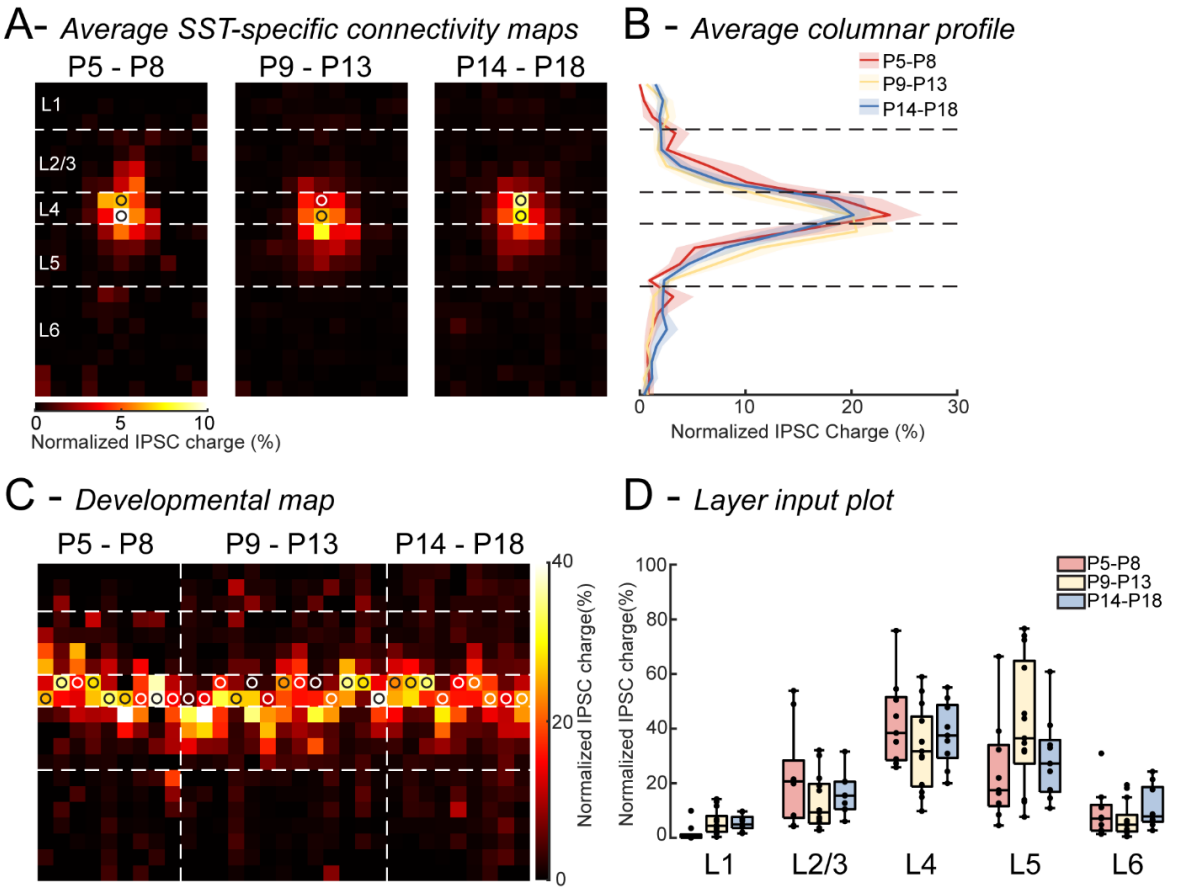


Fig. 3.13. Development of SSTCre+ interneuron connectivity onto V1 L4 pyramidal neurons.
(A) Average normalised maps of SSTCre+ connectivity onto L4 Pyr in V1 obtained through LSPS of caged ATP in *SSTCre;P2X2R* transgenic animals. Individual connectivity maps are grouped by developmental window (P5-P8, n = 9; P9-P13, n = 13; P14-P18, n = 9). White or black circles indicate approximate location of the recorded cell in the map; horizontal dashed lines indicate layer boundaries.
(B) Columnar SSTCre+ connectivity profile onto L4 Pyr in V1, colour-coded for developmental window (P5-P8, red; P9-P13, yellow; P14-P18, blue). Solid line indicates average normalised connectivity; shaded area shows the SEM.
(C) Developmental maps of SSTCre+ connectivity onto L4 Pyr in V1, as described in Fig. 3.12.
(D) Box plot of normalised SSTCre+ connectivity inputs from each layer (Input layer) onto L4 Pyr in V1, grouped and colour-coded for developmental window (as in B).

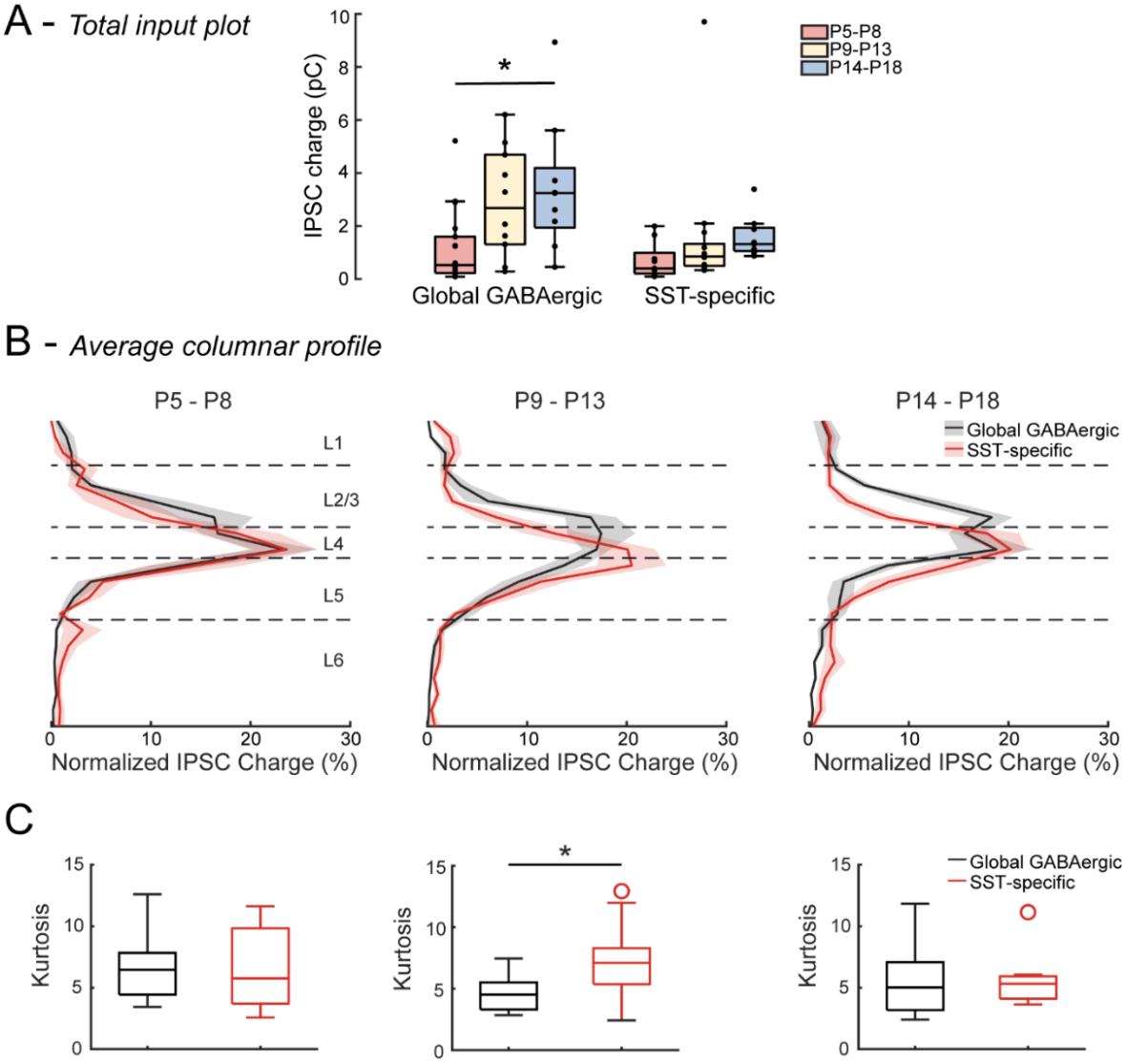


Fig. 3.14. Comparison between global GABAergic and SST-specific connectivity onto V1 L4 Pyr. (A) Box plot of raw total GABAergic or total SST-specific inputs onto L4 Pyr in V1, grouped and colour-coded for developmental window (P5-P8, red; P9-P13, yellow; P14-P18, blue). Sample size are the same as in Fig. 3.10 (for global GABAergic input data onto L4 Pyr) and Fig. 3.13 (for SST-specific input data onto L4 Pyr). There are statistically significant effects for both "*Development*" and "*Stimulus*" (glutamate uncaging vs. ATP uncaging, for global GABAergic vs. SST-specific inputs, respectively) factors (Two-way ANOVA: $F(1, 64) = 6.6$, $p \leq 0.05$ for "*Stimulus*" and $F(2,64) = 5.9$, $p \leq 0.01$ for "*Development*"). Asterisk in the plot show statistically significant differences between groups, when tested with post-hoc Tukey's test corrected for multiple comparisons, according to the following notation: *$p \leq 0.05$.
(B) Columnar normalised connectivity profile for total GABAergic inputs (black) and SSTCre+ inputs (red) onto L4 Pyr in V1 at different developmental stages (P5-P8, left; P9-P13, middle; P14-P18, right). Solid line indicates average normalised connectivity; shaded area shows the SEM.
(D) Box plot of kurtosis value obtained from the columnar distribution profiles in C at different developmental stages (P5-P8, left; P9-P13, middle; P14-P18, right). There is a statistically significant difference in kurtosis values between global GABAergic and SST-specific profiles at P9-P13 (unpaired t-test: $t(21) = -2.4$, *$p \leq 0.05$) but not at P5-P8 or P14-P18.

3.5.2 – Excitatory connectivity networks of infragranular SST+ interneurons in V1

In S1BF, L5b SST+ interneurons form a reciprocal synaptic loop with L4 SSNs between P5 and P8 (Marques-Smith et al., 2016). To further test the distinct nature of early GABAergic circuits between V1 and S1BF, I used LSPS of caged glutamate to map excitatory connectivity onto infragranular L5-6 SST+ interneurons in V1 across development (n = 36 cells). Average normalised heatmaps of excitatory connectivity onto L5-6 SST+ interneurons show they are mostly dominated by glutamatergic inputs from local infragranular pyramidal neurons (**Fig. 3.15A**). However, at the earliest time window under investigation (P5-P8), SST+ interneurons in deep cortical layers also receive excitatory inputs from L2/3 pyramidal neurons, as confirmed by columnar profile plot in **Fig. 3.15B**. Developmental timeline of inputs (**Fig. 3.15C**) reveals heterogeneity among the SST+ interneurons recorded between P5 and P8, with some cells possessing local excitatory inputs from infragranular layers and others receiving both local and translaminar inputs from infragranular and supragranular layers, respectively. This pattern is also confirmed by the large variance in the normalised layer input data in **Fig. 3.15D**. A few recordings (total of n = 4) were performed on SST+ interneurons localised near the boundary between L4 and L5. Two representative examples of the global excitatory connectivity maps obtained for a P7 and a P18 cell are shown in **Fig. 3.15E**. These SST+ interneurons receive excitatory inputs from pyramidal neurons located within L4.

Overall, these results confirm the difference between GABAergic networks of SST+ interneurons between S1BF and V1. L4 pyramidal neurons in V1 are engaged in a reciprocal network with SST+ interneurons located within L4 itself (or near the L4-L5 boundary), unlike S1BF where a reciprocal, translaminar network is established between L5b SST+ interneurons and L4 excitatory neurons (Marques-Smith et al., 2016).

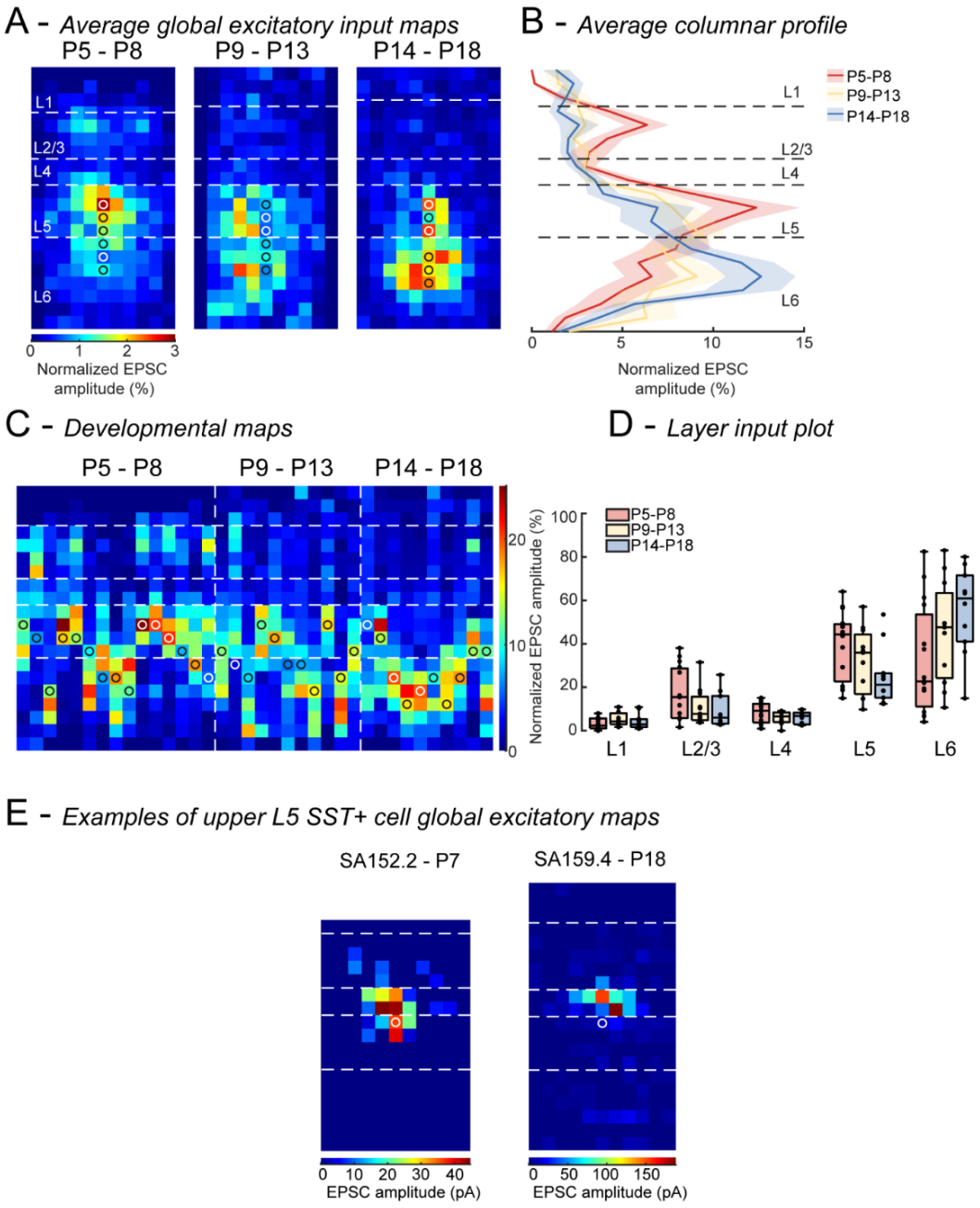


Fig. 3.15. Development of excitatory connectivity onto V1 infragranular SSTCre+ interneurons. (A) Average normalised maps of excitatory connectivity onto infragranular SSTCre+ interneurons in V1 obtained through LSPS of caged glutamate. SSTCre+ interneurons are targeted via the *SSTCre;Ai9* transgenic line. Individual connectivity maps are grouped by developmental window (P5-P8, n = 15; P9-P13, n = 11; P14-P18, n = 10). White or black circles indicate approximate location of the recorded SSTCre+ interneuron in the map; horizontal dashed lines indicate layer boundaries.
(B) Columnar excitatory connectivity profile onto infragranular SSTCre+ interneurons in V1, colour-coded for developmental window (P5-P8, red; P9-P13, yellow; P14-P18, blue). Solid line indicates average normalised connectivity; shaded area shows the SEM.
(C) Developmental maps of excitatory connectivity onto infragranular SSTCre+ interneurons in V1, as described in Fig. 3.12.
(D) Box plot of normalised excitatory connectivity inputs from each layer (Input layer) onto infragranular SST+ interneurons in V1, grouped and colour-coded for developmental window (as in B).
(E) Representative examples of global excitatory connectivity maps obtained from two SST+ interneurons recorded in upper L5 near the L4 boundary.

3.6 – Development of dis-inhibitory interneuron networks in developing V1

3.6.1 – Establishing an optogenetic strategy to identify PV+ interneurons during early postnatal development

SST+ interneurons have been proposed to play a key role in regulating information flow in early cortical networks through connections onto pyramidal neurons as well as other interneurons (Marques-Smith et al., 2016; Tuncdemir et al., 2016; Baruchin et al., 2021). Beside targeting the apical dendrite of pyramidal neurons (Wang et al., 2004), SST+ interneurons provide inhibitory control over other interneuron subtypes (Pfeffer et al., 2013) in a layer-dependent manner (Xu et al., 2013). During neuronal network development, SST+ interneurons switch from providing inhibitory action to V1 L2/3 pyramidal neurons to providing dis-inhibition through PV+ interneurons around the time of eye-opening (Guan et al., 2017). Later in development, this dis-inhibitory network regulates synaptic plasticity during the critical period for binocular plasticity in V1 in the fourth postnatal week (Yaeger et al., 2019). It is however currently unknown whether L4 pyramidal neurons follows the same connectivity logic as L2/3 cells as well as when disinhibitory networks in L4 are established during early postnatal development of V1.

To address this, I characterised the development of GABAergic connectivity between cortical interneurons, with a particular focus on the SST+ to PV+ interneuron network. I used the combinatorial genetic strategy described previously to label Lhx6+ interneurons with eGFP while simultaneously expressing Cre-dependent actuators in SST+ interneurons to enable circuit mapping. First, I generated *Lhx6-eGFP; SSTCre; Ai32* offspring in which Channelrhodospin-2 (ChR2) was conditionally expressed in SSTCre+ interneurons. Even at early ages I could reliably recruit V1 SSTCre+ neurons (**Fig. 3.16A**) upon stimulation of ChR2 with blue (470nm) LED light. Further, I could discern the identity of both SST (Lhx6+ SSTCre+; **Fig. 3.16B**) and putative PV+ interneurons (Lhx6+ SSTCre− cells; **Fig. 3.16C**) from recordings of Lhx6+ interneurons voltage-clamped near the reversal potential for

glutamate (E_{Glu} ≈ 0 mV) upon optogenetic stimulation. Lhx6+ SSTCre+ cells responded to optogenetic stimulation with a mixture of inward and outward current deflections, reflecting direct activation of ChR2 and inputs from other SSTCre+ interneurons, respectively (**Fig. 3.16B**, left). Conversely, Lhx6+ SSTCre− cells were characterised solely by an outward current, due to inputs received from SSTCre+ interneurons (**Fig. 3.16C**, left). Bath-application of the broad $GABA_A$ channel blocker bicuculline (10 µM) attenuated the outward current to reveal the ChR2-dependent inward current in Lhx6+ SSTCre+ cells (**Fig. 3.16B**, right). The identity of the interneuron subtype was further confirmed following morphology reconstruction of the Lhx6+ SSTCre+ cell, which exhibited features of SST+ Martinotti cells, including the ascending axon arborising in L1 (see **Fig. 3.16B**, right). Similarly, the morphology of the Lhx6+ SSTCre− cells showed features of a basket cell with the axon arborising extensively within L4 (see **Fig. 3.16C**, right). Based on previous immunohistochemical (**Fig. 3.5**) and electrophysiological experiments (**Fig. 3.6**), Lhx6+ SSTCre− cells correspond to FS PV+ interneurons and thus can be isolated from *Lhx6-eGFP; SSTCre; Ai32* animals through the optogenetic strategy described above.

I also conditionally expressed the P2X2 receptor in SSTCre+ to enable ATP uncaging experiments (see *Methods*) and mapping of the presynaptic location of SSTCre+ cells. **Fig. 3.16D** shows the GABAergic connectivity map (left) and representative current traces of a SSTCre+ interneuron expressing the P2X2 receptor recorded in voltage-clamp configuration (V_h = 0 mV) during an ATP uncaging experiment. Both the connectivity maps and current traces show little inhibitory postsynaptic activity (see traces 2 and 3), reflecting exclusively spontaneous activity and confirming poor connectivity between SST+ interneurons (Pfeffer et al., 2013). However, UV laser fired in close proximity to the cell evoked a robust inward current deflection (see **Fig. 3.16D**, bottom trace), due to direct activation of the P2X2 receptor in the recorded SSTCre+ interneurons.

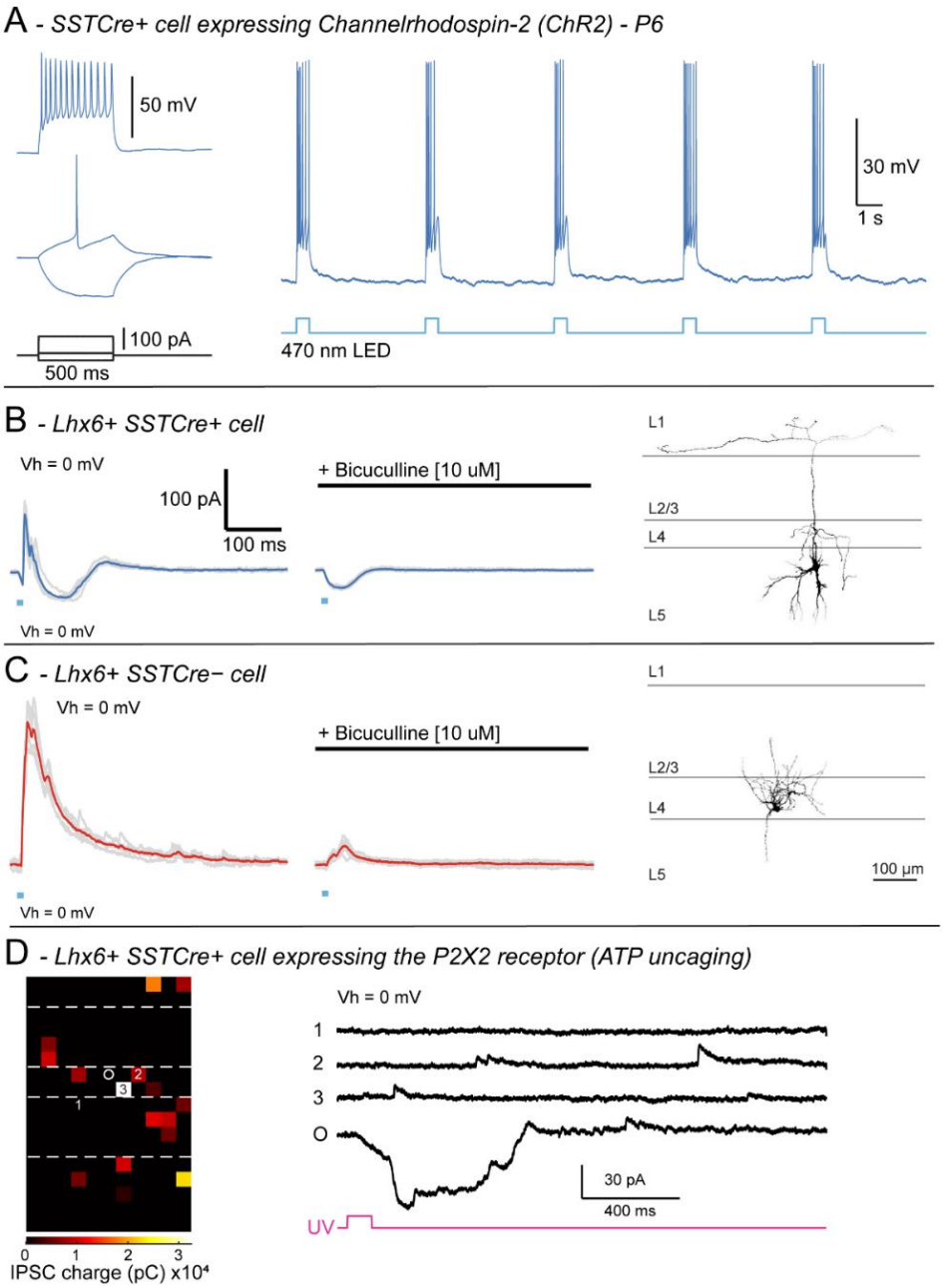
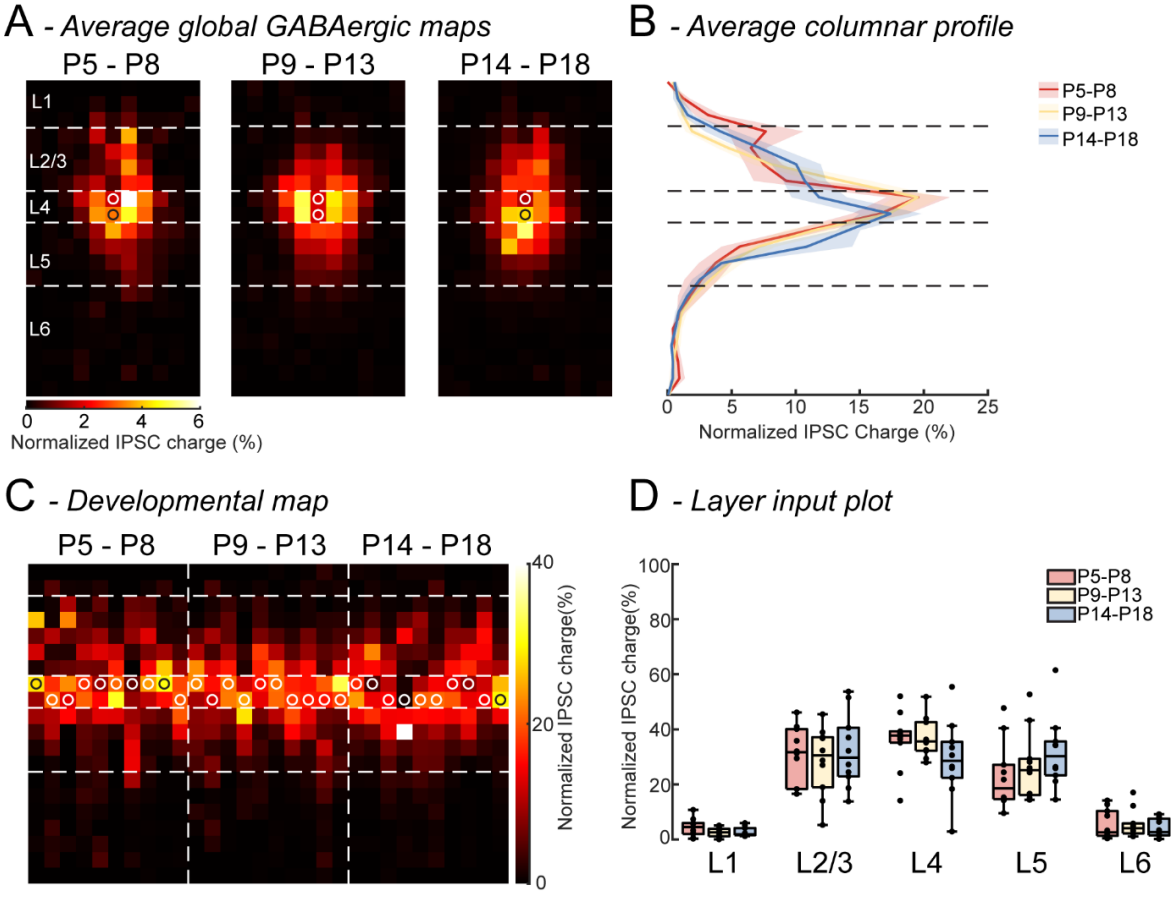


Fig. 3.16. Optogenetic strategy to identify putative parvalbumin-expressing (PV+) interneurons during early postnatal development. (A) Current-clamp recordings of a representative Cre-expressing SST+ interneuron (P6) conditionally expressing Channelrhodospin-2 (ChR2) during current steps applications (left) and blue (470 nm) LED pulses (right; 500 ms duration, indicated by light blue line).
(B) Voltage-clamp recordings (holding potential, V_h = 0 mV) of a Lhx6+ SSTCre+ cell during brief (10 ms) blue light pulse in control conditions (left) and during bath-administration of Bicuculline [10 µM] (middle). Right, morphological reconstruction of a P7 Lhx6+ SSTCre+ cell showing both dendritic and axonal arbours.
(C) Voltage-clamp recordings (V_h = 0 mV) of a Lhx6+ SSTCre− cell during brief (10 ms) blue light pulse in control conditions (left) and during bath-administration of Bicuculline [10 µM] (middle). Right, morphological reconstruction of a P8 Lhx6+ SSTCre− cell.
(D) Heatmap (left) showing GABAergic connectivity from SST+ interneurons onto a L4 Lhx6+ SSTCre+ cell (indicated by white circle) and corresponding voltage-clamp recordings (V_h = 0 mV) obtained during ATP uncaging experiments (right) with UV light (indicated by purple line). Numbers and circle indicate traces recorded when stimulating a specific location in the heatmap shown on the left.

3.6.2 – Development of SST+ interneuron connectivity onto L4 FS interneurons in V1

To characterise the development of dis-inhibitory network in V1, I first performed LSPS experiments coupled with glutamate uncaging to map total columnar GABAergic connectivity onto L4 Lhx6+ PV+ interneurons over the three developmental windows of interest. First, the optogenetic approach described previously (**Fig. 3.16B, C**) was utilised to identify Lhx6+ SSTCre− cells as PV+ interneurons; total GABAergic connectivity was then assessed using LSPS mapping. Similar to L4 pyramidal neurons (**Fig. 3.9**), L4 PV+ interneurons (n = 30) are dominated by local, mostly intralaminar GABAergic input from L4 and its immediate vicinity (**Fig. 3.17A**), as confirmed by columnar profile (**Fig. 3.17B**) and total normalised layer input (**Fig. 3.17D**), with little heterogeneity among individually recorded cells (**Fig. 3.17C**).



Experiments performed in the adult mouse V1 suggested PV+ interneurons strongly inhibit each other (Pfeffer et al., 2013) and thus the global GABAergic connectivity described in the previous section might still reflect PV+ to PV+ interneuron interconnectivity. To study SST+ inputs onto PV+ interneurons, I quantified optogenetically induced inhibitory postsynaptic currents (IPSC) recorded from L4 Lhx6+ SSTCre− cells (n = 33) and compared with data obtained from L4 pyramidal neurons (n = 27; **Fig. 3.18A**). All the recorded cells from P9 onwards responded to optogenetic stimulation with a reliable IPSC, whereas a few interneurons and around half of the pyramidal cells recorded between P5 and P8 were classified as non-responsive (**Fig. 3.18B**). Quantification of evoked IPSC amplitude at different LED power intensities and different developmental windows (**Fig. 3.18C**) shows that, at P9-P13, optogenetic-evoked IPSC are larger in PV+ interneurons than pyramidal neurons across LED power intensity values employed. Quantification of IPSC latency (**Fig. 3.18D**) and jitter (**Fig. 3.18E**) shows significant developmental reduction in both features but no difference between L4 PV+ interneurons and L4 pyramidal neurons. IPSC decay time constant did not change over development as well as between different cell types (**Fig. 3.18F**). These results suggest that PV+ interneurons are engaged by SST+ interneurons from the earliest developmental window investigated, with large-amplitude, low-latency, and low-jitter IPSC being recorded from P9 onwards. Moreover, SST+ connectivity is biased towards L4 PV+ interneurons between P9 and P13, when they respond to optogenetic stimulation with larger IPSCs than pyramidal neurons.

Fig. 3.17 (previous page). Development of GABAergic connectivity onto L4 Lhx6+ PV+ interneurons in V1. (A) Average normalised maps of global GABAergic connectivity onto L4 Lhx6+ PV+ interneurons in V1 obtained through LSPS of caged glutamate in *Lhx6-eGFP;SSTCre;Ai32* transgenic animals. Individual connectivity maps are grouped by developmental window (P5-P8, n = 10; P9-P13, n = 10; P14-P18, n = 10). White or black circles indicate approximate location of the recorded cell in the map; horizontal dashed lines indicate layer boundaries.
(B) Columnar global GABAergic connectivity profile onto L4 Lhx6+ PV+ interneurons in V1, colour-coded for developmental window (P5-P8, red; P9-P13, yellow; P14-P18, blue). Solid line indicates average normalised connectivity; shaded area shows the SEM.
(C) Developmental maps of global GABAergic connectivity onto L4 Lhx6+ PV+ interneurons in V1, as described in Fig. 3.12.
(D) Box plot of normalised global GABAergic connectivity inputs from each layer (Input layer) onto L4 Lhx6+ PV+ interneurons in V1, grouped and colour-coded for developmental window (as in B).

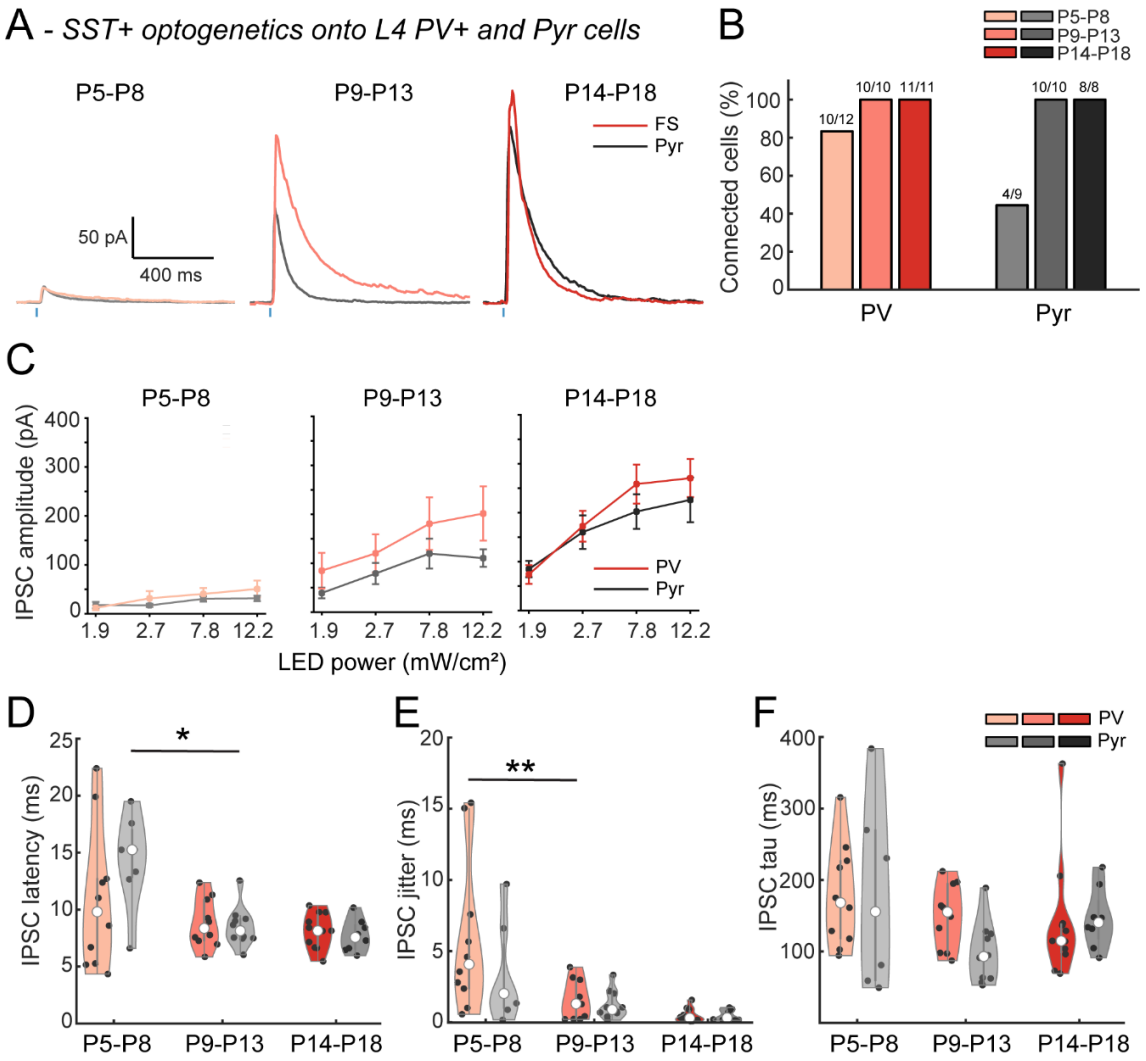
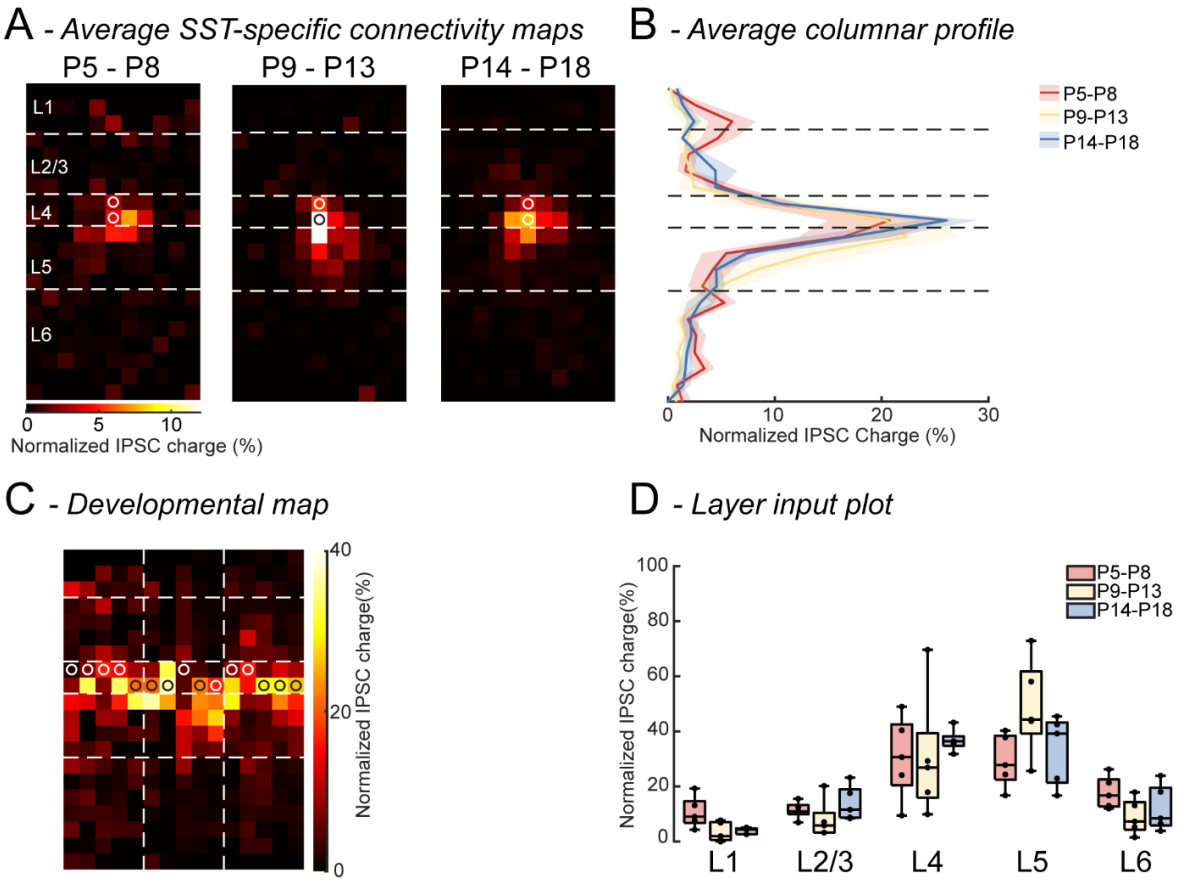


Fig. 3.18. Development of SST+ interneuron connectivity onto Lhx6+ PV+ interneurons in V1.
(A) Representative voltage-clamp recordings (V_h = 0 mV) of L4 Lhx6+ PV+ interneurons (red) and L4 Pyr (black) in V1 upon optogenetic stimulation (470 nm; indicated by blue line) of SSTCre+ interneurons in *Lhx6-eGFP;SSTCre;Ai32* transgenic animals, at different developmental stages (P5-P8, left; P9-P13, middle; P14-P18, right).
(B) Bar plot of percentage of Lhx6+ PV+ interneurons (red) or Pyr cells (black) responsive to optogenetic stimulation of SSTCre+ interneurons at different developmental windows.
(C) Error-bar plot of optogenetically-induced IPSC amplitude onto Lhx6+ PV+ interneurons (red) and Pyr (black) at 4 distinct LED power levels and at different developmental windows (as in A). Three-way ANOVA shows a statistically significant effect of the factors "*LED Power*" ($F(3,179) = 8.1$, $p \leq 0.001$), "*Cell Type*" ($F(1,179) = 4.3$, $p \leq 0.05$), and "*Development*" ($F(2,179) = 39.9$, $p \leq 0.001$).
(D) Violin plot of optogenetically-induced IPSC latency for L4 Lhx6+ PV+ interneurons (red) and L4 Pyr (black), at different developmental ages. Two-way ANOVA shows a statistically significant effect of the factor "*Development*" ($F(2,50) = 8.6$, $p \leq 0.001$), but not "*Cell Type*".
(E) Violin plot of optogenetically-induced IPSC jitter (standard deviation of IPSC latency) for L4 Lhx6+ PV+ interneurons (red) and L4 Pyr (black), at different developmental ages. Two-way ANOVA shows a statistically significant effect of the factor "*Development*" ($F(2,50) = 14.5$, $p \leq 0.001$), but not "*Cell Type*".
(F) Violin plot of optogenetically-induced IPSC decay time constant (tau) for L4 Lhx6+ PV+ interneurons (red) and L4 Pyr (black), at different developmental ages. Two-way ANOVA does not show statistically significant effect of either "*Development*" or "*Cell Type*." Asterisks in the plot show statistically significant differences between groups, when tested with post-hoc test corrected for multiple comparisons (Tukey's test), according to the following notation: * $p \leq 0.05$ and ** $p \leq 0.01$.

Wide field optogenetic experiments do not provide any insight into the location of the presynaptic SST+ interneurons. Thus, I exploited *Lhx6-eGFP; SSTCre; P2X2R* transgenic mice to conditionally express the P2X2 receptor in SSTCre+ cells and enable selective mapping of their input connectivity through LSPS and ATP uncaging. Lhx6+ SSTCre− cells (thus PV+ interneurons) in L4 were identified as described in **Fig. 3.16D** and their SST+ connectivity mapped. Similar to total GABAergic input maps, average normalised maps of SST-specific GABAergic connectivity onto L4 PV+ interneurons (n = 15; **Fig. 3.19A**) reveal local connectivity patterns at every developmental window investigated that extends in the upper portion of L5, with little heterogeneity among individual maps (**Fig. 3.19C**). This mostly local connectivity motif is confirmed by columnar profile (**Fig. 3.19B**) and total layer input plots (**Fig. 3.19D**).



Finally, I compared total GABAergic versus SST interneuron-specific input onto L4 PV+ interneurons across early development (**Fig. 3.20**). Despite differences originating from the employment of either glutamate or ATP uncaging, analysis of total GABAergic inputs onto L4 PV+ interneurons in the two conditions showed larger total GABAergic IPSC charge than SST-specific ones as well as a general developmental increase (**Fig. 3.20A**). In analogy with the connectivity profiles for L4 pyramidal neurons described in previous sections (**Fig. 3.14**), comparison of average columnar profiles obtained from total and SST-specific GABAergic connectivity maps of L4 PV+ interneurons showed a bias towards the L4-L5 boundary for SST-specific profiles (**Fig. 3.20B**). While this could be observed both at P5-P8 and P9-P13 developmental windows, analysis of the profile kurtosis showed statistically significant difference only in the earliest window under investigation (**Fig. 3.20C**).

In conclusion, I described the developmental timeline of dis-inhibitory connectivity motifs in L4 of the mouse V1, by focusing on SST-specific GABAergic connectivity onto L4 PV+ interneurons. These cells are characterised by local GABAergic connections that include SST+ interneurons located near the L4-L5 boundary. Our optogenetics data suggest SST+ interneurons send stronger projections onto L4 PV+ interneurons than L4 pyramidal neurons between P9 and P13, critical developmental period that precede eye opening.

Fig. 3.19 (previous page). Mapping SSTCre+ interneurons connectivity onto L4 Lhx6+ PV+ interneurons in V1. (A) Average normalised maps of SSTCre+ connectivity onto L4 Lhx6+ PV+ interneurons in V1 obtained through LSPS of caged ATP in *Lhx6-eGFP;SSTCre;P2X2R* transgenic animals. Individual connectivity maps are grouped by developmental window (P5-P8, n = 5; P9-P13, n = 5; P14-P18, n = 5). White or black circles indicate approximate location of the recorded cell in the map; horizontal dashed lines indicate layer boundaries.
(B) Columnar SSTCre+ connectivity profile onto L4 Lhx6+ PV+ interneurons in V1, colour-coded for developmental window (P5-P8, red; P9-P13, yellow; P14-P18, blue). Solid line indicates average normalised connectivity; shaded area shows the SEM.
(C) Developmental maps of SSTCre+ connectivity onto L4 Lhx6+ PV+ interneurons in V1, as described in Fig. 3.12.
(D) Box plot of normalised SSTCre+ connectivity inputs from each layer (Input layer) onto L4 Lhx6+ PV+ interneurons in V1, grouped and colour-coded for developmental window (as in B).

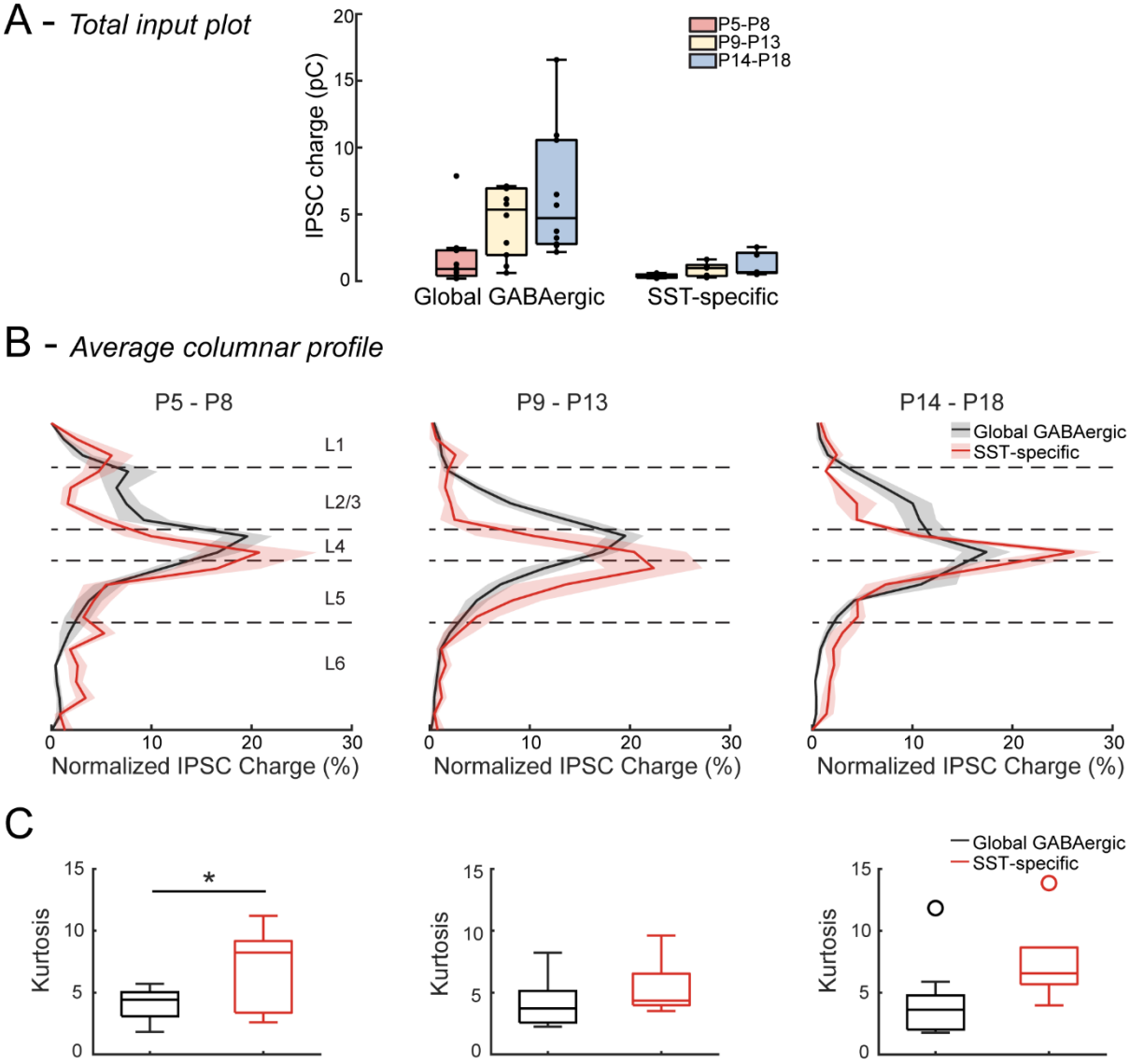


Fig. 3.20. Comparison between global GABAergic and SST-specific connectivity onto V1 PV+ Pyr. (A) Box plot of raw total GABAergic or total SST-specific inputs onto L4 PV+ interneurons in V1, grouped and colour-coded for developmental window (P5-P8, red; P9-P13, yellow; P14-P18, blue). Sample size are the same as in Fig. 3.17 (for global GABAergic input data onto L4 PV+ cells) and Fig. 3.19 (for SST-specific input data onto L4 PV+ cells). There are statistically significant effects for both "*Development*" and "*Stimulus*" (glutamate uncaging vs. ATP uncaging, for global GABAergic vs. SST-specific inputs, respectively) factors (Two-way ANOVA: $F(1, 41) = 13.7$, $p \leq 0.001$ for "*Stimulus*" and $F(2,41) = 5.4$, $p \leq 0.01$ for "*Development*").
(B) Columnar normalised connectivity profile for total GABAergic inputs (black) and SST-specific inputs (red) onto L4 PV+ interneurons in V1 at different developmental stages (P5-P8, left; P9-P13, middle; P14-P18, right). Solid line indicates average normalised connectivity; shaded area shows the SEM.
(D) Box plot of kurtosis value obtained from the columnar distribution profiles in C at different developmental stages (P5-P8, left; P9-P13, middle; P14-P18, right). There is a statistically significant difference in kurtosis values between global GABAergic and SST-specific profiles at P5-P8 (unpaired t-test: $t(13) = -2.2$, $*p \leq 0.05$) but not at P9-P13 or P14-P18.

3.7 – Development of thalamocortical connectivity in the developing V1

The intricate cortical network of V1 described thus far has the "primary" role of interpreting thalamic inputs. Functional studies mapping the developmental timeline of thalamic input in S1BF have highlighted transient connectivity onto SST+ interneurons that precedes the maturation of the canonical feed-forward inhibitory motif involving PV+ interneurons (Marques-Smith et al., 2016; Tuncdemir et al., 2016). Corresponding studies in V1, however, have been limited due to the lack of a reliable acute *in vitro* slice preparation which preserves thalamocortical connections. In this section, I used optogenetics to overcome this limitation and functionally map the development of thalamic connection onto excitatory neurons and GABAergic interneurons in V1.

ChR2 was conditionally expressed in the early postnatal thalamus using the *Olig3Cre* transgenic line while cortical interneurons were targeted for patch-clamp recordings by breeding *Lhx6-eGFP* onto the same background with SST+ or FS interneurons identified according to their intrinsic electrophysiological profile and/or morphology (see **Fig. 3.6** and **Fig. 3.8**). Blue light stimulation of thalamic terminal expressing ChR2 under the *Olig3Cre* driver line resulted in excitatory postsynaptic currents (EPSCs) in recorded neurons voltage-clamped near the resting membrane potential (V_h = −60 mV; **Fig. 3.21A, B**). Minimal stimulation was defined as the smallest LED power to elicit a postsynaptic response (**Fig. 3.21A, B**, middle). Stimulation with larger LED power often led to bursts of EPSCs which likely include multiple thalamic inputs as well as recurrent excitatory connections between cortical neurons (**Fig. 3.21A**, right). ChR2 assisted circuit mapping of excitatory connections *in vitro* typically employ a pharmacological approach to reveal direct, monosynaptic connections and suppress polysynaptic excitatory responses using tetrodotoxin (TTX) to block voltage-dependent sodium channels and 4-aminopyridine (4-AP) to increase presynaptic terminal excitability (Petreanu et al., 2007). Using this protocol, I was, however, unable to reveal ESPCs in V1 in a manner independent of developmental age and cell type (n = 10 recorded in the presence of TTX and 4-AP; **Fig. 3.21C**). The only

exception was one L4 excitatory neuron recorded in S1BF at P18 which responded with reduced EPSCs to optogenetic stimulation in the presence of TTX and 4-AP (not shown). In the absence of a pharmacological approach to isolate direct EPSCs, I quantify optogenetically induced EPSCs obtained at minimal LED power stimulation for all cells recorded and apply criteria based on EPSC latency and jitter to determine neurons receiving putative monosynaptic thalamic inputs (henceforth defined as connected cell).

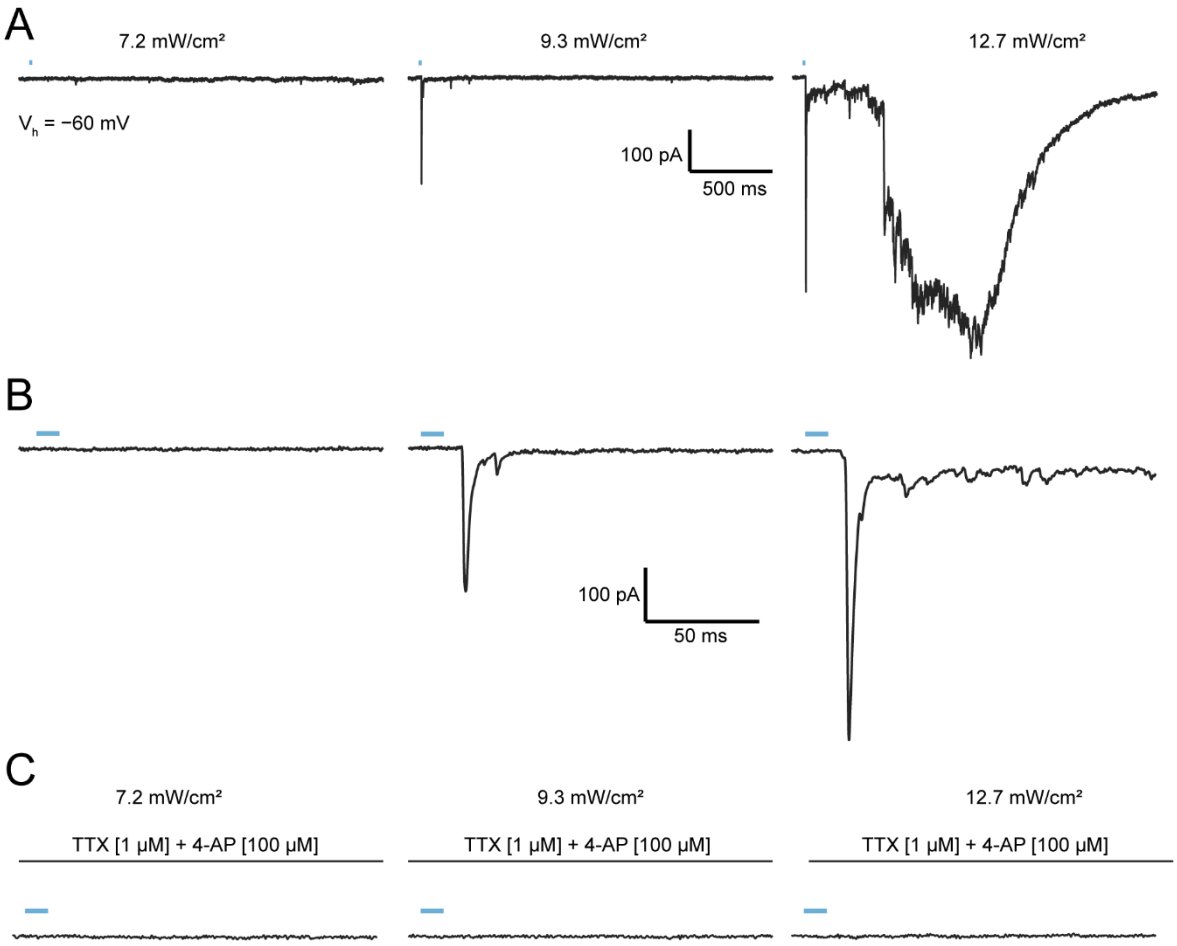


Fig. 3.21. Optogenetic approach to study thalamocortical connectivity in the developing V1. (A) Representative current traces (V_h = −60 mV) obtained from a L4 PV+ interneuron upon optogenetic stimulation of thalamic fibres in V1 with blue LED light (470 nm; shown with light blue lines). ChR2 is expressed in the whole thalamus by its conditional expression in *Olig3Cre;Ai32* transgenic animals. Traces on the left, middle and right correspond to optogenetic stimulation with increasing LED power. The middle trace is showing the recording obtained at minimal stimulation, i.e., the minimal LED power to obtain any excitatory postsynaptic current (EPSC).
(B) Same current traces as in A but at a faster time scale to show the putative direct EPSC evoked by optogenetic stimulation of thalamic terminals.
(C) Representative current traces obtained by the same cell shown in A and B during optogenetic stimulation of corresponding LED power but in the presence of tetrodotoxin (TTX; 1µM) and 4-aminopyridine (4-AP; 100 µM).

3.7.1 – Development of thalamocortical connectivity onto pyramidal neurons in V1

The canonical cortical circuit of primary sensory areas is based on the notion that L4 excitatory neurons are the main target for thalamocortical connections (Harris and Shepherd, 2015). For this reason, I recorded L4 pyramidal neurons in V1 during optogenetic stimulation of thalamic terminals and used them as benchmark to determine connectivity of other cortical neurons. L4 pyramidal neurons responded to optogenetic minimal stimulation with reliable EPSCs (**Fig. 3.22A-C**), whose latency and jitter (SD of the latency over multiple sweeps) are plotted in **Fig. 3.22D-F**, for cells recorded at the three different developmental window. These plots show that the majority of L4 pyramidal neurons have EPSC jitter and latency clustering together, apart from a few outliers, likely receiving polysynaptic connections. Based on this, I set cut-off values for latency (20 and 18 ms for recordings performed prior to and after eye opening, respectively) and jitter (3.5 and 2.5 ms) which were then used to identify L4 neurons receiving putative monosynaptic connection. This yields a total of 12/15 (80%), 14/19 (74%), and 17/17 (100%) L4 pyramidal neurons classified as connected. For these connected cells, EPSC amplitude significantly increased after eye opening (**Fig. 3.22G**), whereas EPSC latency (**Fig. 3.22H**) and jitter (**Fig. 3.22I**) significantly decreased around the same time. This data suggest eye opening to be an important milestone for the development of thalamocortical connectivity onto L4 pyramidal neurons.

Fig. 3.22 (next page). Development of thalamocortical connectivity onto L4 Pyr in V1. (A) Left, representative current-clamp recording of an electrophysiological intrinsic profile obtained upon current injection (bottom) from a P7 L4 Pyr in V1. Right, voltage-clamp recording (V_h = −60 mV) of an EPSC recorded upon optogenetic minimal stimulation (470 nm; indicated by blue line) of thalamic terminals for the same cell shown on the left. ChR2 is expressed in the whole thalamus by its conditional expression in *Olig3Cre;Ai32* transgenic animals. Light grey traces show individual optogenetic responses, darker grey trace shows their average.
(B) Same as in A, but for a P12 L4 Pyr in V1.
(C) Same as in A but for a P16 L4 Pyr in V1. Vertical dotted line spanning A to C shows onset of EPSC for the cell recorded at P16.
(D) Scatter plot of EPSC latency vs. EPSC jitter (standard deviation of the latency over multiple sweeps) for L4 Pyr recorded at P5-P8. Dashed lines indicate cut-off values (latency = 20 ms; jitter = 3.5 ms) used to define neurons receiving putative direct thalamic input (connected).
(E) Same as in D but for L4 Pyr recorded at P9-P13.
(F) Same as in D but for L4 Pyr recorded at P14-P18 (cut-off values after eye opening are the following: latency = 18 ms; jitter = 2.5 ms).

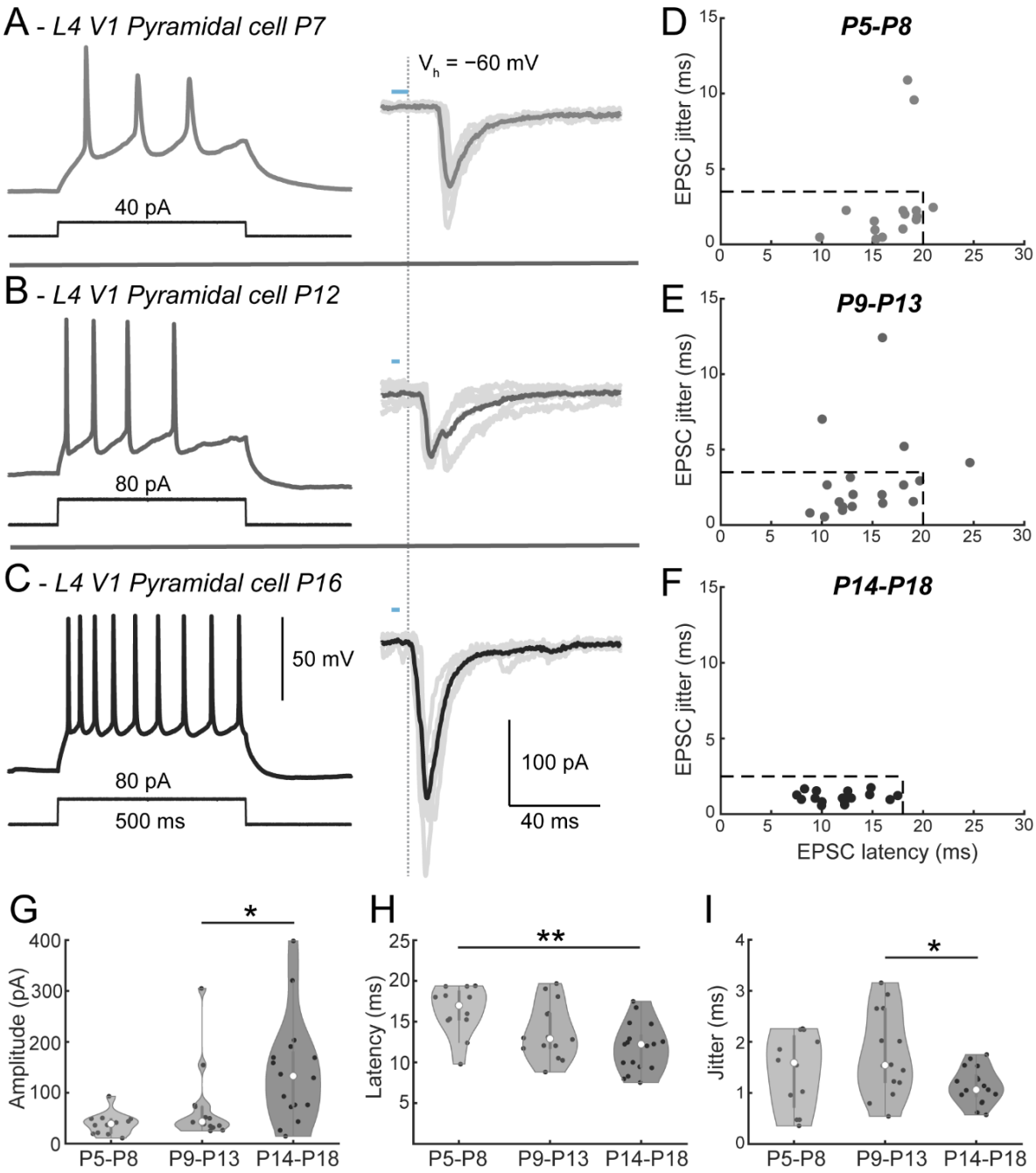
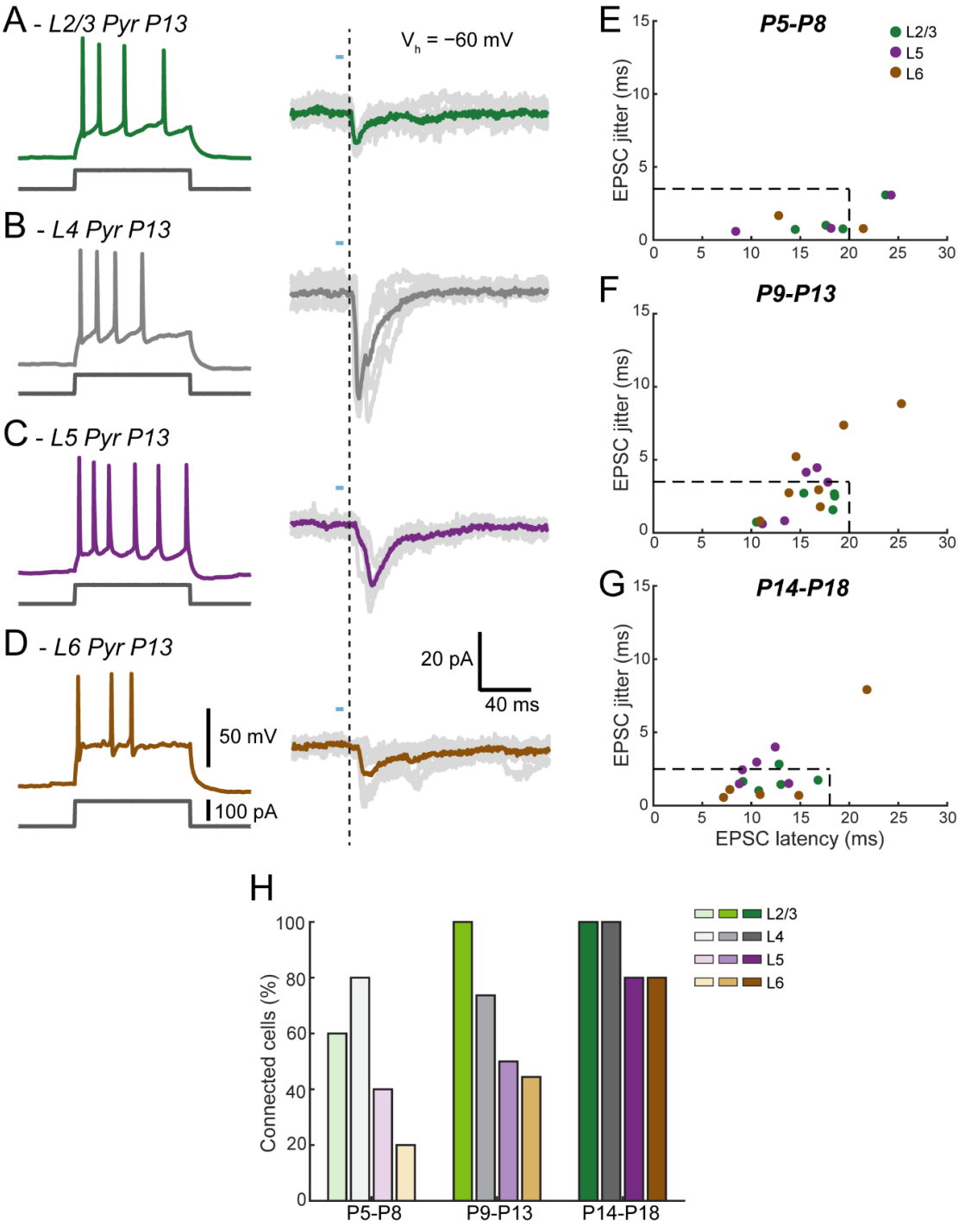


Fig. 3.22 (continue). (G) Violin plot of optogenetically-induced EPSC amplitude recorded from connected L4 Pyr in V1 at different developmental stages (P5-P8, n = 12; P9-P13, n = 14; P14-P18, n = 17). There is a statistically significant effect of the factor "*Development*" (One-way ANOVA: F (2, 41) = 6.5, p = 0.003).
(H) Same as in G but for EPSC latency. There is a statistically significant effect of the factor "*Development*" (One-way ANOVA: F (2, 41) = 7.4, p = 0.002).
(I) Same as in G but for EPSC jitter. There is a statistically significant effect of the factor "*Development*" (One-way ANOVA: F (2, 41) = 3.6, p = 0.03). Asterisks in the plots show statistically significant differences between groups, when tested with post-hoc test corrected for multiple comparisons (Tukey's test), according to the following notation: *p ≤ 0.05.

I next examined thalamocortical connectivity on pyramidal neurons outside L4 (**Fig. 3.23A-D**) and used the EPSC latency and jitter cut-off values to identify pyramidal neurons in L2/3, L5, and L6 which receive putative direct thalamic inputs (**Fig. 3.23E-G**). Based on this approach, pyramidal neurons in supragranular layers show similar ratio of connected cells to L4 neurons before eye opening, while the majority of neurons irrespective of cortical layers are classified as connected after eye opening (**Fig. 3.23H**).



3.7.2 – Development of thalamocortical connectivity onto GABAergic interneurons in V1

Having established the developmental timeline of thalamocortical connectivity onto V1 pyramidal neurons, I next explored how thalamic input engage cortical GABAergic interneurons. To this aim, *Lhx6-eGFP; Olig3Cre; Ai32* animals were generated to target Lhx6-eGFP+ interneurons for whole-cell patch-clamp recordings and allow optogenetic stimulation of thalamic terminals. Lhx6-eGFP interneuron identity (PV+ FS vs. SST+ NFS interneurons) was determined based on their intrinsic electrophysiological properties and/or morphological features (**Fig. 3.6** and **Fig. 3.8**). Given the sparsity of SST+ interneurons captured with this transgenic line, I also generated *Lpar1-eGFP; Olig3Cre; Ai32* animals and targeted Lpar1-eGFP SST+ interneurons in L5 of V1 for whole-cell recordings during optogenetic stimulation of thalamic terminals. Lpar1-expressing SST+ interneurons were previously shown to be transiently engaged by thalamic input in S1BF (Marques-Smith et al., 2016).

Fig. 3.23 (previous page). Development of thalamocortical connectivity onto V1 infragranular and supragranular Pyr. (A-D) Left, representative current-clamp recordings of an electrophysiological intrinsic profile obtained upon current injection (bottom) from a L2/3 (A, green), L4 (B, grey), L5 (C, purple), and L6 (D, brown) Pyr in V1 recorded in the same slice from a P13 *Olig3Cre;Ai32* transgenic mouse. Right, voltage-clamp recordings (V_h = −60 mV) of EPSCs recorded upon optogenetic stimulation (470 nm; indicated by blue line) of thalamic terminals for the same cells shown on the left. Light grey traces show individual optogenetic responses, darker grey or coloured traces show their average. Dashed vertical line shows onset of EPSC recorded from the L4 Pyr cell (in B).
(E) Scatter plot of EPSC latency vs. EPSC jitter (standard deviation of the latency over multiple sweeps) for L2/3 (green), L5 (purple), and L6 (brown) Pyr recorded at P5-P8. Dashed lines indicate cut-off values (latency = 20 ms; jitter = 3.5 ms) used to define neurons receiving putative direct thalamic input (connected).
(F) Same as in D but for cells recorded at P9-P13.
(G) Same as in D but for cells recorded at P14-P18 (cut-off values after eye opening are the following: latency = 18 ms; jitter = 2.5 ms).
(H) Bar plot of percentage of L2/3 (green), L5 (purple), or L6 (brown) Pyr cells at different developmental windows, classified as connected to direct thalamic inputs based on the scatter plots shown in E-G.

In contrast to the recordings obtained from V1 pyramidal neurons, responses of GABAergic interneurons to optogenetic stimulation were more diverse. Before eye opening, a fraction (6/14, 43%) of L4 PV+ interneurons did not display any synaptic response to optogenetic stimulation; of the remaining 8/14, some responded with EPSC characterised by large latency variability (see **Fig. 3.24A**). After eye opening, L4 PV+ interneurons responded to optogenetic minimal stimulation with EPSC with reliably latency (**Fig. 3.24C**). In contrast, all (n = 6 before eye opening and n = 5 after eye opening) Lpar1-eGFP SST+ interneurons in L5 of V1 responded with EPSCs upon minimal optogenetic stimulation, regardless of developmental stage. However, their responses often included multiple summating EPSCs (**Fig. 3.24B, D**) with large latency and/or jitter. By applying the cut-off EPSC latency and jitter values obtained from L4 pyramidal neurons (**Fig. 3.24E, F**), only a small fraction of interneurons, both PV+ and SST+, were classified as monosynaptically connected before eye opening (**Fig. 3.24G**). After eye opening, all PV+ interneurons (6/6) were classified as connected, whereas a fraction of Lpar1-eGFP SST+ interneurons were not (3/5 connected cells). I calculated the relative EPSC latency for PV+ and SST+ interneurons (relative to the EPSC latency of a L4 pyramidal neuron recorded in the same slice as the interneuron) and observed that this value was larger in SST+ than PV+ cells at both developmental stages investigated (**Fig. 3.24H**). In addition, quantification of the EPSC onset to peak time showed statistically higher values in L5 SST+ interneurons than L4 pyramidal or PV+ neurons (**Fig. 3.24I**), confirming EPSC summation in the former. In summary, despite some SST+ interneurons were classified as monosynaptically connected based on EPSC latency and jitter values (**Fig. 3.24E, F**), they display features of polysynaptic activity, such as longer latency (**Fig. 3.24H**) and summating responses (**Fig. 3.24I**), with little evidence for direct monosynaptic inputs. These results also suggest that eye opening is a critical milestone for the maturation of thalamic connection onto PV+ interneurons.

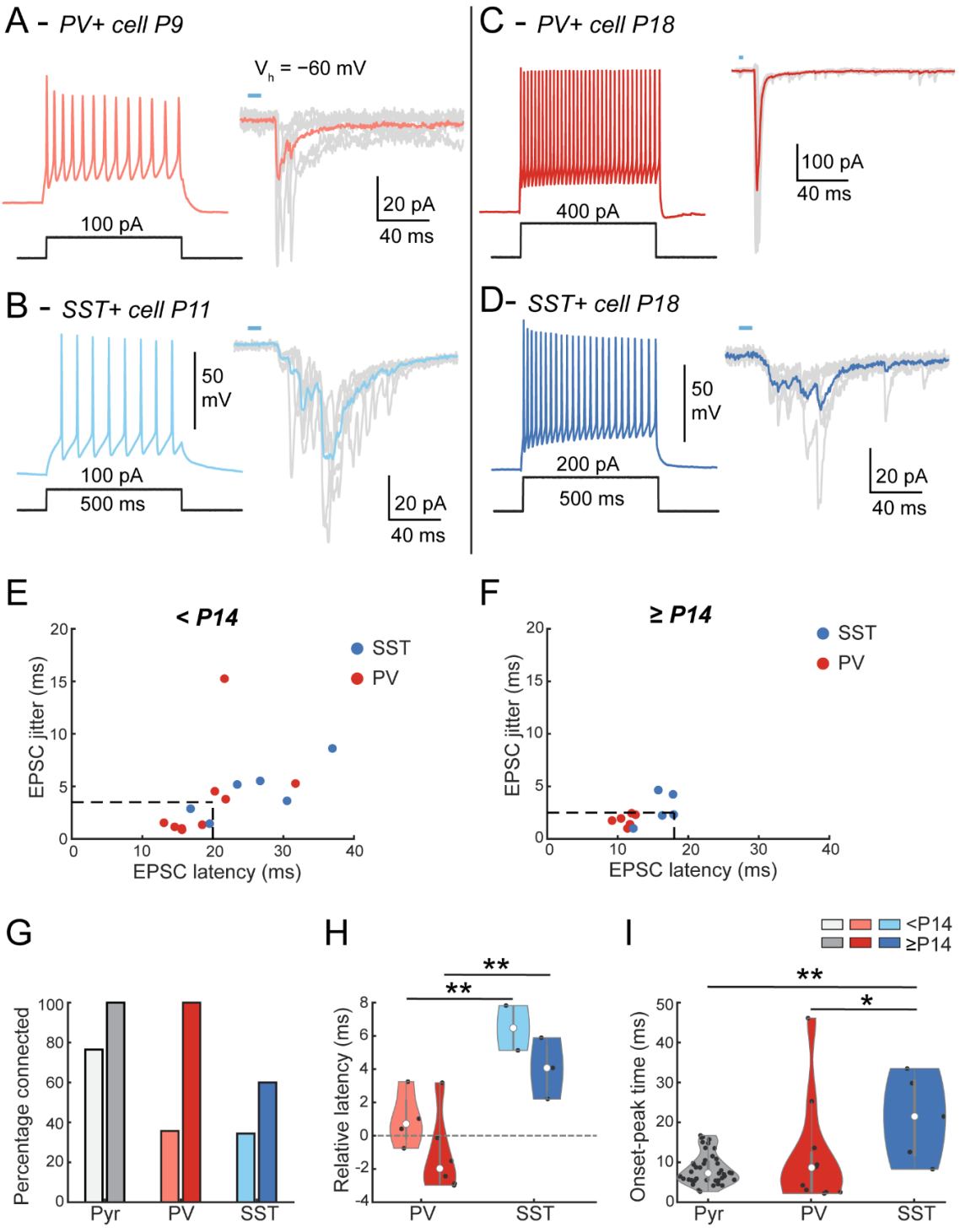


Fig. 3.24. Development of thalamocortical connectivity onto L4 PV+ interneurons and L5 SST interneurons. (A-D) Left, representative current-clamp recordings of an electrophysiological intrinsic profile obtained upon current injection (bottom) from L4 PV+ (A, P9; C, P18) and L5 SST+ (B, P11; D, P18) interneurons in V1 from *Lhx6-eGFP; Olig3Cre; Ai32* or *Lpar1-eGFP; Olig3Cre; Ai32* transgenic mice, respectively. Right, voltage-clamp recordings (V_h = −60 mV) of EPSCs recorded upon optogenetic stimulation (470 nm; indicated by blue line) of thalamic terminals for the same cells shown on the left. Light grey traces show individual optogenetic responses, coloured traces show their average.
(E) Scatter plot of EPSC latency vs. EPSC jitter (standard deviation of the latency over multiple sweeps) for PV+ (red) or SST+ (blue) interneurons recorded prior to eye opening (<P14). Dashed lines indicate cut-off values (latency = 20 ms; jitter = 3.5 ms) used to define neurons receiving putative direct thalamic input (connected).

3.7.3 – Development of fast feed-forward inhibition in V1 L4

The end of the first postnatal week is a critical milestone for the appearance of the fast feed-forward inhibition in L4 of S1BF (Cruikshank et al., 2007; Daw et al., 2007). Our optogenetic experiments suggest this connection might be delayed in V1. To test this hypothesis, I recorded L4 pyramidal neurons in V1 using a Cs-based internal solution (**Fig. 3.25A**) to allow us to record both thalamic ESPCs (V_h = −60 mV; **Fig. 3.25B, C**, black traces) and then switch to the reversal potential for glutamatergic receptors (V_h = 0 mV) to extract feed-forward IPSCs (**Fig. 3.25B, C**, red traces). I compared the latency and amplitude of the recorded EPSCs and IPSCs in the same cell, for a set of L4 pyramidal neurons recorded before and after eye opening (n = 10; P9-P13 and P14-P18, respectively). All recorded IPSCs were delayed relative to the onset of the EPSC (delta, Δ) consistent with feed-forward inhibition (**Fig. 3.25D**). Difference between EPSC and IPSC amplitude was close to zero before eye opening (**Fig. 3.25E**) suggesting balanced excitatory and inhibitory inputs at this stage. After eye opening, however, there is a strong imbalance between larger IPSCs than EPSCs, leading to large negative values of Δ amplitude (**Fig. 3.25E**). Together with previous optogenetic experiments on PV+ interneuron, this result suggests that eye opening is a critical milestone for the appearance of fast feed-forward inhibition onto V1 L4 pyramidal neurons.

Fig. 3.24 (continue from previous page). (F) Same as in D but for cells recorded after eye opening (≥P14).
(G) Bar plot of percentage of L4 Pyr (grey), L4 PV+ interneurons (red), or L5 SST+ interneurons (blue) responsive to optogenetic stimulation of thalamic terminals at different developmental windows (P5-P8 and P9-P13 grouped to obtain a <P14 developmental window compared with ≥ P14).
(H) Violin plot of relative EPSC latency of L4 PV+ interneurons (red; <P14, n = 4; ≥P14, n = 6) and L5 SST+ interneurons (blue; <P14, n = 2; ≥P14, n = 3). For each recorded cell, EPSC latency is subtracted from the latency value obtained from a L4 Pyr cell recorded in the same slice. There are statistically significant effects of the factor "*Cell Type*" (Two-way ANOVA: $F(1, 12) = 24$, $p \leq 0.001$) but not "*Development*" (Two-way ANOVA: $F(1,12) = 4.5$, $p = 0.06$).
(I) Violin plot of EPSC onset to peak time for all connected L4 Pyr (grey; n = 43), L4 PV+ interneurons (red; n = 11), or L5 SST+ interneurons (blue; n = 5), regardless of their developmental stage. There is a statistically significant effect of the factor "*Cell Type*" (One-way ANOVA: $F(2, 58) = 7.3$, $p = 0.002$). Asterisks in the plots show statistically significant differences between groups, when tested with post-hoc test corrected for multiple comparisons (Tukey's test), according to the following notation: * $p \leq 0.05$ and ** $p \leq 0.01$.

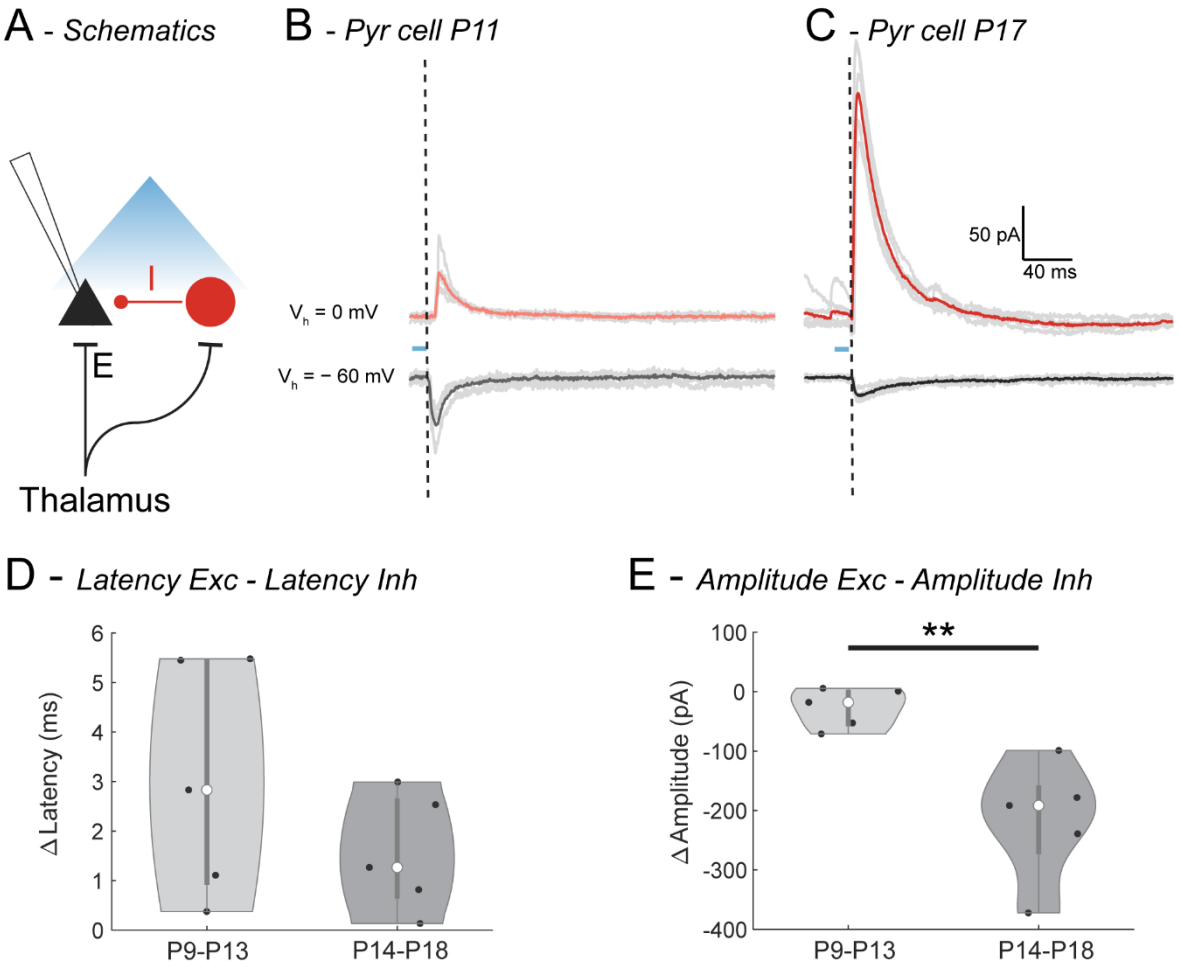


Fig. 3.25. Development of feed-forward inhibition in V1. (A) Schematics of the optogenetic experiments used to study the development of feed-forward inhibition in V1. A L4 Pyr (black triangle) was targeted for patch-clamp whole-cell recordings using a Cs-based internal solution. Direct thalamic excitatory connection (black, E) was probed with optogenetic stimulation of ChR2-expressing thalamic terminals by voltage-clamping the recorded cell near resting membrane potential (V_h = − 60 mV, close to the reversal potential for Cl^-). Indirect inhibitory connection (red, I) was probed voltage-clamping the recorded cell near the reversal potential for glutamatergic channels (V_h = 0 mV).
(B, C) Representative EPSCs (black) and IPSCs (red) recorded from a P11 (B) or P17 (C) L4 Pyr, using the protocols described in A.
(D) Violin plot of delta (Δ) latency, defined as the latency of the EPSC (Exc) minus the latency of the IPSC (Inh) recorded from the same cell, at the two developmental windows (P9-P13, n = 5; P14-P18, n = 5). There is no statistically significant difference between the two groups.
(D) Violin plot of Δ amplitude, defined as the amplitude of the EPSC (Exc) minus the amplitude of the IPSC (Inh) recorded from the same cell, at the two developmental windows P9-P13 and P14-P18. The two groups are statistically different (unpaired t-test: t (8) = −3.9, *p ≤ 0.01).

3.8 – Development of dis-inhibitory interneuron networks in S1BF

In *Section 3.6*, I described the developmental timeline of the dis-inhibitory network between SST+ interneurons and PV+ interneurons in V1 and highlighted a transient increase in the strength of this connection compared to SST+ interneuron inhibition of pyramidal neurons in L4 at P9-P13. Previous experiments in a different primary sensory area, S1BF, showed a critical role for SST+ inhibition of excitatory L4 neurons in a precedent developmental critical period, between P5-P8 (Marques-Smith et al., 2016; Tuncdemir et al., 2016). To further explore possible difference between S1BF and V1, I investigated the timeline for the development of the SST to PV dis-inhibitory network in S1BF.

3.8.1 – Characterisation of S1BF L4 neurons intrinsic electrophysiological properties.

V1 and S1BF are characterised by distinct developmental timeline. For example, while sensory perception in V1 is initiated at eye opening at P14 (Shen and Colonnese, 2016), S1BF is responsive to passive stimulation of the whisker from the first postnatal week (Minlebaev et al., 2011). I therefore recorded intrinsic electrophysiological profiles of L4 neurons in S1BF to understand whether they are characterised by earlier maturation compared to V1 neurons. I recorded from either excitatory neurons or Lhx6+ interneurons in L4 of S1BF; Lhx6+ interneurons were then classified as either PV+ or SST+ interneurons based on their spiking profile (FS vs. NFS; **Fig. 3.26**) or expression of tdTomato in *Lhx6-eGFP; SSTCre; Ai9* animals. At the latest developmental window investigated, L4 excitatory neurons in S1BF comprised a homogeneous class of neurons with classic features of regular-spiking neurons, with wide spike and relatively low firing frequency (see **Fig. 3.26A** and **Table 7**). Similarly, L4 Lhx6+ FS interneurons also comprised a homogeneous population of classic FS cells with low spike half-width and high firing frequency (**Fig. 3.26B** and **Table 8**). Lhx6+ NFS cells, classified as SSTCre+ interneurons, instead showed a

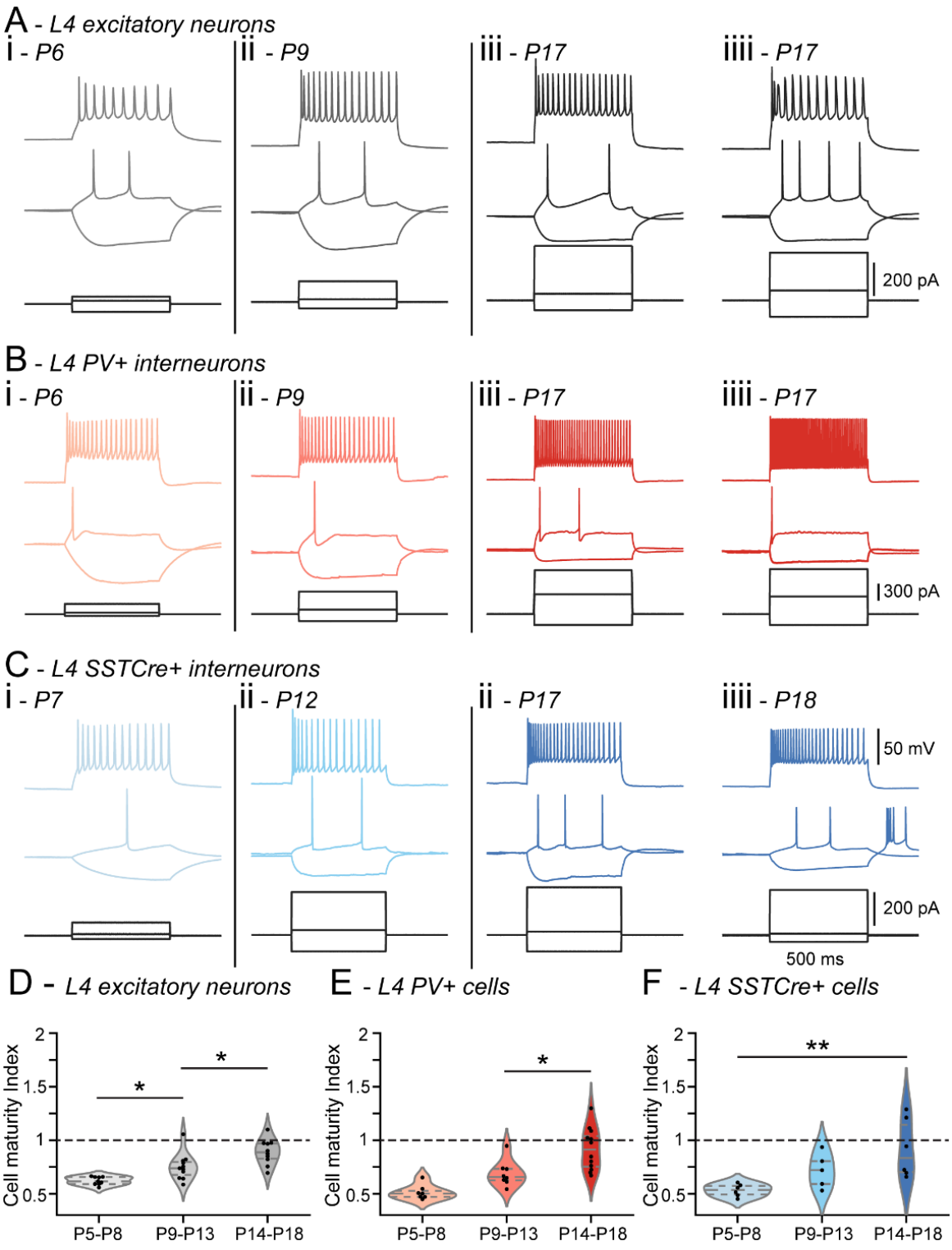


Fig. 3.26. Electrophysiological characterization of L4 excitatory and inhibitory neurons in S1BF. (A) Representative current-clamp recordings of L4 excitatory neurons in S1BF at P6 (i), P9 (ii), and P17 (iii, iiii) during current steps application; recorded traces show electrophysiological profiles for a negative current step, a positive current step close to rheobase (bottom) and a positive current step close to maximum firing rate (top).
(B, C) Current clamp recordings of representative L4 PV+ (B) and L4 SSTCre+ interneurons (C) at different ages as described in A. For the later developmental window, representative traces for L4 SSTCre+ NFS and rIB cells are shown in (iii) and (iiii), respectively.

certain degree of variability with classic NFS cells and rIB cells (**Fig 3.26C**) that were observed in the later developmental window (see also **Table 9**). Quantification of electrophysiological features of these three cell types demonstrated their maturation profile extends well beyond the first postnatal week (see **Table 7-9**). Indeed, cell maturity index of all three neuronal types significantly moves closer to 1.0 in the last developmental window investigated (**Fig. 3.26D-F**). Therefore, despite the apparent earliest maturation of sensory perception in S1BF, maturation of intrinsic electrophysiological properties of L4 neurons continues until the third postnatal week.

Unlike maturation of electrophysiological properties, L4 PV+ interneurons in S1BF display mature morphological features from the earliest ages tested. In the small sample of Lhx6+ PV+ interneurons whose morphology was reconstructed, the majority of those recorded between P5-P8 (**Fig. 3.27A**) and P9-P13 (**Fig. 3.27B**) already show features of classical basket cell, such as high density of axonal arborisation within their cortical layer.

Fig. 3.26 (continue from previous page). (D) Violin plot of cell maturity index values for L4 excitatory neurons at different developmental ages (P5-P8, n = 9; P9-P13, n = 11; P14-P18, n = 10); there is a statistically significant effect of "*Development*" (Kruskal-Wallis test: $X^2(2) = 17.3$, $p \leq 0.001$).
(E) Violin plot of cell maturity index values for L4 PV+ interneurons at different developmental ages (P5-P8, n = 7; P9-P13, n = 8; P14-P18, n = 12); there is a statistically significant effect of "*Development*" (Kruskal-Wallis test: $X^2(2) = 17.9$, $p \leq 0.001$).
(F) Violin plot of cell maturity index values for L4 SSTCre+ interneurons at different developmental ages (P5-P8, n = 6; P9-P13, n = 5; P14-P18, n = 6); there is a statistically significant effect of "*Development*" (Kruskal-Wallis test: $X^2(2) = 9.7$, $p \leq 0.01$). Asterisks in the plot show statistically significant differences between groups, when tested with post-hoc analysis corrected for multiple comparisons (Dunn's test with Benjamini-Hochberg correction), according to the following notation: * $p \leq 0.05$, ** $p \leq 0.01$.

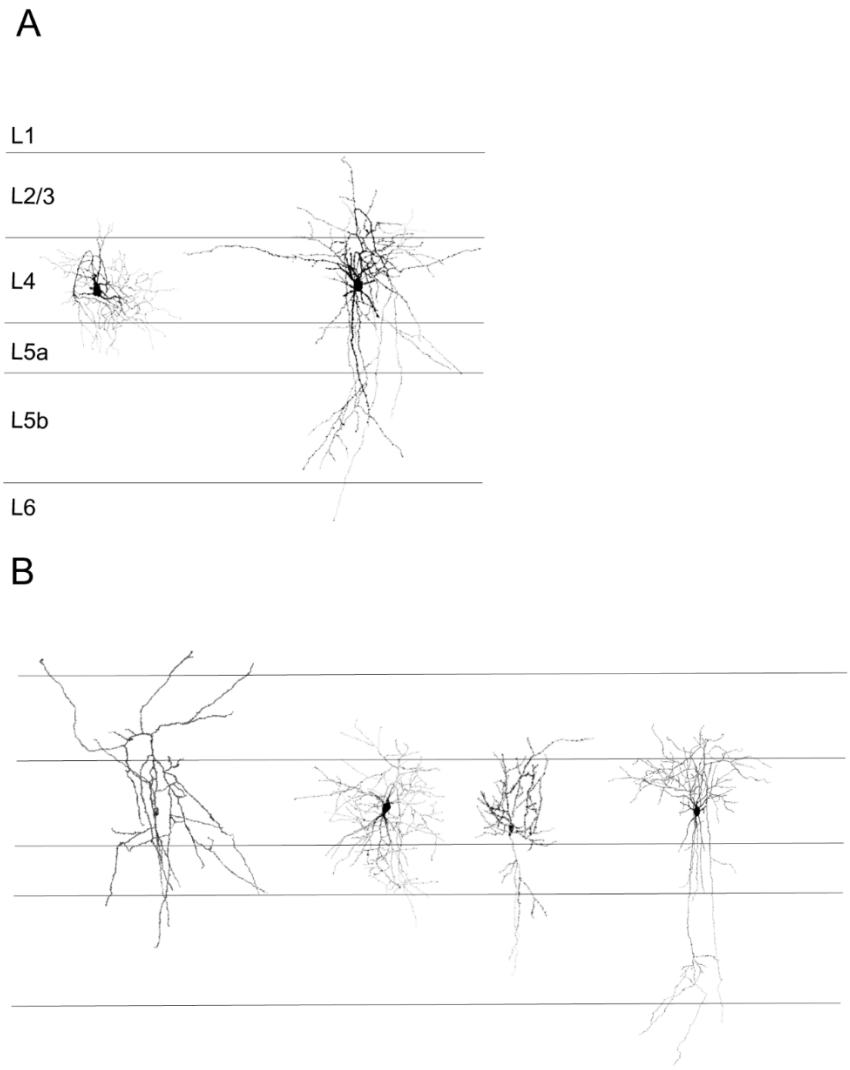


Fig. 3.27: Cell morphology of L4 PV+ interneurons in S1BF. (A) Representative morphological reconstructions of the axonal arbours of L4 PV+ interneurons in S1BF at P5-P8.
(B) Same as in A but for cells recorded at P9-P13.

3.8.2 – Development of SST+ interneuron connectivity onto L4 FS interneurons in S1BF

I next moved on to study the development of SST+ interneuron connectivity onto L4 PV+ interneurons and started from a description of total columnar GABAergic network connectivity onto L4 PV+ interneurons (n = 31; **Fig. 3.28**). Average connectivity heatmaps (**Fig. 3.28A**) show that the main source of GABAergic inputs onto L4 PV+ interneurons in S1BF is other interneurons within L4 itself. However, unlike V1, I also observed GABAergic inputs from infragranular layers, notably L5b, that peaks at P9-P13 (**Fig. 3.28B**). Columnar profiles in the developmental heatmaps (**Fig. 3.28C**) shows that the majority of neurons

recorded between P9-P13 are characterised by a secondary source of GABAergic inputs from L5b, while a few cells in the earlier and later developmental windows also receive L5b inputs.

To identify the contribution from SST+ interneurons, I first used optogenetics to compare the development of SST+ interneuron inputs onto L4 PV+ interneurons and excitatory neurons in S1BF (**Fig. 3.29A**). Most of the cells recorded (n = 39 PV+ interneurons and n = 28 excitatory neurons) responded to optogenetic stimulation with an IPSC, with the remaining classified as non-responsive (**Fig. 3.29B**). Quantification of IPSCs between cell types and over development showed a developmental increase in IPSC amplitude with no difference between PV+ interneurons and excitatory neurons (**Fig. 3.29C**). Similarly, IPSC latency (**Fig. 3.29D**), jitter (**Fig. 3.29E**), and tau (**Fig. 3.29F**) also decreased over development, with a statistically significant difference between cell types only found for IPSC tau.

Lastly, I performed LSPS experiments with ATP uncaging in *Lhx6-eGFP; SSTCre; P2X2R* animals to map the presynaptic location of SST+ interneurons providing inputs onto L4 PV+ interneurons in S1BF (n = 22; **Fig. 3.30**). Similar to total columnar GABAergic connectivity maps (**Fig. 3.28**), the main source of SST+ inputs onto L4 FS interneurons is from within L4 itself, with a secondary source from L5a/L5b that appears only at P9-P13 and is maintained in the later developmental window (**Fig. 3.30A** and **Fig. 3.30B**). This data is mainly evident in the layer input box plot (**Fig. 3.30D**), showing that the strength of GABAergic inputs from L5 increases at P9-P13 compared to P5-P8.

Overall, these experiments demonstrate that, in S1BF, SST+ interneurons engage with PV+ interneurons from the earliest developmental window investigated but between P9 and P13 there is a reconfiguration of the network whereby L5 SST+ interneurons project to L4 PV+ cells.

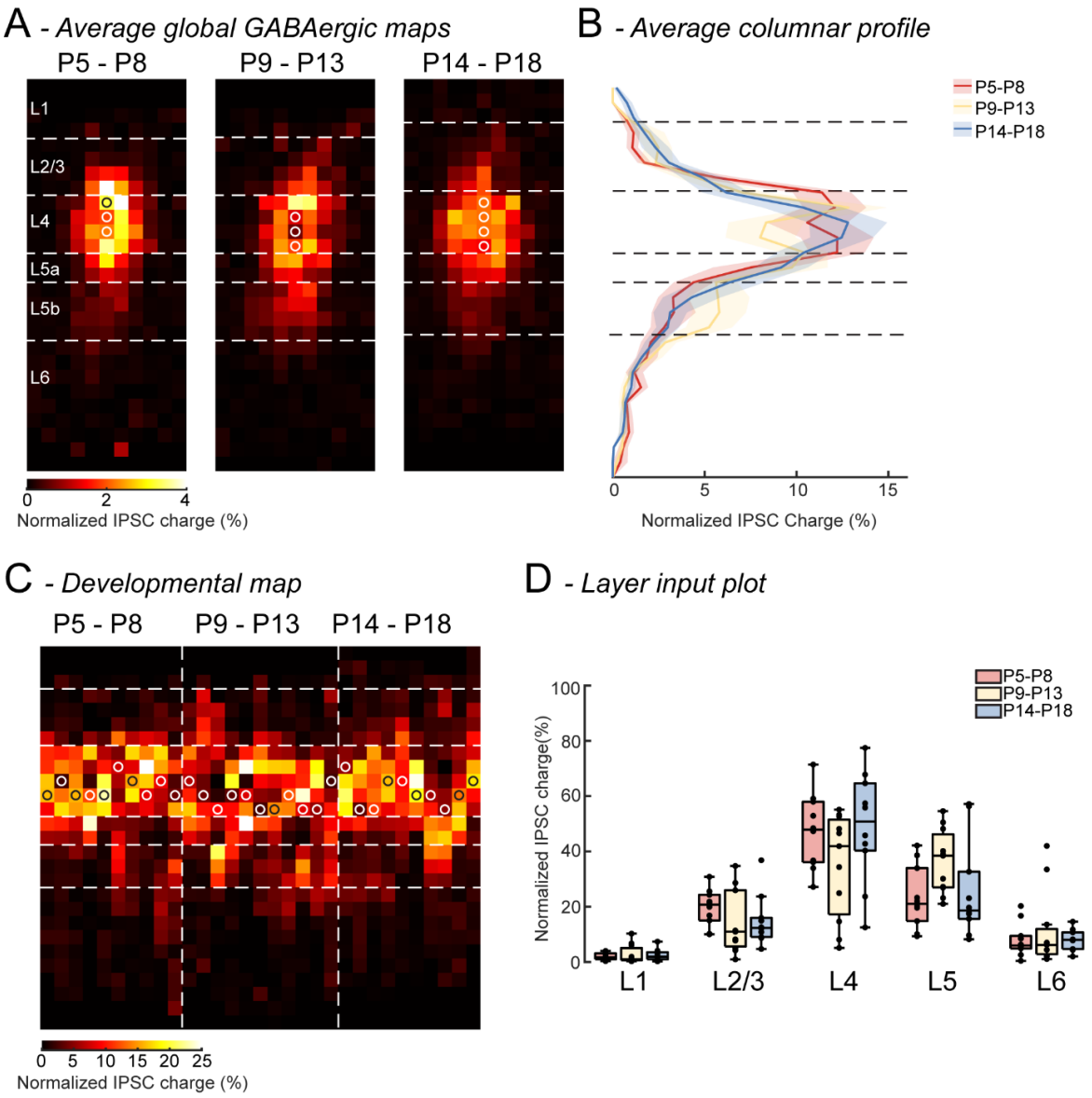


Fig. 3.28. Development of GABAergic connectivity onto L4 Lhx6+ PV+ interneurons in S1BF.
(A) Average normalised maps of global GABAergic connectivity onto L4 Lhx6+ PV+ interneurons in S1BF obtained through LSPS of caged glutamate in *Lhx6-eGFP;SSTCre;Ai32* transgenic animals. Individual connectivity maps are grouped by developmental window (P5-P8, n = 10; P9-P13, n = 11; P14-P18, n = 10). White or black circles indicate approximate location of the recorded cell in the map; horizontal dashed lines indicate layer boundaries.
(B) Columnar global GABAergic connectivity profile onto L4 Lhx6+ PV+ interneurons in S1BF, colour-coded for developmental window (P5-P8, red; P9-P13, yellow; P14-P18, blue). Solid line indicates average normalised connectivity; shaded area shows the SEM.
(C) Developmental maps of global GABAergic connectivity onto L4 Lhx6+ PV+ interneurons in S1BF, as described in Fig. 3.12.
(D) Box plot of normalised global GABAergic connectivity inputs from each layer (Input layer) onto L4 Lhx6+ PV+ interneurons in S1BF, grouped and colour-coded for developmental window (as in B).

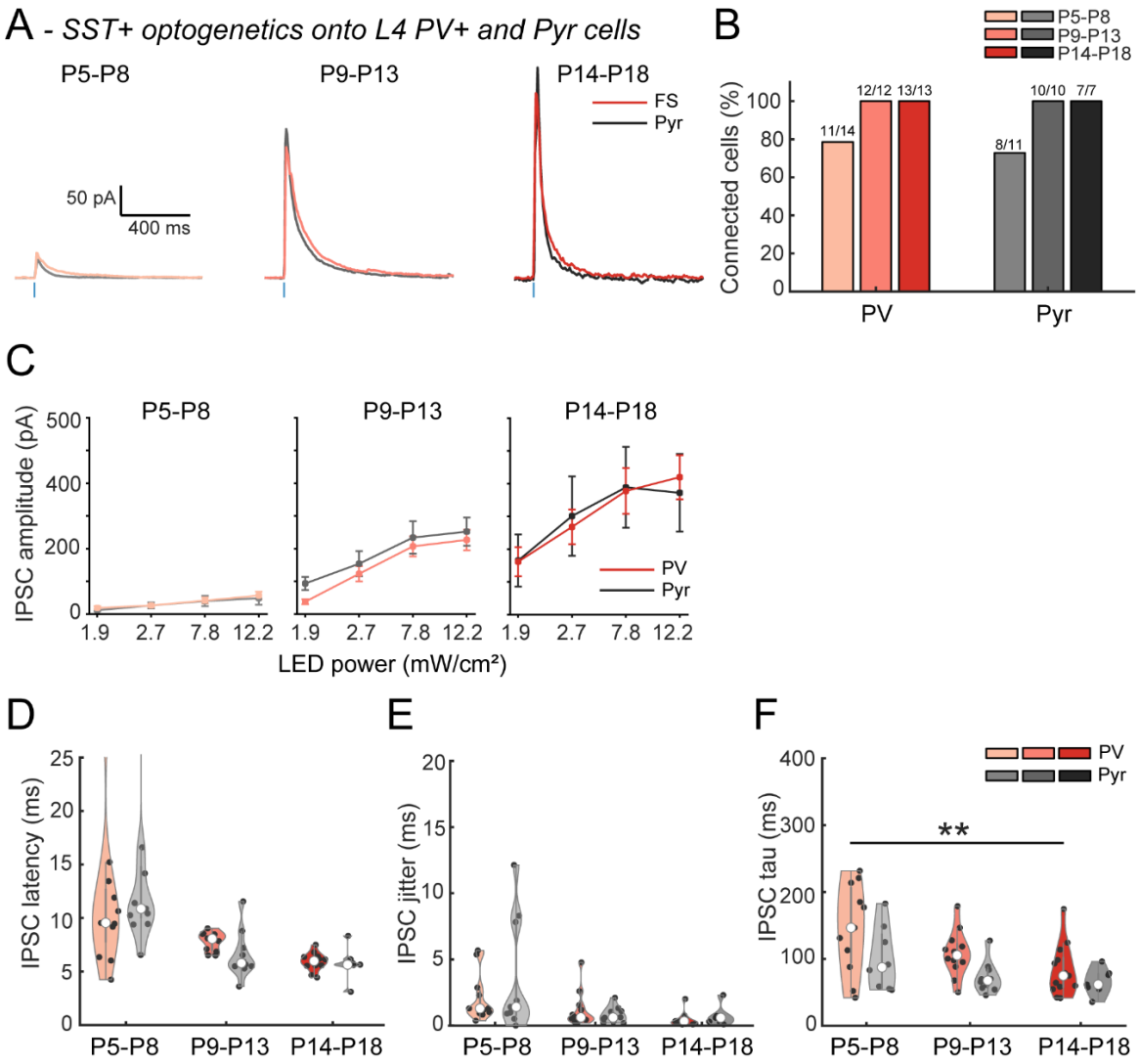


Fig. 3.29. Development of SST+ interneuron connectivity onto Lhx6+ PV+ interneurons in S1BF. (A) Representative voltage-clamp recordings (V_h = 0 mV) of L4 Lhx6+ PV+ interneurons (red) and L4 excitatory neuron (black) in S1BF upon optogenetic stimulation (470 nm; indicated by blue line) of SSTCre+ interneurons in *Lhx6-eGFP;SSTCre;Ai32* transgenic animals, at different developmental stages (P5-P8, left; P9-P13, middle; P14-P18, right).
(B) Bar plot of percentage of Lhx6+ PV+ interneurons (red) or Pyr cells (black) responsive to optogenetic stimulation of SSTCre+ interneurons at different developmental windows in S1BF.
(C) Plot of optogenetically-induced IPSC amplitude onto Lhx6+ PV+ interneurons (red) and Pyr (black) at 4 distinct LED power levels and at different developmental windows (as in A). Three-way ANOVA shows a statistically significant effect of the factors "*LED Power*" ($F_{(3,209)} = 6.3$, $p \leq 0.001$) and "*Development*" ($F_{(2,209)} = 53.8$, $p \leq 0.001$) but not "*Cell Type*".
(D) Violin plot of optogenetically-induced IPSC latency for L4 Lhx6+ PV+ interneurons (red) and L4 Pyr (black) in S1BF, at different developmental ages. Two-way ANOVA shows a statistically significant effect of the factor "*Development*" ($F_{(2,57)} = 12.6$, $p \leq 0.001$), but not "*Cell Type*".
(E) Violin plot of optogenetically-induced IPSC jitter (standard deviation of IPSC latency) for L4 Lhx6+ PV+ interneurons (red) and L4 Pyr (black) in S1BF, at different developmental ages. Two-way ANOVA shows a statistically significant effect of the factor "*Development*" ($F_{(2,57)} = 4.6$, $p \leq 0.05$), but not "*Cell Type"*.
(F) Violin plot of optogenetically-induced IPSC decay time constant (tau) for L4 Lhx6+ PV+ interneurons (red) and L4 Pyr (black) in S1BF, at different developmental ages. Two-way ANOVA show statistically significant effect of the factors "*Development*" ($F_{(1,55)} = 7.5$, $p \leq 0.01$) and "*Cell Type*" ($F_{(2,55)} = 8.1$, $p \leq 0.01$). Asterisks in the plot show statistically significant differences between groups, when tested with post-hoc test corrected for multiple comparisons (Tukey's test), according to the following notation: ** $p \leq 0.01$.

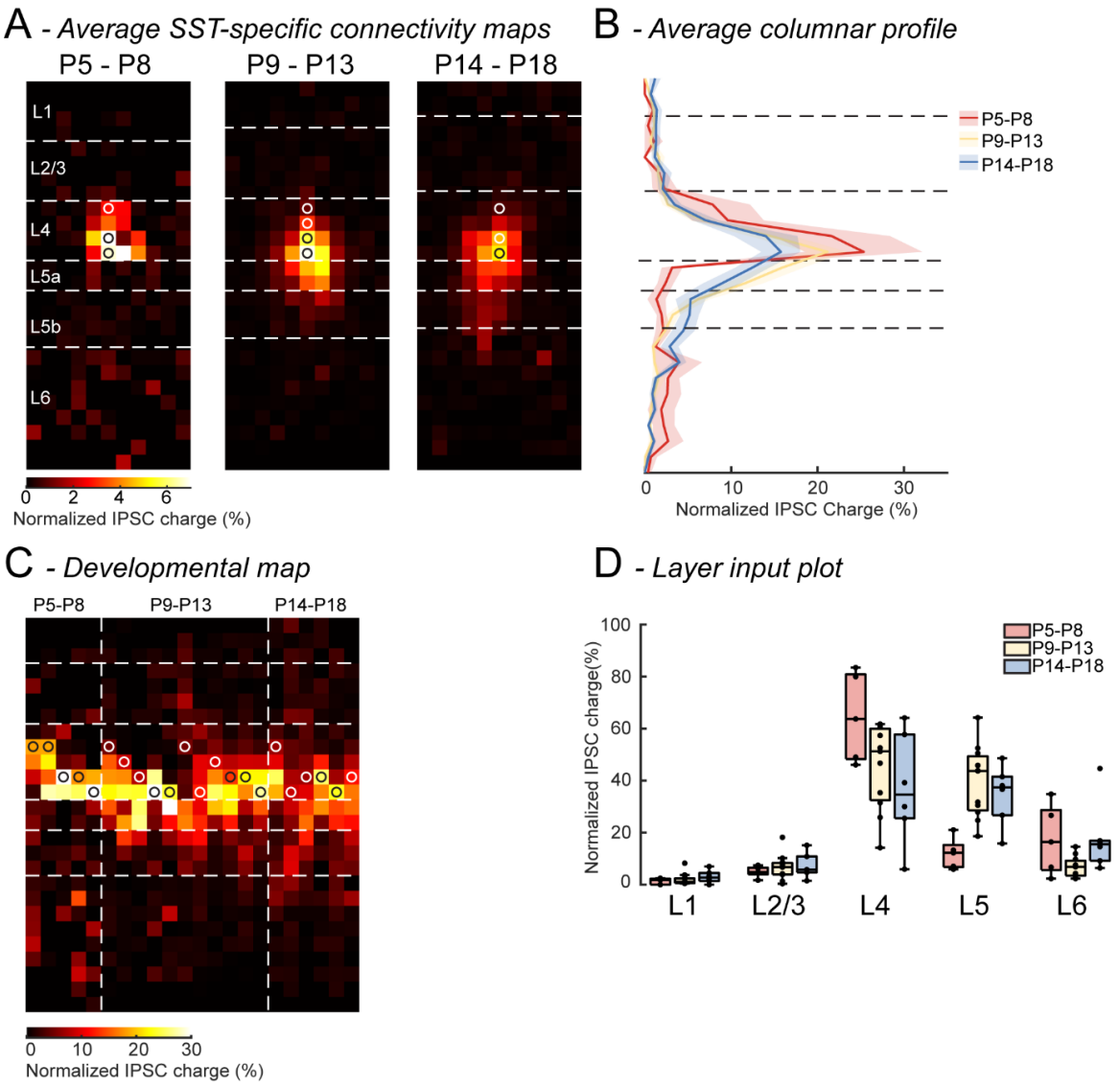


Fig. 3.30. Mapping SST+ interneurons connectivity onto L4 Lhx6+ PV+ interneurons in S1BF.
(A) Average normalised maps of SSTCre+ connectivity onto L4 Lhx6+ PV+ interneurons in S1BF obtained through LSPS of caged ATP in *Lhx6-eGFP;SSTCre;P2X2R* transgenic animals. Individual connectivity maps are grouped by developmental window (P5-P8, n = 5; P9-P13, n = 11; P14-P18, n = 6). White or black circles indicate approximate location of the recorded cell in the map; horizontal dashed lines indicate layer boundaries.
(B) Columnar SSTCre+ connectivity profile onto L4 Lhx6+ PV+ interneurons in S1BF, colour-coded for developmental window (P5-P8, red; P9-P13, yellow; P14-P18, blue). Solid line indicates average normalised connectivity; shaded area shows the SEM.
(C) Developmental maps of SSTCre+ connectivity onto L4 Lhx6+ PV+ interneurons in S1BF, as described in Fig. 3.12.
(D) Box plot of normalised SSTCre+ connectivity inputs from each layer (Input layer) onto L4 Lhx6+ PV+ interneurons in V1, grouped and colour-coded for developmental window (as in B).

3.9 – Summary of results

In ***Chapter 3***, I described the GABAergic circuits of V1 over the course of the first three postnatal weeks. Comparison with prior data and current experiments performed in S1BF revealed a number of differences in the fundamental logic of the GABAergic networks between these two primary sensory areas, rooted in the connectivity patterns of SST+ interneurons with other neurons. The main results obtained in ***Chapter 3*** are the following:

- Pyramidal neurons in V1 undergo rapid development of their intrinsic electrophysiological properties that follows an inside-out developmental pattern.
- Lhx6+ PV+ interneurons also undergo maturation of their electrophysiological properties after eye opening, whereas maturation of SST+ interneuron properties is largely completed before that milestone.
- Pyramidal neurons in L4 of V1 are engaged by local L4 interneurons throughout development. SST+ interneurons that engage with L4 pyramidal neurons are localised at the boundary between L4 and L5; these interneurons are reciprocally connected with L4 pyramidal neurons in V1. In contrast with S1BF, SST+ interneurons in deep L5 of V1 are not engaged by L4 excitatory neurons. These results establish a critical difference between V1 and S1BF, namely the lack of the L5b-L4 loop which is thought to be critical for the development of the latter brain area (Marques-Smith et al., 2016).
- Pyramidal neurons outside L4 are also dominated by local GABAergic connectivity, except for L5 and L6 pyramidal neurons which are involved in a transient network with interneurons in supragranular layers early in development (see ***Chapter 5***). This pattern is mirrored by translaminar excitatory connections from supragranular pyramidal neurons onto L5/6 SST+ interneurons, suggesting developmental networks in V1 link supragranular and infragranular layers.
- Similar to L4 pyramidal neurons, L4 PV+ interneurons in V1 are dominated by local GABAergic connectivity from interneurons located in L4; these interneurons again include SST+ cells that are localised at the boundary between L4 and L5. Optogenetics

experiments showed that L4 PV+ interneurons receive stronger connections from SST+ interneurons than L4 pyramidal neurons in a developmental window that immediately precede eye opening.

- Investigation of the SST+ interneuron connection onto L4 PV+ interneurons in S1BF highlighted a further difference with V1. Indeed, while the strength of the connection from SST+ interneurons onto L4 PV+ interneurons and L4 excitatory neurons does not differ, L4 PV+ cells are involved in a transient network with L5 SST+ interneurons just before eye opening (which roughly correspond to the onset of active whisking).
- Finally, optogenetic investigation of the development of thalamic input onto pyramidal neurons in V1 showed that L4 pyramidal cells are engaged by the thalamus from the end of the first postnatal week and this connectivity matures up until eye opening. Thalamic inputs are instead less prominent in PV+ interneurons prior to eye opening, but rapidly develop after this milestone. Eye opening is also a critical for the appearance of fast feed-forward inhibitory motifs between L4 PV+ interneurons and L4 pyramidal neurons.
- In stark contrast with S1BF, direct thalamic input might be absent onto L5 SST+ interneurons in V1, which are only engaged by local excitatory neurons, in turn activated by the thalamus.

3.10 – Tables

	P5-P8	P9-P13	P14-P18
Rin (MΩ)	1685±520	711±268	346±140
RMP (mV)	−59.7±7.1	−61.1±8.5	−74.9±6.2
Tau (ms)	115±26	111±29	91±35
Rheobase (pA)	8.6±6.0	13.8±2.7	22.9±8.1
MaxFiring (Hz)	10.3±4.3	13.2±6.3	20.3±3.9
AI	1.3±0.7	1.3±0.1	1.8±0.5
VoltSag (mV)	0.5±0.3	1.2±0.9	1.3±0.8
AP_Th (mV)	−31.1±3.7	−36.4±6.5	−39.1±4.8
AP_Hw (ms)	4.6±1.1	2.5±0.7	2.2±0.3
AP_Height (mV)	47.8±11.6	66.9±15.8	75.6±5.3
AP_AHP (mV)	15.0±2.4	17.0±3.0	15.1±6.3

Table 1. Electrophysiological intrinsic properties of V1 L2/3 pyramidal neurons. The table shows mean ± standard deviation of the following intrinsic properties: cell input resistance (Rin), resting membrane potential (RMP), membrane time constant (Tau), rheobase, maximum firing frequency (MaxFiring), adaptation index (AI), hyperpolarisation-induced voltage sag (VoltSag), action potential (AP) threshold (AP_Th), AP half-width (AP_Hw), AP height (AP_Height), and AP after-hyperpolarising potential (AP_AHP). There is a statistically significant effect of the factor "*Development*" (P5-P8, n = 6; P9-P13, n = 5; P14-P18, n = 6) for the following features (shown as shaded groups in the table): Rin (Kruskal-Wallis test: X^2 (2) = 13.4, p = 0.001), RMP (One-way ANOVA: F (2,14) = 7.8, p = 0.005), Rheobase (Kruskal-Wallis test: X^2 (2) = 8.6, p = 0.012), MaxFiring (One-way ANOVA: F (2,14) = 6.8, p = 0.008), AP_Th (One-way ANOVA: F (2,14) = 3.9, p = 0.04), AP_Hw (Kruskal-Wallis test: X^2 (2) = 10.3, p = 0.006), and AP_Height (One-way ANOVA: F (2,14) = 9.4, p = 0.003).

	P5-P8	P9-P13	P14-P18
Rin (MΩ)	1213±400	722±250	430±140
RMP (mV)	−59.5±6.4	−63.3±6.0	−72.3±7.1
Tau (ms)	113±31	117±28	114±39
Rheobase (pA)	20.6±11.8	16.0±7.0	17.8±11.4
MaxFiring (Hz)	9.0±6.9	17.2±8.7	26.9±9.7
AI	1.4±0.4	1.4±0.3	1.4±0.2
VoltSag (mV)	0.8±0.7	1.1±1.7	1.1±0.9
AP_Th (mV)	−31.4±4.2	−35.6±4.6	−37.8±5.0
AP_Hw (ms)	4.2±1.0	2.7±0.5	2.3±0.6
AP_Height (mV)	49.8±7.2	65.7±9.1	69.4±10.7
AP_AHP (mV)	16.3±3.4	16.8±3.5	17.3±3.4

Table 2. Electrophysiological intrinsic properties of V1 L4 pyramidal neurons. The table shows mean ± standard deviation of the cell intrinsic properties (abbreviation in **Table 1** legend). Details of the statistics can be found in **Fig. 3.2**. Values are reported here for ease of comparison with other cell types.

	P5-P8	P9-P13	P14-P18
Rin (MΩ)	850±367	288±85	220±88
RMP (mV)	−62.8±1.9	−61.4±3.7	−61.1±4.7
Tau (ms)	108±17	112±51	87±64
Rheobase (pA)	15.9±8.5	23.7±23.8	21.8±9.8
MaxFiring (Hz)	12.7±7.2	22.0±5.8	27.7±4.3
AI	1.2±0.3	1.6±0.5	2.4±2.4
VoltSag (mV)	3.5±2.5	5.2±2.0	8.2±3.1
AP_Th (mV)	−33.2±3.1	−39.9±4.5	−40.3±5.4
AP_Hw (ms)	5.1±1.0	2.7±0.5	1.8±0.3
AP_Height (mV)	60.7±11.2	76.9±6.4	86.8±3.5
AP_AHP (mV)	21.2±6.5	19.9±5.2	13.4±6.3

Table 3. Electrophysiological intrinsic properties of V1 L5 pyramidal neurons. The table shows mean ± standard deviation of the cell intrinsic properties (abbreviation in **Table 1** legend). There is a statistically significant effect of the factor "*Development*" (P5-P8, n = 6; P9-P13, n = 7; P14-P18, n = 6) for the following features (shown as shaded groups in the table): Rin (Kruskal-Wallis test: X^2 (2) = 12.5, p = 0.002), MaxFiring (One-way ANOVA: F (2,16) = 9.4, p = 0.002), VoltSag (One-way ANOVA: F (2,16) = 5.7, p = 0.014), AP_Th (One-way ANOVA: F (2,16) = 4.4, p = 0.03), AP_Hw (Kruskal-Wallis test: X^2 (2) = 13.9, p ≤ 0.001), and AP_Height (Kruskal-Wallis test: X^2 (2) = 12.0, p = 0.002).

	P5-P8	P9-P13	P14-P18
Rin (MΩ)	1260±406	460±166	320±121
RMP (mV)	−59.1±2.7	−63.4±5.4	−71.7±4.3
Tau (ms)	97±38	71±26	78±37
Rheobase (pA)	21.0±13.4	39.3±39.8	49.6±68.8
MaxFiring (Hz)	24±4.2	20.9±10.6	29.7±12.1
AI	1.0±0.4	1.4±0.4	3.0±2.7
VoltSag (mV)	4.2±2.9	3.7±2.9	3.2±4.7
AP_Th (mV)	−32.3±2.4	−34.8±6.7	−37.5±2.4
AP_Hw (ms)	2.6±0.9	2.1±0.8	2.1±0.6
AP_Height (mV)	58.9±4.8	64.6±10.1	57.8±10.0
AP_AHP (mV)	15.9±4.8	16.5±4.3	10.2±8.6

Table 4. Electrophysiological intrinsic properties of V1 L6 pyramidal neurons. The table shows mean ± standard deviation of the cell intrinsic properties (abbreviation in **Table 1** legend). There is a statistically significant effect of the factor "*Development*" (P5-P8, n = 5; P9-P13, n = 9; P14-P18, n = 6) for the following features (shown as shaded groups in the table): Rin (Kruskal-Wallis test: X^2 (2) = 12.5, p = 0.002), RMP (Kruskal-Wallis test: X^2 (2) = 10.5, p = 0.005), and AI (Kruskal-Wallis test: X^2 (2) = 8.6, p = 0.013).

	P5-P8	P9-P13	P14-P18
Rin (MΩ)	1387±697	616±490	195±125
RMP (mV)	−62.3±5.7	−62.7±5.5	−65.8±5.3
Tau (ms)	112±38	108±44	78±77
Rheobase (pA)	18.9±15.7	35.6±23.8	122.7±70.2
MaxFiring (Hz)	37.0±7.8	43.4±12.1	74.4±18.2
AI	1.1±0.1	1.2±0.1	1.2±0.3
VoltSag (mV)	0.6±0.4	2.7±2.3	2.3±0.9
AP_Th (mV)	−35.3±5.0	−35.6±2.9	−37.2±6.1
AP_Hw (ms)	2.4±0.4	1.9±0.3	0.9±0.2
AP_Height (mV)	51.4±4.9	54.8±4.3	61.9±7.7
AP_AHP (mV)	20.9±5.0	22.2±3.1	22.6±3.5

Table 5. Electrophysiological intrinsic properties of V1 L4 FS interneurons. The table shows mean ± standard deviation of the cell intrinsic properties (abbreviation in **Table 1** legend). There is a statistically significant effect of the factor "*Development*" (P5-P8, n = 10; P9-P13, n = 14; P14-P18, n = 11) for the following features (shown as shaded groups in the table): Rin (Kruskal-Wallis test: X^2 (2) = 21.7, p ≤ 0.001), Rheobase (Kruskal-Wallis test: X^2 (2) = 16.2, p ≤ 0.001), MaxFiring (One-way ANOVA: F (2,32) = 24.3, p ≤ 0.001), VoltSag (Kruskal-Wallis test: X^2 (2) = 13.1, p = 0.001), AP_Hw (One-way ANOVA: F (2,32) = 74.6, p ≤ 0.001), and AP_Height (One-way ANOVA: F (2,32) = 9.2, p ≤ 0.001).

	P5-P8	P9-P13	P14-P18
Rin (MΩ)	1003±412	375±207	290±90
RMP (mV)	−64.8±4.9	−64.6±5.0	−65.1±4.1
Tau (ms)	110±27	108±44	117±58
Rheobase (pA)	9.8±8.8	29.4±21.5	24.9±15.1
MaxFiring (Hz)	33.0±10.4	42.3±11.3	46.0±12.4
AI	1.1±0.1	1.2±0.3	1.2±0.2
VoltSag (mV)	3.2±4.8	3.1±3.1	2.6±2.1
AP_Th (mV)	−40.2±4.0	−41.7±5.0	−42.9±2.8
AP_Hw (ms)	2.9±1.0	1.9±0.5	1.4±0.3
AP_Height (mV)	60.9±9.3	66.1±11.1	69.8±10.4
AP_AHP (mV)	17.8±5.6	14.7±3.8	12.5±3.5

Table 6. Electrophysiological intrinsic properties of V1 SST+ interneurons. The table shows mean ± standard deviation of the cell intrinsic properties (abbreviation in **Table 1** legend). There is a statistically significant effect of the factor "*Development*" (P5-P8, n = 20; P9-P13, n = 14; P14-P18, n = 23) for the following features (shown as shaded groups in the table): Rin (Kruskal-Wallis test: X^2 (2) = 32.6, p ≤ 0.001), Rheobase (Kruskal-Wallis test: X^2 (2) = 21.6, p ≤ 0.001), MaxFiring (One-way ANOVA: F (2,54) = 7.1, p = 0.002), AP_Hw (Kruskal-Wallis test: X^2 (2) = 35.8, p ≤ 0.001), AP_Height (One-way ANOVA: F (2,54) = 4.0, p = 0.02), and AP_AHP (One-way ANOVA: F (2,54) = 7.8, p = 0.001).

	P5-P8	P9-P13	P14-P18
Rin (MΩ)	920±243	609±229	309±89
RMP (mV)	-61.1±7.1	-65.8±3.2	-73.1±7.0
Tau (ms)	79±17	76±21	81±36
Rheobase (pA)	14.7±7.9	14.8±6.0	35.0±17.7
MaxFiring (Hz)	18.7±6.3	27.8±15.2	24.0±7.1
AI	1.5±0.3	1.6±0.4	3.5±3.8
VoltSag (mV)	5.5±2.2	4.9±2.4	3.1±2.3
AP_Th (mV)	-31.3±1.7	-33.4±3.0	-34.4±4.4
AP_Hw (ms)	3.0±0.3	2.3±0.6	2.2±0.5
AP_Height (mV)	58.8±8.3	61.5±9.5	62.4±7.6
AP_AHP (mV)	15.4±2.9	19.0±3.2	20.4±3.7

Table 7. Electrophysiological intrinsic properties of S1BF L4 excitatory neurons. The table shows mean ± standard deviation of the cell intrinsic properties (abbreviation in **Table 1** legend). There is a statistically significant effect of the factor "*Development*" (P5-P8, n = 9; P9-P13, n = 11; P14-P18, n = 10) for the following features (shown as shaded groups in the table): Rin (One-way ANOVA: $F(2,27) = 23.2$, $p \leq 0.001$), RMP (One-way ANOVA: $F(2,27) = 10.1$, $p \leq 0.001$), Rheobase (Kruskal-Wallis test: $X^2(2) = 11.5$, $p = 0.003$), AP_Hw (One-way ANOVA: $F(2,27) = 7.2$, $p = 0.003$), and AP_AHP (One-way ANOVA: $F(2,27) = 5.8$, $p = 0.008$).

	P5-P8	P9-P13	P14-P18
Rin (MΩ)	872±470	168±67	123±63
RMP (mV)	-66.7±6.1	-65.0±4.7	-64.2±6.0
Tau (ms)	99±31	76±18	58±73
Rheobase (pA)	41.8±44.3	110.3±70.6	179.3±105.0
MaxFiring (Hz)	38.0±8.6	54.2±22.1	99.5±41.6
AI	1.2±0.1	1.2±0.1	1.3±0.3
VoltSag (mV)	3.4±3.8	6.1±3.8	2.2±1.4
AP_Th (mV)	-34.8±4.4	-32.5±5.0	-37.3±7.3
AP_Hw (ms)	2.1±0.5	1.3±0.3	0.8±0.2
AP_Height (mV)	58.6±7.5	57.0±7.8	61.5±9.6
AP_AHP (mV)	19.6±2.1	18.6±4.0	17.3±3.1

Table 8. Electrophysiological intrinsic properties of S1BF L4 FS interneurons. The table shows mean ± standard deviation of the cell intrinsic properties (abbreviation in **Table 1** legend). There is a statistically significant effect of the factor "*Development*" (P5-P8, n = 7; P9-P13, n = 8; P14-P18, n = 12) for the following features (shown as shaded groups in the table): Rin (Kruskal-Wallis test: $X^2(2) = 14.7$, $p \leq 0.001$), Rheobase (One-way ANOVA: $F(2,24) = 6.1$, $p = 0.007$), MaxFiring (One-way ANOVA: $F(2,24) = 10.3$, $p \leq 0.001$), VoltSag (One-way ANOVA: $F(2,27) = 4.2$, $p = 0.02$), and AP_Hw (One-way ANOVA: $F(2,27) = 39.6$, $p \leq 0.001$).

	P5-P8	P9-P13	P14-P18
Rin (MΩ)	804±189	374±239	231±124
RMP (mV)	-60.0±6.4	-65.5±3.2	-63.9±6.2
Tau (ms)	97±32	87±45	124±82
Rheobase (pA)	11.8±6.8	46.1±44.7	77.7±73.2
MaxFiring (Hz)	29.3±12.2	54.4±17.2	84.7±26.6
AI	1.2±0.2	1.5±0.3	1.3±0.3
VoltSag (mV)	2.3±1.6	3.2±1.2	8.1±3.6
AP_Th (mV)	-41.5±4.9	-36.8±4.9	-41. 5±5.0
AP_Hw (ms)	2.8±0.4	1.6±0.4	1.1±0.3
AP_Height (mV)	70.1±5.8	64.9±15.2	62.5±10.8
AP_AHP (mV)	15.1±3.4	18.4±4.9	9.1±1.3

Table 9. Electrophysiological intrinsic properties of S1BF L4 SST+ interneurons. The table shows mean ± standard deviation of the cell intrinsic properties (abbreviation in **Table 1** legend). There is a statistically significant effect of the factor "*Development*" (P5-P8, n = 6; P9-P13, n = 5; P14-P18, n = 6) for the following features (shown as shaded groups in the table): Rin (One-way ANOVA: $F(2,14) = 15.3$, $p \leq 0.001$), MaxFiring (One-way ANOVA: $F(2,14) = 11.8$ $p \leq 0.001$), VoltSag (Kruskal-Wallis test: $X^2(2) = 8.5$, $p = 0.01$), AP_Hw (One-way ANOVA: $F(2,14) = 31.6$, $p \leq 0.001$), and AP_AHP (One-way ANOVA: $F(2,14) = 10.5$, $p = 0.002$).

Chapter 4

Function of GABAergic interneurons in the developing V1

4.1 – Introduction

Chapter 3 provides a detailed description of the developmental trajectory of neuronal circuits in the primary visual cortex (V1), with a particular focus on the role played by somatostatin-expressing (SST+) interneurons. In ***Chapter 4***, the focus shifts towards the function of these neuronal networks *in vivo*, studied through electrophysiological recordings in neonatal mice in combination with optogenetic and chemogenetic approaches. I will focus on the role played by GABAergic interneurons during spontaneous and sensory-evoked activity, aiming at understanding how they dynamically regulate information flow in postnatal V1. Similar to the circuit level analysis in the previous chapter, one of the main objectives of ***Chapter 4*** is to provide a comparative analysis with the primary somatosensory barrel cortex (S1BF), whose *in vivo* networks have been characterised and studied before (Baruchin et al., 2021). To allow referencing between networks and functions, the experiments described here are grouped by the same developmental windows described in ***Chapter 3*** (P5-P8, P9-P13, and P14-P18).

4.2 – Characterisation of spontaneous and sensory-evoked activity in developing V1 in anaesthetised mice

Most *in vivo* experiments described in this chapter were performed in anaesthetised animals. Experiments on *in vivo* V1 activity during development described so far in the literature were mostly performed in non-anaesthetised, head fixed rodents (Colonnese et al., 2010; Shen and Colonnese, 2016), hence I start the current chapter with a characterisation of spontaneous and sensory-evoked activity in anaesthetised neonatal mice. As anaesthetic protocol, I employed urethane which led to an anaesthetised brain state that mimics sleep (Clement et al., 2008). Since neonatal mice spend most of their time

sleeping (Rensing et al., 2018), I reasoned urethane-anaesthesia could provide the most realistic setting for our experiments, and in parallel with observations from other brain regions (Chini et al., 2019) would not significantly alter sensory processing in primary sensory areas.

After anaesthesia induction with urethane (1-2 mg/kg), mice were implanted with 32-channels silicon probes with various configurations. Following recovery, I recorded at least 20 minutes of spontaneous activity followed by a set of visual stimulations. As previously described for non-anaesthetised, head fixed neonatal mice (Shen and Colonnese, 2016), local field potential (LFP) spontaneous activity in layer (L)4 of V1 before eye opening is dominated by prolonged periods of network “silence” separated by bursts of oscillatory activity in the beta frequency, termed spindle bursts (**Fig. 4.1A, B**). Overrepresentation of beta frequency oscillations is evidenced in the power spectral density (PSD) plots in **Fig. 4.1D, E**, with peaks in the PSD power at around 15 and 22 Hz, respectively. After eye opening (**Fig. 4.1C**), spontaneous activity is similar to the adult one, characterised by broadband activity and PSD without noticeable peaks (**Fig. 4.1F**). Over development, I observed a reduction in overall beta frequency power (**Fig. 4.1G**), which statistically differ for animals recorded after eye opening compared to before. I also identified individual spindle burst events through an automated method (see Methods section) and quantified their duration and frequency of occurrence. I found a statistically significant decrease in the duration of individual spindle burst events (**Fig. 4.1H**), in line with a reduction of busting activity after eye opening (Shen and Colonnese, 2016). This was coupled with an increase spindle burst occurrence (**Fig. 4.1I**), which might be due to a general increase in beta frequency oscillations (due to increase in broadband activity) or to sleep spindle-like events.

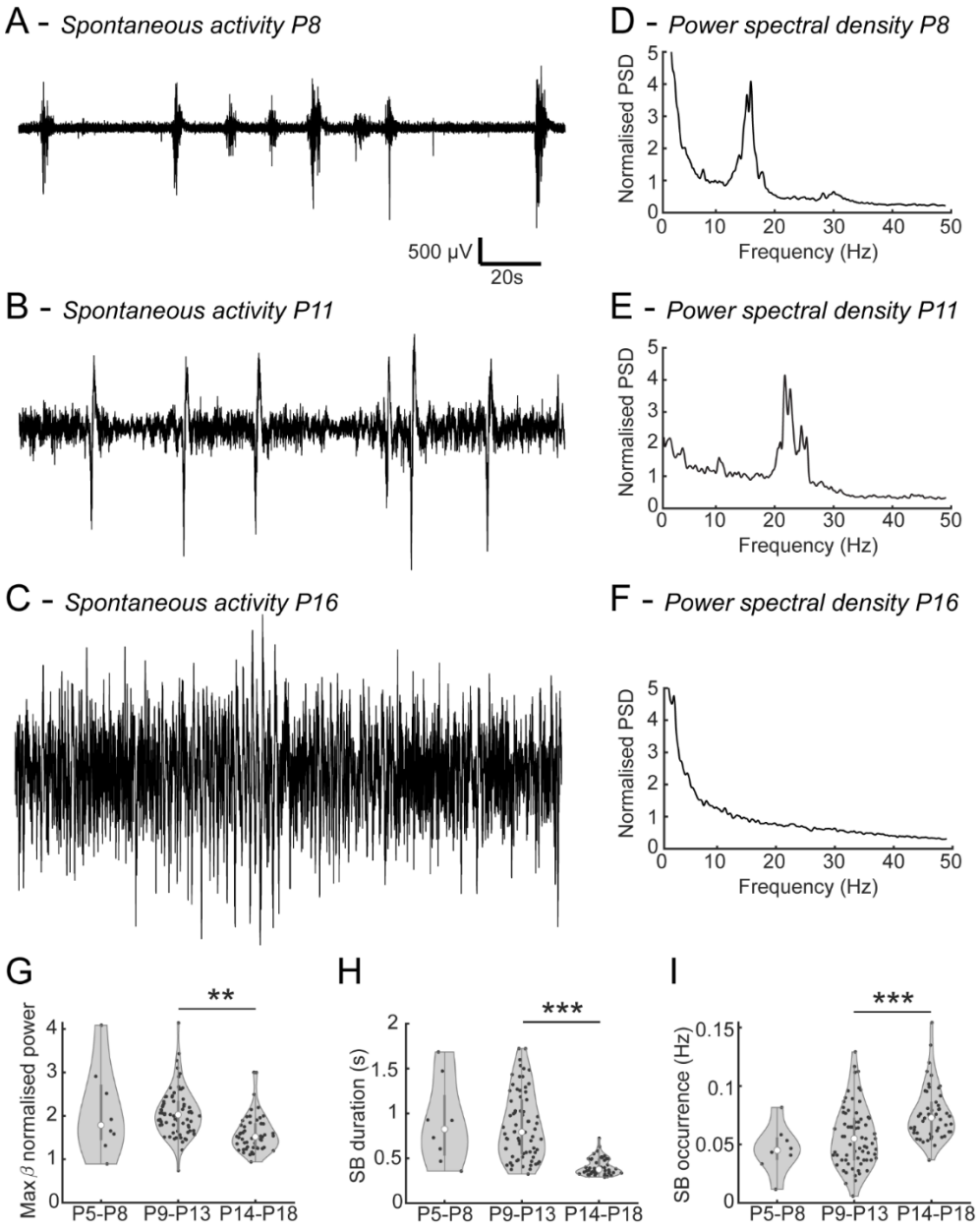


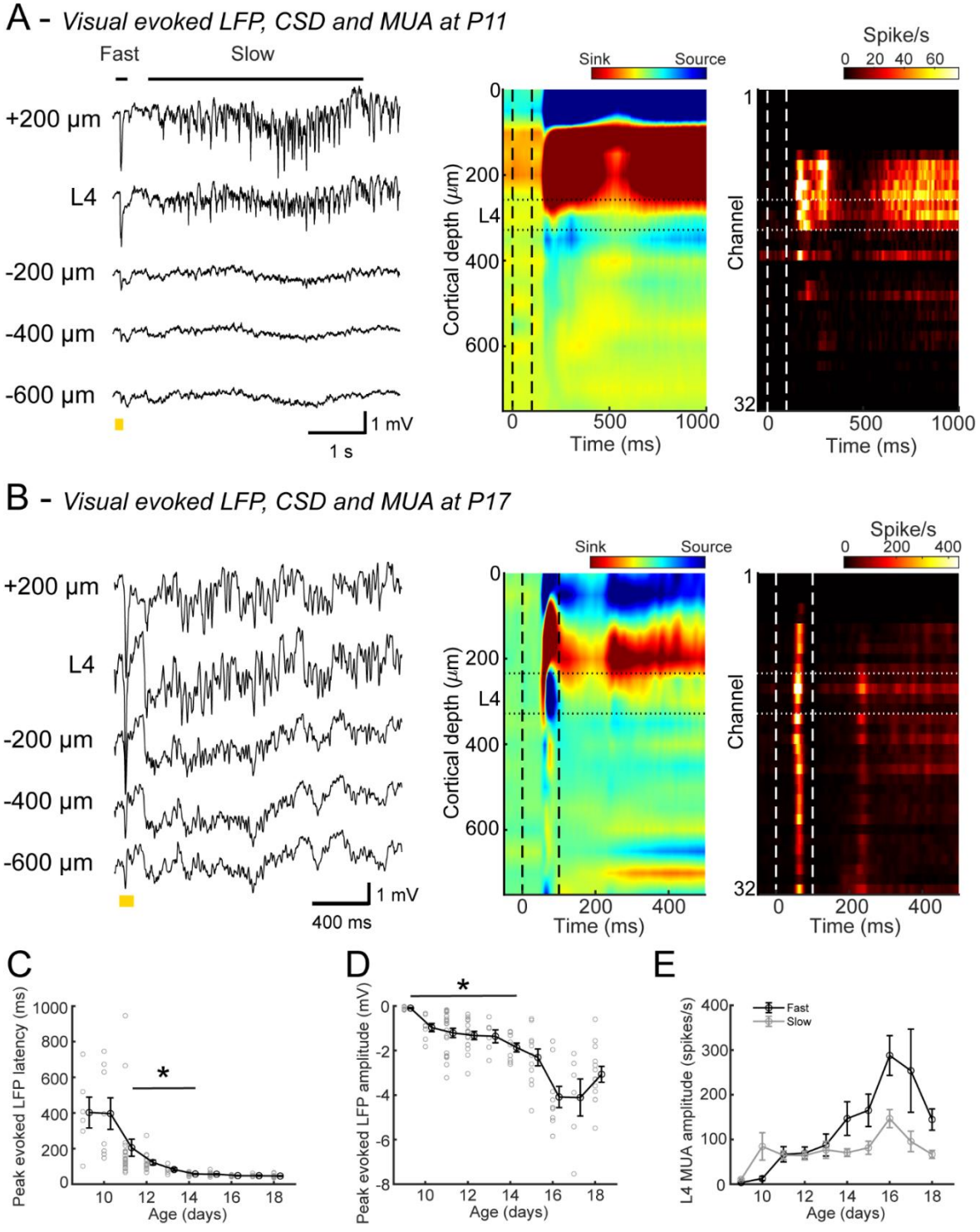
Fig. 4.1. Characterisation of spontaneous activity in developing V1 of anaesthetised mice. (A-C) Representative local field potential (LFP) voltage traces of spontaneous activity in V1, recorded with multi-channel silicon probes in a P8 (A), P11 (B), and P16 (C) mouse.
(D-F) Normalised power spectral density (PSD) plots for the recordings shown in (A-C) respectively, showing a clear peak in the beta frequency range before eye opening (D, E), and adult-like pattern after eye opening (F).
(G) Violin plot of peak normalised power in the beta (β) range for mice recorded in three different developmental windows (P5-P8, n = 8; P9-P13, n = 55; and P14-P18, n = 48). There is a statistically significant effect of the factor "*Development*" (One-way analysis of variance (ANOVA): $F(1,106) = 14.6$, $p \leq 0.001$).
(H) Violin plot of spindle burst (SB) duration for mice recorded at the same developmental windows as in (G). There is a statistically significant effect of the factor "*Development*" (One-way ANOVA: $F(1,106) = 38.6$, $p \leq 0.001$).
(I) Violin plot of SB occurrence for mice recorded at the same developmental windows as in (G). There is a statistically significant effect of the factor "*Development*" (One-way ANOVA: $F(1,106) = 10.2$, $p \leq 0.001$). Asterisks in the plot show statistically significant differences between groups, when tested with post-hoc analysis corrected for multiple comparisons (Tukey's test), according to the following notation: ** $p \leq 0.01$ and *** $p \leq 0.001$.

I next analysed the development of sensory-evoked activity in V1. Previous experiments employed a short flash of white LED light to trigger sensory-evoked activity in V1 in mice before eye opening (Shen and Colonnese, 2016), indeed it was shown to be the most salient stimulus for the visual system during this early postnatal period (Krug et al., 2001; Akerman et al., 2002). Similar to previous experiments in non-anaesthetized animals (Shen and Colonnese, 2016), no reliable sensory responses could be elicited through this stimulation during the first developmental window investigated (P5-P8, n = 8 mice), which is therefore excluded from subsequent analysis. Responses to visual stimulation during the period before eye opening (P9-P13) are characterised by an initial deflection in the LFP (fast response) followed by prolonged oscillatory activity lasting a few seconds (slow response) that is confined to upper cortical layers (**Fig. 4.2A**). This response profile is observed also in the current source density (CSD) heatmap, where a current sink is generated upon visual stimulation and is maintained for extended time across granular and supragranular layers. Multi-unit activity (MUA) heatmaps clearly show spiking activity embedded within the LFP response, with an initial short-latency volley of spikes followed by sustained spiking during the oscillatory response concentrated in upper cortical layer neurons. Based on previous experiments, the secondary oscillatory activity likely reflects a spindle burst in the thalamocortical system triggered by a light-induced retinal wave (Tiriac et al., 2018). Mature responses to visual stimulation are observed after eye opening (**Fig. 4.2B**), when only a fast response phase can be identified in the LFP trace (left), CSD heatmap (middle) and MUA heatmap (right), which extends to infragranular layers. A weaker secondary slow response evident in the MUA heatmap has been previously observed during visual stimulation in sleeping animals (Colonnese et al., 2010) and might be due to the anaesthetic protocol employed in the current experiments. Analysis of the fast visual response latency (**Fig. 4.2C**) shows this to be reliable only by P11 and progressively decreasing; amplitude of the fast LFP response increases (**Fig. 4.2D**), reaching mature values only after P14 (n = 103 mice). Quantification of peak MUA responses (**Fig. 4.2E**)

shows that the slow response peaks around P10 and remains constant up until P18 whereas the fast response peaks only after eye opening.

Our initial characterisation of spontaneous and sensory-evoked activity in anaesthetised mice show they are characterised by classic hallmarks previously described in non-anaesthetised neonatal mice (Shen and Colonnese, 2016). Spontaneous activity prior to eye opening is dominated by spindle bursts while sensory-evoked activity shows a fast initial response followed by a sustained oscillatory response. Spontaneous and sensory-evoked activity after eye opening resembles the patterns observed in adult mice, characterised by lack of clear oscillatory bursts in the beta range during spontaneous activity and a fast response to sensory stimulation. The only significant confound due to anaesthesia would appear to be the long latency, reverberatory oscillation observed in animals post eye-opening.

Fig. 4.2 (next page). Characterisation of sensory-evoked responses in developing V1 of anaesthetised mice. (A, B) Representative LFP voltage traces (left) recorded upon visual stimulation with a flash of white LED light (yellow line) at different cortical depth (relative to layer 4, L4) and corresponding current-source density (CSD, middle) and multi-unit activity (MUA, right) heatmaps obtained from a P11 (A) and P17 (B) mouse. In the LFP plots in (A), black lines show the presence of a fast and rapid initial response to the visual stimulus followed by a slower secondary oscillatory response. In the CSD and MUA plots, vertical dashed lines indicated onset and offset of the visual stimulus while horizontal dotted lines indicated the approximate location of L4.
(C, D) Error bar plots (mean ± standard error of the mean, SEM) and scatter plot for peak visual evoked LFP latency (C) and amplitude (D) of the fast response to the visual stimulus for mice recorded at different ages (P9, n = 6; P10, n = 8; P11, n = 20; P12, n = 15; P13, n = 6; P14, n = 9; P15, n = 11; P16, n = 9; P17, n = 6; and P18, n = 13). There is a statistically significant effect of the factor "*Age*" for both LFP latency (Kruskal-Wallis test: X^2 (9) = 84.1, $p \leq 0.001$) and LFP amplitude (Kruskal-Wallis test: X^2 (9) = 57.1, $p \leq 0.001$).
(E) Error bar plot of peak visual-evoked MUA in L4 for the fast (black line) or slow (grey line) for mice recorded at different ages. There is a statistically significant effect of the factor "*Age*" for both the fast (Kruskal-Wallis test: X^2 (9) = 50.8, $p \leq 0.001$) and slow (Kruskal-Wallis test: X^2 (9) = 28.1, $p \leq 0.001$) MUA response. Asterisks in the plot show statistically significant differences between groups, when tested with post-hoc analysis corrected for multiple comparisons (Dunn's test), according to the following notation: * $p \leq 0.05$.



4.3 – Optogenetic strategy for interneurons tagging in the developing V1

To understand how different interneuron subtypes contribute to activity in postnatal V1, I adapted standard optogenetic spike-tagging approaches previously used in adult animals (Kvitsiani et al., 2013; Senzai et al., 2019). I used the *SSTCre* transgenic mouse line –

characterised in ***Chapter 3*** – to conditionally express Channelrhodopsin-2 (ChR2) in SSTCre+ interneurons via the *Ai32* driver line. To target the second major class of cortical GABAergic interneurons – parvalbumin-expressing (PV+) fast-spiking (FS) interneurons – I used an *Nkx2-1Cre* transgenic line (Xu et al., 2008). Similar to Lhx6-eGFP transgenic mice characterised in ***Chapter 3***, the *Nkx2-1Cre* line captures cortical GABAergic interneurons originating from the medial ganglionic eminence, comprising SST+ and PV+ subtypes (Xu et al., 2008). The idea was that use of both lines through early development would enable us, through a subtractive approach, to parse out the contribution of putative PV+ cells prior to expression of PV that starts towards the end of the second postnatal week (del Rio et al., 1994). To explore the relationship between the interneurons labelled by the *Nkx2-1Cre* and *Lhx6-eGFP* lines, I performed immunohistochemistry to label SST+ and PV+ interneurons in these two transgenic animals. Attempts to breed triple transgenic *Lhx6-eGFP; Nkx2-1Cre; Ai9* animals to express GFP in Lhx6+ interneurons and tdTomato in Nkx2-1-expressing (Nkx2-1+) interneurons to directly compare Lhx6-eGFP+ and Nkx2-1+ cohorts failed. For this reason, I characterised interneuron subtypes in *Nkx2-1Cre; Ai9* animals by collecting slices of V1 (and S1BF, as comparison) and staining them with antibodies against tdTomato (to label Nkx2-1+ interneurons) and PV (**Fig. 4.3A, B**). Similar to my previous characterisation of Lhx6-eGFP+ cells (**Fig. 3.5**), Nkx2-1+ neuron distribution is biased toward granular and infragranular layers, with a higher overall density of positive cells in L4 of V1 compared to S1BF (**Fig. 4.3C**). The percentage of double positive (Nkx2-1+ and PV+) cells ranges approximately between 30 and 60% of the total Nkx2-1+ population, with the larger proportion found in L4 for both primary sensory areas (**Fig. 4.3D**). Of the whole PV+ population, the majority of these cells also expressed Nkx2-1 (67% ± 3% in V1 and 66% ± 3% in S1BF). While a direct comparison between Lhx6-eGFP+ and Nkx2-1Cre+ cells was not possible, this data shows both transgenic lines capture a similar proportion of PV+ interneurons in V1 and S1BF.

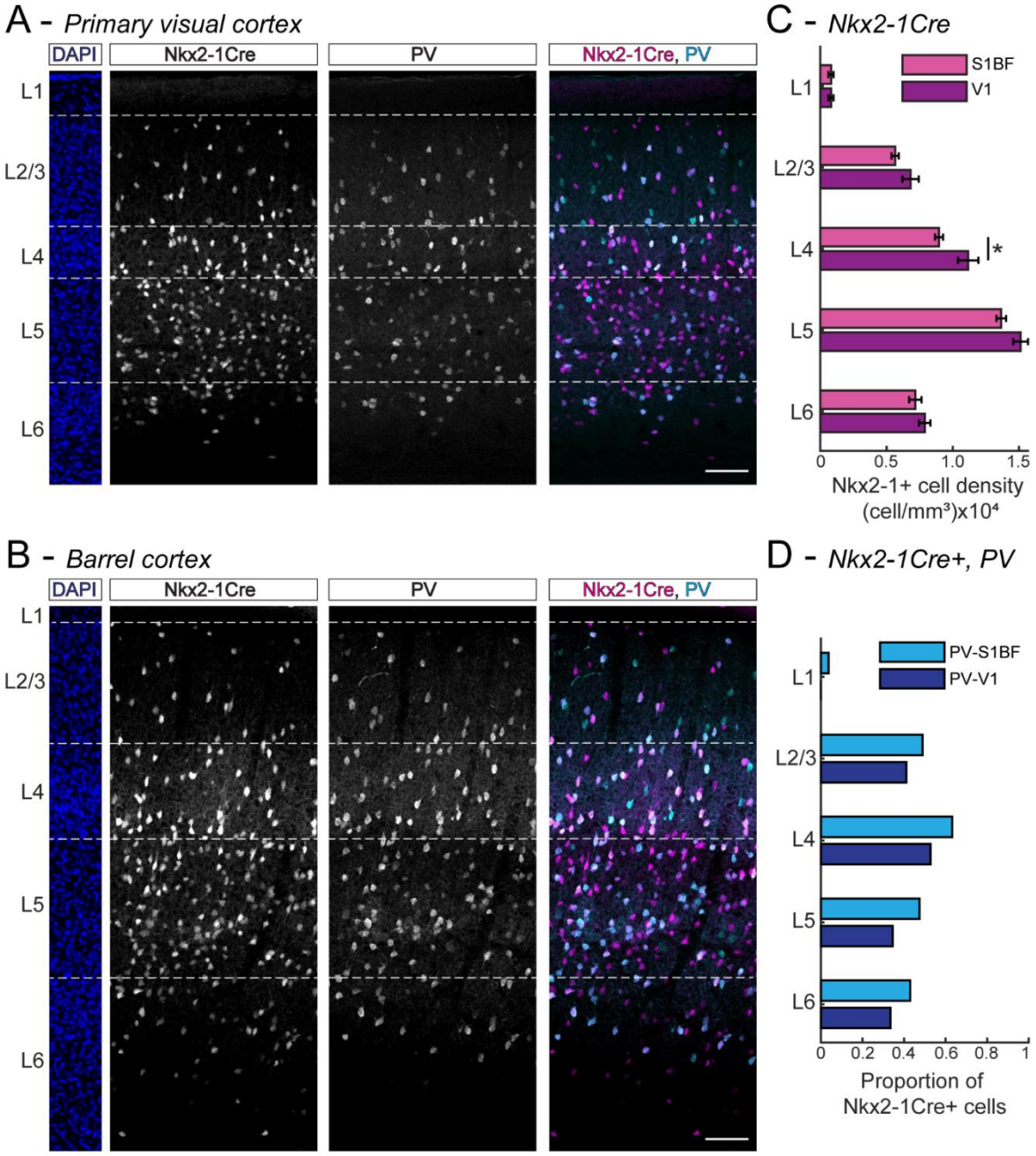


Fig. 4.3. Histological characterisation of Nkx2-1-Cre mouse line. (A) Representative confocal images of a V1 slice (50 µm thickness) obtained from a *Nkx2-1Cre; Ai9* transgenic animal stained with an anti-tdTomato antibody (to label Nkx2-1Cre+ interneurons) and PV. DAPI profile (blue, left) was used to determine layer boundaries (dashed white lines). In the merge image on the right, Nkx2-1Cre signal is in magenta, PV signal is in cyan. Scale bar = 100 µm.
(B) Same as in A but for a slice containing the primary somatosensory barrel cortex (S1BF).
(C) Bar plot (± SEM) of the density of Nkx2-1+ cells in S1BF (light magenta; n = 9 images from 3 animals) and V1 (dark magenta; n = 9 images from 3 animals). There is a statistically significant of the factor "*Layer*" on the cell density data (Two-way ANOVA: $F(4,64) = 160.7$, $p \leq 0.001$).
(D) Bar plot of the proportion of Nkx2-1+ cells that also express PV in S1BF (light blue) and V1 (dark blue). There is a statistically significant of the factor "*Layer*" on the cell density data (Two-way ANOVA: $F(4,64) = 104.6$, $p \leq 0.001$). Asterisks in the plot show statistically significant differences between groups, when tested with post-hoc analysis corrected for multiple comparisons (Estimated marginal means method; *emmeans* function in R), according to the following notation: * $p \leq 0.05$.

SSTCre; Ai32 and *Nkx2-1Cre; Ai32* animals were then used for *in vivo* electrophysiological recordings to allow optogenetic-spike tagging of either SST+ or Nkx2-1+ interneurons. Isolated single units (SUs) were considered tagged interneurons if they significantly increased firing rate during the optogenetic stimulus (100 trials, 50 ms, 10 s inter-trial interval; see **Fig. 4.4A**). These units, recorded in animals before eye opening, were characterised by immature spike waveform (**Fig. 4.4B**), but could however be well isolated from other SUs and MUA. Tagged units could be then specifically analysed regarding their spiking pattern during spontaneous activity or sensory-evoked activity. For example, **Fig. 4.4C** shows raster plots and peri-stimulus time histogram (PSTH) upon visual stimulation for the two units shown in **Fig. 4.4A**.

Out of a total of 832 SUs obtained from *SSTCre; Ai32* animals, 51 (6%) were tagged as SST+ interneurons while 43 out of 444 SUs (10%) recorded from *Nkx2-1Cre; Ai32* animals were tagged as Nkx2-1+ interneurons. The spike waveform trough to peak latency and half-width of these tagged units is represented in the scatter plot in **Fig. 4.4D, E**, together with data from all other untagged units. Spike waveform features are immature for units obtained before eye opening (**Fig. 4.4D**). Indeed, only after eye opening, a clear separation between putative regular-spiking (RS) and fast-spiking (FS) single units could be observed in the scatter plot as well as in the spike trough to peak latency histogram (**Fig. 4.4E**). Similar to previous approaches, I classified as FS single units, all units obtained from mice after eye opening characterised by spike trough to peak latency less than 0.75 ms. A total of 233 SUs were classified as FS neurons based on the above criteria, including 49 units obtained from *Nkx2-1Cre; Ai32* animals. Analysis of the cortical depth of all interneuron SUs (SST+, Nkx2-1+, and FS) suggest all subtypes could be found throughout every cortical layer (**Fig. 4.4F**), indicating FS units identified in *Nkx2-1Cre; Ai32* animals are not those in which the optogenetic spike tagging strategy failed. Rather, it is conceivable the Nkx2-1Cre line does not capture the whole extent of FS interneuron population in the cortex; our optotagging strategy might hence under-report GABAergic interneurons. In agreement with the

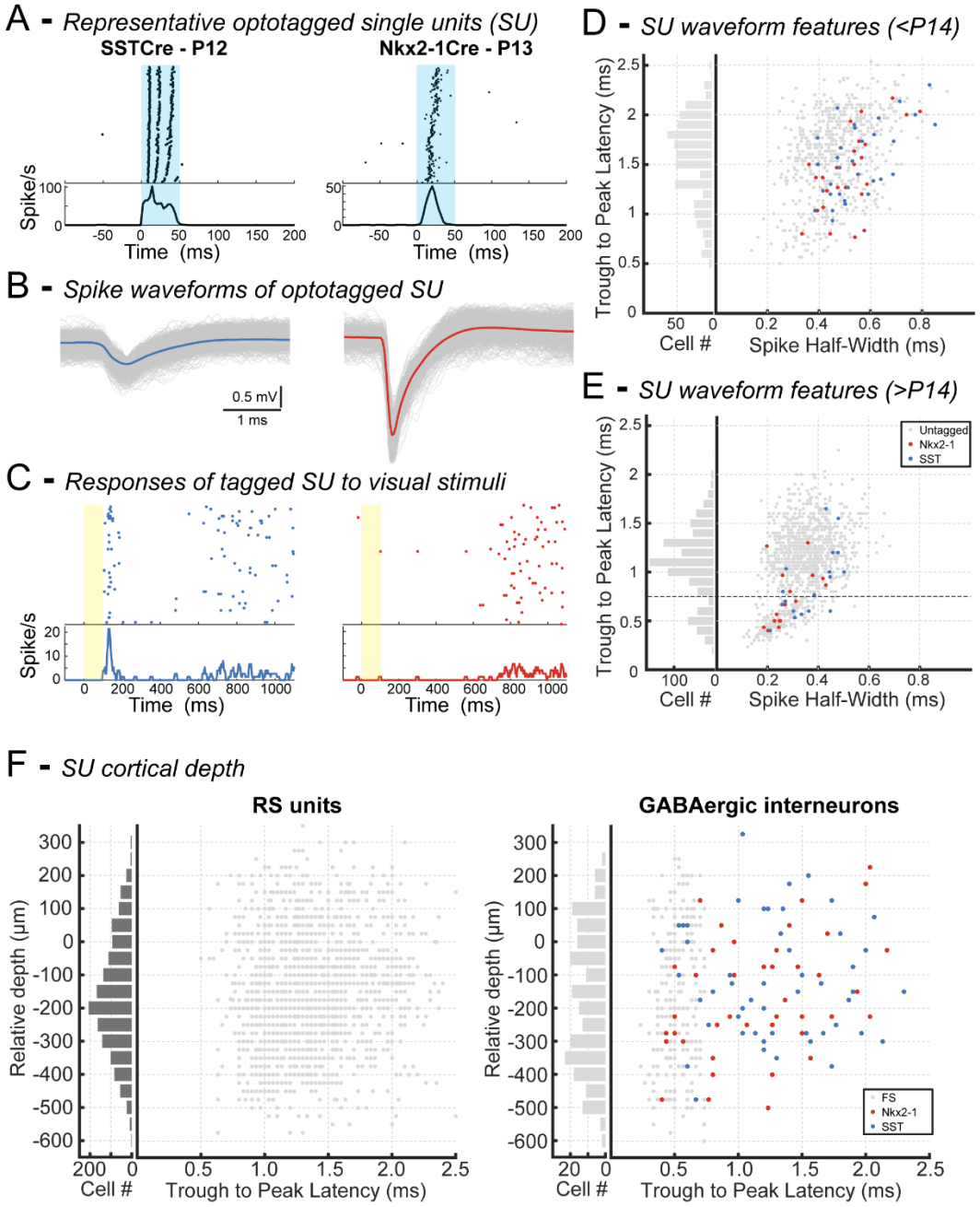


Fig. 4.4. Optogenetic spike-tagging of interneurons in developing mouse V1 *in vivo*. (A) Raster plots of representative single units (SUs) from a *SSTCre; Ai32* transgenic mouse (left) and *Nkx2-1Cre; Ai32* transgenic mouse (right) during blue light stimulation showing reliable spiking activity used to tag SST+ or Nkx2-1+ interneurons.
(B) Spike waveforms for the SUs tagged in (A); grey lines indicate individual spike waveforms coloured line shows average spike waveform (blue, SSTCre; red, Nkx2-1Cre).
(C) Raster plot (top) and peri-stimulus time histogram (PSTH) plot for the SUs shown in (A, B); yellow lines indicate the time of the visual stimulus.
(D, E) Scatter plot of spike half-width vs. spike through to peak latency (right) and histogram plot for spike through to peak latency (left) for SUs obtained from animals before eye opening (D) and after eye opening (E). Grey dots and bars show untagged SUs, blue dots indicate tagged SST+ interneurons, red dots indicate tagged Nkx2-1 interneurons. Horizontal dashed line in E shows the arbitrary cut-off spike through to peak latency value (0.75 ms) used to identify fast-spiking (FS, below to the line) vs. regular spiking (RS, above the line) SU.
(F) Scatter plot of spike through to peak latency vs. cortical depth (relative to L4, corresponding to 0 µm; right) and histogram plot for cortical depth (left) for SUs classified as RS (left plots) or GABAergic interneurons (FS, grey; SST+, blue, Nkx2-1+, red).

immunohistochemical characterisation, 9/17 (53%) of the Nkx2-1+ tagged interneurons obtained after eye opening were also classified as FS units. Half (8/16) of the SST+ interneurons obtained after eye opening were also characterised as FS units. While SSTCre+ cells with FS characteristics have been observed before (Hu et al., 2013), the cut-off value of 0.75 ms used for these experiments is larger than values commonly used in adult animals (Bortone et al., 2014). In addition, SST+ interneurons in V1 show mature electrophysiological properties earlier than FS interneurons (see ***Chapter 3***), with spike features intermediate between the ones of RS and FS interneurons. Data analysis shown in the next sections will focus on optogenetically tagged GABAergic interneurons which consistently identifies interneuron subtypes across developmental stages.

4.4 – Involvement of cortical neurons in spontaneous and sensory-evoked activity in V1 during development

4.4.1 – Involvement of RS neurons in spontaneous and sensory-evoked activity in V1

I next isolated RS neurons in different cortical layers and investigated how they are entrained by spontaneous spindle burst and evoked visual responses. Spindle burst events are mostly observed in electrode channels located in granular and supragranular layers yet, they entrain the firing of single units distributed throughout the cortical column (**Fig. 4.5A**). Indeed, before eye opening, the majority of the single RS units identified were significantly entrained by spindle burst oscillations (**Fig. 4.5B**). Entrained RS units fired on average ≈ 40% of their total number of spikes concomitantly with spindle bursts events (**Fig. 4.5C**), although with high variability among individual units. Statistical analysis shows that L5/6 neurons fire significantly less spikes during spindle bursts period compared with SUs in the granular layer (**Fig. 4.5C**).

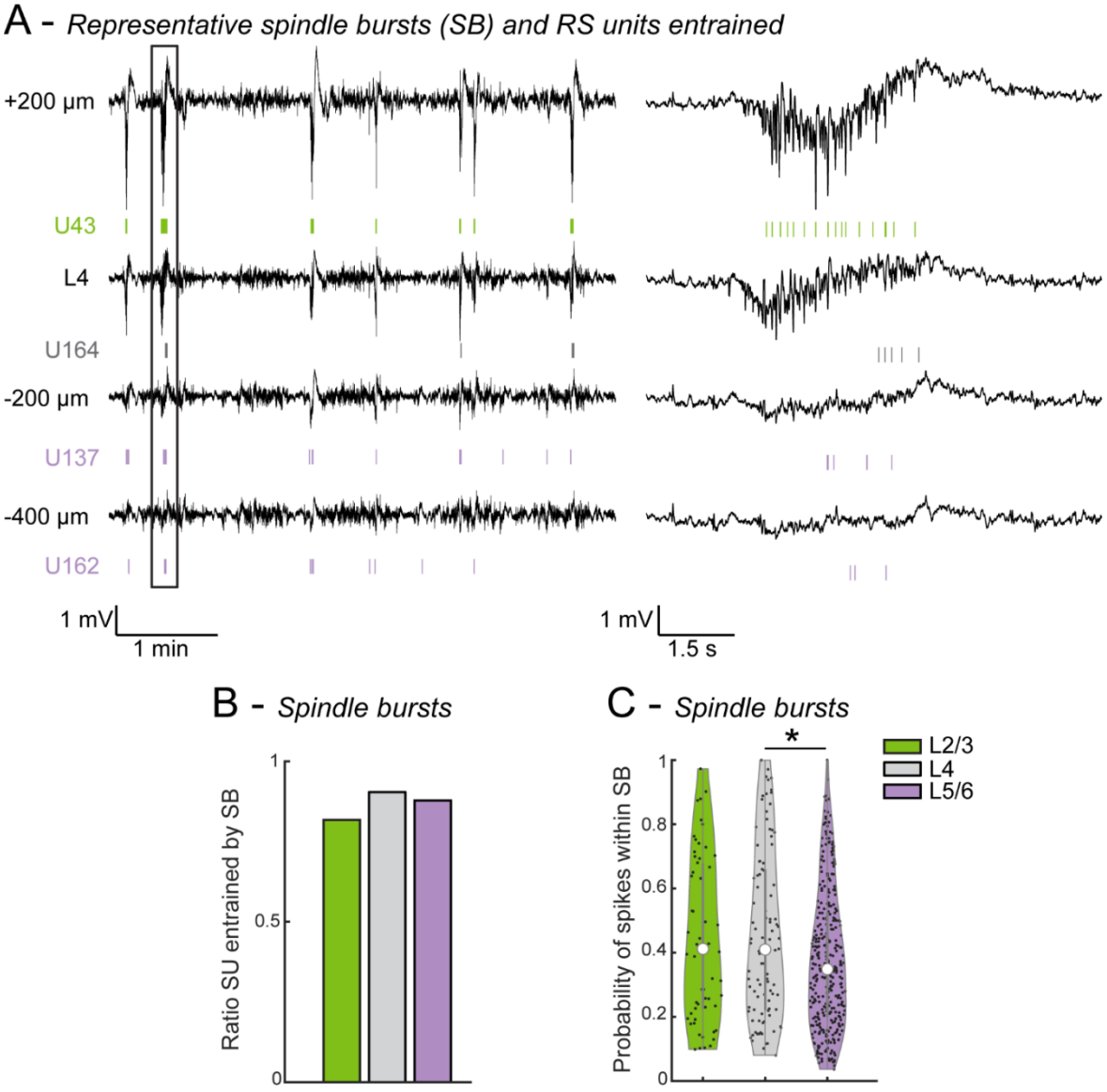


Fig. 4.5. Involvement of RS neurons in spontaneous activity in V1 during development. (A) Representative LFP voltage traces obtained from a P12 mouse recorded with multi-channel silicon probes showing spontaneous spindle bursts (enlarged traces of one event is shown on the right). Depth of LFP trace recordings is referred to L4. Coloured lines show spike times for 4 single units (U43 in L2/3, U164 in L4, U137 and U162 in L5/6) recorded from the same animal.
(B) Bar plot of the ratio of single units (SU) that are statistically significantly entrained by a spindle burst, for units in L2/3 (green), L4 (grey) and L5/6 (purple).
(C) Violin plot of probability of spikes occurring within SB over the total number of spikes fired throughout spontaneous activity recording (20 min) for units in different layers (colour-coding as in B). There is a statistically significant effect of the factor "Cell *Layer*" (Kruskal-Wallis test: X^2 (2) = 7.1, $p \leq 0.05$).

Analysis of entrainment of firing by spindle bursts described thus far is based on an arbitrary definition of a spindle burst event. To address this limitation, I also computed the entrainment between SU spike times and oscillations in the beta frequency (10-30 Hz), for

all RS SUs (**Fig. 4.6A**). Instead of using the classical mean vector length to represent spike-LFP entrainment (**Fig. 4.6B**), I calculated a pairwise phase consistency (PPC) value, which is more robust than the former when analysing units with low firing frequency (Vinck et al., 2010; Chen et al., 2017; Veit et al., 2017). Similar to our previous analysis, the majority of the RS units are significantly entrained by beta oscillations (**Fig. 4.6C**), with infragranular SUs characterised by lower PPC values compared to L4 and L2/3 units (**Fig. 4.6D**).

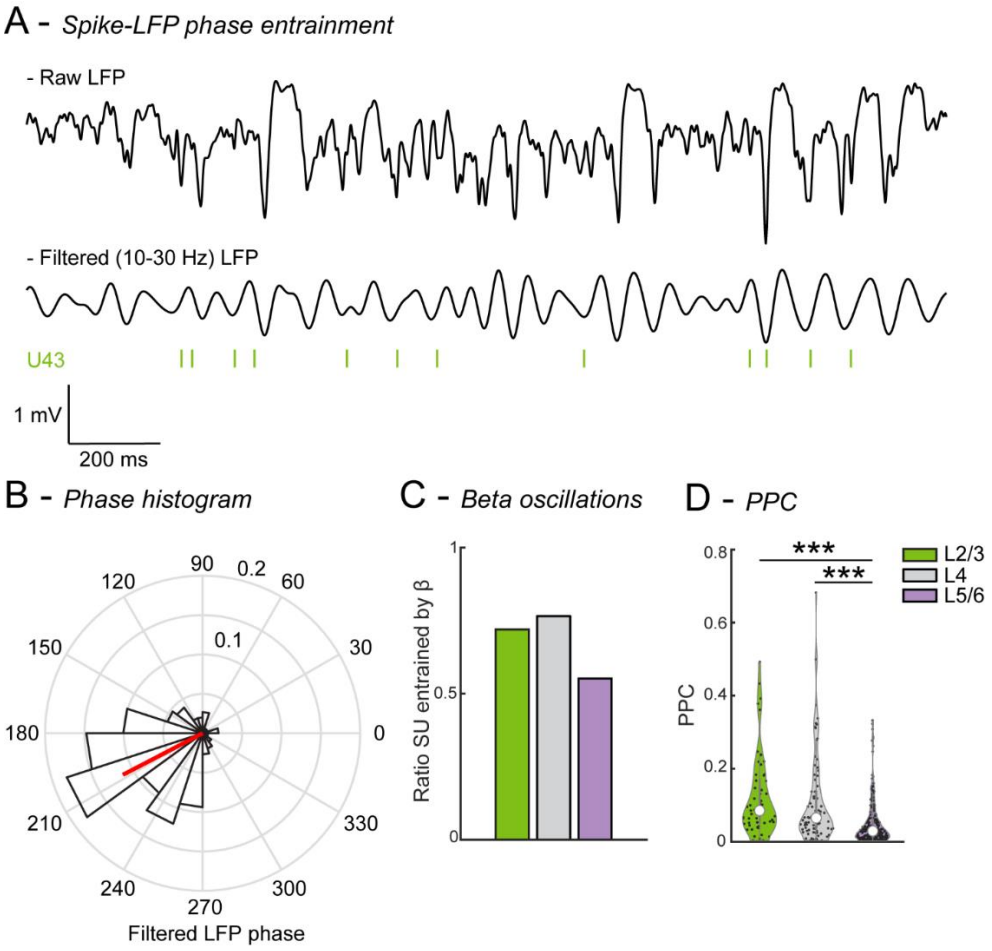


Fig. 4.6. Spike-LFP entrainment of RS neurons in V1 during spontaneous activity. (A) Inset of voltage trace LFP recording obtained during spontaneous activity in a P12 mouse during a spindle burst event (same recording as in Fig. 4.5A, top), showing the raw LFP (top) and the bandpass filtered LFP trace between 10-30 Hz. Green lines indicate spike times for a SU (U43) recorded in the same channel of the LFP trace, located within L2/3.
(B) Polar histogram plot of the phase of the bandpass filtered (10-30 Hz) LFP signal at the time of each spike for U43 shown in B. Red line, resultant mean vector obtained from the histogram.
(C) Bar plot of the ratio of RS SUs that are statistically significantly entrained by beta (β) oscillations, for units in L2/3 (green), L4 (grey) and L5/6 (purple).
(D) Violin plot of pairwise phase-consistency (PPC) value between spike times and beta oscillations for units in different layers (colour-coding as in C). There is a statistically significant effect of the factor "Cell *Layer*" (Kruskal-Wallis test: X^2 (2) = 27.5, $p \leq 0.001$). Asterisks in the plot show statistically significant differences between groups, when tested with post-hoc analysis corrected for multiple comparisons (Dunn's test), according to the following notation: *** $p \leq 0.001$.

I then looked at how RS units respond to visual stimulations. Based on their firing patter upon visual stimulation (**Fig. 4.7A**), SU were classified as either fast responsive, slow responsive, responsive to both phases and non-responsive. SUs responsive during the slow phase of the visual response can be recorded from P9, they peak at ages between P10 and P13, when most of the SU are slow responsive, and decline starting from eye opening (**Fig. 4.7B**, light grey), in line with maturation of sensory responses previously described for LFP and MUA. Conversely, responsive units during the fast phase appear at P10 and slowly and gradually increase throughout the next days (**Fig. 4.7B**, dark grey). Peak firing for all responsive RS units during the fast response (**Fig. 4.7C**) does not change with development, with L4 firing at a higher rate than L5/6 units regardless of their development stage. Peak firing of responsive SU during the slow response phase is stronger in supragranular layers compared to infragranular layer SUs before eye opening and shows a general decrease over development (**Fig. 4.7D**), in line with a transition from dense to sparse coding after eye opening (Rochefort et al., 2009). Finally, I also calculated the Fano factor as an index of reliability of spiking during the fast response to the visual stimulus (see **Fig. 4.7E**). There is a general reduction in the reliability (increase Fano factor) of fast responses over development, especially for L2/3 and L5/6 neurons but not L4 SUs (**Fig. 4.7F**).

Overall, these results suggest that spindle bursts oscillations in the beta frequency entrain the majority of SUs throughout cortical layers, with granular and supragranular neurons firing the large majority of their spikes during spindle bursts events. Moreover, most of the SUs isolated are also responsive to the slow phase of sensory-evoked responses in V1, in the period immediately preceding eye opening. Despite being found in lower numbers, SUs recruited during the fast visual response do not undergo change in their maximum firing frequency but only a reduction in spike reliability (especially for cells outside L4) when comparing animals recorded before and after eye opening.

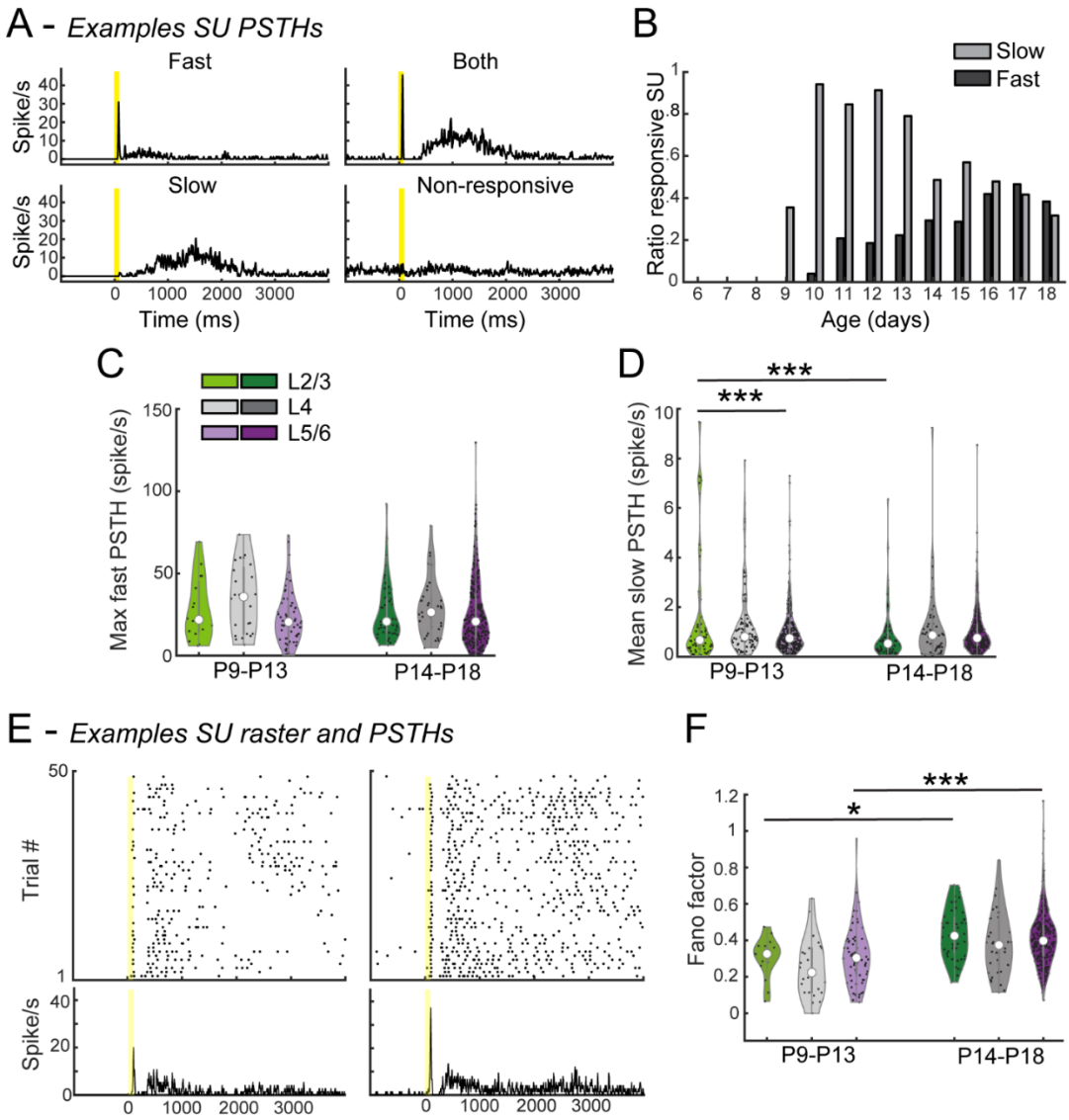


Fig. 4.7. Development of V1 regular spiking single unit responses to visual stimulation. (A) Peri-stimulus time histograms (PSTHs) obtained from four SUs, showing increased firing during the fast response only (upper left), the slow response only (lower left), both phases (upper right) and no response to visual stimulation (shown in yellow).
(B) Bar plot of ratio of RS SU classified as responsive to either the fast (dark grey) or slow (light grey) phase of the visual response for each day from P6 to P18.
(C) Violin plot of RS units peak firing during the fast visual response in different layers (L2/3, green; L4, grey; and L5/6, purple) and at different developmental windows (P9-P13 and P14-P18). There is a statistically significant effect of the factor "*Cell Layer*" (Two-way ANOVA: $F(2,438) = 3.21$, $p \leq 0.05$), multiple comparisons test shows an overall difference between L4 and L5 without taking into account the developmental stages (Tukey's test: $p \leq 0.05$).
(D) Violin plot of RS units peak firing during the slow visual response in different layers and at different developmental windows (colour coded as in C). There is a statistically significant effect of the factors "*Cell Layer*" (Two-way ANOVA: $F(2,893) = 3.9$, $p \leq 0.05$) and "*Development*" (Two-way ANOVA: $F(1,893) = 12.7$, $p \leq 0.001$).
(E) Representative raster plot and PSTH for two single units characterised by low reliability (high Fano factor, left) and high reliability (low Fano factor, right).
(F) Violin plot of RS units Fano factor during the fast visual response in different layers and at different developmental windows (colour coded as in C). There is a statistically significant effect of the factor "*Development*" (Two-way ANOVA: $F(1,438) = 25.5$, $p \leq 0.001$). Asterisks in the plot show statistically significant differences between groups, when tested with post-hoc analysis corrected for multiple comparisons (Tukey's test), according to the following notation: x* $p \leq 0.05$ and *** $p \leq 0.001$.

4.4.1 – Involvement of GABAergic interneurons in spontaneous and sensory-evoked activity in V1

To study how cortical GABAergic interneurons are involved in spontaneous activity in the developing V1, I first analysed how spindle burst events entrain SU firing pattern. Similar to our analysis of RS unit firing, SST+ and Nkx2-1+ interneurons firing is clustered within spindle bursts events before eye opening (**Fig. 4.8A**), with the majority of SUs significantly entrained by these events (**Fig. 4.8B**). Both optogenetically tagged interneuron subtypes fired a large fraction of their spontaneous spikes within spindle bursts, with no difference between SST+ and Nkx2-1+ interneurons (**Fig. 4.8C**). Analysis of phase consistency with beta oscillations showed similar fraction of SUs entrained (**Fig. 4.8D**), with SST+ interneurons characterised by larger PPC value than Nkx2-1+ cells (**Fig. 4.8E**), suggesting the former are more strongly coupled to beta oscillations.

Next, I investigated the pattern of responsivity of SST+ SUs upon stimulation of the visual system with white LED light. Prior to eye opening, only a small fraction of SST+ units were classified responsive during the fast phase of the visual response, whereas the large majority of them responded during the slow phase only (**Fig. 4.9A** and quantification in **Fig. 4.9C**). After eye opening, the fraction of responsive SST+ units during the fast phase of the visual response suddenly increased, with comparable ratios to SST+ units responding during the slow phase (**Fig. 4.9B** and quantification in **Fig. 4.9C**). I did not observe any difference between the peak firing rate of responsive SST+ interneurons during the slow phase of the visual response when comparing cells recorded before and after eye opening (**Fig. 4.9E**). The small number of responsive SST+ units during the fast phase of the visual responses did not allow statistical analysis on peak firing (**Fig. 4.9D**) and Fano factor (**Fig. 4.9F**) during this phase.

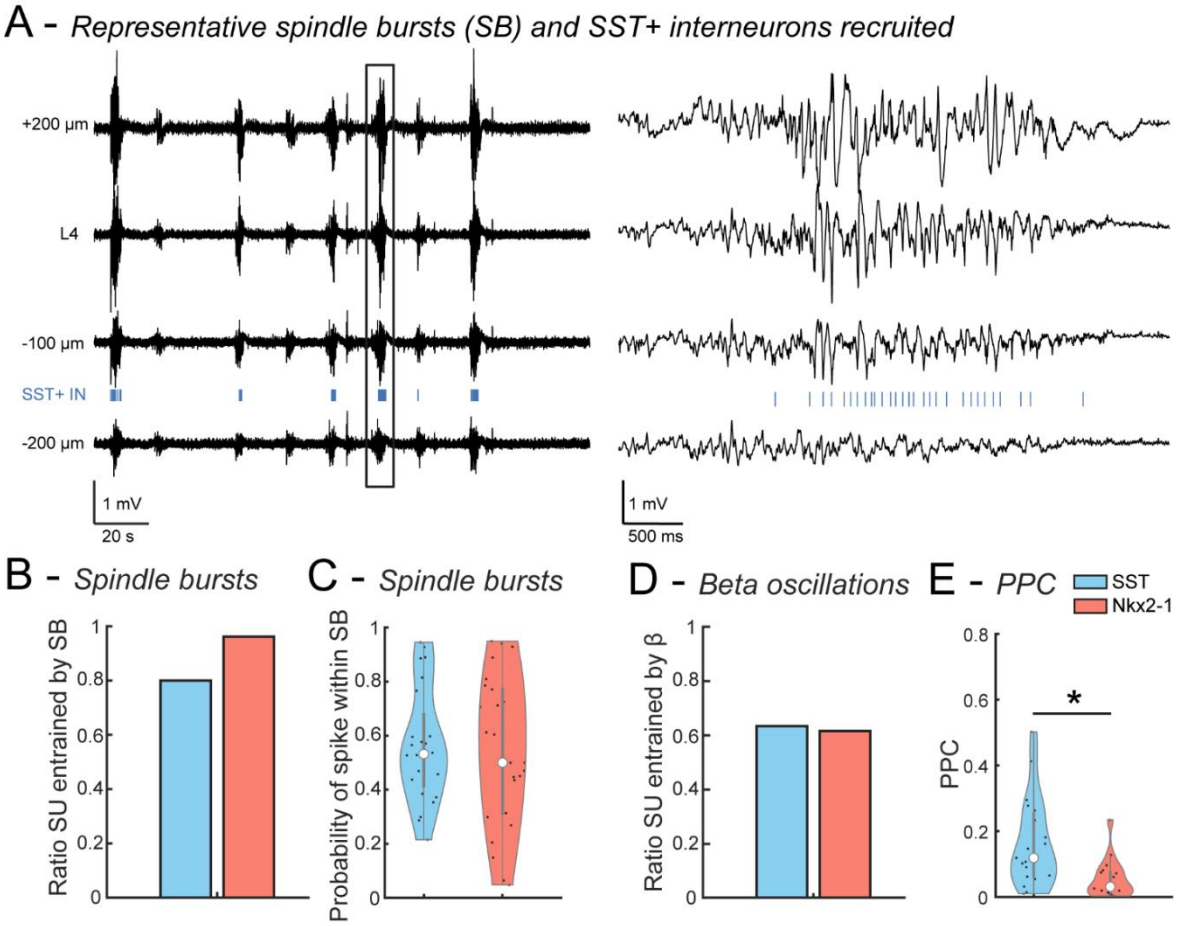


Fig. 4.8. Involvement of GABAergic interneurons in spontaneous activity in V1 during development. (A) Representative LFP voltage traces obtained from a P11 mouse recorded with multi-channel silicon probes showing spontaneous spindle bursts (enlarged traces of one event is shown on the right). Depth of LFP trace recordings is referred to L4. Blue lines show spike times for an optogenetically tagged SST+ single unit recorded from the same animal.
(B) Bar plot of the ratio of single units (SU) that are statistically significantly entrained by a spindle burst, for optogenetically tagged SST+ (blue, n = 30) or Nkx2-1+ (red) units before eye opening.
(C) Violin plot of probability of spikes occurring within SB over the total number of spikes fired throughout spontaneous activity recording (20 min) for SST+ and Nkx2-1+ SUs (colour-coding as in B).
(D) Bar plot of the ratio of SU that are statistically significantly entrained by beta (β) oscillations, for SST+ and Nkx2-1+ SUs (colour-coding as in B).
(E) Violin plot of pairwise phase-consistency (PPC) value between spike times and β oscillations for SST+ and Nkx2-1+ SUs (colour-coding as in B). There is a statistically significant effect of the factor "Cell *Layer*" (unpaired t-test: t (47) = -1.9, *p ≤ 0.05).

Nkx2-1 interneurons displayed similar responsivity patterns to SST+ single units. Before eye opening, only 4/26 tagged cells were characterised fast responsive with 16/26 characterised as slow responsive instead (**Fig. 4.10A** and quantification in **Fig. 4.10C**). Statistical analysis shows these ratios do not differ from ratio of responsive SST+ neurons (fast response, $X^2(1) = 1.1$, $p = 0.29$; slow response, $X^2(1) = 1.5$, $p = 0.22$). At P14-P18, nearly all (15/16) units significantly increased firing during the fast phase of the visual response and a comparable fraction was classified slow responsive (**Fig. 4.10B** and quantification in **Fig. 4.10C**). I also observed a developmental increase in the maximum firing rate for slow responsive cells (**Fig. 4.10E**), while I did not statistically analyse peak firing (**Fig. 4.10D**) and spike reliability (**Fig. 4.10F**) during the fast phase.

Overall, these results point to a similar role played by SST+ and Nkx2-1+ interneurons in the developing V1, the only notable difference being in the coupling strength to beta frequency oscillations. Both interneurons are similarly entrained by spindle bursts or beta oscillations, although SST+ cells are more strongly coupled to the latter. The large majority of these interneurons are classified as slow responsive upon visual stimulation, with only a small fraction increasing firing during the fast response. After eye opening, most of the interneurons are classified as fast responsive.

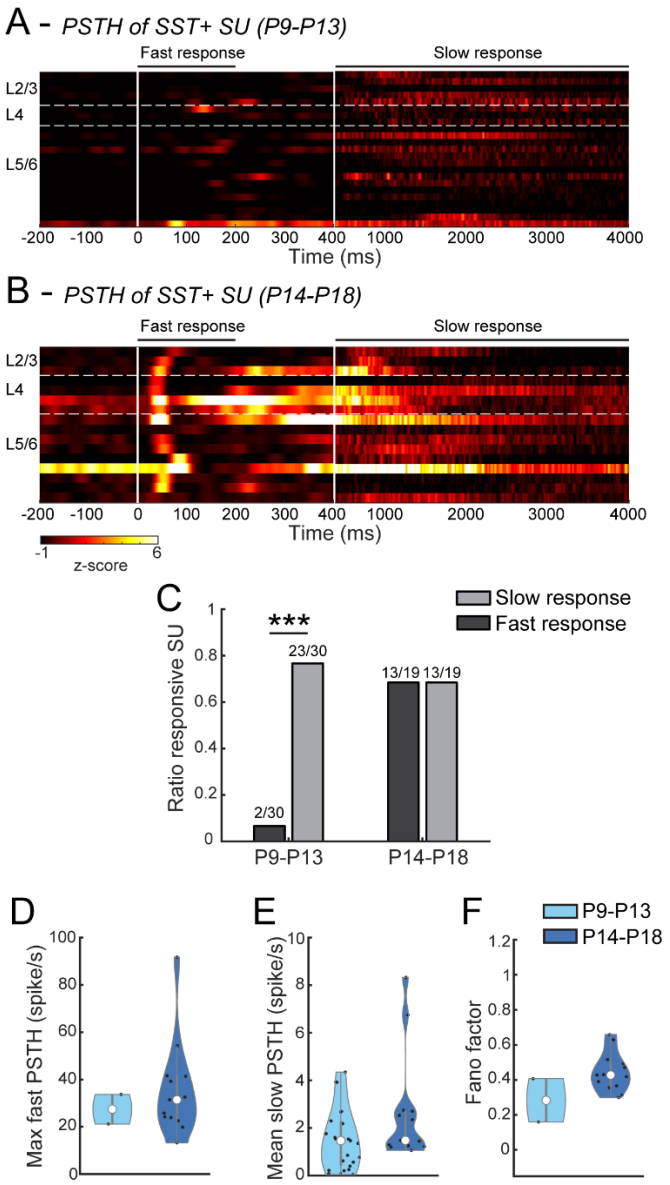


Fig. 4.9. Involvement of SST+ interneurons in sensory-evoked activity in V1 during development. (A) Heatmap showing the z-scored PSTH upon visual stimulation of all optogenetically tagged SST+ SUs recorded at P9-P13, classified as responsive to either the fast or slow phase of the visual response (shown by black lines). Onset of the visual stimulus is shown by solid vertical line (aligned on 0 s). Horizontal dashed lines demarcate SU recorded in different cortical layers; within layers, SU PSTHs are sorted by cortical depth. The first half of the plot shows PSTH at a smaller time resolution to highlight firing patterns during the fast response phase to the visual stimulus whereas the second half of the plot (right) shows PSTH at larger time resolution to show the full extent of the slow response phase.
(B) Same as in A but for SST+ SUs recorded between P14-P18.
(C) Bar plot of the ratio of SST+ SU classified as fast responsive (dark grey) or slow responsive (light grey) to visual stimulation, for units recorded at P9-P13 vs. P14-P18. There is a statistically significant difference in the proportion between responsive and non-responsive cells at P9-P13 (Chi-square test: X^2 (1) = 27.4, ***p ≤ 0.001).
(D) Violin plot of peak firing rate during the fast phase for SST+ SUs classified fast responsive to the visual stimulation at P9-P13 (light blue, n = 2) and P14-P18 (dark blue, n = 13).
(E) Violin plot of peak firing rate during the slow phase for SST+ SUs classified slow responsive to the visual stimulation at P9-P13 (light blue, n = 23) and P14-P18 (dark blue, n = 13).
(F) Violin plot of Fano factor during the fast response phase for SST+ SUs classified fast responsive to the visual stimulation at P9-P13 (light blue, n = 2) and P14-P18 (dark blue, n = 13).

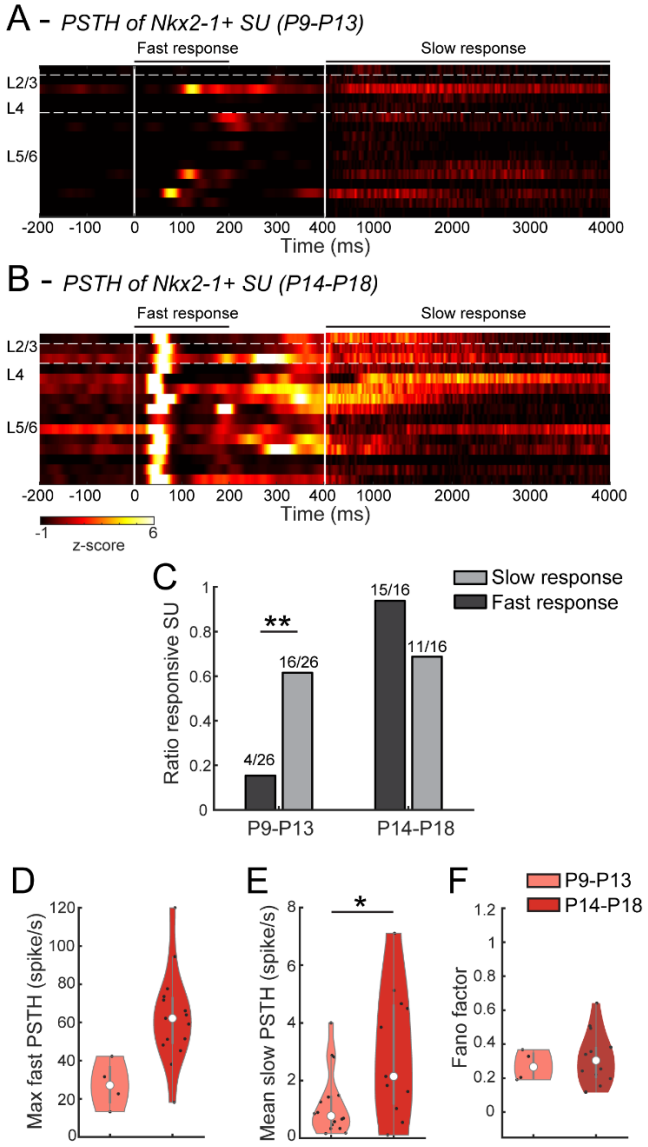


Fig. 4.10. Involvement of Nkx2-1+ interneurons in sensory-evoked activity in V1 during development. (A) Heatmap showing the z-scored PSTH upon visual stimulation of all optogenetically tagged Nkx2-1+ SUs recorded at P9-P13, classified as responsive to either the fast or slow phase of the visual response (shown by black lines). Onset of the visual stimulus is shown by solid vertical line (aligned on 0 s). Horizontal dashed lines demarcate SU recorded in different cortical layers; within layers, SU PSTHs are sorted by cortical depth. The first half of the plot shows PSTH at a smaller time resolution to highlight firing patterns during the fast response phase to the visual stimulus whereas the second half of the plot (right) shows PSTH at larger time resolution to show the full extent of the slow response phase.
(B) Same as in A but for Nkx2-1+ SUs recorded between P14-P18.
(C) Bar plot of the ratio of Nkx2-1+ SU classified as fast responsive (dark grey) or slow responsive (light grey) to visual stimulation, for units recorded at P9-P13 vs. P14-P18. There is a statistically significant difference in the proportion between responsive and non-responsive cells at P9-P13 (Chi-square test: X^2 (1) = 9.8, **p ≤ 0.01).
(D) Violin plot of peak firing rate during the fast phase for Nkx2-1+ SUs classified fast responsive to the visual stimulation at P9-P13 (light red, n = 4) and P14-P18 (dark red, n = 15).
(E) Violin plot of peak firing rate during the slow phase for Nkx2-1+ SUs classified slow responsive to the visual stimulation at P9-P13 (light red, n = 16) and P14-P18 (dark red, n = 11). There is a statistically significant difference between the two groups (unpaired t-test: t (25) = −2.7, *p ≤ 0.05).
(F) Violin plot of Fano factor during the fast response phase for Nkx2-1+ SUs classified fast responsive to the visual stimulation at P9-P13 (light red, n = 4) and P14-P18 (dark blue, n = 15).

4.5 – Impact of optogenetic activation of GABAergic interneurons on spontaneous and sensory-evoked activity in the developing V1

My experiments so far showed that, prior to eye opening, GABAergic interneurons are involved in spontaneous activity in V1 as well as in the slow phase of the sensory response. To better understand how these neurons contribute to emergent activity I used optogenetic and chemogenetic approaches to probe how activation or inhibition of interneurons subtypes affects spontaneous and evoked activity in the developing V1.

4.5.1 – Impact of optogenetic activation of GABAergic interneurons on spontaneous activity

To study how SST+ interneurons affects spontaneous activity of V1 SUs, I used *SSTCre; Ai32* transgenic animals and activated SST+ cells with blue light for 200 ms (**Fig. 4.11A**). Under these conditions, RS SUs recorded across layers reduced their firing frequency after optogenetic stimulation onset, both before (**Fig. 4.11B**) and after eye opening (**Fig. 4.11C**). Quantification of the ratio of SUs that are inhibited during the first 100 ms of the optogenetic stimulation of SST+ interneurons shows only a limited number of units that significantly reduced their firing frequency (**Fig. 4.11D**). I also observed a developmental increase in the ratio of inhibited units limited to L5/6 RS SUs, with stable values for granular and supragranular RS SUs being inhibited over development (**Fig. 4.11D**). Moreover, nearly 60% of the total FS units identified at later ages are significantly inhibited by the optogenetic stimulus. I also repeated this analysis for an optogenetic stimulus of shorter duration (50 ms), which has comparable effects to the 200 ms stimulus for all groups of SUs analysed (**Fig. 4.11E**). The low ratio of SUs significantly inhibited by activation of SST+ interneurons might be due to the low spontaneous firing frequency of SUs during development. For this reason, I quantified the change in firing frequency during the first 100 ms of the optogenetic stimulus (vs. baseline firing) for all RS and FS SUs across layers. In all groups of SUs investigated, I observed a statistically significant reduction in firing frequency (**Fig. 4.11F**),

suggesting widefield activation of SST+ interneurons lead to general network inhibition from the earliest developmental window investigated.

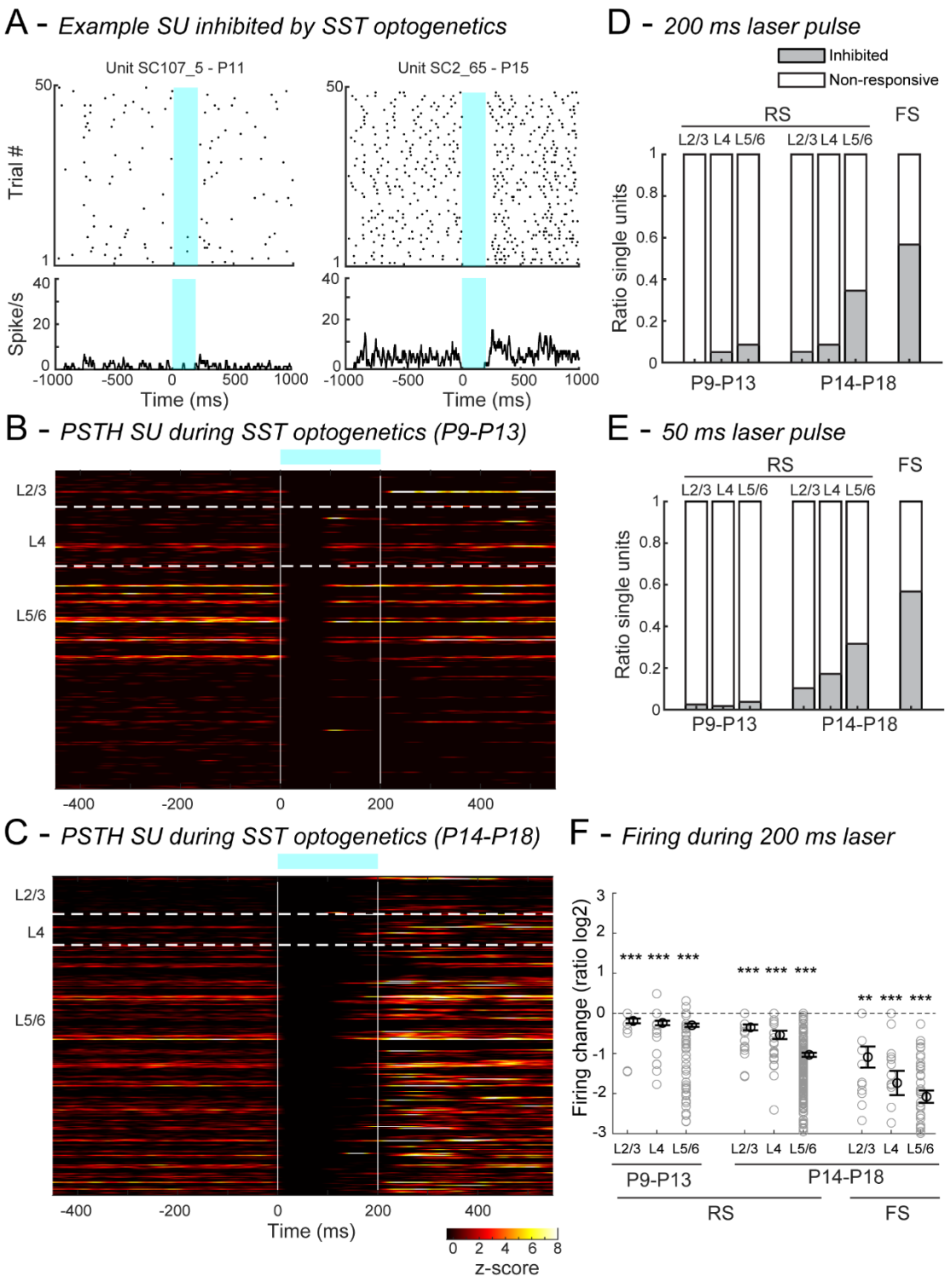


Fig. 4.11 (previous page). Impact of optogenetic activation of SST+ interneurons on spontaneous activity in the developing V1. (A) Representative raster plot (top) and PSTH (bottom) from two SUs (P11, left; P15, right) during optogenetic activation of SST+ interneurons expressing Channelrhodopsin-2 (ChR2) with blue light (200 ms, indicated by blue line, time 0 indicates optogenetic stimulation onset).
(B) Heatmap of z-scored PSTHs from all SUs recorded between P9-P13 during optogenetic activation of SST+ interneurons as in A. Vertical white lines indicate onset and offset of the optogenetic stimulus (also shown as blue light). Horizontal dashed lines show demarcation between cells recorded in different cortical layers; within layers, cells are sorted by cortical depth.
(C) Same as in B but for SUs recorded between P14 and P18.
(D) Bar plot of ratio of SUs in each layer and developmental window which are significantly inhibited by optogenetic activation of SST+ interneurons, through a 200 ms optogenetic stimulus. Results of the statistical tests are as follows: L2/3 RS at P9-P13 vs. L2/3 RS at P14-P18: Fisher exact test: $p = 0.23$; L4 RS at P9-P13 vs. L4 RS at P14-P18: Fisher exact test: $p = 0.66$; L5/6 RS at P9-P13 vs. L5/6 RS at P14-P18: Chi-squared test: $X^2 = 50.2$, $p \leq 0.001$.
(E) Same as in D but for an alternative optogenetic stimulus lasting 50 ms. Results of the statistical tests are as follows: L2/3 RS at P9-P13 vs. L2/3 RS at P14-P18: Fisher exact test: $p = 0.23$; L4 RS at P9-P13 vs. L4 RS at P14-P18: Fisher exact test: $p = 0.11$; L5/6 RS at P9-P13 vs. L5/6 RS at P14-P18: Chi-squared test: $X^2 = 12.1$, $p \leq 0.001$.
(F) Error bar (black, showing mean ± SEM) and scatter plot representing the change (log2 of the ratio) between SU firing frequency before the optogenetic stimulus (baseline) and firing frequency during the first 100 ms of the optogenetic stimulus used to activate SST+ interneurons. Results of the statistical tests are as follows: L2/3 RS at P9-P13, Wilcoxon signed rank test: ***$p \leq 0.001$; L4 RS at P9-P13, Wilcoxon signed rank test: $Z = 16.5$, ***$p \leq 0.001$; L5/6 RS at P9-P13, Wilcoxon signed rank test: $Z = 41$, ***$p \leq 0.001$; L2/3 RS at P14-P18, Wilcoxon signed rank test: ***$p \leq 0.001$; L4 RS at P14-P18: Wilcoxon signed rank test: ***$p \leq 0.001$, L5/6 RS at P14-P18: Wilcoxon signed rank test: ***$p \leq 0.001$; L2/3 FS at P14-P18: **$p \leq 0.01$; L4 FS at P14-P18: $t(13) = -5.7$, ***$p \leq 0.001$; L5/6 FS at P14-P18: $t(35) = -13.6$, ***$p \leq 0.001$.

Similar analysis was also performed in *Nkx2-1Cre; Ai32* transgenic animals, to understand the impact of Nkx2-1+ interneurons activation on spontaneous activity of V1 SUs (**Fig. 4.12A**). RS units recorded across layers reduced their firing frequency during optogenetic activation of Nkx2-1+ interneurons both before (**Fig. 4.12B**) and after (**Fig. 4.12C**) eye opening. By quantifying the ratio of significantly inhibited units by the 200 ms optogenetic stimulus, I observed again a generally low ratio of inhibited SUs, with a developmental increase for L4 and L5/6 units (**Fig. 4.12D**). In contrast to optogenetic activation of SST+ interneurons, a 50 ms pulse of blue light used to activate Nkx2-1+ interneurons led to smaller ratio of significantly inhibited SUs (**Fig. 4.12E**). Despite this, RS and FS SUs in every cortical layer significantly reduced their firing rate during the first 100 ms of the optogenetic stimulation of Nkx2-1+ interneurons (**Fig. 4.12F**).

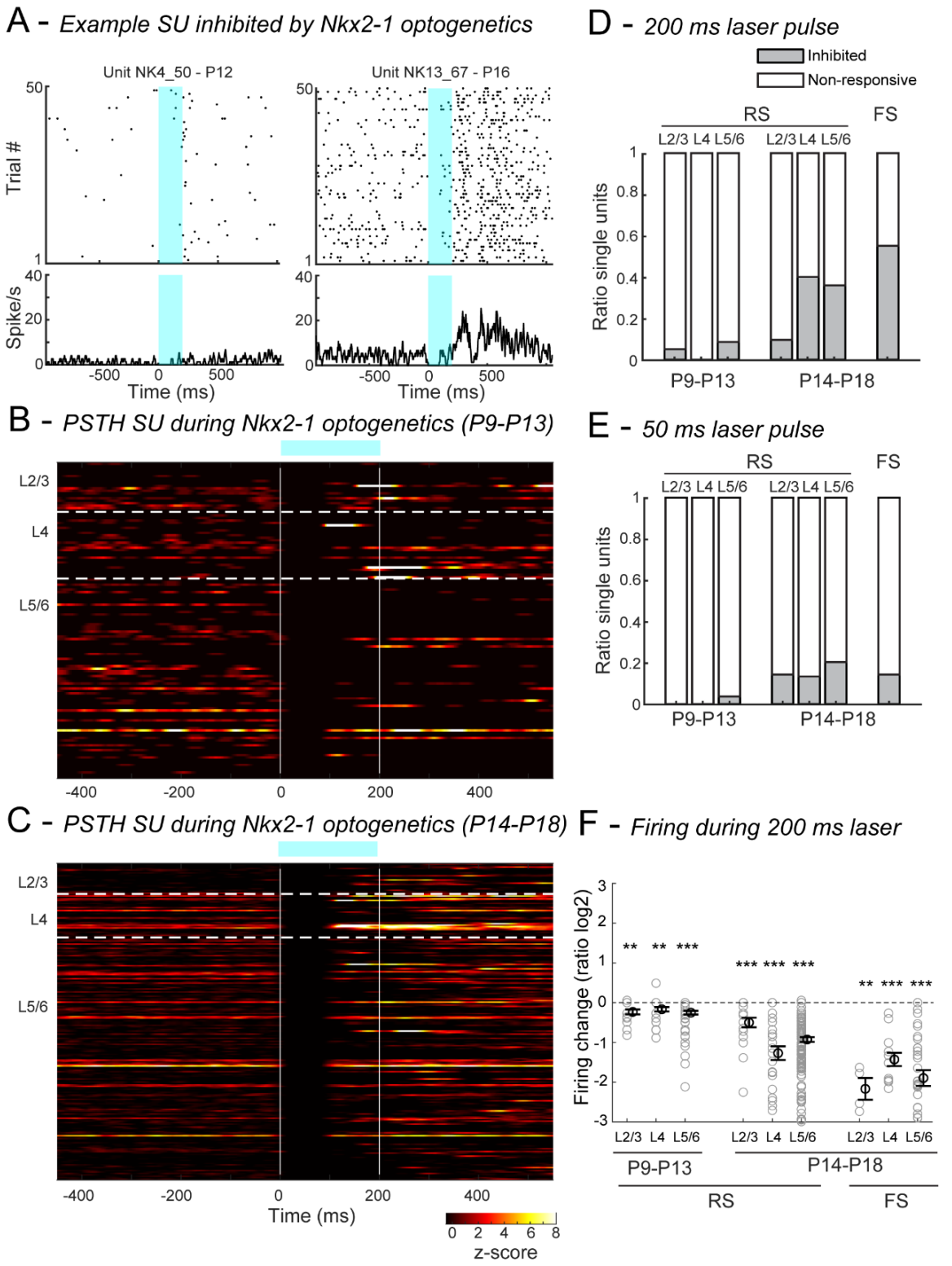


Fig. 4.12. Impact of optogenetic activation of Nkx2-1+ interneurons on spontaneous activity in the developing V1. (A) Representative raster plot (top) and PSTH (bottom) from two SUs (P12, left; P16, right) during optogenetic activation of Nkx2-1+ interneurons expressing ChR2 with blue light (200 ms, indicated by blue line, time 0 indicates optogenetic stimulation onset).
(B) Heatmap of z-scored PSTHs from all SUs recorded between P9-P13 during optogenetic activation of Nkx2-1+ interneurons as in A. Vertical white lines indicate onset and offset of the optogenetic stimulus (also shown as blue light). Horizontal dashed lines show demarcation between cells recorded in different cortical layers; within layers, cells are sorted by cortical depth.

Fig. 4.12 (continue). (C) Same as in B but for SUs recorded between P14 and P18.
(D) Bar plot of ratio of SUs in each layer and developmental window which are significantly inhibited by optogenetic activation of Nkx2-1+ interneurons, through a 200 ms optogenetic stimulus. Results of the statistical tests are as follows: L2/3 RS at P9-P13 vs. L2/3 RS at P14-P18: Fisher exact test: $p = 1.0$; L4 RS at P9-P13 vs. L4 RS at P14-P18: Fisher exact test: $p \leq 0.001$; L5/6 RS at P9-P13 vs. L5/6 RS at P14-P18: Fisher exact test: $X^2 = 20.9$, $p \leq 0.001$.
(E) Same as in D but for an alternative optogenetic stimulus lasting 50 ms. Results of the statistical tests are as follows: L2/3 RS at P9-P13 vs. L2/3 RS at P14-P18: Fisher exact test: $p = 0.23$; L4 RS at P9-P13 vs. L4 RS at P14-P18: Fisher exact test: $p = 0.11$; L5/6 RS at P9-P13 vs. L5/6 RS at P14-P18: Fisher exact test: $X^2 = 12.1$, $p \leq 0.001$.
(F) Error bar (black, showing mean ± SEM) and scatter plot representing the change (log2 of the ratio) between SU firing frequency before the optogenetic stimulus (baseline) and firing frequency during the first 100 ms of the optogenetic stimulus used to activate Nkx2-1+ interneurons. Results of the statistical tests are as follows: L2/3 RS at P9-P13, Wilcoxon signed rank test: ***$p \leq 0.001$; L4 RS at P9-P13, Wilcoxon signed rank test: $Z = 16.5$, ***$p \leq 0.001$; L5/6 RS at P9-P13, Wilcoxon signed rank test: $Z = 41$, ***$p \leq 0.001$; L2/3 RS at P14-P18, Wilcoxon signed rank test: ***$p \leq 0.001$; L4 RS at P14-P18: Wilcoxon signed rank test: ***$p \leq 0.001$, L5/6 RS at P14-P18: Wilcoxon signed rank test: ***$p \leq 0.001$; L2/3 FS at P14-P18: **$p \leq 0.01$; L4 FS at P14-P18: $t(13) = -5.7$, ***$p \leq 0.001$; L5/6 FS at P14-P18: $t(35) = -13.6$, ***$p \leq 0.001$.

Fig. 4.11C and **Fig. 4.12C** also suggest that a proportion of SUs increase firing rate (compared with baseline firing rate) after optogenetic stimulation offset, after eye opening. I quantified the ratio of rebound-excited SUs during optogenetic activation of SST+ interneurons (**Fig. 4.13A**), showing that indeed a small fraction of units significantly increased firing rate in the 100 ms immediately following the end of optogenetic stimulation. Quantification of firing change for all SUs showed distinct effects across layers and development (**Fig. 4.13B**): L5/6 RS SU before eye opening significantly reduced firing rate, suggesting the inhibitory effect of SST+ interneurons is maintained beyond the time of the optogenetic stimulus. Rebound-excited SUs are observed after eye opening, particularly in L2/3 and L4 for both RS and FS units. A fraction of SUs was also classified as rebound-excited after optogenetic activation of Nkx2-1+ interneurons (**Fig. 4.13C**). At population level, quantification of firing change showed an overall reduction in firing rate for SUs in L5/6 both before and after eye opening, and general rebound-excitation limited to FS units in L2/3 after eye opening (**Fig. 4.13D**).

This data suggests both SST+ and Nkx2-1+ interneuron subtypes have an inhibitory effect on other SUs in the developing V1, even before eye opening. After eye opening, activation of SST+ interneurons also lead to rebound excitation in granular and supragranular RS and

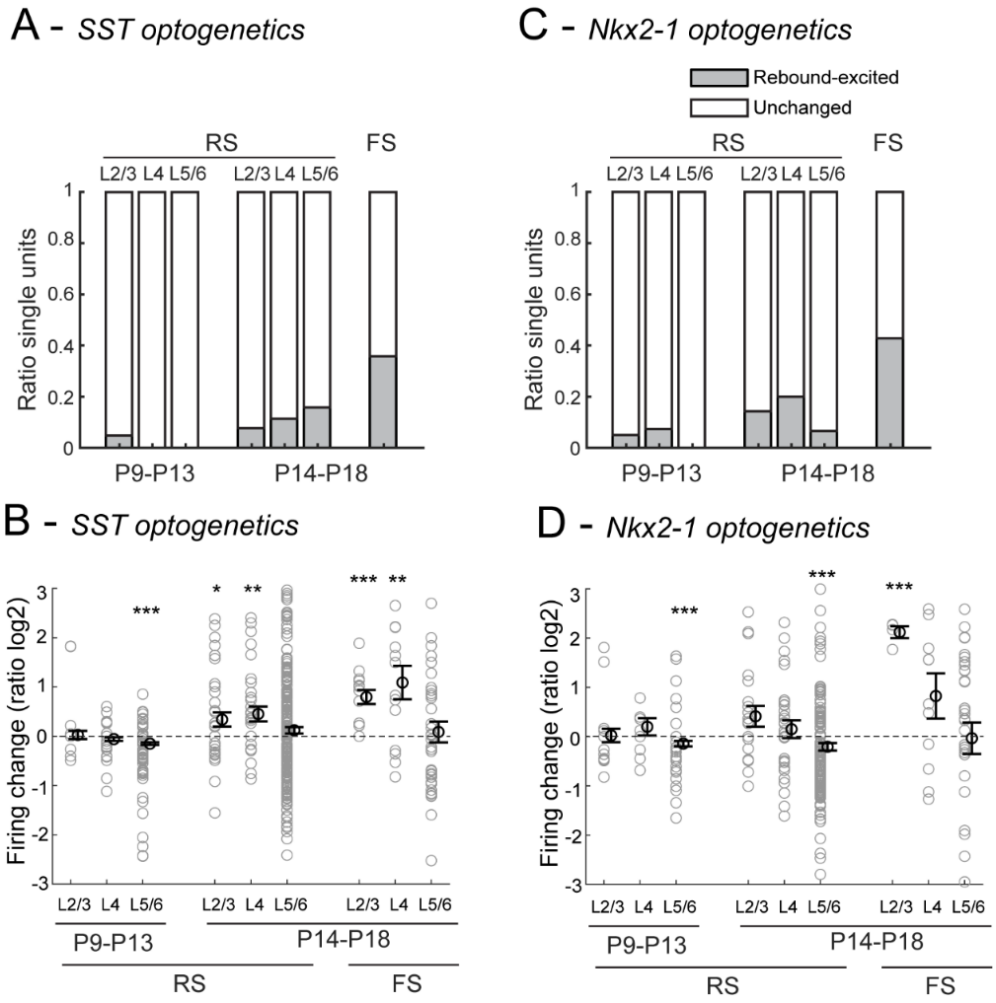


Fig. 4.13. Excitatory effects during rebound from optogenetic activation of GABAergic interneurons. (A) Bar plot of the ratio of SUs in different layers and at different developmental windows (L2/3 RS at P9-P13, n = 41; L4 RS at P9-P13, n = ; L5/6 RS at P9-P13, n = ; L2/3 RS at P14-P18, n = 39; L4 RS at P14-P18; L5/6 RS at P14-P18; FS at P14-P18, n =),which significantly increase firing rate in the 100 ms immediately following the offset of the optogenetic stimulation used to activate SST+ interneurons (rebound-excited). Results of the statistical tests are as follows: L2/3 RS at P9-P13 vs. L2/3 RS at P14-P18: $X^2 = 0.27$, p = 0.60; L4 RS at P9-P13 vs. L4 RS at P14-P18: Fisher exact test: p = 0.11; L5/6 RS at P9-P13 vs. L5/6 RS at P14-P18: Fisher exact test: $X^2 = 12.1$, p ≤ 0.001.

(B) Error bar (black lines, mean ± SEM) and scatter plot of the change (log2 of the ratio) in baseline firing rate vs. firing rate in the 100 ms immediately following the optogenetic activation of SST+ interneurons, for all RS and FS SUs in different layers and at different developmental window. Results of the statistical tests are as follows: L2/3 RS at P9-P13, Wilcoxon signed rank test: p = 0.23; L4 RS at P9-P13, Wilcoxon signed rank test: Z = -1.0, p ≤ 0.29; L5/6 RS at P9-P13, Wilcoxon signed rank test: Z = -5.7, ***p ≤ 0.001; L2/3 RS at P14-P18, Wilcoxon signed rank test: Z = 1.9, *p ≤ 0.05; L4 RS at P14-P18: Wilcoxon signed rank test: Z = 2.7, **p ≤ 0.006, L5/6 RS at P14-P18: Wilcoxon signed rank test: Z = 0.84, p = 0.39; L2/3 FS at P14-P18: One-sample t-test: t(13) = 5.5, ***p ≤ 0.001; L4 FS at P14-P18, One-sample t-test: t(13) = 3.2, **p ≤ 0.007; L5/6 FS at P14-P18, One-sample t-test: t(35) = 0.4, p ≤ 0.68.

(C) Same as A but for optogenetic activation of Nkx2-1. interneurons.

(D) Same as B but for optogenetic activation of Nkx2-1+ interneurons. Results of the statistical tests are as follows: L2/3 RS at P9-P13, Wilcoxon signed rank test: p = 0.45; L4 RS at P9-P13, Wilcoxon signed rank test: p ≤ 0.79; L5/6 RS at P9-P13, Wilcoxon signed rank test: Z = -3.0, **p ≤ 0.002; L2/3 RS at P14-P18, One-sample t-test: t(20) = 1.9, p ≤ 0.06; L4 RS at P14-P18: One-sample t-test: t(29) = 0.84, p ≤ 0.40, **p ≤ 0.006, L5/6 RS at P14-P18: Wilcoxon signed rank test: Z = -3.6, ***p ≤ 0.001; L2/3 FS at P14-P18: One-sample t-test: t(3) = 17.7, ***p ≤ 0.001; L4 FS at P14-P18, One-sample t-test: t(12) = 1.8, p ≤ 0.09; L5/6 FS at P14-P18, Wilcoxon signed rank test: Z = 0.4, p = 0.68.

FS SUs. This result cannot be simply explained by intrinsic electrophysiological features of rebound-excited neurons, since rebound intrinsic bursting cells were only found in infragranular layers of V1 (see **Fig. 3.4**), thus pointing to network effects.

4.5.2 – Impact of optogenetic activation of GABAergic interneurons on sensory-evoked activity

To study the impact of activating GABAergic interneurons on sensory-evoked activity in the developing V1, I performed experiments where I combined stimulation of the visual system with white LED light with optogenetic activation of either SST+ or Nkx2-1+ interneurons. Optogenetic activation of SST+ interneurons suppressed or reduced the fast response to the visual stimulation in SUs recorded before and after eye opening (**Fig. 4.14A**). In trials where visual stimulation was combined with optogenetic activation of SST+ interneurons, peak firing rate during the fast response was reduced for all classes of responsive SUs in every layer, with the exception of L2/3 RS SUs at P9-P13 (**Fig. 4.14B**). In addition, peak firing during the slow phase of the visual response was reduced, although to a smaller extent, but only for RS units before eye opening and FS units post-eye opening (**Fig. 4.14C**). I also observed a decrease in spike reliability during the fast response in L4-6 RS units after eye opening and in L5/6 RS units before eye opening (**Fig. 4.14D**).

Fig. 4.14 (next page). Impact of optogenetic activation of SST+ interneurons on visual-evoked activity. (A) Representative raster plot (upper) and corresponding PSTH (lower) for two RS SU recorded at P12 (left) and P16 (right) upon visual stimulation with white LED light (yellow line) either alone or combined with optogenetic activation of SST+ interneurons (blue line) in *SSTCre; Ai32* animals.
(B) Error bar plot (black, mean ± standard error of the mean, SEM) and scatter plot (grey) of the peak firing rate during the fast visual response for responsive RS single units in L2/3 (first column), L4 (second column), and L5/6 (third column) as well as responsive FS SUs (last column) comparing trials with visual stimulation only (control, Ctrl) vs. trial with visual stimulation plus optogenetic stimulation of SST+ interneurons (Opto), grouped by developmental window. Results of the statistical test are as follows: L2/3 RS at P9-P13, Paired t-test: $t(5) = 1.9$, $p = 0.11$; L2/3 RS at P14-P18, Paired t-test: $t(10) = 3.5$, $^{**}p = 0.005$; L4 RS at P9-P13, Wilcoxon signed rank test: $Z = 2.8$, $^{**}p = 0.005$; L4 RS at P14-P18, Paired t-test: $t(12) = 3.2$, $^{**}p = 0.007$; L5/6 RS at P9-P13, Wilcoxon signed rank test: $Z = 4.1$, $^{***}p \leq 0.001$; L5/6 RS at P14-P18, Wilcoxon signed rank test: $Z = 7.4$, $^{***}p \leq 0.001$; FS at P14-P18, Wilcoxon signed rank test: $Z = 5.8$, $^{***}p \leq 0.001$.

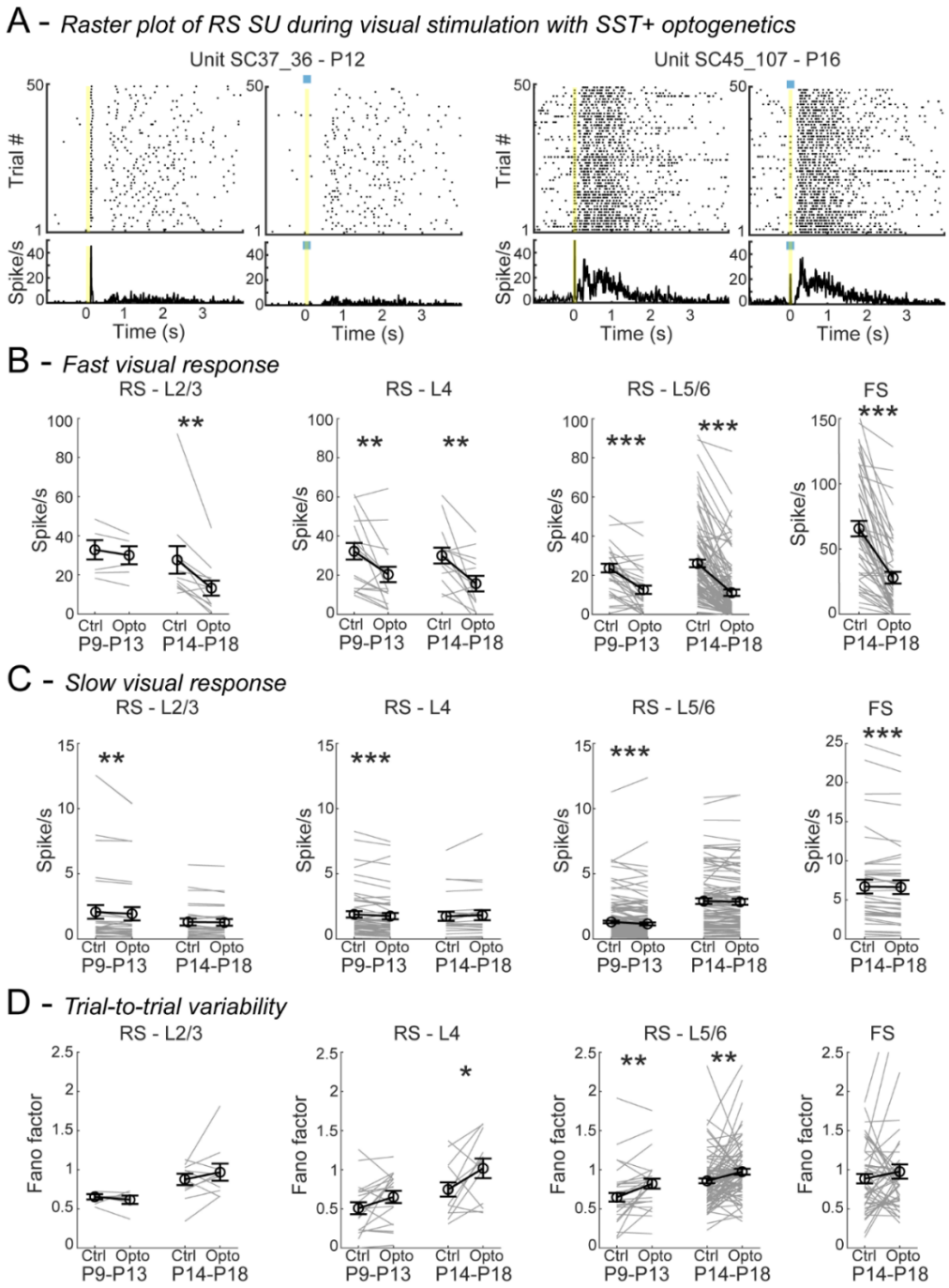
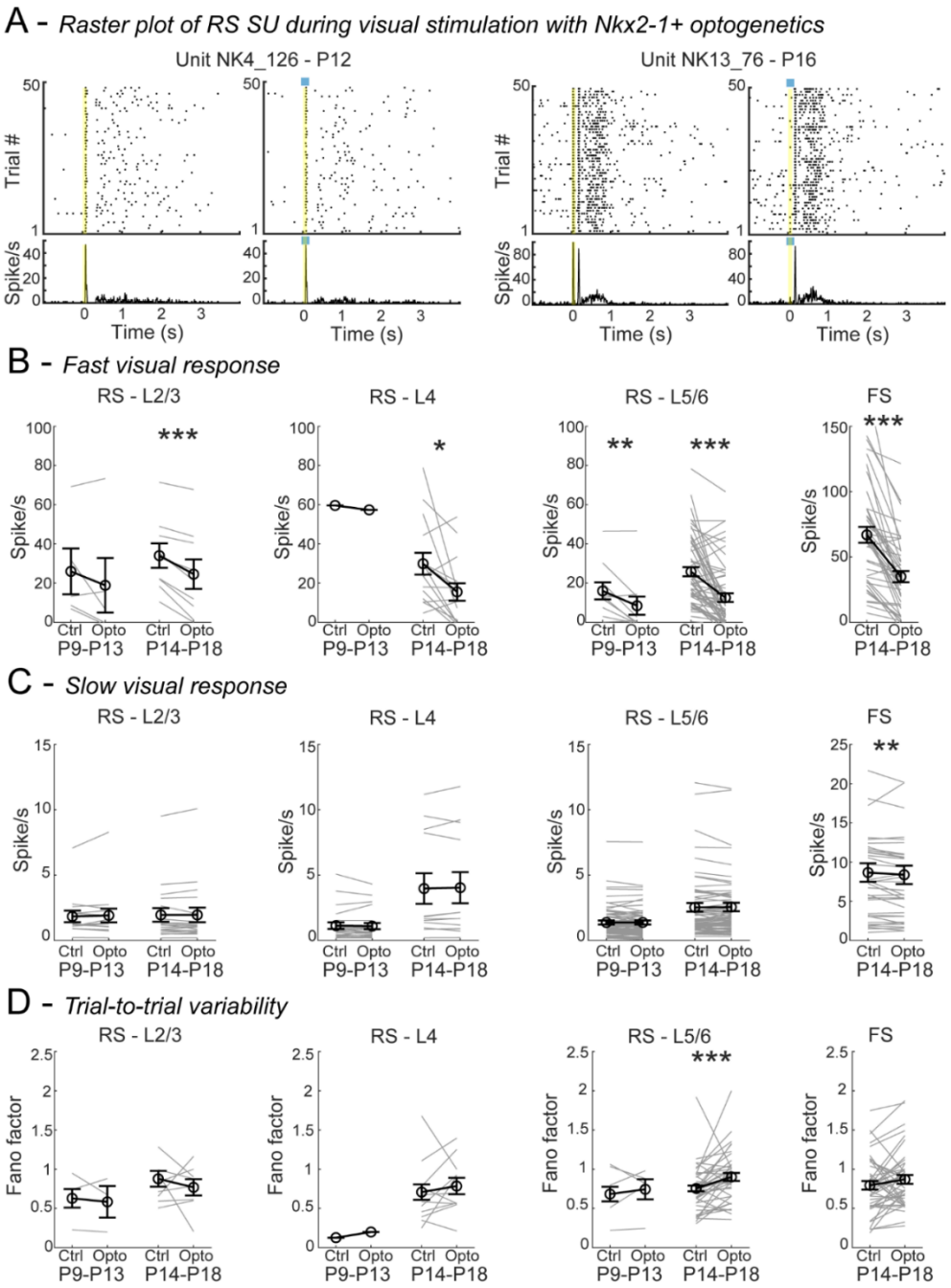


Fig. 4.14 (continue). (C) Same as in B, but for peak firing during the slow phase of the visual response, for SU responsive during this phase. Results of the statistical test are as follows: L2/3 RS at P9-P13, Wilcoxon signed rank test: Z = 3.2, **p = 0.001; L2/3 RS at P14-P18, Wilcoxon signed rank test: Z = 0.8, p = 0.44; L4 RS at P9-P13, Wilcoxon signed rank test: Z = 3.6, ***p ≤ 0.001; L4 RS at P14-P18, Wilcoxon signed rank test: Z = −0.7, p =0.46; L5/6 RS at P9-P13, Wilcoxon signed rank test: Z = 4.2, ***p ≤ 0.001; L5/6 RS at P14-P18, Wilcoxon signed rank test: Z = 1.8, p =0.07; FS at P14-P18, Wilcoxon signed rank test: Z = 3.7, ***p ≤ 0.001.
(D) Same as in B, but for Fano factor of SU spiking during the fast phase of the visual response, for SU responsive during this phase. Results of the statistical test are as follows: L2/3 RS at P9-P13, Paired t-test: t(5) = 0.3, p = 0.76; L2/3 RS at P14-P18, Paired t-test: t(9) = −1.2, p = 0.25; L4 RS at P9-P13, Paired t-test: t(17) = −1.9, p = 0.07; L4 RS at P14-P18, Paired t-test: t(11) = −2.1, *p = 0.05; L5/6 RS at P9-P13, Wilcoxon signed rank test: Z = −2.6, **p = 0.008; L5/6 RS at P14-P18, Wilcoxon signed rank test: Z = −2.9, **p = 0.003; FS at P14-P18, Paired t-test: t(45) = −1.2, p = 0.22.

Optogenetic activation of Nkx2-1+ interneurons instead led to a greater reduction in firing rate during the fast response phase only after eye opening (**Fig. 4.15A**), with RS and FS units throughout layers significantly reducing their firing rate (**Fig. 4.15B**). Additionally, no impact of optogenetic activation on the slow phase of the visual response was observed for RS units, with only a small reduction found for FS SUs after eye opening (**Fig. 4.15C**). Finally, activation of Nkx2-1+ interneurons led to a reduction in spike reliability only for L5/6 RS units after eye opening (**Fig. 4.15D**).

Overall, these results points to SST+ interneurons as providing more inhibitory control in the V1 cortical network before eye opening, when they affect both fast and slow phases of the visual response of RS SUs. After eye opening, both SST+ and Nkx2-1+ interneurons activation led to a reduction in firing during the fast phase of the visual response only, while SST+ interneurons alone also reduce spike reliability of L4 RS SUs.

Fig. 4.15 (next page). Impact of optogenetic activation of Nkx2-1+ interneurons on visual-evoked activity. (A) Representative raster plot (upper) and corresponding PSTH (lower) for two RS SU recorded at P12 (left) and P16 (right) upon visual stimulation with white LED light (yellow line) either alone or combined with optogenetic activation of Nkx2-1+ interneurons (blue line) in *Nkx2-1Cre; Ai32* animals.
(B) Error bar plot (black, mean ± standard error of the mean, SEM) and scatter plot (grey) of the peak firing rate during the fast visual response for responsive RS single units in L2/3 (first column), L4 (second column), and L5/6 (third column) as well as responsive FS SUs (last column) comparing trials with visual stimulation only (control, Ctrl) vs. trial with visual stimulation plus optogenetic stimulation of Nkx2-1+ interneurons (Opto), grouped by developmental window. Results of the statistical test are as follows: L2/3 RS at P9-P13, Paired t-test: $t(4) = 1.3$, $p = 0.24$; L2/3 RS at P14-P18, Paired t-test: $t(8) = 5.7$, ***$p \leq 0.001$; L4 RS at P9-P13, not tested; L4 RS at P14-P18, Paired t-test: $t(14) = 2.7$, *$p = 0.017$; L5/6 RS at P9-P13, Paired t-test: $t(9) = 3.2$, **$p = 0.01$; L5/6 RS at P14-P18, Wilcoxon signed rank test: $Z = 5.0$, ***$p \leq 0.001$; FS at P14-P18, Wilcoxon signed rank test: $Z = 5.5$, ***$p \leq 0.001$.
(C) Same as in B, but for peak firing during the slow phase of the visual response, for SU responsive during this phase. Results of the statistical test are as follows: L2/3 RS at P9-P13, Wilcoxon signed rank test: $Z = 0.1$, $p = 0.90$; L2/3 RS at P14-P18, Wilcoxon signed rank test: $Z = -0.2$, $p = 0.86$; L4 RS at P9-P13, Wilcoxon signed rank test: $Z = 1.1$, $p = 0.28$; L4 RS at P14-P18, Wilcoxon signed rank test: $Z = -0.1$, $p = 0.52$; L5/6 RS at P9-P13, Wilcoxon signed rank test: $Z = 0.8$, $p = 0.42$; L5/6 RS at P14-P18, Wilcoxon signed rank test: $Z = -1.0$, $p = 0.30$; FS at P14-P18, Wilcoxon signed rank test: $Z = 2.5$, **$p = 0.01$.
(D) Same as in B, but for Fano factor of SU spiking during the fast phase of the visual response, for SU responsive during this phase. Results of the statistical test are as follows: L2/3 RS at P9-P13, Paired t-test: $t(2) = 0.46$, $p = 0.69$; L2/3 RS at P14-P18, Paired t-test: $t(7) = 0.35$, $p = 0.73$; L4 RS at P9-P13, not tested; L4 RS at P14-P18, Paired t-test: $t(10) = -0.87$, $p = 0.41$; L5/6 RS at P9-P13, Paired t-test: $t(4) = -0.19$, $p = 0.85$; L5/6 RS at P14-P18, Wilcoxon signed rank test: $Z = -3.3$, ***$p \leq 0.001$; FS at P14-P18, Paired t-test: $t(42) = -1.5$, $p = 0.32$.



4.6 – Impact of chemogenetic inhibition of SST+ interneurons on *in vivo* activity

In the last section of this ***Chapter***, I exploited a chemogenetic approach to acutely silence SSTCre-expressing interneurons in the developing V1 to gain insight on the impact of this intervention on spontaneous and sensory-evoked activity. At birth, *SSTCre; Ai9* animals were injected with a viral vector to conditionally express the inhibitory K-opioid receptor (KORD) in SSTCre+ interneurons. As a control, some mice were injected with a virus

expressing GFP only. I initially used immunohistochemistry to quantify the percentage of SSTCre interneurons infected by the virus in P7-P18 mice (**Fig. 4.15A, B**). The distribution of tdTomato+ cells is in line with our characterisation shown in ***Chapter 3*** (**Fig. 4.15C**, red). Further, the majority of these cells were also successfully infected with the virus containing KORD. Double positive cells could be found in higher percentage in deeper cortical layers (**Fig. 4.15C**, green), where SSTCre+ interneurons are mostly localised; the data however, points to a high variability in the proportion of SSTCre+ cells infected with KORD between animals. Overall (n = 6 mice), 57% ± 7% of SSTCre+ cells were also infected with KORD, whereas 67% ± 6% of KORD-expressing cells were also SSTCre+.

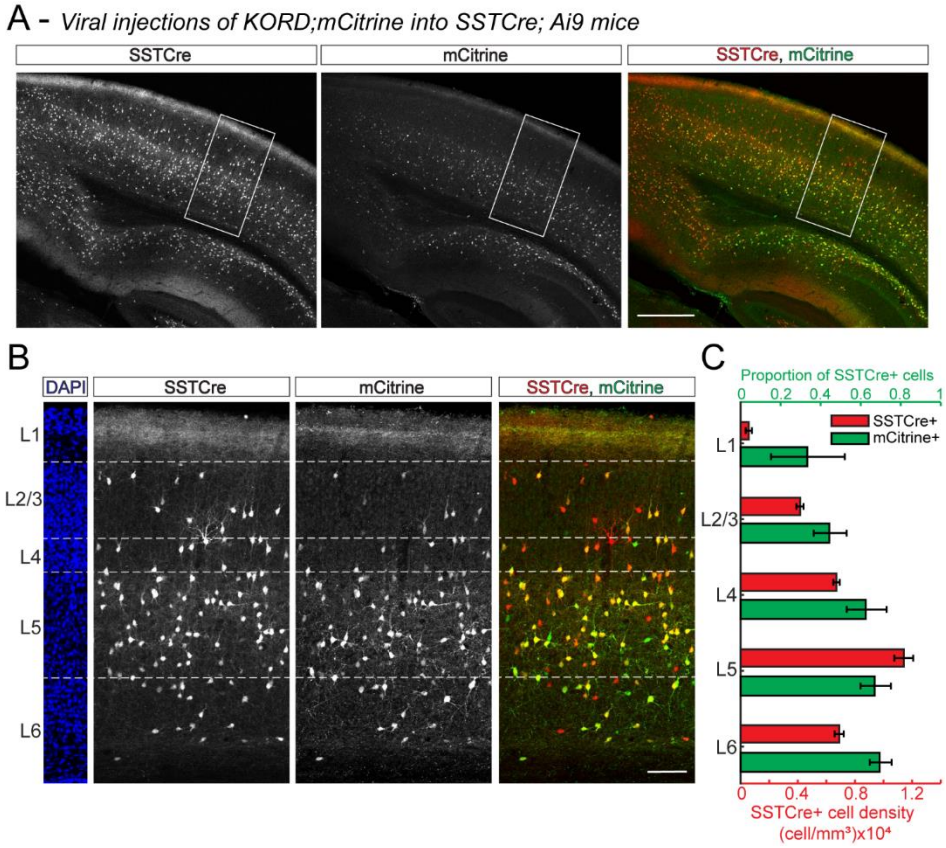


Fig. 4.16. Immunohistochemical characterisation of viral injections of KORD-mCitrine into *SSTCre; Ai9* transgenic mice. (A) Representative confocal image (4X magnification) of a V1 slice (50 µm thickness) obtained from a P11 *SSTCre; Ai9* transgenic mouse that was injected (at birth, P0) with a viral vector to conditionally express the chemogenetic receptor KORD tagged with mCitrine. Slice was stained with an antibody against tdTomato (to label SSTCre+ cells, red in the merge image on the right) and an antibody against GFP (to label mCitrine+ cells infected with KORD, green in the merge image). Scale bar = 500 µm.
(B) Higher magnification (10X) confocal image showing the area in the white box in A. Horizontal dashed white lines indicate approximate layer boundaries. Scale bar = 100 µm.
(C) Bar plot of SSTCre+ cell density (red) and proportion of SSTCre+ cells that also express GFP (green) in different cortical layer (average of 6 animals). Error bars show the SEM.

4.6.1 – Impact of chemogenetic inhibition of SST+ interneurons on spontaneous and sensory-evoked activity in the developing V1

Mice expressing either KORD or GFP were then used for *in vivo* electrophysiological recordings to compare spontaneous and sensory-evoked activity before and after activation of the designer receptor exclusively activated by designer drug (DREADD) with Salvinorin B (SalB). Analysis of L4 MUA upon visual stimulation with white LED light showed apparent lack of effect of SalB application, in mice recorded before and after eye opening (**Fig. 4.17A, B**). I quantified peak L4 MUA in the fast (**Fig. 4.17C**) and slow (**Fig. 4.17D**) phases of the visual response and did not observe any change in KORD injected animals vs. animals injected with GFP. Quantification of L4 spontaneous MUA showed a general increase in firing rate after application of SalB in mice recorded before eye opening, that however, did not reach statistical significance in the comparison with activity recorded from animals injected with GFP and treated with SalB (**Fig. 4.17E**). Chemogenetic inhibition of SST+ interneurons also did not affect spontaneous V1 activity, when analysing average power in the beta frequency (**Fig. 4.17F**), spindle burst duration (**Fig. 4.17G**), and spindle burst occurrence (**Fig. 4.17H**).

Fig. 4.17 (next page). Impact of chemogenetic inhibition of SST+ interneurons on V1 spontaneous activity and MUA. (A) Representative L4 multi-unit activity (MUA) for one animal recorded between P9 and P13 during visual stimulation alone (Control) and during visual stimulation after administration of Salvinorin B (SalB) to inhibit SST+ interneurons expressing the inhibitory chemogenetic receptor KORD.
(B) Same as in (A) but for one animal recorded at P14-P18.
(C) Errorbar plot (solid black or red line) and scatter plot of peak L4 MUA during the fast phase of the visual response for animals recorded at P9-P13 (left) or P14-P18 (right) in animals injected with a virus harbouring the KORD receptor (black) or with a control GFP virus (red). The y axis indicate change between data recorded in control condition prior to the administration of SalB and data recorded from visual stimulation performed after administration of SalB. Results of the statistical test are as follows: KORD vs. GFP at P9-P13, two sample t-test: $t(7) = -1.7$, $p = 0.13$; KORD vs. GFP at P14-P18, two sample t-test: $t(6) = 0.45$, $p = 0.67$.
(D) Same as in (C) but for peak L4 MUA during the slow phase of the visual response. Results of the statistical test are as follows: KORD vs. GFP at P9-P13, two sample t-test: $t(7) = -0.9$, $p = 0.36$; KORD vs. GFP at P14-P18, two sample t-test: $t(6) = 0.28$, $p = 0.78$.
(E) Same as in (C) but for average spontaneous L4 MUA. Results of the statistical test are as follows: KORD vs. GFP at P9-P13, two sample t-test: $t(7) = 1.6$, $p = 0.16$; KORD vs. GFP at P14-P18, two sample t-test: $t(6) = -1.6$, $p = 0.16$.
(F) Same as in (C) but for power in the beta frequency during recording of spontaneous activity. Results of the statistical test are as follows: KORD vs. GFP at P9-P13, two sample t-test: $t(8) = 0.24$, $p = 0.81$; KORD vs. GFP at P14-P18, two sample t-test: $t(6) = 0.23$, $p = 0.82$.

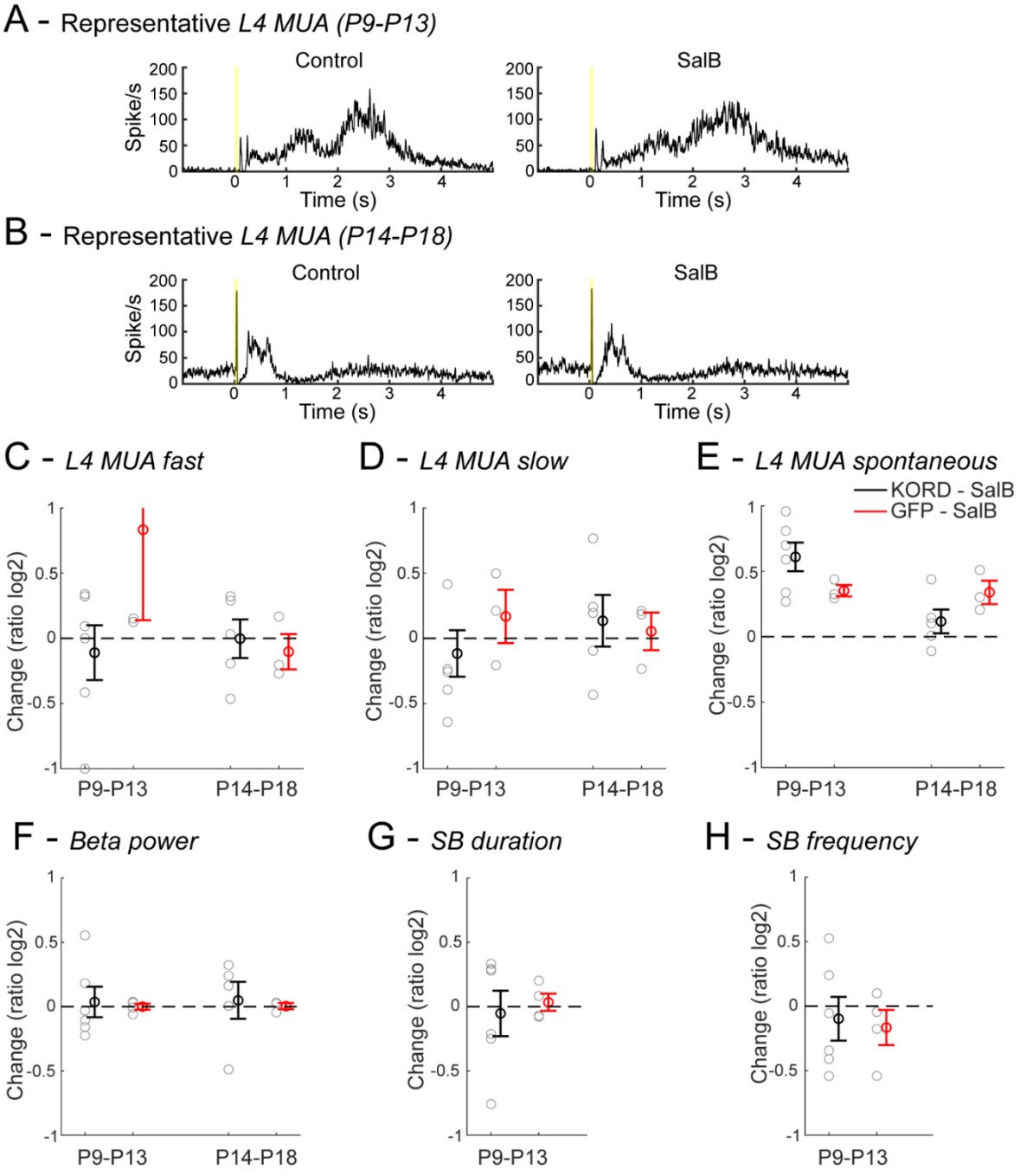


Fig. 4.17 (continue). (G) Same as in (C) but for average spindle burst (SB) event duration. Results of the statistical test are as follows: KORD vs. GFP at P9-P13, two sample t-test: t(8) = −0.38, p = 0.71.
(H) Same as in (C) but for SB event frequency of occurrence. Results of the statistical test are as follows: KORD vs. GFP at P9-P13, two sample t-test: t(8) = 0.28, p = 0.78.

I next investigated the impact of chemogenetic inhibition of SSTCre+ interneurons on SU activity in the developing V1. Analysis of raster plots obtained during visual stimulation showed no effects of SalB application on the fast and slow phase of the visual responses,

but only an apparent increase in spontaneous firing rate for units recorded before eye opening (**Fig. 4.18A**). Indeed, I did not observe any change in the ratio of responsive SUs (**Fig. 4.18B**), as well as in the peak firing of responsive SUs during the fast (**Fig. 4.18C**) and slow (**Fig. 4.18D**) phases of the visual response and reliability of spiking (**Fig. 4.18G**). No change in peak firing rate was observed when splitting SUs recorded after eye opening in FS and RS units (**Fig. 4.18E**). I did, however, observe an increase in spontaneous firing rate of SUs after application of SalB to chemogenetically inhibit SST+ interneurons, which is significantly different than change in firing rate recorded in animals injected with GFP (**Fig. 4.18F**). Chemogenetic inhibition of SST+ interneurons did not change the ratio of SUs entrained by spindle burst or beta oscillations before eye opening (**Fig. 4.18H**) yet, led to a reduction in the probability of spikes fired within spindle burst events when compared to control animals (**Fig. 4.18I**). No difference in PPC value for beta oscillation entrainment was observed (**Fig. 4.18J**).

Overall, these results indicate that chemogenetic inhibition of SST+ interneurons alter the spontaneous firing pattern of *in vivo* V1 activity, especially before eye opening. Increase baseline firing frequency of V1 SUs together with reduced probability for spikes to occur within spindle burst events point to a role for SST+ interneurons in regulating early synchronous activity.

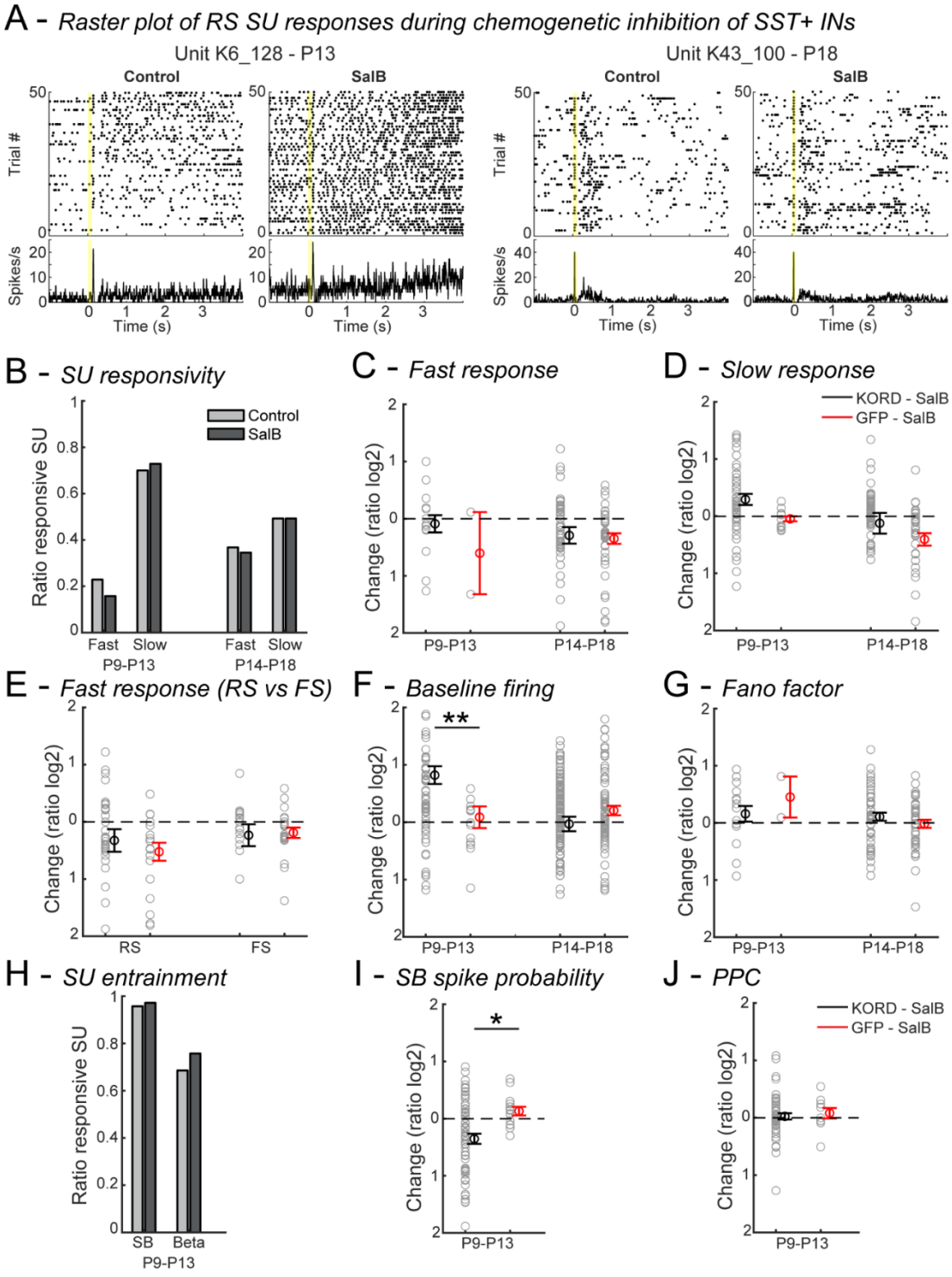


Fig. 4.18. Impact of chemogenetic inhibition of SST+ interneurons on V1 single unit activity. (A) Representative raster plot and PSTH obtained from two RS SUs at P13 (left) and P18 (right) upon visual stimulation with white LED light in normal conditions (Control) or after chemogenetic inhibition of SST+ interneurons (SalB).
(B) Bar plot of the ratio of responsive SUs during the fast or slow phases of the response to visual stimulation (Fast and Slow, respectively), and in control condition (Control, light grey) or after chemogenetic inhibition of SST+ interneurons (SalB, dark grey).

Fig. 4.18 (continue). (C) Errorbar plot (solid black or red lines) and scatter plot of the change in peak firing rate during the fast phase of the visual response for responsive SUs recorded at P9-P13 or P14-P18 in animals infected with a virus containing the KORD receptor (black lines) or GFP (red lines). Results of the statistical tests are as follows: KORD vs. GFP at P9-P13, not tested; KORD vs. GFP at P14-P18, Wilcoxon rank sum test: Z = 1.0, p = 0.29.
(D) Same as in C but for peak firing during the slow phase of the visual responses for responsive SUs. Results of the statistical tests are as follows: KORD vs. GFP at P9-P13, two sample t-test: t(60) = 1.8, p= 0.08; KORD vs. GFP at P14-P18, two sample t-test: t(60) = 1.1, p = 0.27.
(E) Same as in C but splitting SUs into RS and FS units. Results of the statistical tests are as follows: KORD vs. GFP at P9-P13, two sample t-test: t(48) = 0.7, p= 0.49; KORD vs. GFP at P14-P18, Wilcoxon rank sum test: Z = 0.69, p = 0.49.
(F) Same as in C but for spontaneous firing rate of all SUs. Results of the statistical tests are as follows: KORD vs. GFP at P9-P13, Wilcoxon rank sum test: Z = 2.6, **p = 0.01; KORD vs. GFP at P14-P18, Wilcoxon rank sum test: Z = −0.4, p = 0.69.
(G) Same as in C but for Fano factor of fast responsive units during the fast phase of the visual response. Results of the statistical tests are as follows: KORD vs. GFP at P9-P13, not tested; KORD vs. GFP at P14-P18, two sample t-test: t(85) = 1.3, p = 0.21.
(H) Same as in H but for ratio of SU entrained by spindle bursts (SB) or beta frequency oscillations (Beta).
(I) Same as in C but for probability of SU spikes to occur within SB events, for units recorded only at P9-P13. Results of the statistical tests are as follows: KORD vs. GFP at P9-P13, two sample t-test: t(79) = −2.5, *p= 0.02.
(J) Same as in I but for pairwise phase consistency (PPC) value. Results of the statistical tests are as follows: KORD vs. GFP at P9-P13, two sample t-test: t(56) = −0.5, p= 0.66.

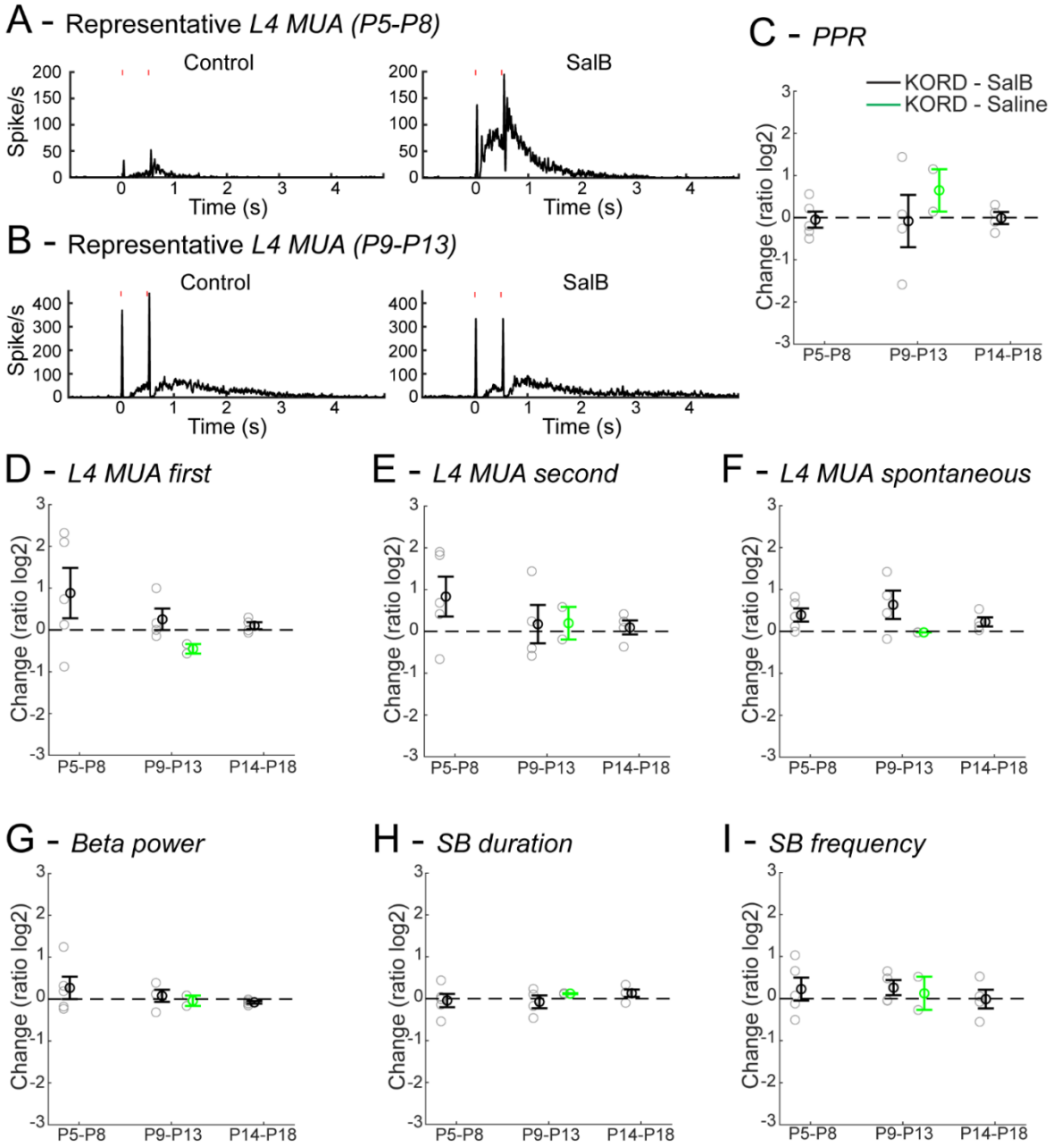
4.6.2 – Impact of chemogenetic inhibition of SST+ interneurons on spontaneous and sensory-evoked activity in the developing S1BF

To compare the function of SST+ interneurons in V1 and S1BF, I performed similar chemogenetic experiments in the latter brain area during early postnatal development. Previous experiments using chronic inhibition of SST+ interneurons in the developing S1BF showed an impairment of paired-pulse facilitation observed when stimulating the whiskers at 0.5 s interval, in animals recorded during the first postnatal week (Baruchin et al., 2021). I utilised the same experimental paradigm to compare responses to whisker stimulation before and after application of SalB in animals injected with the KORD DREADD to understand whether acute inhibition of SST+ interneuron led to the same effect. As controls, animals infected with KORD were injected with saline instead of SalB. During the first postnatal week, I observed a substantial increase in the peak L4 MUA response following both whisker stimuli after administration of SalB, compared to stimulation in the absence of

the drug (**Fig. 4.19A**); these effects were not observed in animals recorded between P9-P13 (**Fig. 4.19B**). Quantification of these data in **Fig. 4.19D** and **Fig. 4.19E** confirms the increase peak response after both whisker stimulations in P5-P8 animals (statistical analysis not performed due to low sample size in the control experiments). Similar to previous reports, two whisker stimuli interleaved by a 0.5 s interval led to pronounced facilitation of the second response in P5-P8 animals (paired pulse ratio, PPR = 2.2 ± 0.6). However, chemogenetic inhibition of SST+ interneurons did not lead to any change in PPR at any age investigated (**Fig. 4.19C**). I also observed an increase in L4 spontaneous MUA in animals recorded between P9-P13 after administration of SalB (**Fig. 4.19F**). No effect of chemogenetic inhibition of SST+ interneurons was observed for average power in the beta frequency during spontaneous activity (**Fig. 4.19G**), as well as spindle burst duration (**Fig. 4.19H**) and frequency of occurrence (**Fig. 4.19I**).

In conclusion, chemogenetic inhibition of SST+ interneurons lead to higher MUA responses to sensory stimulation of the whiskers, which is confined to the first developmental window investigated (P5-P8).

Fig. 4.19 (next page). Impact of chemogenetic inhibition of SST+ interneurons on barrel cortex spontaneous activity and MUA. (A) Representative L4 MUA from the barrel cortex (S1BF) of one animal recorded between P5 and P8 during stimulation of the whiskers alone (Control) and after administration of SalB to inhibit SST+ interneurons expressing the inhibitory chemogenetic receptor KORD. The paradigm of whisker stimulation employed 2 stimuli (red lines) at 500 ms inter-stimulus interval.
(B) Same as in (A) but for one animal recorded at P14-P18.
(C) Error bar plot (solid black line or green line) and scatter plot of change in paired pulse ratio (PPR) calculated from two successive whisker stimulation as described in A, for animals recorded at P5-P8, P9-P13, or P14-P18. The y axis indicate change between data recorded in control condition prior to the administration of SalB (black) or saline (green) as control and data recorded from whisker stimulation performed after administration of the drug.
(D) Same as in (C) but for peak L4 MUA after the first whisker stimulation. (E) Same as in (C) but for peak L4 MUA after the second whisker stimulation.
(E) Same as in (C) but for average spontaneous L4 MUA.
(F) Same as in (C) but for power in the beta frequency during recording of spontaneous activity.
(G) Same as in (C) but for average spindle burst (SB) event duration.
(H) Same as in (C) but for SB event frequency of occurrence.



4.7 – Effects of urethane anaesthesia on *in vivo* V1 SU activity

A limitation of our *in vivo* experimental approach is the use of urethane anaesthesia, which might change the pattern of SU activity in the developing V1. To address this limitation, I performed *in vivo* recordings in non-anaesthetised head-fixed neonatal mice before eye opening and compare the involvement of RS SUs in spontaneous and sensory-evoked activity between these recordings and data obtained from mice under urethane-anaesthesia. In term of spontaneous activity, I observed a significant reduction in the ratio

of SU significantly entrained by spindle bursts or beta frequency oscillations (**Fig. 4.20A**) in non-anaesthetised animals compared to experiments performed under urethane anaesthesia. This was coupled with increase spontaneous firing rate (**Fig. 4.20B**) and reduction in the probability of spikes occurring within spindle burst events (**Fig. 4.20C**) and PPC for spike-LFP coupling in the beta frequency (**Fig. 4.20D**) for awake animals. Responses to visual stimulation were affected to a lesser degree than spontaneous activity, with no change in the ratio of units responsive during the fast phase of the visual stimulation and a small reduction in the units responsive during the slow phase (**Fig. 4.20E**) in awake animals. I did not observe any difference in peak firing during the fast (**Fig. 4.20F**) and slow (**Fig. 4.20G**) phases of the visual response, but only a decrease reliability (**Fig. 4.20H**) in non-anaesthetised animals compared to urethane anaesthetised mice.

During *in vivo* experiments in non-anaesthetised head-fixed animals, I also tagged 3 SSTCre+ interneurons with optogenetics. Of these, none was significantly entrained by spindle bursts while only 1/3 was entrained by beta frequency oscillations. In term of responsivity to visual stimulation, 1/3 was characterised as fast responsive whereas all were characterised as slow responsive. In conclusion, urethane anaesthesia led to a notable change in the pattern of spontaneous V1 activity but has only minor effects on sensory responses of RS SU.

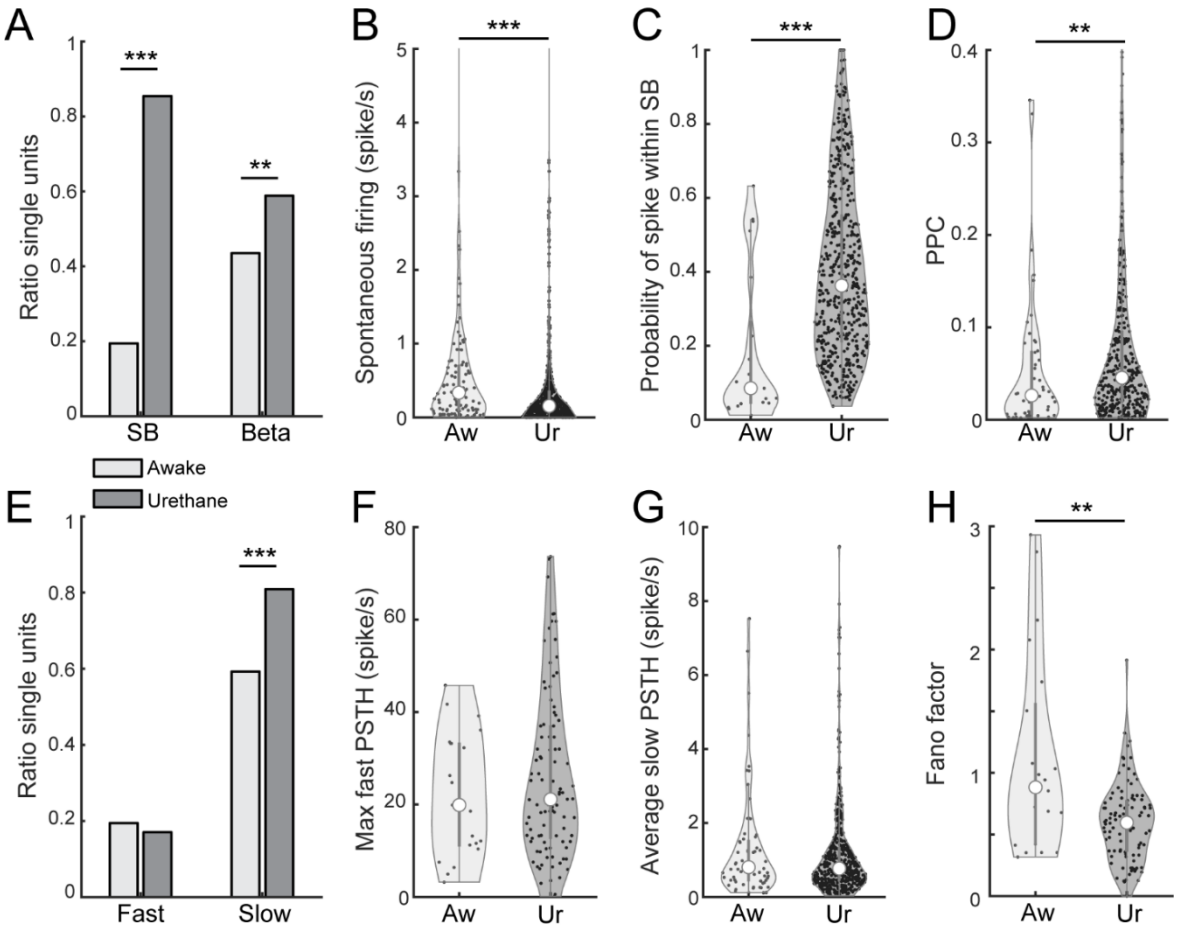


Fig. 4.20. Spontaneous and sensory evoked activity of RS neurons in awake and urethane-anaesthetised neonatal mice before eye opening. (A) Bar plot of the ratio of RS SUs significantly entrained by spindle bursts (Chi-square test: $X^2 = 214$; $p \leq 0.001$) or by beta frequency oscillations (Chi-square test: $X^2 = 8.7$; p =-0.003) obtained from awake head-fixed (light grey) vs. urethane-anaesthetised (dark grey) mice.
(B) Violin plot of spontaneous firing rate of RS SUs in awake head-fixed (Aw) vs. urethane-anaesthetised (Ur) mice. There is a statistically significant difference between the groups (Wilcoxon rank sum test: Z = -3.7, $p \leq 0.001$).
(C) Violin plot of probability of RS units spiking within spindle bursts (SB). There is a statistically significant difference between the groups (Wilcoxon rank sum test: Z = 4.6, $p \leq 0.001$).
(D) Violin plot of pairwise phase consistency (PPC) value between RS units spiking and beta oscillations in the LFP. There is a statistically significant difference between the group (Wilcoxon rank sum test: Z = 2.85, p = 0.004).
(E) Bar plot of the ratio of single units responsive during the fast phase (Chi-square test: $X^2 = 0.36$; p = 0.5) or the slow (Chi-square test: $X^2 = 24.7$; $p \leq 0.001$) phases of the visual responses.
(F) Violin plot of maximum firing rate of responsive RS SUs during the fast phase of the visual response (Unpaired t-test: t(121) = 1.03, p = 0.3).
(G) Violin plot of maximum firing rate of responsive RS SUs during the slow phase of the visual response (Wilcoxon rank sum test: Z = 0.3, p = 0.7).
(H) Violin plot of Fano factor of responsive RS SUs during the fast phase of the visual response. There is a statistically significant difference between the groups (Wilcoxon rank sum test: Z = -2.9, p = 0.003).

4.8 – Summary of results

In this chapter, I investigated the function of GABAergic interneurons during *in vivo* electrophysiological recordings in V1 of neonatal mice. The main results of this chapter are summarised below:

- The majority of *in vivo* electrophysiological experiments were performed in mice under urethane anaesthesia. Under these conditions, spontaneous activity before eye opening is dominated by spindle burst events and extended periods of network "silence." Responses to visual stimulation before eye opening are characterised by a fast rapid response followed by a secondary, slower response with oscillatory activity. The latter reflects a spindle burst event triggered by retinal stimulation. Features of spontaneous and sensory-evoked activity develops in the period preceding eye opening to achieve mature characteristics after eye opening.

- I used optogenetics into *SSTCre; Ai32* and *Nkx2-1Cre; Ai32* (to label both SST+ and PV+ interneurons) transgenic animals to tag GABAergic interneurons in the developing V1. Given the immature spike waveform of interneurons prior to eye opening, optogenetic tagging provides the only available strategy to record electrophysiological responses of GABAergic interneurons over early development.

- Regular spiking (RS) neurons – putative pyramidal excitatory neurons – are significantly entrained by spontaneous spindle burst activity and are coupled with oscillations in the beta frequency before eye opening. At the same developmental stage, most of RS units are responsive during the slow oscillatory phase of the visual response while responses to the fast phase rapidly develop up to P14. In particular, RS neurons in L4 show stable firing features during the fast and slow phase of the visual response, including reliability of their responses over development.

- Optogenetically tagged SST+ and Nkx2-1+ interneurons are also entrained by spindle burst activity, while SST+ appears to show stronger coupling with beta oscillations than

the Nkx2-1+ cohort. Only a small fraction of both interneuron subtypes shows increase firing during the fast phase of the visual responses before eye opening, whereas most of the tagged interneurons responded during the slow phase. Firing rate of Nkx2-1+ interneurons during both phases of the visual response significantly increased with development, in line with the maturation of PV+ interneurons (see ***Chapter 3***).

- Optogenetics was also used to probe the effect of activating GABAergic interneurons on spontaneous and sensory-evoked V1 activity. Optogenetic activation of SST+ and Nkx2-1+ interneurons led to general inhibitory effects on RS SUs before and after eye opening, with some differences. Inhibitory effects of SST+ interneurons appear to develop mainly for L5/6 RS units, whereas the ratio of inhibited units by Nkx2-1+ interneurons increased in both L4 and L5/6. Given Nkx2-1+ interneurons include both SST+ and PV+ subtypes, it is conceivable the latter are responsible for the observed increase inhibitory effects onto L4 RS neurons after eye opening, in line with the maturation of feed-forward inhibition showed in ***Chapter 3***. Finally, a large fraction of FS units in every layer was significantly inhibited by activation of SST+ interneurons, providing *in vivo* proof for the existence of a putative dis-inhibitory motif between them.

- I also observed a significant excitatory effect during the rebound from optogenetic activation of GABAergic interneurons. At the population level, this was observed for L2/3 and L4 RS and FS neurons after eye opening following optogenetic activation of SST+ interneurons.

- During visual stimulation, optogenetic activation of SST+ interneurons caused a reduction in firing rate during both the fast and slow phases of the visual stimulation before eye opening, for RS neurons in every layer. Conversely, the effects of Nkx2-1+ interneurons activation were confined to a reduction in firing rate during the fast phase of the visual responses only after eye opening. This might point to SST+ interneurons providing the main inhibitory drive to excitatory neurons in the period preceding eye opening.

- Acute inhibition of SST+ interneurons with chemogenetic did not affect the responses to visual stimulation of MUA as well as SU activity but led to an increase in spontaneous firing rate of RS SUs coupled with a reduction of spike probability within spindle burst events. This data suggests SST+ interneurons exert control over synchronous activity in V1 and that their inhibition causes spontaneous activity to be less synchronised.

- Preliminary chemogenetic experiments in S1BF showed that inhibition of SST+ interneurons led to larger L4 MUA in animals recorded between P5-P8. These experiments are in line with the different networks established by SST+ interneurons in the two sensory areas and point to SST+ interneurons as exerting tight control over sensory inputs in S1BF but not in V1, prior to active perception.

- Finally, experiments performed in non-anaesthetised head-fixed animals demonstrated that urethane anaesthesia impacts spontaneous activity in the developing V1 but has minor effects on sensory-evoked activity. Remarkably, some changes in activity observed in awake animals vs. urethane anaesthetised (namely, increase spontaneous activity and reduction of spike probability within spindle bursts) are the same as during chemogenetic inhibition of SST+ interneurons. These results might point to SST+ interneurons to exert state-dependent control on spontaneous activity in V1 prior to eye opening.

Chapter 5

Networks and functions of L6 neurons in the developing mouse brain

5.1 – Introduction

My characterisation of postnatal circuits of V1 in ***Chapter 3*** revealed transient GABAergic synaptic inputs from supragranular layers onto infragranular pyramidal cells in layers 5 and 6. The contribution of infragranular excitatory neurons during cortical development is less understood and under-studied compared to excitatory neurons in layer (L)4 and L2/3. However, they are critical players in the canonical cortical circuit, as they represent the "output" neurons of primary sensory areas, targeting a variety of subcortical structures including the sensory thalamus (Harris and Shepherd, 2015). ***Chapter 5*** will be focused on investigating the role L6 pyramidal neurons in the developing networks of primary sensory areas, again comparing postnatal circuits in V1 and S1BF. Pyramidal neurons in L6 are particularly interesting as they densely project back to the primary sensory thalamus (Thomson, 2010), through corticothalamic networks that, in V1, support developmental *in vivo* activity(Murata and Colonnese, 2016).

I first investigated the transient GABAergic connectivity from supragranular GABAergic interneurons identified in V1 in more detail, using a conditional optogenetic approach to determine which subtype of interneuron is involved. Next, I switched to S1BF to confirm if this transient connectivity motif is generalised between the two primary sensory areas or whether this is specific to V1. Finally, I used the *Ntsr1Cre-GN220* transgenic mouse line to reveal whether a specific subtype of L6 neurons is the target of the transient network and what role these neurons play during sensory-evoked activity *in vivo*.

5.2 – GABAergic networks of L6 pyramidal neurons in primary sensory areas over early postnatal development

5.2.1 – GABAergic networks of L6 pyramidal neurons in V1

In ***Chapter 3***, I described a transient GABAergic synaptic connection from supragranular interneurons onto L6 pyramidal neurons in V1, present only before the end of the first postnatal week (P5-P8 in our developmental window definition). Embedded within those data was a large degree of variability between individual L6 pyramidal neurons, with some cells dominated by local intralaminar connectivity while others exhibited this prominent translaminar motif. To better understand GABAergic networks of L6 neurons, I expanded the dataset presented in ***Chapter 3*** and mapped GABAergic connectivity of other L6 cells through laser-scanning photostimulation (LSPS) and glutamate uncaging (**Fig. 5.1**). Comprehensive analysis of average GABAergic connectivity maps (**Fig. 5.1A**) and columnar profiles (**Fig. 5.1B**) shows the increase prevalence of translaminar GABAergic inputs from supragranular layers between P5 and P8. However, examining connectivity maps from individual cells (**Fig. 5.1C**; see also **Supp. Fig. 5.1**) shows that, within the P5-P8 window, neurons receiving prominent GABAergic inputs from supragranular layers are mostly found at earlier developmental ages than neurons characterised by local connectivity. At later developmental windows, only a minority of L6 pyramidal neurons are characterised by translaminar connections, with the majority having ~60-80% of total GABAergic inputs from within L6 (**Fig. 5.1D**).

Fig. 5.1 (next page). Transient and translaminar GABAergic connectivity onto layer 6 pyramidal neurons in primary visual cortex. (A) Average normalised maps of global GABAergic connectivity onto layer (L)6 pyramidal neurons (Pyr) in primary visual cortex (V1) obtained through laser-scanning photostimulation (LSPS) of caged glutamate. Individual connectivity maps are grouped by developmental window (P5-P8, n = 18; P9-P13, n = 14; P14-P18, n = 15). White or black circles indicate approximate location of the recorded cell in the map; horizontal dashed lines indicate layer boundaries. (B) Columnar global GABAergic connectivity profile onto L6 Pyr in V1, colour-coded for developmental window (P5-P8, red; P9-P13, yellow; P14-P18, blue). Solid line indicates average normalised connectivity; shaded area shows the standard error of the mean (SEM).

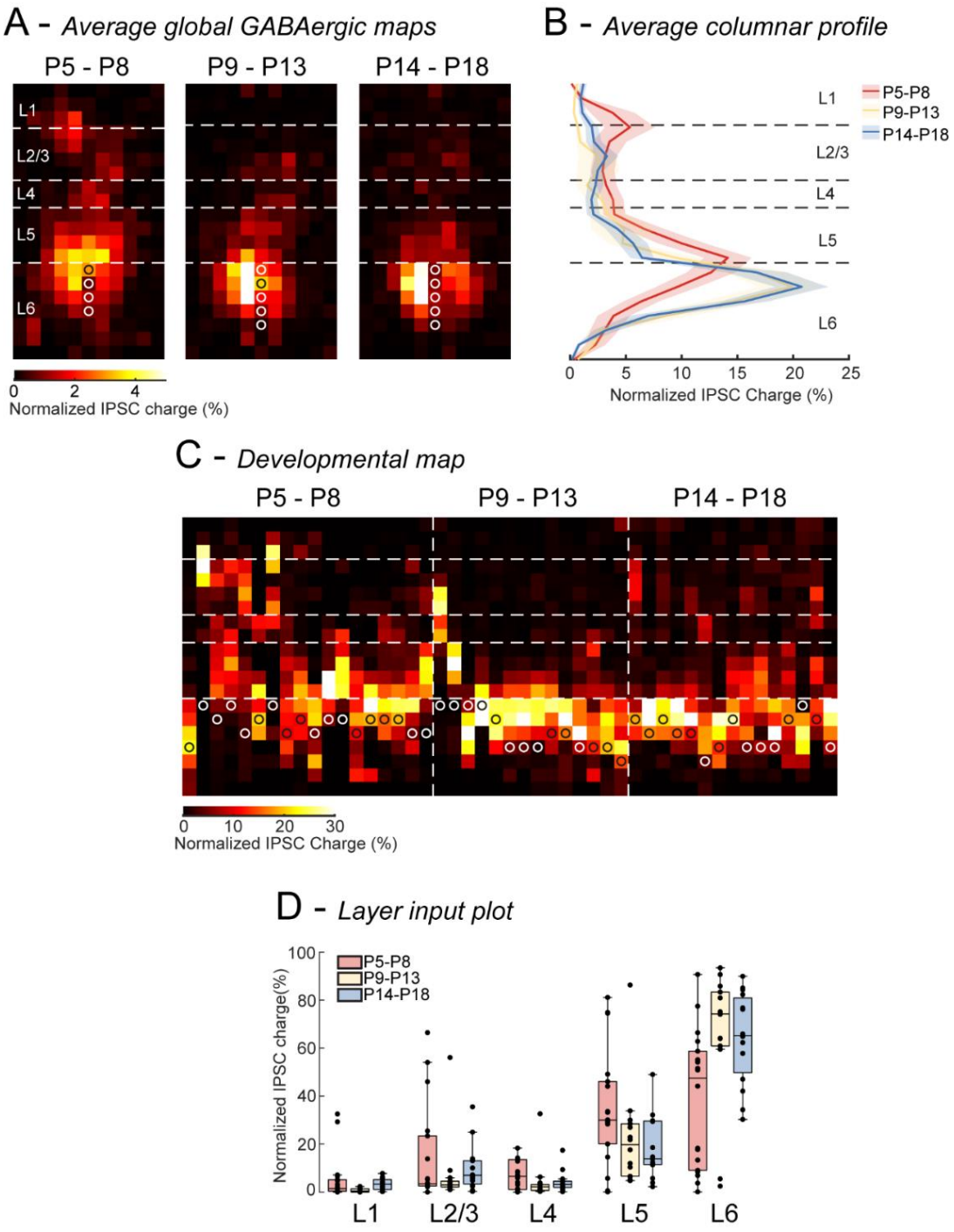


Fig. 5.1 (continue). (C) Developmental maps of global GABAergic connectivity onto L6 Pyr in V1. Each column in the map shows the normalised GABAergic connectivity map obtained from an individual cell, collapsed along its rows to obtain a linear columnar profile. Columns (i.e., individual cells) are sorted by age while vertical dashed lines indicate the transition between developmental windows (P5-P8, P9-P13, and P14-P18). Horizontal lines indicate layer boundaries, and white or black circles indicate the location of the cell recorded in the linear map.
(D) Box plot of normalised global GABAergic connectivity inputs from each layer (Input layer) onto L6 Pyr in V1, grouped and colour-coded for developmental window (as in B).

These data suggest translaminar GABAergic connections onto L6 pyramidal neurons are present only at the earliest postnatal ages investigated. Since somatostatin-expressing (SST+) interneurons represent some of the earliest to populate the developing neocortex, I reasoned they contribute to the transient connectivity motif. To test this hypothesis, I performed *in vitro* optogenetic experiments in *SSTCre; Ai32* animals and investigated whether L6 pyramidal neurons across development responded to blue light stimulation. I was able to evoke short-latency inhibitory postsynaptic currents (IPSCs; **Fig. 5.2A**), time locked to widefield blue light LED stimulation at all ages, with the amplitude of IPSCs significantly increasing over development (**Fig. 5.2B**, blue). The number of cells receiving putative monosynaptic connections from SST+ interneurons also increased over development, reaching 100% connectivity after eye opening (**Fig. 5.2C**). In contrast, at P5-P8, only 4/7 neurons were found to receive inputs from SST+ interneurons. A comparison of IPSC amplitude with data obtained from L4 pyramidal neurons (data shown in **Fig. 3.18**) revealed a significant smaller IPSC amplitude onto L6 pyramidal neurons compared with neurons in L4. While I did not observe developmental changes in the optogenetically induced IPSC latency (**Fig. 5.2D**) and decay time constant (tau; **Fig. 5.2F**) onto L6 pyramidal neurons, IPSC jitter significantly lowered over early postnatal development (**Fig. 5.2E**). Thus, SST+ connectivity onto L6 pyramidal neurons appears relatively weak during the first postnatal week in contrast to my hypothesis, with connected pyramidal cells only exhibiting low-amplitude, high-jitter IPSCs in response to optogenetic stimulation of SST+ interneurons during the early ages over which the translaminar connection is observed.

To broaden this analysis and assess if other interneuron subtypes contribute to the transient connectivity onto L6 pyramidal neurons in V1, I used the *Nkx2-1Cre* transgenic line to target both SST+ and parvalbumin-expressing (PV+) interneurons (see ***Chapter 4***). I generated *Nkx2-1Cre; Ai32* animals and repeated wide-field optogenetic experiments during whole-cell patch-clamp recordings of L6 pyramidal neurons, comparing animals at P5-P8 vs. P9-P13. Under these experimental conditions, all L6 neurons (n = 8 at P5-P8; n = 9 at P9-P13)

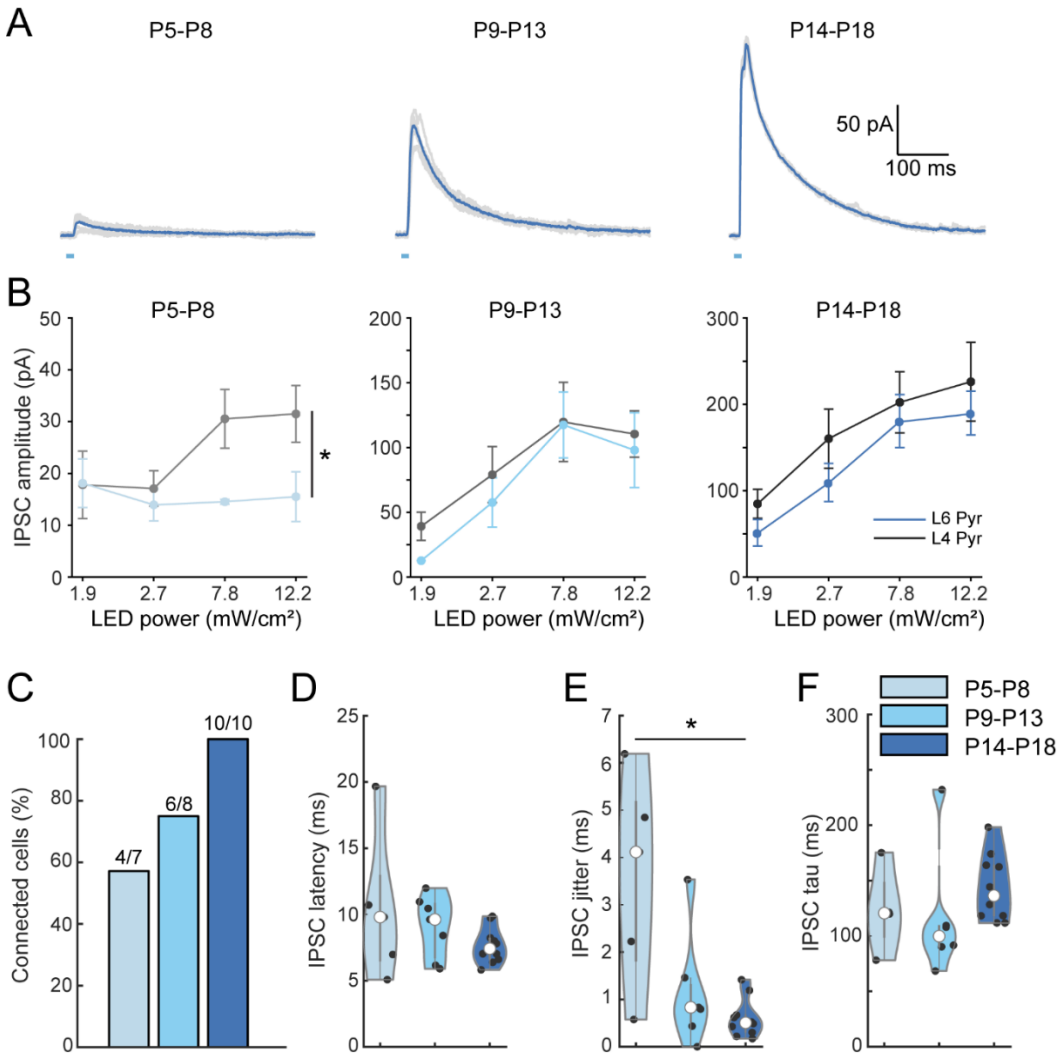


Fig. 5.2. Development of somatostatin interneurons connectivity onto L6 pyramidal neurons in V1. (A) Representative voltage-clamp recordings (V_h = 0 mV) of L6 Pyr in V1 upon optogenetic stimulation (470 nm; indicated by blue line) of somatostatin-expressing (SST+) interneurons in *SSTCre;Ai32* transgenic animals, at different developmental stages (P5-P8, left; P9-P13, middle; P14-P18, right). Grey lines represent individual sweeps of optogenetic stimulation, blue lines indicate their average trace.

(B) Error-bar plot of optogenetically-induced inhibitory postsynaptic current (IPSC) amplitude onto L6 Pyr (blue; see sample size in Fig. 5.2C) and L4 Pyr (black; as in Fig. 3.18) at 4 distinct LED power levels and at different developmental windows (as in A). There is an overall effect of "*Development*" in the full model (Three-way ANOVA: F(3,134) = 8.7, p ≤ 0.001). At P5-P8 there is a statistically significant effect of "*Cell Layer*" (Two-way ANOVA: F(1,22) = 5.1, *p = 0.03) but not "*LED Power*" (Two-way ANOVA: F(3,22) = 1.1, p = 0.38). At P9-P13 there is a statistically significant effect of "*LED Power*" (Two-way ANOVA: F(3,48) = 3.2, p = 0.03) but not "Cell Layer" (Two-way ANOVA: F(1,48) = 0.4, p = 0.55). At P14-P18 there is a statistically significant effect of "*LED Power*" (Two-way ANOVA: F(3,64) = 8.6, p ≤ 0.001) but not "*Cell Layer*" (Two-way ANOVA: F(1,64) = 2.7, p = 0.10).

(C) Bar plot of percentage of L6 Pyr responsive to optogenetic stimulation of SST+ interneurons at different developmental windows.

(D) Violin plot of optogenetically-induced IPSC latency for L6 Pyr in V1. There is no statistically significant effect of the factor "*Development*" (One-way ANOVA: F(2,19) = 2.0, p = 0.16).

(E) Violin plot of optogenetically-induced IPSC jitter for L6 Pyr in V1. There is a statistically significant effect of the factor "*Development*" (Kruskal-Wallis test: X^2 (2) = 7.7, p = 0.02; Dunn's test with Benjamini-Hochberg correction: *p ≤ 0.05).

(F) Violin plot of optogenetically-induced IPSC decay time constant (tau) for L6 Pyr in V1. There is no statistically significant effect of the factor "*Development*" (One-way ANOVA: F(2,19) = 0.8, p = 0.45).

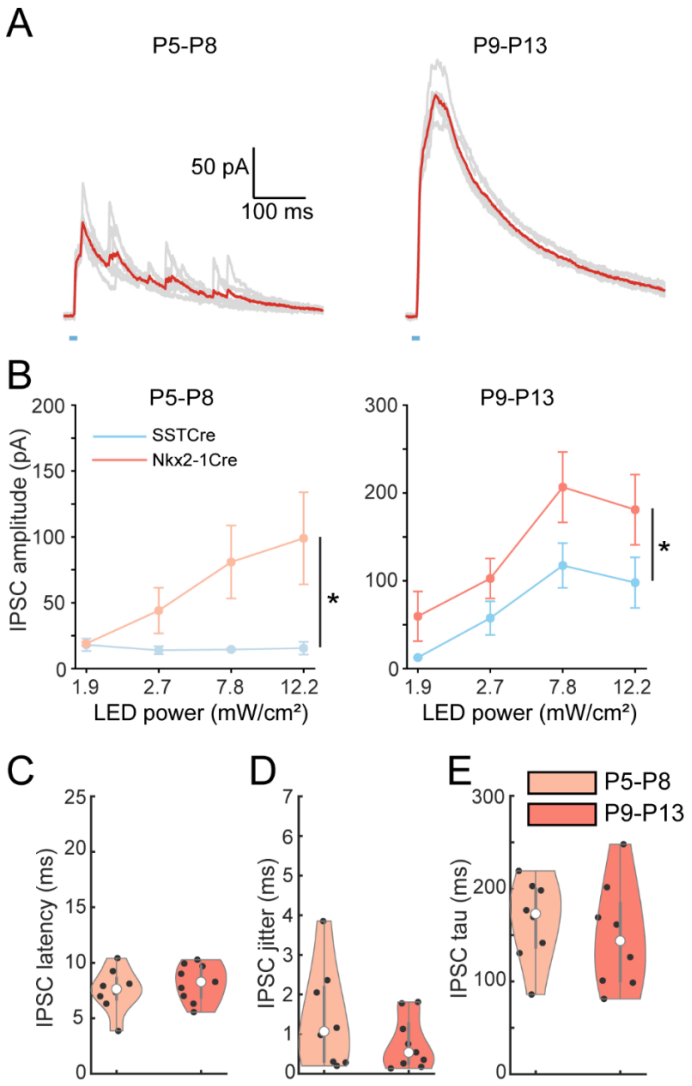


Fig. 5.3. Development of Nkx2-1 interneurons connectivity onto L6 pyramidal neurons in V1.
(A) Representative voltage-clamp recordings (V_h = 0 mV) of L6 Pyr in V1 upon optogenetic stimulation (470 nm; indicated by blue line) of Nkx2-1-expressing (Nkx2-1+) interneurons in *Nkx2-1; Ai32* transgenic animals, at different developmental stages (P5-P8, left; P9-P13, right). Grey lines represent individual sweeps of optogenetic stimulation, red lines indicate their average trace.
(B) Error-bar plot of optogenetically-induced IPSC amplitude onto L6 Pyr by activation of SST+ (blue, as in Fig. 5.2) or Nkx2-1+ (red; n = 8 at P5-P8 and n = 9 at P9-P13) interneurons at 4 distinct LED power levels and at different developmental windows (as in A). In the full model, there is a statistically significant effect of "*Development* (Three-way ANOVA: F(1,68) = 4.0, p = 0.01) and "*Mouse Genetics* (Three-way ANOVA: F(1,68) = 7.8, p = 0.006). At P5-P8 there is a statistically significant effect of "*Mouse Genetics*" (Two-way ANOVA: F(1,30) = 4.6, *p = 0.04) but not "*LED Power*" (Two-way ANOVA: F(3,30) = 0.9, p = 0.47). At P9-P13 there is a statistically significant effect of "*LED Power*" (Two-way ANOVA: F(3,38) = 2.9, p = 0.04) and "*Mouse Genetics*" (Two-way ANOVA: F(1,38) = 6.1, *p = 0.02).
(C) Violin plot of optogenetically-induced IPSC latency for L6 Pyr after stimulation of Nkx2-1+ interneurons. There is no statistically significant effect of the factor "*Development*" (Unpaired t-test: t(15) = -0.8, p = 0.46).
(D) Violin plot of optogenetically-induced IPSC jitter for L6 Pyr after stimulation of Nkx2-1+ interneurons. There is no statistically significant effect of the factor "*Development*" (Unpaired t-test: t(15) = 1.3, p = 0.21).
(E) Violin plot of optogenetically-induced IPSC tau for L6 Pyr after stimulation of Nkx2-1+ interneurons. There is no statistically significant effect of the factor "*Development*" (Unpaired t-test: t(15) = 0.7, p = 0.51).

responded to optogenetic activation of Nkx2-1+ interneurons with short-latency, low-jitter IPSCs (**Fig. 5.3A**). Comparison of IPSC amplitude with data obtained from *SSTCre; Ai32* animals, revealed that Nkx2-1+ interneuron-evoked IPSCs had higher values across both time window tested (**Fig. 5.3B**). IPSC latency (**Fig. 5.3C**), jitter (**Fig. 5.3D**) and tau (**Fig. 5.3E**) did not change over early development. Given Nkx2-1+ interneurons include both SST+ and PV+ subtypes and that connectivity from SST+ interneurons is relatively weak, our data suggests PV+ interneurons might be the more likely contributor to the transient GABAergic connectivity motif observed in the LSPS data. Experiments combining LSPS and *in vitro* optogenetic would be needed to substantiate this finding.

5.2.2 – GABAergic networks of L6 pyramidal neurons in S1BF

Throughout my studies, I have highlighted several differences in the connectivity motifs between GABAergic interneurons and excitatory neurons over early postnatal development between V1 and S1BF. I next investigated networks of L6 pyramidal neurons in the primary somatosensory cortex S1BF, to understand if the transient GABAergic connectivity from supragranular layers is a general feature of developing L6 neurons. GABAergic connectivity maps of L6 neurons in S1BF showed that they are dominated by GABAergic inputs from infragranular layers (**Fig. 5.4A**), either within L6 or L5b as shown in the average columnar profiles in **Fig. 5.4B**, with no discernible difference between the three developmental windows under investigation (see normalised layer inputs in **Fig. 5.4D**). Analysis of individual connectivity maps (**Fig. 5.4C**; see also **Supp Fig. 5.2**) revealed some cells to receive inputs exclusively from L6, whereas other were dominated by L5b input, a third subset receiving inputs from both L6 and L5b. However – at the time points tested – we did not observe input from supragranular interneurons highlighting a further difference in the developing GABAergic networks of S1BF and V1.

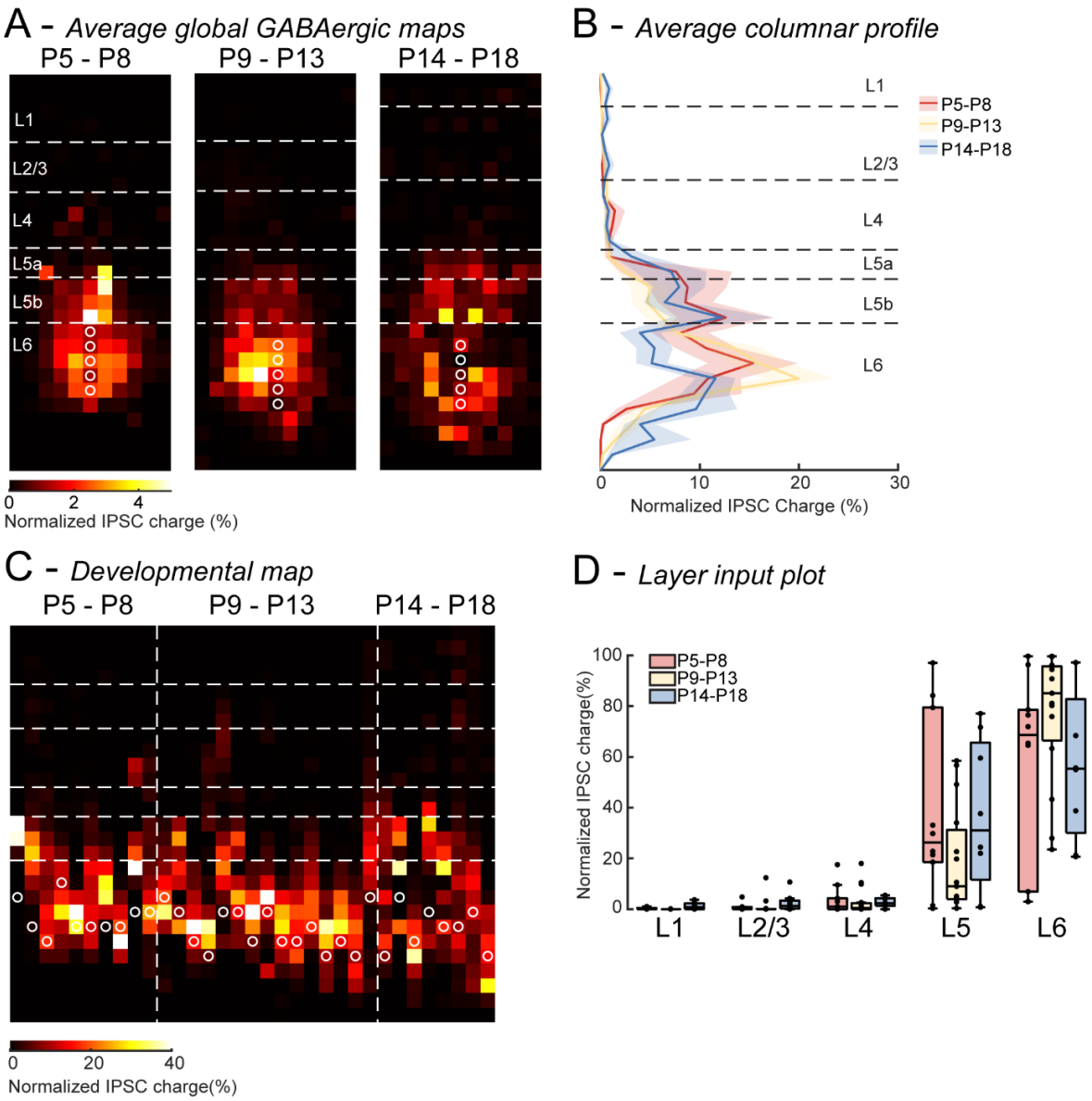


Fig. 5.4: Development of GABAergic connectivity onto L6 pyramidal neurons in the barrel cortex. (A) Average normalised maps of global GABAergic connectivity onto L6 Pyr in primary somatosensory barrel cortex (S1BF) obtained through LSPS of caged glutamate. Individual connectivity maps are grouped by developmental window (P5-P8, n = 10; P9-P13, n = 15; P14-P18, n = 8). White or black circles indicate approximate location of the recorded cell in the map; horizontal dashed lines indicate layer boundaries.
(B) Columnar global GABAergic connectivity profile onto L6 Pyr in S1BF, colour-coded for developmental window (P5-P8, red; P9-P13, yellow; P14-P18, blue). Solid line indicates average normalised connectivity; shaded area shows the standard error of the mean.
(C) Developmental maps of global GABAergic connectivity onto L6 Pyr in S1BF, as described in Fig. 5.1.
(D) Box plot of normalised global GABAergic connectivity inputs from each layer (Input layer) onto L6 Pyr in S1BF, grouped and colour-coded for developmental window (as in B).

S1BF SST+ interneurons in L5b appear to form an important hub for the co-ordination of early postnatal development, connecting sequentially with subplate neurons (Ghezzi et al., 2021), L4 spiny stellate cells (Marques-Smith et al., 2016) and L2/3 pyramidal cells (Anastasiades et al., 2016). Given the prominence of SST+ interneurons in early circuits in S1BF, I hypothesised that this subtype is responsible for L5b connection onto L6 pyramidal neurons. To test this, I performed *in vitro* optogenetic experiments and recorded L6 pyramidal neurons during optogenetic activation of SST+ interneurons in *SSTCre; Ai32* animals. All recorded L6 pyramidal neurons (n = 6 at P5-P8; n = 9 at P9-P13; and n = 5 at P14-P18) responded with low-jitter, low-amplitude IPSCs in response to optogenetic stimulation (**Fig. 5.5A**). Comparison of S1BF IPSC data with that obtained in V1 did not reveal a difference between the two areas (**Fig. 5.5B**), albeit I observed large variability in S1BF data. I also did not observe any developmental change in IPSC latency (**Fig. 5.5C**), jitter (**Fig. 5.5D**), or tau (**Fig. 5.5E**) for the data collected from S1BF L6 pyramidal neurons. This data suggests no difference in the strength of SST+ interneuron input onto L6 neurons across V1 and S1BF in early life. However, the large variability in the optogenetic data mirrors the variability in the LSPS experiments, suggesting cells with prominent inputs from L5b might also be recipient of high-amplitude IPSCs during optogenetic stimulation of SST+ interneurons. This idea would need to be tested in future experiments combining LSPS and optogenetics.

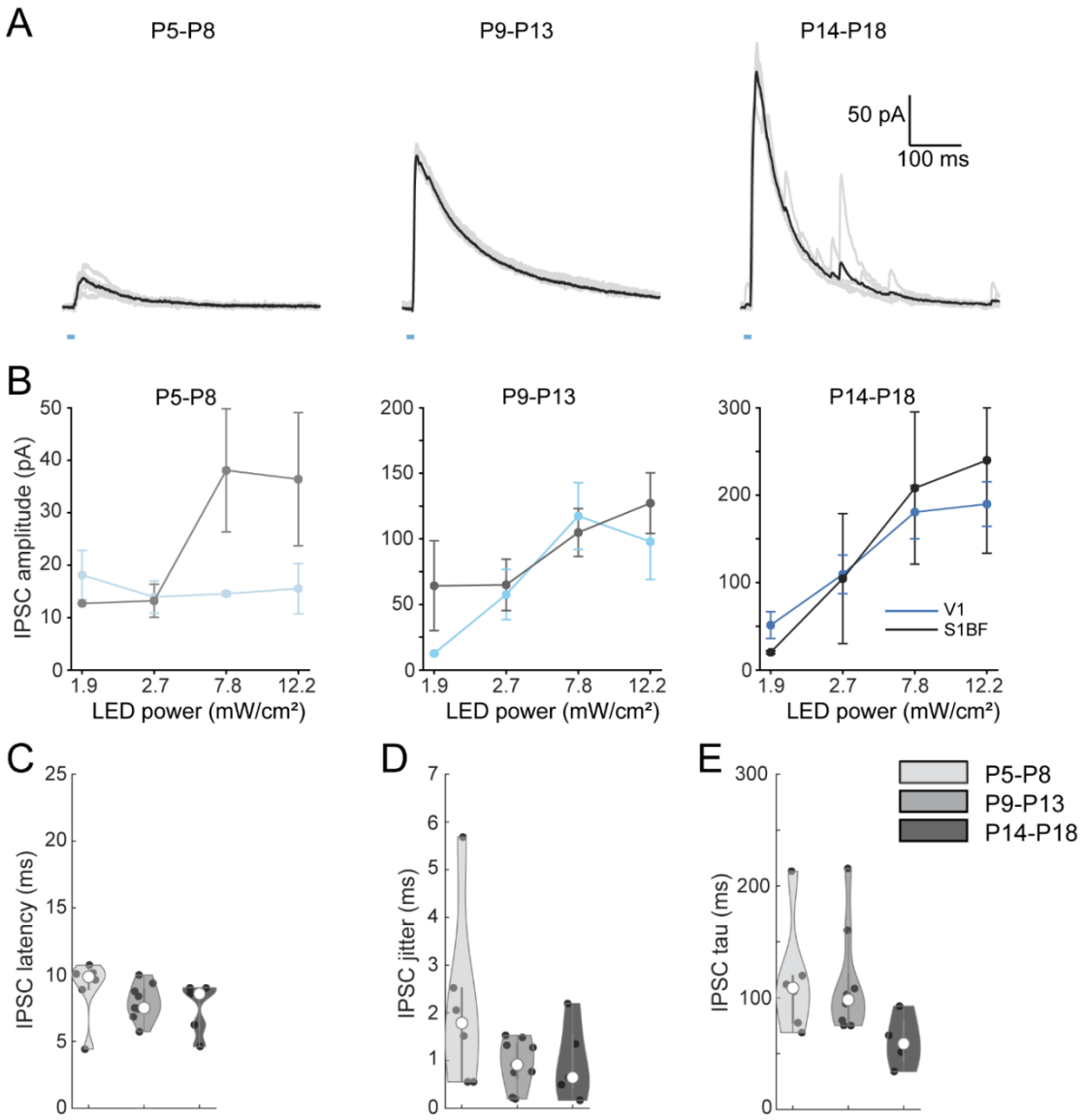
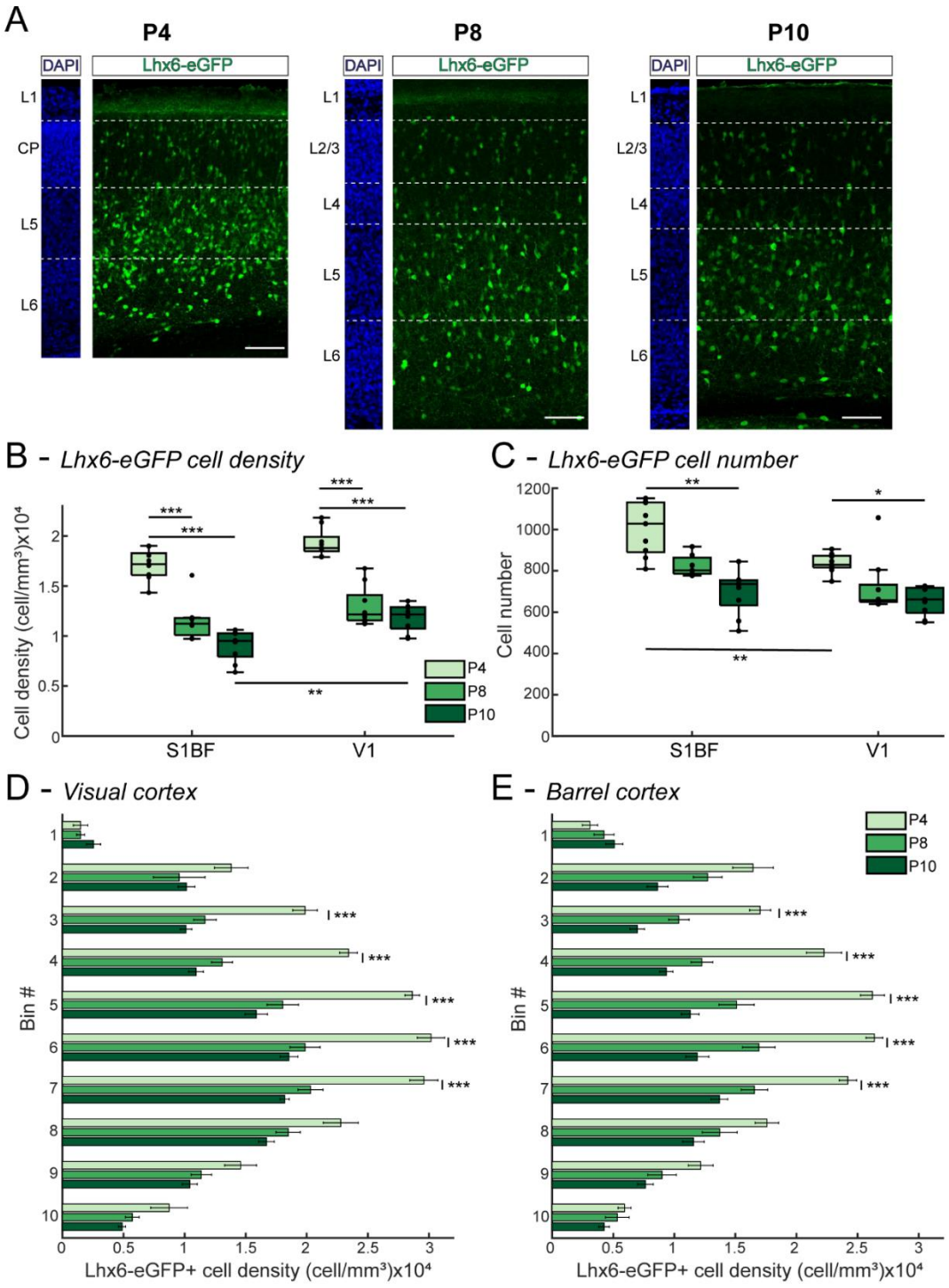


Fig. 5.5. Development of SST+ interneurons connectivity onto L6 pyramidal neurons in the barrel cortex. (A) Representative voltage-clamp recordings (V_h = 0 mV) of L6 Pyr in S1BF upon optogenetic stimulation (470 nm; indicated by blue line) of somatostatin-expressing (SST+) interneurons in *SSTCre;Ai32* transgenic animals, at different developmental stages (P5-P8, left; P9-P13, middle; P14-P18, right). Grey lines represent individual sweeps of optogenetic stimulation, black lines indicate their average trace.
(B) Error-bar plot of optogenetically-induced IPSC amplitude onto L6 Pyr in S1BF (black; n = 6 at P5-P8, n = 9 at P9-P13, and n = 5 at P14-P18) and V1 (blue, as in Fig. 5.2) at 4 distinct LED power levels and at different developmental windows (as in A). In the full model, there is an overall effect of "*Development* (Three-way ANOVA: $F(2,112) = 18.4$, $p \leq 0.001$) and "*LED Power*" (Three-way ANOVA: $F(1,68) = 5.4$, $p = 0.002$). At P5-P8 there are no significant effect of "*Brain Area*" (Two-way ANOVA: $F(1,22) = 2.2$, $p = 0.15$) and "*LED Power*" (Two-way ANOVA: $F(3,22) = 1.1$, $p = 0.39$). At P9-P13 there are no significant effect of "*Brain Area*" (Two-way ANOVA: $F(1,42) = 0.4$, $p = 0.55$) and "*LED Power*" (Two-way ANOVA: $F(3,42) = 2.2$, $p = 0.10$). At P14-P18 there is a statistically significant effect of "*LED Power*" (Two-way ANOVA: $F(3,48) = 4.5$, $p = 0.007$) but not "*Brain Area*" (Two-way ANOVA: $F(1,48) = 0.2$, $p = 0.65$).
(C) Violin plot of optogenetically-induced IPSC latency for L6 Pyr in S1BF. There is no statistically significant effect of the factor "*Development*" (One-way ANOVA: $F(2,17) = 1.0$, $p = 0.39$).
(D) Violin plot of optogenetically-induced IPSC jitter for L6 Pyr in S1BF. There is no statistically significant effect of the factor "*Development*" (One-way ANOVA: $F(2,17) = 2.2$, $p = 0.14$).
(E) Violin plot of optogenetically-induced IPSC tau for L6 Pyr in S1BF. There is no statistically significant effect of the factor "*Development*" (One-way ANOVA: $F(2,17) = 2.2$, $p = 0.15$).

5.2.3 – Distribution of GABAergic interneurons in V1 and S1BF over early postnatal development

Primary visual and somatosensory cortices differ greatly in their developmental timeline in early postnatal mice. I next tested whether delayed migration of GABAergic interneurons in V1 compared to S1BF might underlie the different GABAergic networks revealed with *in vitro* circuit mapping experiments. I used immunohistochemistry to label Lhx6+ interneurons in *Lhx6-eGFP* transgenic mice at P4, P8, and P10 (**Fig. 5.6A**). I observed a developmental decrease in the overall density of Lhx6+ interneurons, with a sharp drop occurring between P4 and P8 (**Fig. 5.6B**). This decrease was not simply due to expansion of the cortex occurring around the same time, given the raw number of Lhx6+ interneurons (counted within regions of interest with same size) also decreased in a similar fashion (**Fig. 5.6C**). I next looked at the distribution of Lhx6+ interneurons across the depth of neocortex within each area, by binning the full extent of the cortical thickness into 10 sections of equal size. In both V1 and S1BF, I observed a drop in Lhx6+ interneuron density occurring in bins 3 – 7, including an area spanning layer 3 to upper layer 5 (**Fig. 5.6D, E**). These data do not support major migratory mechanisms occurring at the developmental ages tested, suggesting controlled cell death occurring between P4 and P8 account for the reduction of medial ganglionic eminence (MGE)-derived Lhx6+ interneuron density in V1 and S1BF.

Fig. 5.6 (next page). Distribution of Lhx6+ GABAergic interneurons over early postnatal development. (A) Representative confocal images of V1 slices obtained from Lhx6-eGFP transgenic animals at P4 (left), P8 (middle), and P10 (right), stained with an anti-GFP antibody (green). Horizontal dashed lines indicate layer boundaries, identified thanks to DAPI staining (blue). Scale bar = 100 µm.
(B) Box plot of Lhx6-eGFP cell density in S1BF and V1 at P4, P8 and P10 (n = 9 slices from 3 animals each age). There are statistically significant effects of both "*Brain Area*" (Two-way ANOVA: $F(1,40) = 8.0$, $p = 0.007$) and "*Development*" (Two-way ANOVA: $F(2,19) = 53.0$, $p \leq 0.001$) factors.
(C) Box plot of Lhx6-eGFP cell number (counted within a ~500 µm wide cortical column) in S1BF and V1 at P4, P8 and P10. There are statistically significant effects of both "*Brain Area*" (Two-way ANOVA: $F(1,40) = 14.8$, $p \leq 0.001$) and "*Development*" (Two-way ANOVA: $F(2,13) = 15.6$, $p \leq 0.001$) factors.
(D, E) Bar plot (error bar indicates SEM) of Lhx6-eGFP cell density in each bin (bin 1 close to the pial surface, bin 10 close to the white matter) in V1 (D) and S1BF (E). There is a statistically significant effect of the factor "*Bin*" (Two-way ANOVA: $F(9, 484) = 133.9$, $p \leq 0.001$) but not "*Development*" (Two-way ANOVA: $F(2,94) = 0.9$, $p = 0.4$). Asterisks in the plot show statistically significant differences between groups, when tested with post-hoc analysis corrected for multiple comparisons (Estimated marginal means method; *emmeans* function in R), according to the following notation: * $p \leq 0.05$, ** $p \leq 0.01$, and *** $p \leq 0.001$.


A
P4
P8
P10
DAPI
Lhx6-eGFP
L1
CP
L2/3
L4
L5
L6
B - Lhx6-eGFP cell density
Cell density (cell/mm³)x10⁴
S1BF
V1
P4
P8
P10
C - Lhx6-eGFP cell number
Cell number
D - Visual cortex
E - Barrel cortex
Bin #
Lhx6-eGFP+ cell density (cell/mm³)x10⁴

5.3 – GABAergic networks of L6 corticothalamic and corticocortical pyramidal neurons in V1

Pyramidal neurons in L6 display a large degree of variability in term of morphology, intrinsic electrophysiological properties, and target areas of the brain (Thomson, 2010; Gouwens et al., 2019). In primary sensory areas, a major classification proposed for L6 excitatory neurons is based on their output targets, distinguishing corticothalamic (CT) L6 neurons from cortico-cortical (CC) neurons (Thomson, 2010). To further explore the heterogeneity in early GABAergic connectivity in V1 (**Fig. 5.1**) and establish if this relates to differential target innervation, I switched to using the *Ntsr1Cre-GN220* (henceforth abbreviated *Ntsr1Cre*) transgenic mouse line to selectively target L6 CT neurons in primary sensory areas (Gong et al., 2007). I generated *Ntsr1Cre; Ai9* mice to express tdTomato in Ntsr1+ L6 CT neurons and imaged slices obtained from those animals at the confocal microscope (**Fig. 5.7**). In line with previous observations (Olsen et al., 2012; Vélez-Fort et al., 2014; Sundberg et al., 2018), the *Ntsr1Cre* line targets a large fraction of cells in the deepest layer of the cerebral cortex (**Fig. 5.7B, C**), most of these cells display an apical dendrite ascending toward the upper cortical layers (**Fig. 5.7B**), while thalamic nuclei were also intensely tdTomato+ due to dense axonal innervation (**Fig. 5.7A**).

Based on previous studies, I hypothesised L6 CT neurons might be the recipient of GABAergic inputs from supragranular interneurons revealed in **Fig. 5.1**. First, CT cells have been shown to be critical for spontaneous spindle burst propagation in V1 prior to eye opening, by establishing a thalamo-cortico-thalamic loop that can sustain oscillatory activity (Murata and Colonnese, 2016). Spindle bursts oscillations are primarily observed in supragranular layers and entrain GABAergic interneurons there (***Chapter 4***). Thus, it is conceivable that a synaptic connection from supragranular layers to L6 CT neurons is necessary to provide GABAergic control over L6 cells entrained by spindle bursts. Second, while innervation by GABAergic interneurons migrating into the cortex via supragranular layers appears unlikely (**Fig. 5.6**), CT Ntsr1+ L6 neurons in V1 are known to retract their

apical dendrite over early postnatal development (Sundberg et al., 2018). At birth, a large fraction of Ntsr1+ CT neurons in V1 is characterised by long apical dendrite ascending to L1, which might be ideally located to receive GABAergic connection from supragranular interneurons in a transient manner.

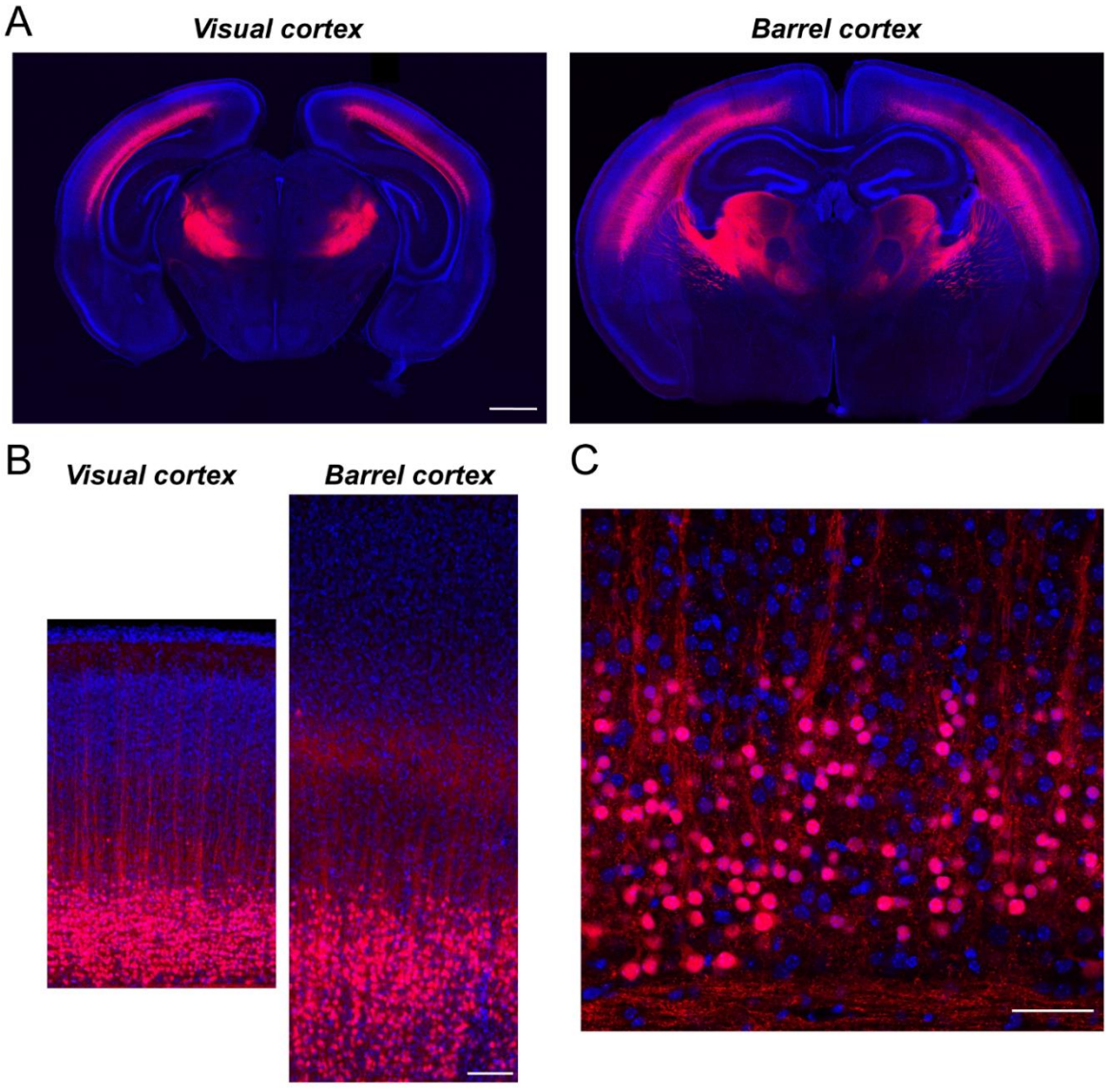


Fig. 5.7. The Ntsr1Cre-GN220 transgenic mouse line identifies corticothalamic L6 Pyr. (A) Representative confocal images (4X) of a slice containing V1 (left) or S1BF (right) obtained from a P6 and P10 *Ntsr1Cre-GN220; Ai9* (red) transgenic mouse, respectively. Blue shows DAPI staining; scale bar = 1 mm.
(B) Higher magnification confocal images (10X) from the slices shown in A. Scale bar = 100 µm.
(C) Higher magnification confocal image (40X) of the V1 slice shown in B. Scale bar = 50 µm.

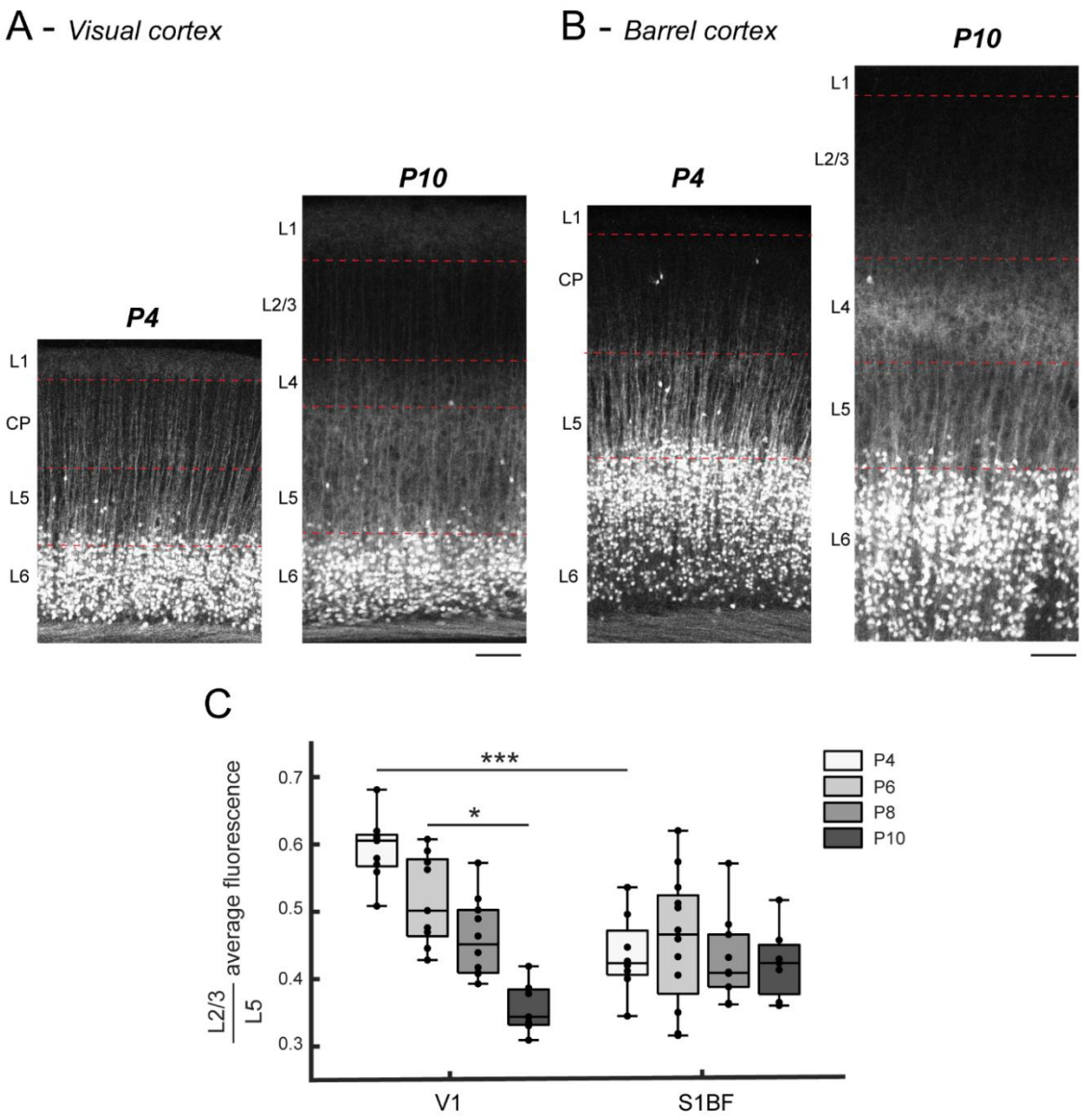


Fig. 5.8. Ntsr1+ L6 Pyr retracts their apical dendrite in V1 over early development. (A) Representative confocal images (10X) of a slice containing V1 obtained from a P4 (left) and P10 (right) *Ntsr1Cre-GN220; Ai9* (grey) transgenic mouse, respectively. Red horizontal lines indicate approximate layer boundaries, determine with the DAPI profile (not shown). Scale bar = 100 µm.
(B) Same as in A, but for slices containing S1BF.
(C) Box plot of the ratio between average fluorescence in L2/3 and in L5 for animals at P4, P6, P8, and P10 (n = 3 slices from 3 animals each age) in V1 and S1BF. There is a statistically significant effect of the factor "Brain Area" (Two-way ANOVA: $F(1,54) = 54.4$, $p \leq 0.001$). Asterisks in the plot show statistically significant differences between groups, when tested with post-hoc analysis corrected for multiple comparisons (Estimated marginal means method; *emmeans* function in R), according to the following notation: * $p \leq 0.05$ and *** $p \leq 0.001$.

I first tested the timing of apical dendrite retraction in L6 Ntsr1+ CT neurons in V1 coincides with the transient GABAergic connectivity revealed by LSPS experiments. Moreover, I investigated whether the same process happens in S1BF, which is not characterised by translaminar connections from supragranular interneurons. To this aim, I imaged coronal cortical slices including V1 or S1BF from *Ntsr1Cre; Ai9* animals at P4, P6, P8, and P10. In V1 at P4, Ntsr1+ cells extend long apical dendrite ascending to L1, which are already largely reduced by P10 (**Fig. 5.8A**). In S1BF instead, I observed a lower fraction of apical dendrite reaching supragranular layers, which did not appear to change over development (**Fig. 5.8B**). I quantified the relative proportion of cells with long apical dendrite by calculating a ratio of the average fluorescence in L5 vs. L2/3. This data revealed that, in V1, there is a decrease in the proportion of TdTomato+ processes in L2/3 over development, with a significant drop occurring between P6 and P10 (**Fig. 5.8C**). In contrast, CT L6 neurons in S1BF do not retract their apical dendrite over the course of the developmental windows investigated and are furthermore characterised by lower proportion of tdTomato+ processes in L2/3 at P4 compared to V1 (**Fig. 5.8C**). Thus, consistent with other reports (Sundberg et al., 2018), a fraction of Ntsr1+ L6 CT cells in V1 is characterised by long apical dendrite extending to L2/3 early in development. The timing for the retraction of these apical dendrite coincides with the disappearance of the translaminar GABAergic connectivity from supragranular layers.

To test whether L6 Ntsr1+ CT neurons in V1 are recipient of the translaminar GABAergic connectivity from supragranular layers early in development, I targeted tdTomato-expressing CT neurons in L6 from *Ntsr1Cre; Ai9* animals for LSPS experiments and mapped their columnar GABAergic afferent input. I further recorded tdTomato− cells within L6 in the same acute *in vitro* slices, to study the GABAergic connectivity of putative L6 CC cells. Contrary to our working hypothesis, L6 Ntsr1+ cells received GABAergic input from local sources, primarily intralaminar connections from L6 which on occasion extended to the lower L5 (**Fig. 5.9A**). This pattern of local GABAergic connectivity did not change over

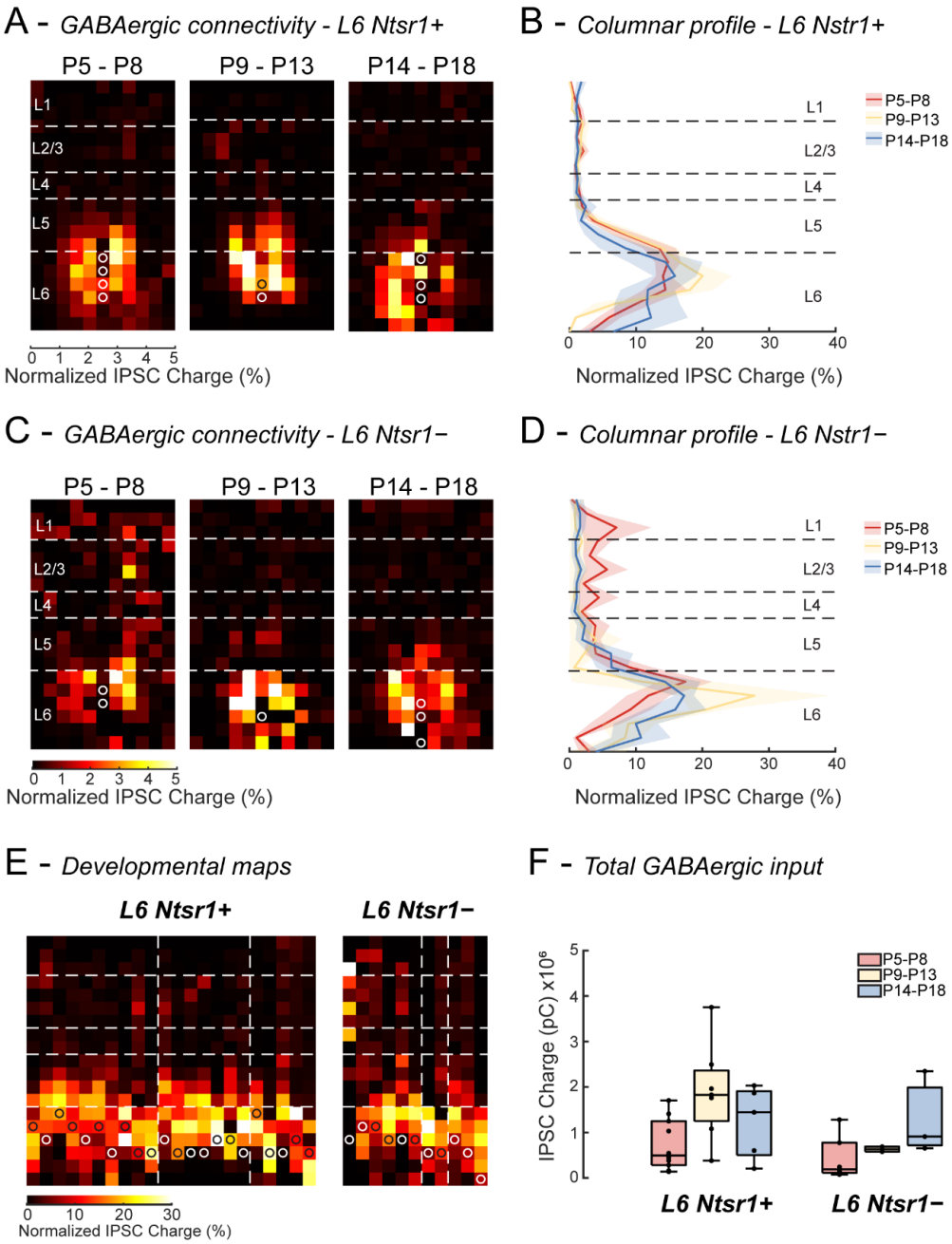


Fig. 5.9: GABAergic networks of corticothalamic and corticocortical L6 Pyr in V1. (A) Average normalised maps of global GABAergic connectivity onto Ntsr1+ L6 Pyr (corticothalamic) in V1 obtained through LSPS of caged glutamate experiments performed in *Ntrs1Cre; Ai9* transgenic animals. Individual connectivity maps are grouped by developmental window (P5-P8, n = 10; P9-P13, n = 7; P14-P18, n = 5). White or black circles indicate approximate location of the recorded cell in the map; horizontal dashed lines indicate layer boundaries.
(B) Columnar global GABAergic connectivity profile onto Ntsr1+ L6 Pyr in V1, colour-coded for developmental window (P5-P8, red; P9-P13, yellow; P14-P18, blue). Solid line indicates average normalised connectivity; shaded area shows the SEM.
(C, D) Same as in A, B but for Ntsr1− L6 Pyr (corticocortical; P5-P8, n = 6; P9-P13, n = 2; P14-P18, n = 3).
(E) Developmental maps of global GABAergic connectivity onto Ntsr1+ (left) and Ntsr1− (right) L6 Pyr in V1, as described in Fig. 5.1.
(F) Box plot of raw total GABAergic input for Ntsr1+ and Ntsr1− L6 Pyr in V1, grouped and colour-coded for developmental window (as in B). There is a statistically significant effect of the factor "Development" (Two-way ANOVA: $F(2,32) = 4.7$, $p = 0.02$) but not "Cell Type" on the data (Two-way ANOVA: $F(1,32) = 2.1$, $p = 0.16$).

development, with similar columnar profiles at P5-P8, P9-P13, and P14-P18 (**Fig. 5.9B**). Average GABAergic connectivity of L6 Ntsr1− (thus CC) cells revealed they might receive GABAergic input from interneurons in supragranular layers (**Fig. 5.9C,D**) at early postnatal ages (P5-P8); from P9, they only received local GABAergic inputs. In term of individual variability, L6 Ntsr1+ cells are found to be homogeneous, with all recorded cells at every age characterised by strong local GABAergic connectivity (**Fig. 5.9E**, left; see also **Supp. Fig. 5.3A**). Regarding L6 Ntsr1− cells, only 1/6 recorded neurons at P5-P8 appear to display strong GABAergic inputs from supragranular layers, whereas the others are primarily characterised by local inputs (**Fig. 5.9E**, right; see also **Supp. Fig. 5.3B**). Both L6 Ntsr1+ and Ntsr1− neurons were characterised by similar developmental increase in total GABAergic inputs (**Fig. 5.9F**).

Overall, the results obtained through experiments on *Ntsr1Cre; Ai9* animals suggest that contrarily to my hypothesis, L6 CT neurons are engaged by local GABAergic interneurons in deep cortical layers and that a minority of L6 Ntsr1− cells is involved in the transient translaminar connection with supragranular interneurons.

5.4 – Involvement of L6 neurons in spontaneous and sensory-evoked activity in V1 *in vivo*

In the last section of this ***Chapter***, I investigated how my observations of the GABAergic networks of L6 neurons *in vitro* translate to early *in vivo* activity using a combination of electrophysiology and optogenetic approaches. Experiments described below were performed in awake head-fixed mice prior to eye opening and were compared with data obtained after eye opening in animals under urethane anaesthesia.

To understand the contribution of L6 CT and L6 CC neurons to developing activity in V1, I first generated *Ntsr1Cre; Ai32* animals to conditionally express Channelrhodospin-2 (ChR2) in L6 Ntsr1+ CT neurons to allow for optogenetic spike tagging. In these animals, a flash of blue (470nm; 50 ms) laser light induced reliable spiking activity in single units (SUs) located in deep cortical layers (**Fig. 5.10A**), that had immature spike waveform resembling regular

spiking (RS) units (**Fig. 5.10B**); the example Ntsr1+ SU in **Fig. 5.10** was responsive to sensory stimulation with a flash of white LED light (**Fig. 5.10C**). Through all the experiments performed, I optogenetically tagged 12 Ntsr1+ SUs and defined them as putative CT L6 neurons (**Fig. 5.10D**, red) while all other untagged RS SUs in L6 were classified as putative CC L6 neurons (**Fig. 5.10D**, blue). Analysis of the spike trough to peak latency of optogenetically tagged units (**Fig. 5.10D**) revealed 5 putative L6 CT cells to be characterised by a value lower than the cut-off of 0.75 ms, possibly representing putative fast-spiking (FS) interneurons. I further investigated these latter cells based on the notion that L6 Ntsr1+ neurons directly excite local L6 FS interneurons (Olsen et al., 2012; Bortone et al., 2014), which might explain the recruitment of FS SU by blue light stimulation. To better explore this issue, in one *Ntsr1Cre; Ai32* animals after eye opening, I exploited two distinct optogenetic stimuli (50 ms and 1 ms) and compared spiking evoked under both conditions. While a 50 ms blue light stimulus recruited both example SUs shown in **Fig. 5.11A** and **Fig. 5.11B**, a 1 ms blue light stimulus only recruited one of the SU (Fig. **5.11C, D**). Comparison of the spike waveform of these two units revealed U97 (recruited by the 50 ms stimulus only) to display classical waveform features of FS cells (small spike half-width and trough to peak latency) whereas U119 (recruited by both 50 and 1 ms optogenetic stimuli) to have feature resembling RS units. Based on these findings, SUs characterised by spike trough to peak latency below the cut-off value of 0.75 ms were classified as FS units, although optically tagged. Subtracting away these 5 FS units yielded a total of n = 6 putative CT units obtained after eye opening, and only 1 obtained before eye opening, together with n = 9 and n = 8 untagged, putative CC L6 neurons before and after eye opening, respectively.

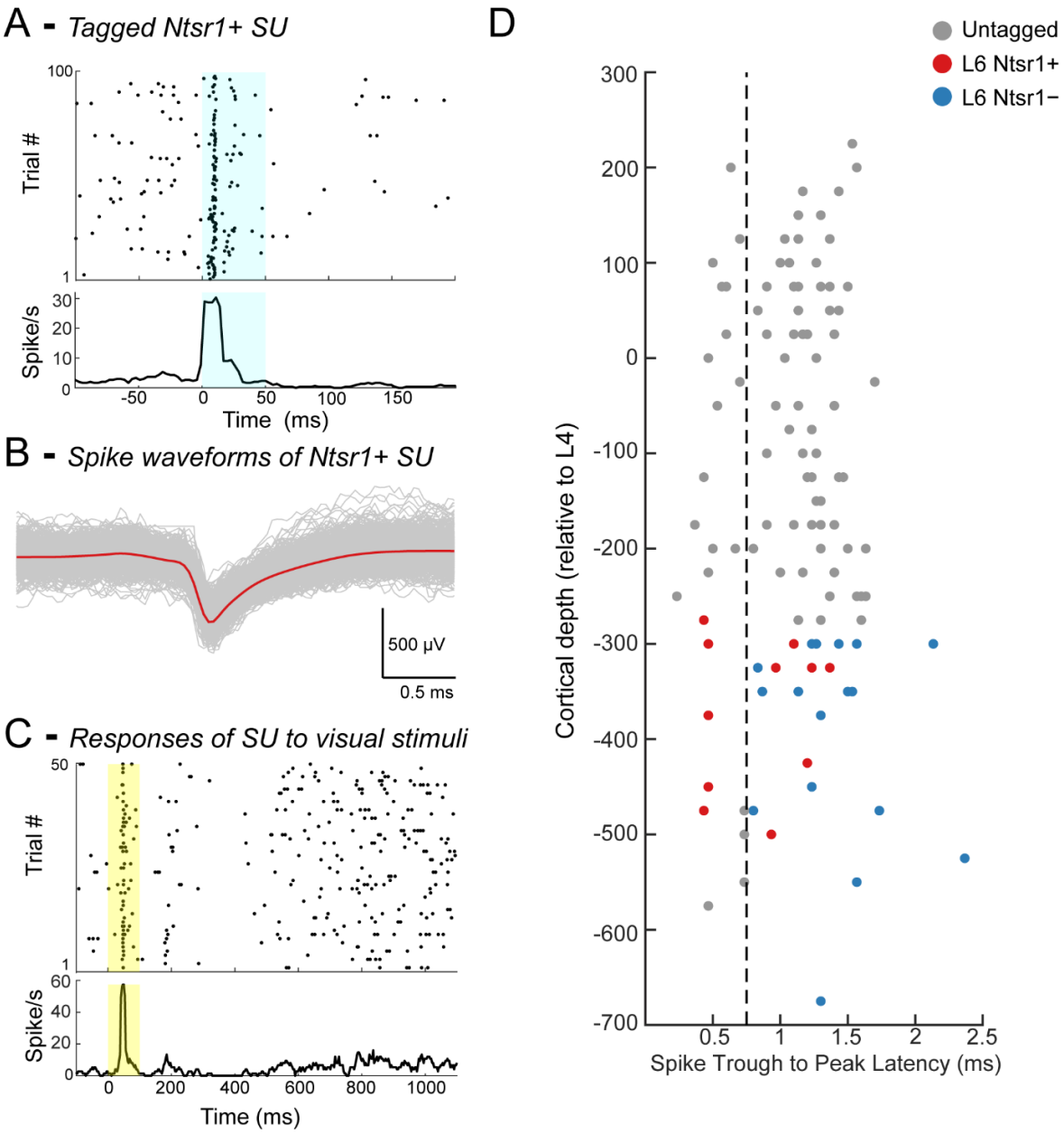


Fig. 5.10. Optogenetic spike tagging of corticothalamic L6 neurons in V1 of *Ntsr1Cre* mice. (A) Raster plot (top) and corresponding peri-stimulus time histogram (PSTH, bottom) of a representative single unit (SU) from a *Ntsr1Cre; Ai32* transgenic mouse during blue light stimulation showing reliable spiking activity used to tag Ntsr1+ corticothalamic (CT) L6 neurons.
(B) Spike waveforms for the SU tagged in A; grey lines indicate individual spike waveforms red line shows average spike waveform.
(C) Raster plot (top) and PSTH plot for the SU shown in A and B; yellow lines indicate the occurrence of the visual stimulus.
(D) Scatter plot of spike through to peak latency vs. cortical depth for all SUs obtained from *Ntsr1Cre;Ai32* animals. Grey dots show untagged SUs, red dots indicate tagged Ntsr1+ L6 neurons (putative CT), blue dots indicate untagged neurons in L6 (putative corticocortical cells, CC). Vertical dashed line in shows the arbitrary cut-off spike through to peak latency value (0.75 ms) used to identify fast-spiking (FS, left to the line) vs. regular spiking (RS, right the line) SUs.

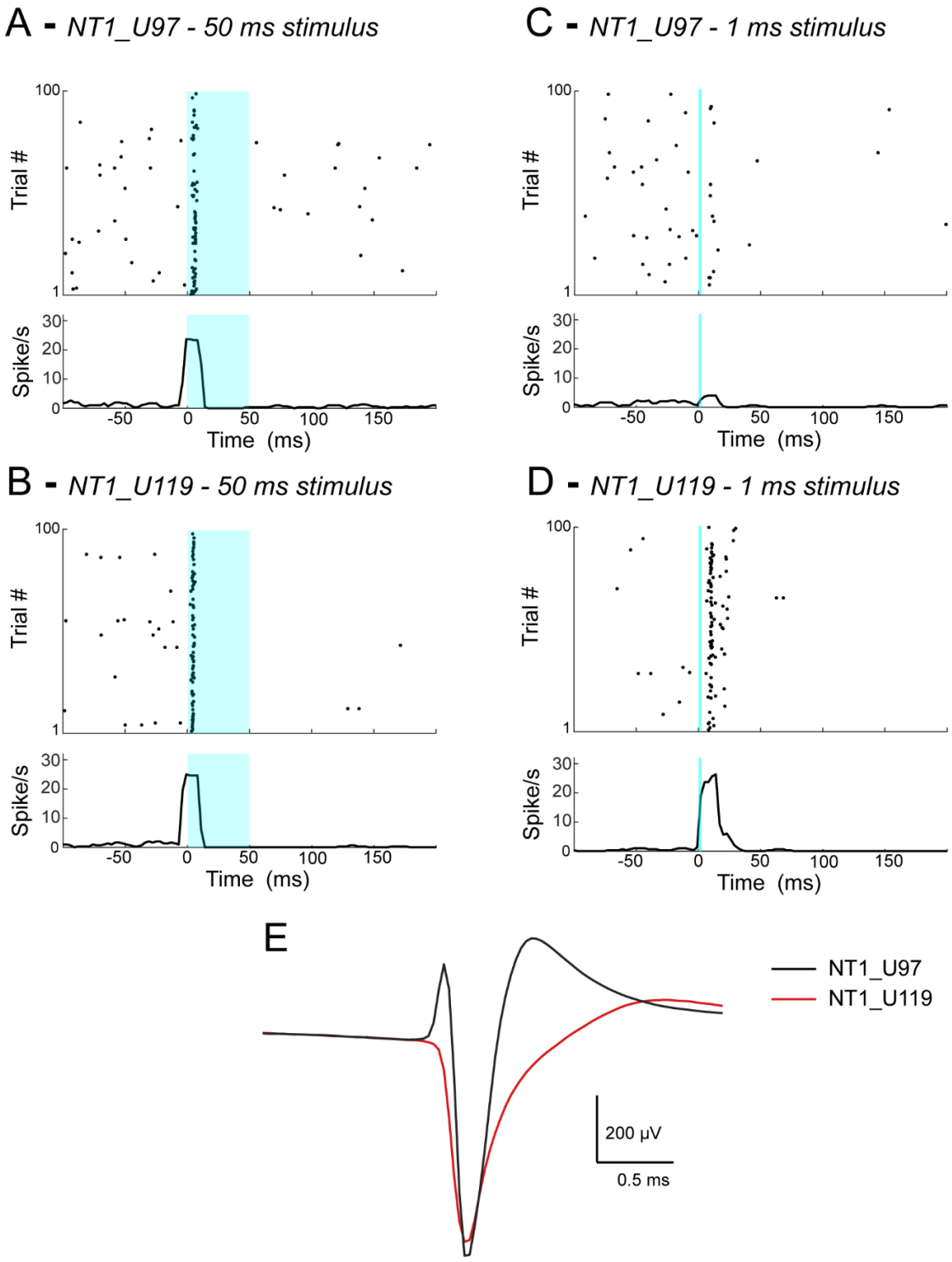


Fig. 5.11. Optotagging stimulus recruits V1 L6 FS interneurons. (A, B) Raster plot (top) and PSTH (bottom) of two distinct SUs (A, U97; B, U119) during blue light stimulation (50 ms) used to optogenetically tagged Ntsr1+ L6 neurons as putative CT neurons.
(C, D) Raster plot (top) and PSTH (bottom) for the same units shown in A and B but during a 1 ms optogenetic stimulus.
(E) Average spike waveform of the two units shown in A-D, showing a true optically tagged Ntsr1+ L6 neuron (red) and a L6 FS interneuron (black).

I next investigated how L6 CT and CC cells are recruited by sensory-evoked activity during stimulation of the visual system with a flash of white LED light near the eye. Prior to eye opening, both L6 neuron subtypes were active during the fast phase of the visual stimulation (**Fig. 5.12A**). Quantification of the ratio of SUs in each layer that are responsive to either the fast or slow phase of the visual stimulation revealed that there is a larger fraction of L6 CC cells that are responsive during the fast phase of the visual stimulation, compared with units in L2-5 (**Fig. 5.12B**). Quantification of L6 CT cells is hindered by the fact only 1 unit (although responsive, see **Fig. 5.12A**, third row) was optogenetically tagged at this age. After eye opening, SUs throughout layers were found to be responsive to visual stimulation (**Fig. 5.12C**), with similar proportions of L6 CC and L6 CT cells activated by the visual stimulation compared to RS neurons in other cortical layers (**Fig. 5.12D**).

Finally, I used optogenetics to understand the impact of activating L6 Ntsr1+ CT neurons in V1 on the cortical network during spontaneous and sensory-evoked activity. Previous work performed in adult animals showed that optogenetic activation of L6 CT cells exerts an inhibitory effect on neurons throughout cortical layers, thus contributing to gain modulation (Olsen et al., 2012). In my experiments, activation of L6 Ntsr1+ neurons had a similar effect on cortical activity reducing spiking activity during a 200-ms long optogenetic stimulus (**Fig. 5.13A, B**). Quantification of this data shows that prior to eye opening, optogenetic activation of Ntsr1+ L6 neurons lead to a reduction in firing frequency of L6 CC neurons (**Fig. 5.13C**). After eye opening, the inhibitory effect of Ntsr1+ L6 neuron activation spread to RS units in every cortical layer as well as to FS interneurons in L5/6 (**Fig. 5.13C**).

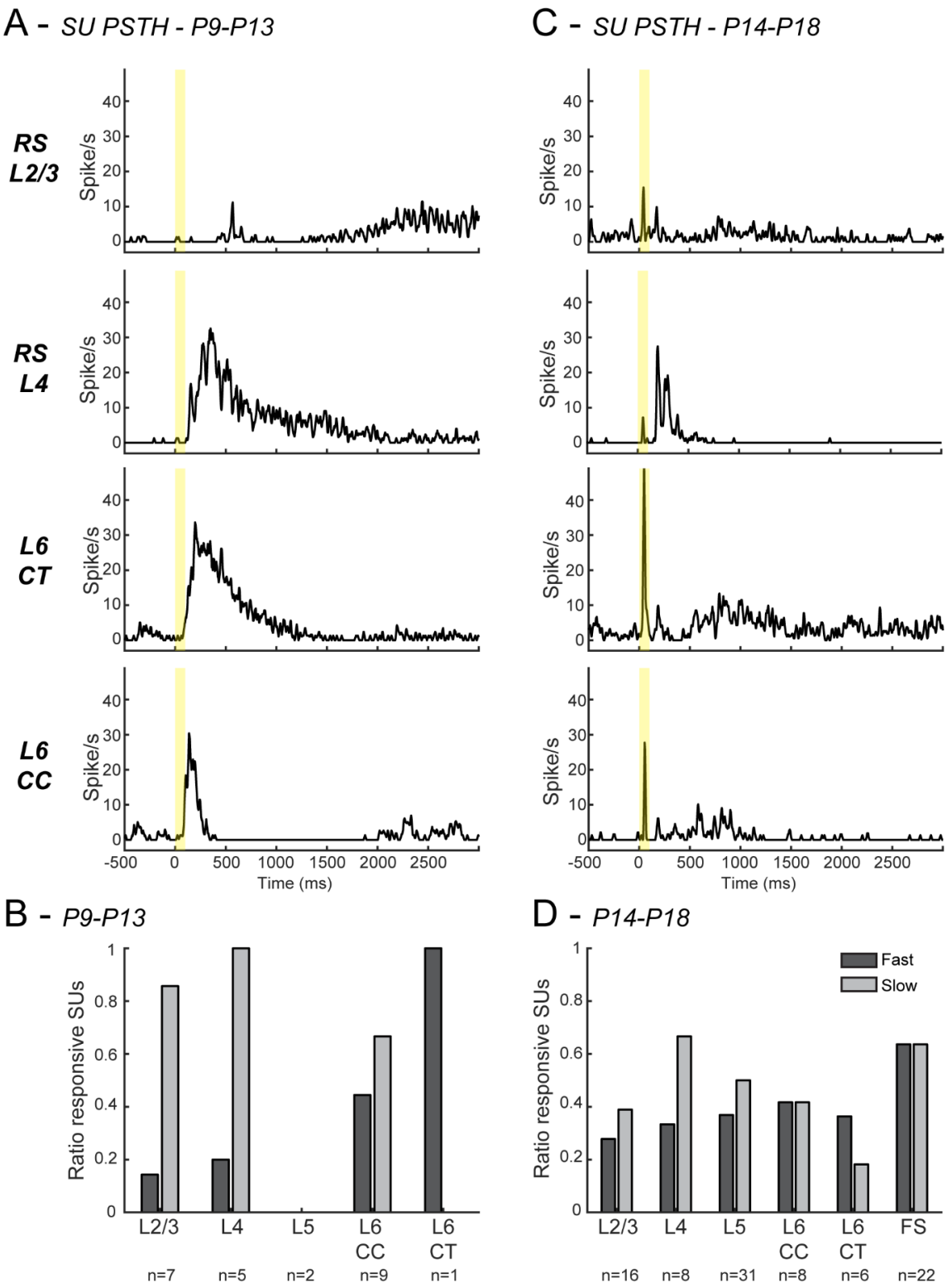


Fig. 5.12: Response of L6 neurons to sensory-evoked activity in V1 over early postnatal development. (A) PSTHs obtained from 4 distinct SUs (first row, L2/3 RS cell; second row, L4 RS cell; third row, L6 CT RS cell; last row, L6 CC RS cell) during stimulation of the visual system with a flash of white light (shown as yellow line) in awake Ntsr1Cre; Ai32 mice at P9-P13.
(B) Bar plots of ratio of responsive units to visual stimulation (total number of SUs per group shown in the plot) during the fast (dark grey) or slow (light grey) phase of the visual stimulation.
(C) Same as in A but for SUs obtained from urethane-anaesthetised Ntsr1Cre; Ai32 animals at P14-P18. (D) Same as in B but for units obtained at P14-P18.

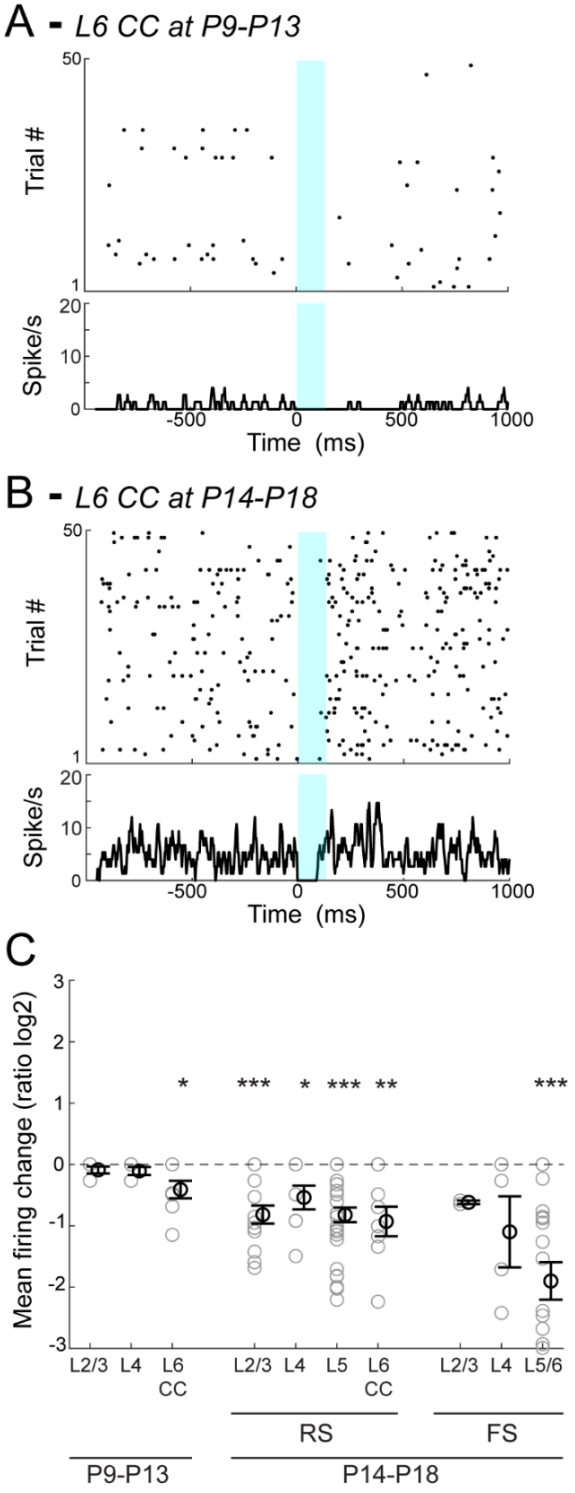


Fig. 5.13. Impact of optogenetic activation of Ntsr1+ L6 neurons on spontaneous activity of V1 SUs. (A) Raster plot (top) and PSTH (bottom) obtained from a L6 CC neuron during optogenetic activation (blue line) of L6 CT neuron in Ntsr1Cre; Ai32 mice at P9-P13.
(B) Same as in A but for a units obtained from a P14-P18 animal.
(C) Error bar (black, showing mean ± SEM) and scatter plot representing the change (log_2 of the ratio) between SU firing frequency before the optogenetic stimulus (baseline) and firing frequency during the first 100 ms of the optogenetic stimulus used to activate Ntsr1+ L6 neurons. Results of the statistical tests are as follows: L2/3 RS at P9-P13, Wilcoxon signed rank test: p = 0.5; L4 RS at P9-P13, Wilcoxon signed rank test: p = 0.5; L6 CC RS at P9-P13, single sample t-test: t(7) = −2.9, *p = 0.02; L2/3 RS at P14-P18, single sample t-test: t(15) = −5.6, ***p ≤ 0.001; L4 RS at P14-P18: single sample t-test: t(7) = −2.8, *p = 0.02, L5 RS at P14-P18: Wilcoxon signed rank test: Z = -4.5, ***p ≤ 0.001; L6 CC RS at P14-P18, single sample t-test: t(7) = −3.8, **p = 0.006; L2/3 FS at P14-P18: not tested, n = 3; L4 FS at P14-P18: single sample t-test: t(3) = −1.9, p = 0.15; L5/6 FS at P14-P18: single sample t-test: t(15) = −6.2, ***p ≤ 0.001.

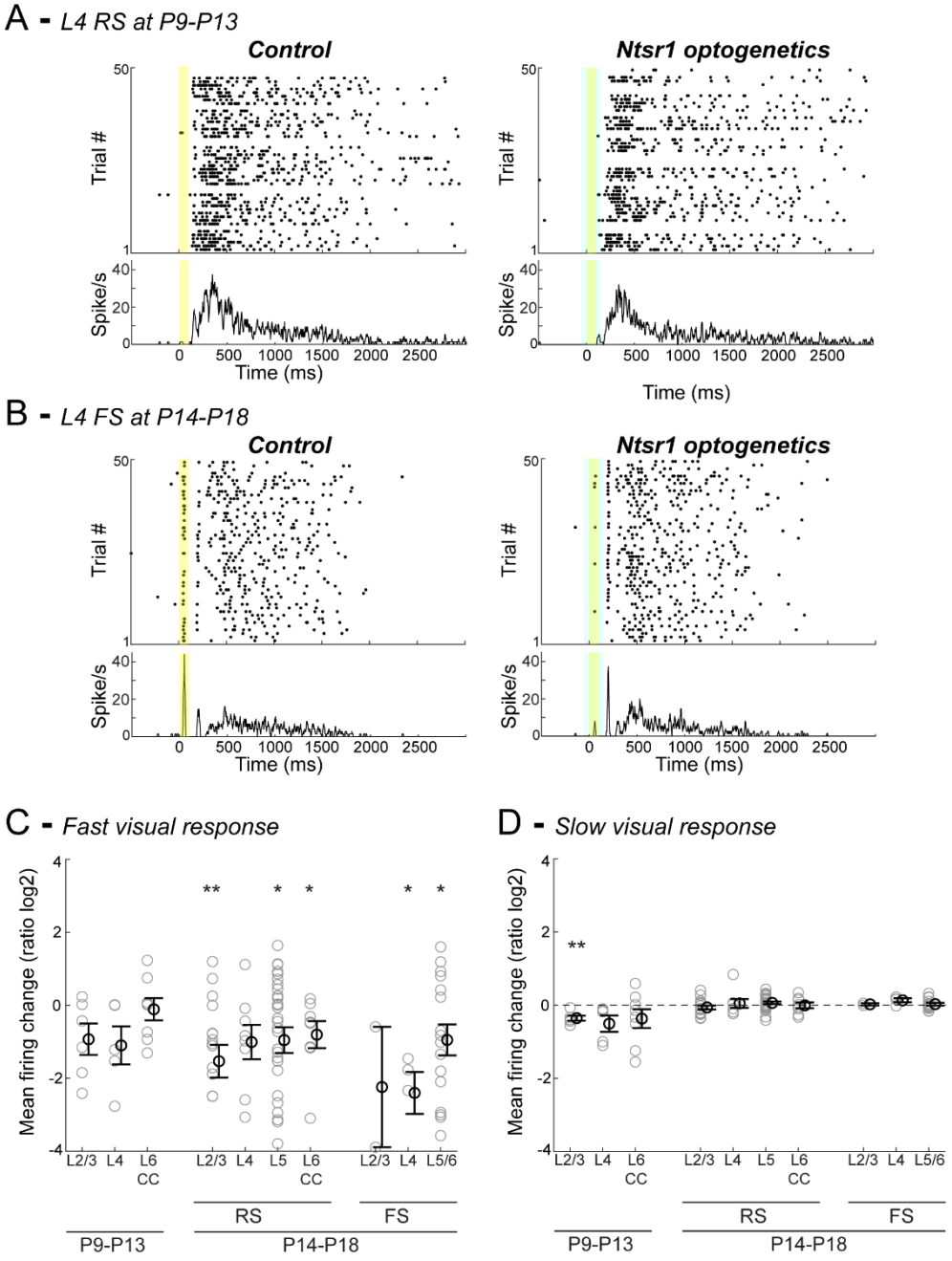


Fig. 5.14. Impact of optogenetic activation of Ntsr1+ L6 neurons on sensory-evoked activity of V1 SUs. (A) Raster plot (top) and PSTH (bottom) of a representative L4 RS unit obtained from a P9-P13 animal during stimulation of the retina with white LED light (yellow line), either alone (left, Control) or during optogenetic activation of L6 CT neurons (right, Ntsr1 optogenetics) with blue laser light (blue line).
(B) Same as in A but for a L4 FS neuron obtained from a P14-P18 animal.
(C) Error bar (black, showing mean ± SEM) and scatter plot representing the change (log_2 of the ratio) between maximum SU firing frequency during the fast phase of the visual response in control conditions and during optogenetic activation of Ntsr1+ neurons. Results of the statistical tests are as follows: L2/3 RS at P9-P13, single sample t-test: $t(5) = -2.1$, $p = 0.08$; L4 RS at P9-P13, single sample t-test: $t(4) = -2.1$, $p = 0.10$; L6 CC RS at P9-P13, single sample t-test: $t(7) = -0.4$, $p = 0.73$; L2/3 RS at P14-P18, single sample t-test: $t(15) = -3.4$, $^{**}p \leq 0.004$; L4 RS at P14-P18: single sample t-test: $t(7) = -2.1$, $p = 0.07$, L5 RS at P14-P18: single sample t-test: $t(30) = -3.2$, $^{*}p = 0.013$; L6 CC RS at P14-P18, Wilcoxon signed rank test: $Z = -3.5$, $^{*}p \leq 0.04$; L2/3 FS at P14-P18: not tested, n = 3; L4 FS at P14-P18: single sample t-test: $t(3) = -4.1$, $^{*}p = 0.02$; L5/6 FS at P14-P18: single sample t-test: $t(15) = -2.2$, $^{*}p = 0.04$.

I further used blue light optogenetic stimulation to probe the impact of activating L6 Ntsr1+ CT neurons on sensory-evoked responses in V1. Response patterns to visual stimulation of V1 SUs prior to eye opening did not appear to be altered by concomitant optogenetic activation of L6 Ntsr1+ neurons (**Fig. 5.14A**) whereas substantial reduction of fast response to sensory stimulation is observed in units after eye opening (**Fig. 5.14B**). Quantification of the change in firing frequency during the fast phase of the visual stimulation confirm the lack of effect of optogenetic activation of L6 CT cells before eye opening and a widespread reduction of responses for RS and FS units throughout layers in animals recorded after eye opening (**Fig. 5.14C**). Although a reduction of firing frequency is statistically significant for most groups at a population level, I also observed a large degree of individual variation between SUs, especially after eye opening. Optogenetic activation of L6 Ntsr1+ neurons did not have an impact on the slow phase of the sensory response, beside a small reduction in firing for L2/3 units before eye opening (**Fig. 5.14D**).

Fig. 5.14 (continue). (D) Same as in C but for average firing during the slow phase of the visual response. Results of the statistical tests are as follows: L2/3 RS at P9-P13, single sample t-test: $t(5) = -5.3$, $^{**}p = 0.003$; L4 RS at P9-P13, Wilcoxon signed rank test: $p = 0.06$; L6 CC RS at P9-P13, single sample t-test: $t(7) = -1.4$, $p = 0.19$; L2/3 RS at P14-P18, single sample t-test: $t(15) = -1.2$, $p \leq 0.26$; L4 RS at P14-P18: Wilcoxon signed rank test: $p = 0.6$; L5 RS at P14-P18: single sample t-test: $t(30) = 1.8$, $p = 0.07$; L6 CC RS at P14-P18, single sample t-test: $t(7) = -0.07$, $p = 0.94$; L2/3 FS at P14-P18: not tested, $n = 3$; L4 FS at P14-P18: single sample t-test: $t(3) = 2.5$, $p = 0.08$; L5/6 FS at P14-P18: single sample t-test: $t(15) = 0.72$, $p = 0.47$.

5.5 – Summary of results

In the final experimental ***Chapter*** of this thesis, I characterised the development of GABAergic networks of L6 excitatory neurons in primary sensory areas of mouse neocortex. The main results are summarised below:

- In V1, pyramidal neurons in L6 are engaged in a transient developmental neuronal network, receiving GABAergic connections from supragranular interneurons during the earliest developmental window studied (P5-P8). From P9 onward, L6 pyramidal cells are dominated by local GABAergic connectivity.

- Through optogenetic experiments, I found connectivity from SST+ interneurons onto L6 pyramidal cells is relatively weak and sparse around the first developmental week, whereas connectivity from Nkx2-1+ interneurons (including both SST+ and PV+) is much stronger.

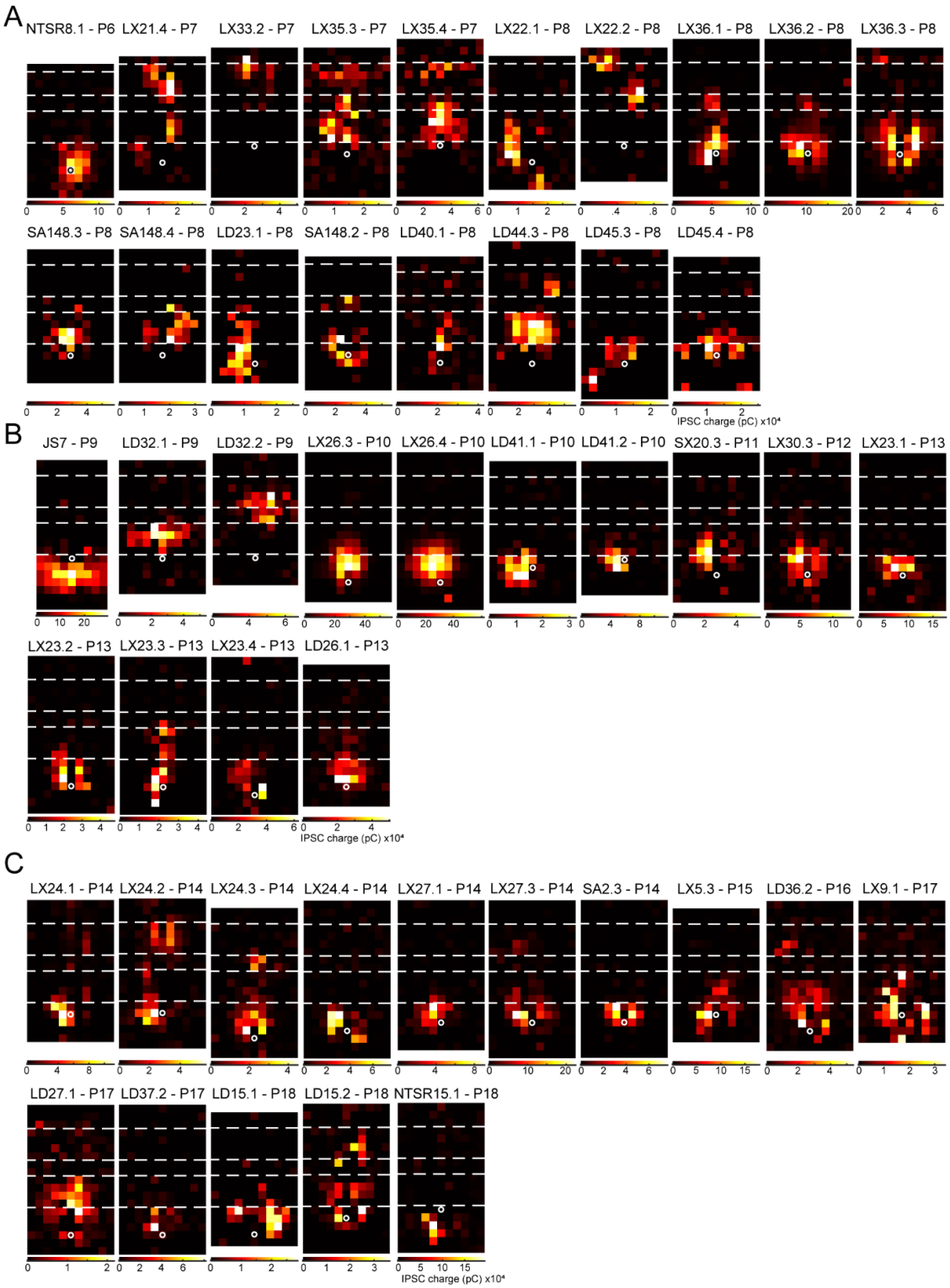
- L6 pyramidal neurons in S1BF display different GABAergic connectivity patterns from corresponding neurons in V1, as they are characterised by local GABAergic inputs from L6 as well as translaminar inputs from L5b. Unlike in V1, GABAergic inputs from L5b might derive from SST+ interneurons.

- Despite the differences in network architectures between V1 and S1BF, the distribution of MGE-derived Lhx6+ interneurons over development is similar between the two sensory areas, thus excluding possible delayed migration of interneurons in V1.

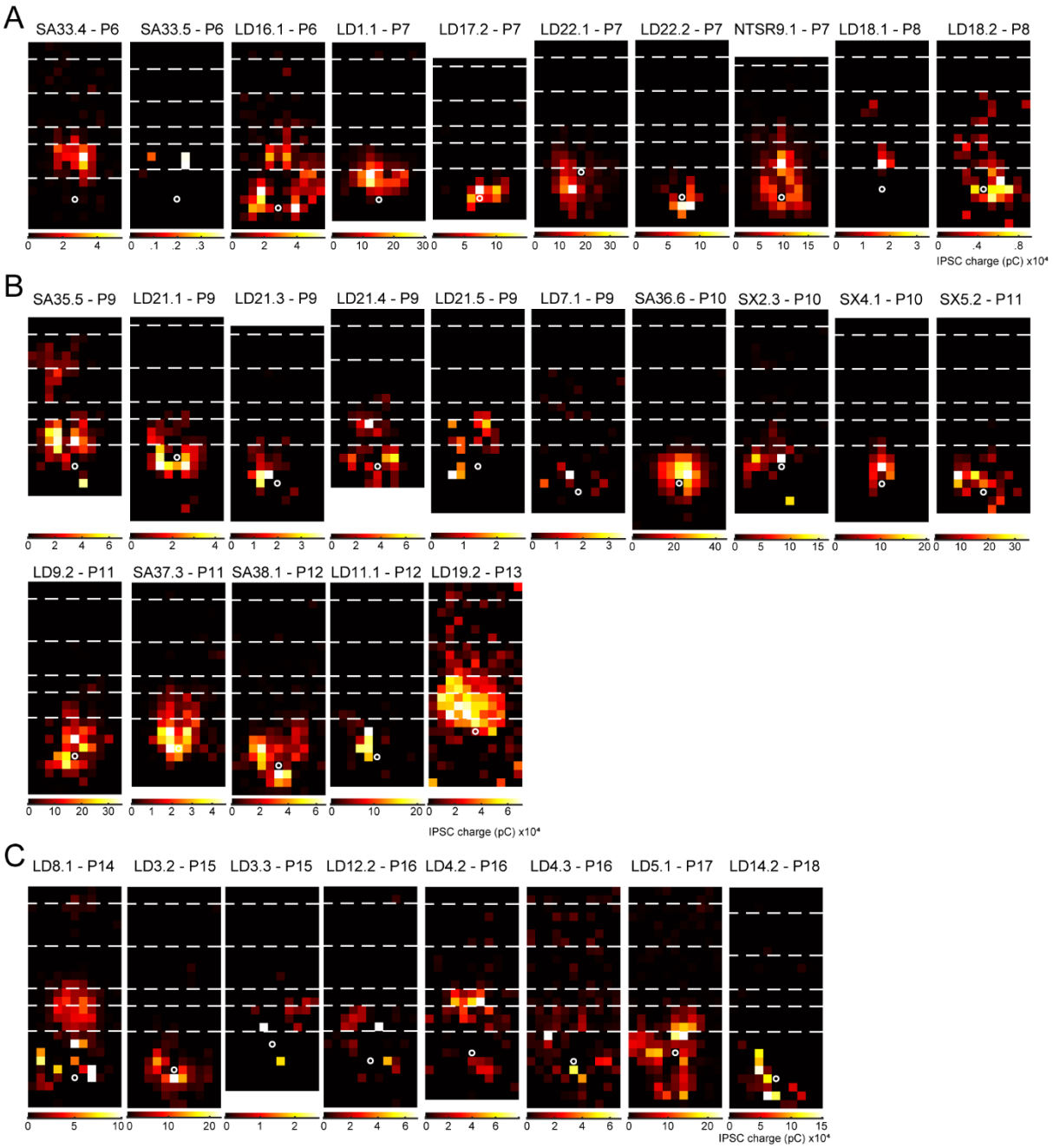
- I then explored the individual differences among L6 pyramidal neurons in V1, by focusing on CT L6 cells expressing Ntsr1. Although Ntsr1+ L6 CT neurons retract their apical dendrite from supragranular layers around the same time the transient GABAergic connectivity is observed, they are characterised exclusively by local GABAergic inputs throughout development. Conversely, a small proportion of CC L6 pyramidal neurons might be engaged in the translaminar GABAergic connections at P5-P8.

- Finally, I employed optogenetics during *in vivo* electrophysiological recordings in awake head-fixed mouse to attempt to understand how L6 CT and CC neurons participate in sensory-evoked activity. Prior to eye opening, L6 CC cells are recruited by visual stimulation in higher proportion than neurons in granular and supragranular layers.

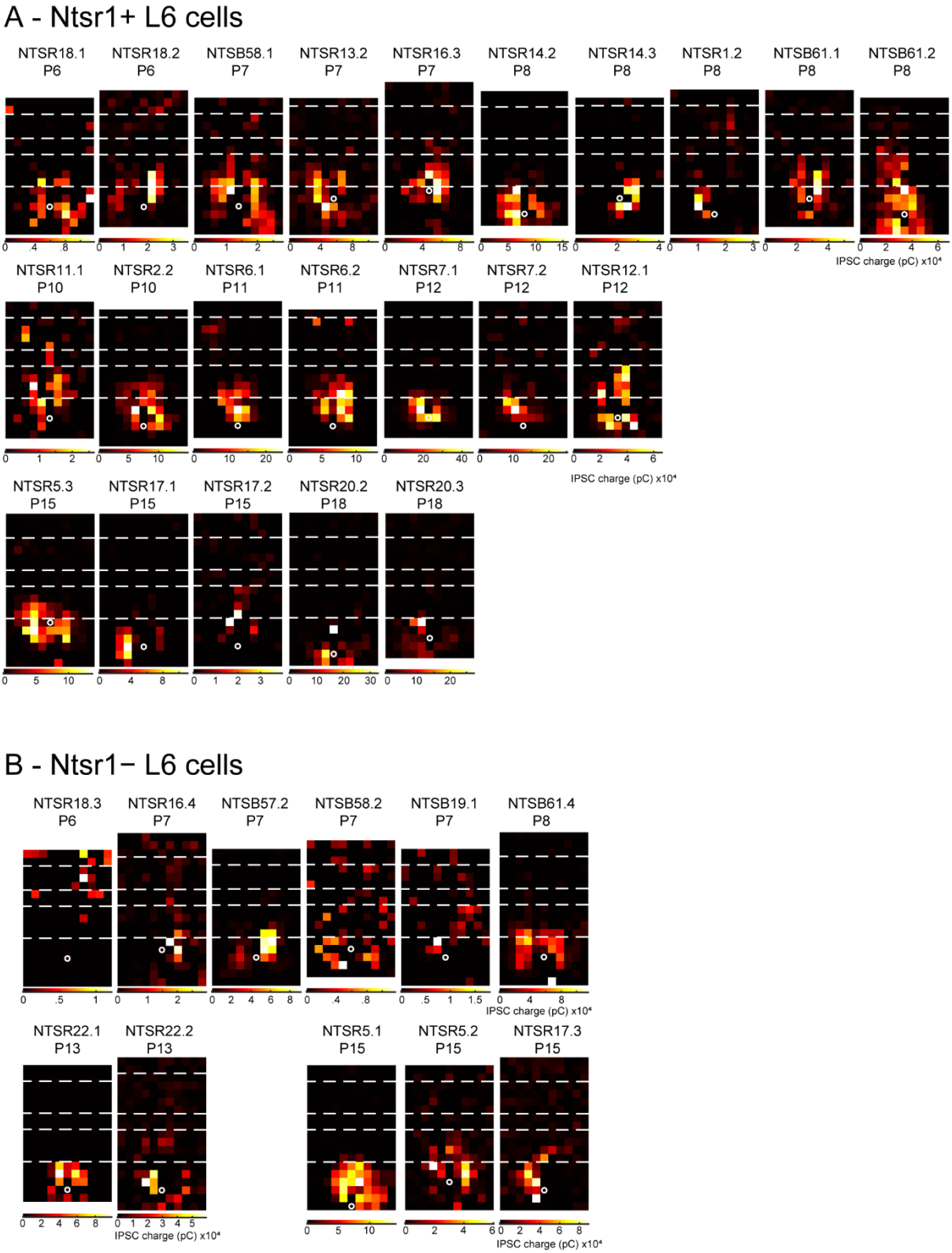
- Optogenetic activation of L6 CT neurons led to widespread inhibitory effects on the spontaneous firing of neurons in other layers after eye opening, whereas only L6 CC cells were inhibited at P9-P13. Activating L6 CT cells during sensory-evoked stimulation led again to a reduction in firing frequency during the fast phase of the visual responses in several neuronal cell types, but only after eye opening.



Supp. Fig. 5.1. GABAergic connectivity maps for L6 pyramidal neurons recorded in V1 at P5-P8 (A), P9-P13 (B), and P14-P18 (C). In every heatmap, white or black circle indicate approximate location of the recorded cell, dashed horizontal lines indicate approximate layer boundaries (from top to bottom: L1, L2/3, L4, L5 and L6).



Supp. Fig. 5.2. GABAergic connectivity maps for L6 pyramidal neurons recorded in S1BF at P5-P8 (A), P9-P13 (B), and P14-P18. In every heatmap, white or black circle indicate approximate location of the recorded cell, dashed horizontal lines indicate approximate layer boundaries (from top to bottom: L1, L2/3, L4, L5 and L6).



Supp. Fig. 5.3. GABAergic connectivity maps for Ntsr1+ L6 pyramidal neurons (A) and Ntsr1− L6 pyramidal neurons (B) recorded in V1 at different ages. In every heatmap, white or black circle indicate approximate location of the recorded cell, dashed horizontal lines indicate approximate layer boundaries (from top to bottom: L1, L2/3, L4, L5 and L6).

Chapter 6

Discussion

This thesis provides a detailed characterisation of neuronal networks and functions of cortical GABAergic interneurons in the primary visual cortex (V1) over early postnatal development in the mouse. The reader is referred to the last section of each experimental ***Chapter*** for a summary of the main results obtained. The overarching theme that permeates our finding is the degree of difference between two primary sensory areas as V1 and the barrel cortex (S1BF). Distinct neuronal networks can be found at the level of cell types, cortical layers, and synaptic connections; differences at the network level links to functional diversity. Of note, somatostatin-expressing (SST+) interneurons differ in term of input and output connectivity between the two sensory areas, establishing networks to control emergent activity in distinct ways. In analogy, L6 pyramidal neurons in the two primary cortices are engaged by distinct GABAergic interneuron subtypes residing in different cortical layers. My *in vivo* electrophysiology experiments provided insights as to functional implication of the different SST+ interneuron network architectures whereas the interpretation of L6 pyramidal cell networks is made more complex by their large degree of heterogeneity.

6.1 – Feedback and feed-forward GABAergic networks by somatostatin interneurons across primary sensory areas

One common developmental pattern that characterises both V1 and S1BF is the early integration of SST+ interneurons in their respective networks. Throughout the cerebral cortex, SST+ interneurons are among the first to integrate (Miyoshi et al., 2007) and display mature electrophysiological properties at early ages (Pan et al., 2019). In line with previous findings, our experiments showed maturation of electrophysiological properties of SST+ interneurons is largely completed by the time of eye opening, while excitatory pyramidal neurons in every layer (except L6) mature later, following an inside-out pattern. Conversely,

PV+ interneurons maturation of electrophysiological and morphological properties is still ongoing around the time of eye opening and continues through the critical period for binocular plasticity (Chattopadhyaya et al., 2004). Therefore, SST+ cells are ideally suited to be the main source of GABAergic signalling in the developing V1.

SST+ interneurons also show critical differences in their integration in the developing cortical network when compared to their counterpart in S1BF, concerning both input and output connectivity. In term of output connectivity, SST+ interneurons at the L4-L5 boundary are integrated in a reciprocal network with thalamo-recipient L4 pyramidal neurons in V1 throughout early development. In S1BF, a reciprocal connection between thalamo-recipient spiny stellate neurons (SSNs) in L4 and SST+ interneurons in L5b is found during the first postnatal week (Marques-Smith et al., 2016), highlighting a critical difference between the developmental trajectories of the two brain areas. In term of input connectivity, I investigated the development of thalamic inputs onto various V1 cell types, including SST+ interneurons. In S1BF, SST+ interneurons receive transient, direct thalamic excitatory connections around the same developmental age when the L5b-L4 loop is present, that is the first postnatal week (Marques-Smith et al., 2016; Tuncdemir et al., 2016). My experiments showed that in V1, SST+ interneurons do not receive direct thalamic projections throughout early development and their responses to optogenetics stimulation of thalamic terminals are consistent with a polysynaptic origin, similarly to experiments performed in juvenile animals (Kloc and Maffei, 2014). This result, combined with direct monosynaptic thalamic connections onto a large fraction of L2/3 and L4 pyramidal neurons and *in vitro* circuit mapping revealing local excitatory connections onto infragranular SST+ cells, points to indirect recruitment of SST+ interneurons by thalamic inputs through local pyramidal cells. Critically, by receiving direct thalamic inputs and providing GABAergic signalling to L4 SSNs, SST+ interneurons in S1BF establish an early, transient feed-forward inhibitory motif during the first postnatal week of development (Fig. 6.1A; Marques-Smith et al., 2016; Tuncdemir et al., 2016). In V1, SST+ interneurons appear only involved in feedback

inhibitory networks (**Fig. 6.1B**), since they are recruited by local excitatory neurons, in turn activated by the thalamus. Thus, while SST+ interneurons are integrated early in both S1BF and V1 cortical networks, they might control information processing in distinct fashions through these distinct network motifs.

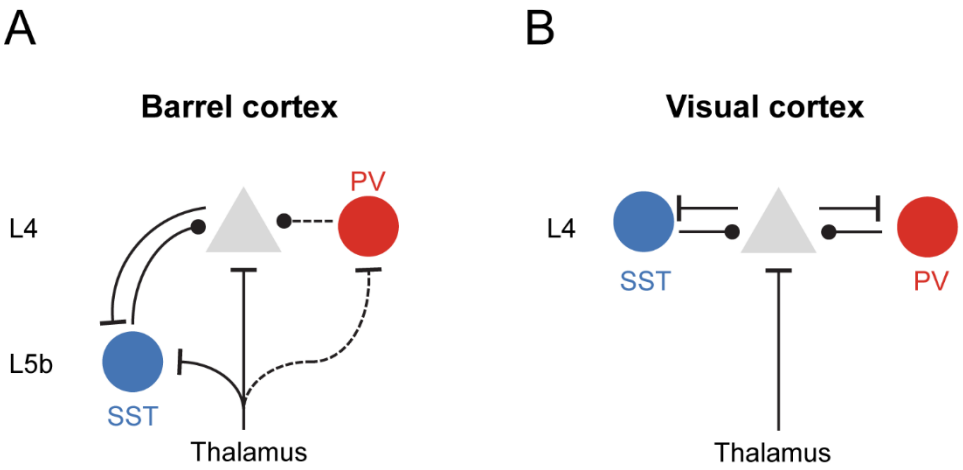


Fig. 6.1. Feedback and feed-forward GABAergic networks by somatostatin interneurons across primary sensory areas. Schematics of the neuronal connections between GABAergic interneurons (SST+, blue; PV+, red) onto L4 excitatory cells (grey), highlighting a transient feed-forward motif through SST+ interneurons in the barrel cortex (A) and feedback GABAergic signalling in the visual cortex (B).

In vivo electrophysiological experiments presented in ***Chapter 4*** shed light on functions of SST+ interneurons in V1 and S1BF. The data presented here are in line with previous experiments showing how GABAergic interneurons (Duan et al., 2020; Modol et al., 2020), and SST+ interneurons in particular (Leighton et al., 2021), are entrained by spontaneous activity, which in V1, take the form of spindle burst oscillations induced by peripheral retinal waves (Hanganu et al., 2006). Prior to eye opening, SST+ cells are activated during the slow oscillatory phase of the response to visual stimulation, which might correspond to light-induced retinal waves (Tiriac et al., 2018). This is in line with the SST+ network description, with recurrent cortical excitation progressively recruiting SST+ interneurons during the oscillatory cycles, likely thanks to facilitating synapses (Miao et al., 2016). Only a minority of SST+ cells responded directly to light stimulation, in support of poor recruitment of GABAergic interneurons by thalamic inputs before eye opening.

Through optogenetic activation of SSTCre-expressing interneurons, I showed they exert an inhibitory action at the population level onto pyramidal neurons throughout cortical layers, already prior to eye opening. Such inhibitory action is observed both at the level of spontaneous firing activity of cortical single units, as well as during sensory responses to visual stimulation, both fast and slow phases. Experiments focussed on Nkx2-1Cre-expressing (Nkx2-1+) interneurons, which comprise both SST+ and PV+ subtypes, suggest SST+ interneurons might play a pivotal role in providing GABAergic signalling before eye opening, given the more subtle effects of optogenetic activation of Nkx2-1+ interneurons at the network level.

Inhibitory GABAergic signalling through SST+ interneurons is ideally suited to exert control over spontaneous activity in more realistic settings that the one attained during optogenetics experiments. Previous research in the developing V1 showed that, by participating in spontaneous network oscillations, SST+ interneurons can limit the recruitment of excitatory neurons as well as the lateral spread of those events (Leighton et al., 2021). Together with analogous results obtained in the early S1BF (Modol et al., 2020), this points to an increase in synchronous activity at the population level with impact on GABAergic interneuron survival (Duan et al., 2020). However, in my hands, chemogenetic inhibition of SST+ interneuron led to an apparent opposite effect, with increase baseline firing rate of V1 single units and reduced percentage of spikes occurring within spindle bursts with no change in the ratio of single units entrained by spontaneous network events. The reason for this discrepancy might reside in the different techniques employed, electrophysiology in my case vs. calcium imaging in the study by Leighton et al. (2021), as well as in the analytical pipeline. Indeed, Leighton et al. (2021) focussed on period of low-participation Ca^{2+} events and observed increased recruitment of excitatory neurons in supragranular layers during such events. Through the “lenses” of electrophysiology, I could observe an increase in spontaneous firing rate, especially occurring outside spindle bursts (given the reduction of spike probability within events). Lack of change in the ratio of V1

single units entrained by spindle burst oscillations might be explained by the statistical tests used to determine significant entrainment, which is based on comparing spikes within and outside events. Other sources of discrepancy might reside in the sampling bias for neurons in supragranular (Ca^{2+} imaging) or infragranular (electrophysiology) layers or in the inability to distinguish between low-participation (retinal-driven) and high-participation network event (cortical-driven; Siegel et al., 2012) through the techniques employed in my experiments.

Despite this discrepancy, inhibition of feedback GABAergic signalling by SST+ interneurons impacts spontaneous activity recorded in V1, which in turn disrupt synchronous activity with implications for network maturation. Since V1 neurons immediately after eye opening already express several sensory responses typical of adult animals (Rochefort et al., 2011; Ko et al., 2013; Hoy and Niell, 2015; Gu and Cang, 2016), it would be interesting to test, in future experiments, the impact of chronic inhibition of SST+ interneurons for the development of response features like orientation- or direction-selectivity.

Preliminary results obtained from chemogenetic inhibition of SST+ interneurons in S1BF are in support of their transient feed-forward role in the cortical network, which allows them exerting control over sensory processing at early ages. Analysis of L4 multi-unit activity in S1BF during acute inhibition of SST+ interneurons led to larger responses to whisker stimulation at P5-P8 but not later. The first postnatal week in the mouse S1BF is defined as the critical period for L4 plasticity (Crair and Malenka, 1995); during this stage, GABAergic signalling to L4 SSNs is provided by SST+ interneurons located in L5b (Anastasiades et al., 2016; Marques-Smith et al., 2016) at a time when the canonical feed-forward motif by PV+ interneurons is not functional (Daw et al., 2007). The experiments presented in this thesis add to the current literature that showed how chronic inactivation of SST+ interneuron function in S1BF led to impairment in short-term facilitation of sensory responses (Baruchin et al., 2021) and disruption of PV+ interneurons signalling to excitatory cells (Tuncdemir et al., 2016).

6.2 – Parvalbumin interneurons establish the canonical feed-forward inhibitory motif at the time of eye opening in V1

The developmental timeline for PV+ interneurons also differs between the two primary sensory areas, V1 and S1BF. In L4 of primary sensory areas, PV+ interneurons establish a canonical theme of inhibitory connection, known as fast feed-forward inhibition whereby L4 PV+ interneurons receive thalamic input similarly to L4 excitatory neurons and, in turn, inhibit the local excitatory cells to limit their excitability upon thalamic activation (Cruikshank et al., 2007). In S1BF, the fast feed-forward inhibitory motif appears at the end of the first postnatal week (Daw et al., 2007), and it is a kay factor driving the closure of the critical period for L4 plasticity (Minlebaev et al., 2011). During this period, activity in S1BF is dominated by bursting activity, whether spontaneous spindle bursts (Khazipov et al., 2004) or early gamma oscillations evoked by whisker stimulation (Minlebaev et al., 2011). These patterns of oscillatory activity are in place to provide multiple windows of opportunity for synaptic plasticity to occur (Butts and Kanold, 2010; Minlebaev et al., 2011), with early GABAergic signalling through SST+ interneurons required to sustain oscillations at cortical level (Minlebaev et al., 2011). The onset of the feed-forward inhibitory motif by PV+ interneurons, around the end of the first postnatal week (Daw et al., 2007), poses an end to the early “bursting” period, with cortical activity progressing toward its mature form (Colonnese et al., 2010).

Experiments presented in ***Chapter 3*** show that, in V1, L4 PV+ interneurons are rather immature in electrophysiological and morphological properties prior to eye opening. Only after eye opening, they are consistently engaged by direct, putative monosynaptic thalamic inputs, when the fast feed-forward inhibitory motif also comes online. This is in line with the disappearance of retinal waves coinciding with eye opening (Blankenship and Feller, 2010). Similar to S1BF, maturation of PV+ interneurons determine the timing of the transition between developmental bursting activity to mature activity in the thalamocortical network. Remarkably, this transition occurs approximately a week later in V1 compared to S1BF.

In vivo electrophysiological experiments presented in ***Chapter 4*** supports the finding at network level. After eye opening, PV+ interneurons dominate GABAergic signalling onto L4 pyramidal neurons in V1, as demonstrated by a stronger inhibitory impact of optogenetic activation of Nkx2-1+ interneurons compared to SST+ cells, especially during spontaneous activity. Before eye opening instead, activity of Nkx2-1+ interneuron does not differ from the one of SST+ interneurons, with only a reduction in coupling to beta frequency oscillations in the former. It is conceivable both PV+ and SST+ interneurons contribute similarly to feedback GABAergic signalling before the onset of active perception, although the early maturation of SST+ interneurons (Pan et al., 2019) may suggest the latter to have a role of priority.

The reason for the delayed appearance of the feed-forward inhibitory motif in V1 might reside in differences at ecological level between the sensory requirements of the two primary sensory areas. Sensory responses to whisker stimulation are essential during early postnatal development, when passive stimulation through contacts with littermates and tactile contacts during movement provide continuous stimulation of the somatosensory system to pups in the nest (Akhmetshina et al., 2016). Conversely, the visual system is dominated by spontaneous activity (Blankenship and Feller, 2010), with light only increasing the likelihood of phase III retinal waves occurrence (Tiriac et al., 2018). In V1, maturation of feed-forward PV+ inhibition could be detrimental to limit bursting activity and must be delayed up until the onset of active perception.

6.3 – A role for dis-inhibitory networks in state-dependent control of sensory processing before active perception

One plausible reason for the delayed integration of L4 PV+ interneurons in the fast feed-forward inhibitory motif in V1 might be found in the development of dis-inhibitory networks between SST+ and PV+ interneurons. My *in vitro* circuit mapping experiments suggest SST+ interneuron connection onto L4 PV+ interneurons in V1 might be stronger than the connection onto L4 pyramidal cells, in the time before eye opening, and precedes dis-

inhibitory networks established in L2/3 (Guan et al., 2017). The functional implications of this connectivity motif are unclear, given the complex role SST+ interneurons play in a mature cortical network, where they integrate bottom-up sensory information (Adesnik et al., 2012; Attinger et al., 2017) with top-down (Shen et al., 2020) and neuromodulatory inputs (Chubykin et al., 2013; Yaeger et al., 2019) and relay them to the local cortical network. Experiments described in ***Chapter 3***, might imply that, regardless of the nature of inputs onto SST+ interneurons, they might favour L4 PV+ interneurons to delay their maturation until the time of eye opening. It is noteworthy, however, that maturation of PV+ interneurons continue throughout the fourth postnatal week (Chattopadhyaya et al., 2004), implicating processes at the transcriptional level.

Comparative experiments on the development of dis-inhibitory connection between SST+ and L4 PV+ interneurons in S1BF highlighted another difference between the two primary sensory areas. Before active whisking, L4 PV+ interneurons in S1BF receive a transient GABAergic connection from SST+ interneurons located in L5b. The appearance of this transient connectivity follows the disappearance of the L5b-L4 loop involving L4 excitatory SSNs in S1BF (Marques-Smith et al., 2016). In agreement with previous findings from our lab, SST+ interneurons in L5b of S1BF appear to progressively target cortical neurons involved in synaptic plasticity mechanisms in relation to developing thalamocortical connection, with subplate neurons first (Ghezzi et al., 2021), followed by L4 (Marques-Smith et al., 2016) and L2/3 excitatory cells (Anastasiades et al., 2016). Of note, L5b SST+ cells target L4 PV+ interneurons and L2/3 pyramidal neurons at the same time (Anastasiades et al., 2016), just before active whisking, at a time of heightened synaptic plasticity at the L4-L2/3 excitatory synapse (Wen and Barth, 2011). Whether GABAergic signalling from L5b SST+ cells is important in this process has yet to be determined.

Despite the difference in the presynaptic layer location of SST+ interneurons, a common pattern that emerged from my experiments is the prevalence of a dis-inhibitory connection from SST+ interneuron onto PV+ cells in the P9-P13 window. Despite differences at the

level of immature sensory processing described in the previous section, this window corresponds to a period that precedes the onset of active perception in both sensory areas, with eye opening and onset of active whisking approximately occurring around the same time. Active perception requires not simply bottom-up sensory processing functions, but also integration with top-down control related to movement information and feedback from higher-order sensory areas (Attinger et al., 2017; Pakan et al., 2018; Shen et al., 2020), as well as neuromodulatory inputs that regulate state transitions, attention, and learning (Khan et al., 2018; Poort et al., 2021). GABAergic interneurons are known to integrate several top-down and neuromodulatory signals. Particularly, the various network connectivity motifs established by SST+ and vasointestinal peptide-expressing (VIP+) interneurons are ideally suited to integrate neural signals from various sources and relaying them to the cortical network through direct inhibition of excitatory cells or dis-inhibitory motifs (Pfeffer et al., 2013; Heintz et al., 2020). I would speculate a possible role for the SST+ connection onto PV+ interneurons in relaying top-down or modulatory information to dis-inhibit L4 pyramidal cells, whose onset might occur in the period preceding active perception. This could be tested in future experiments by mapping the development of inter-areal synaptic connections onto defined interneurons subtypes in V1 and S1BF (Vagnoni et al., 2020).

An insight related to possible state-dependent information gated by SST+ interneurons might be found in my experiments in non-anaesthetised, head-fixed mice. Increased baseline firing frequency and reduced probability of spike within spindle burst events during spontaneous activity could be found both during chemogenetic inhibition of SST+ interneurons and in non-anaesthetised animals when compared to animals under urethane anaesthesia. While these might be converging findings achieved through distinct mechanisms, I would speculate about a possible function of SST+ interneurons in gating effects of the anaesthetic in V1. In this view, inhibition of SST+ interneurons through chemogenetics reverts the cortical network to a seemingly awake state. Investigating the impact of the state of the animal and the integration of top-down information by GABAergic

interneurons during development of primary sensory areas is a promising avenue for future research in developmental neuroscience.

6.4 – A translaminar GABAergic network between supragranular cortical interneurons and L6 pyramidal neurons

Further differences at network level between V1 and S1BF were found when investigating GABAergic network of L6 pyramidal neurons. In V1, I identified a translaminar GABAergic network that involved interneurons located in supragranular cortical layers projecting onto L6 pyramidal cells at the earliest time window investigated, around the end of the first postnatal week. Although SST+ interneurons are the earliest to integrate in developing networks (Miyoshi et al., 2007; Pan et al., 2019), optogenetics experiments revealed that they provide weaker synaptic connections than Nkx2-1+ interneurons, pointing to an involvement of PV+ interneurons in this translaminar motif. Another possible source of GABAergic signalling from supragranular interneurons are VIP+ interneurons, which are known to impact infragranular cells in S1BF (Vagnoni et al., 2020). Corresponding experiments performed in S1BF showed that L6 pyramidal neurons are not targeted by supragranular interneurons at the ages investigated, yet a portion of them receives inputs from L5b, which might include SST+ interneurons. Remarkably, these experiments provided further evidence pointing to a critical role of SST+ interneurons in L5b in providing GABAergic signalling in the early S1BF. Concerning V1, since immunohistochemical experiments did not show any proof related to differences at migration level between the two areas, I propose deep layer pyramidal neurons might receive innervation from supragranular PV+ cells thanks to their immature morphology, characterised by elongated and simple axonal processes that can reach L6 (see ***Chapter 3***).

What might be a plausible reason for a translaminar connection from L2/3 GABAergic interneurons onto L6 pyramidal neurons? Previous research showed that L6 pyramidal neurons are extremely diverse and integrate a variety of local, top-down, and bottom-up inputs (Thomson, 2010). Moreover, it is thought that a portion of L6 cells receive direct

thalamic input from the dorso-lateral geniculate nucleus (Vélez-Fort et al., 2014; Frandolig et al., 2019), together with inputs from L4 pyramidal cells (Cotel et al., 2018). *In vivo*, supragranular and granular layers are known targets of the primary sensory thalamus with spindle burst events mainly recorded there (Shen and Colonnese, 2016). It is conceivable that descending GABAergic signalling from supragranular interneurons engaged in oscillatory activities might support synaptic plasticity mechanisms to establish the direct thalamocortical innervation onto L6 cells. Similarly, I also identified an early excitatory connection from L2/3 pyramidal neurons onto infragranular SST+ cells in V1, pointing to a role for descending translaminar connections in coordinating activity with deep cortical layers at early ages.

I next employed the *Ntsr1Cre-GN220* transgenic mouse line to target corticothalamic L6 neurons for *in vitro* circuit mapping experiments. These cells are characterised by long apical dendrite ascending to L1 which are retracted over early development (Sundberg et al., 2018) but are hence suited to integrate translaminar inputs, including from L2/3. Despite the timing for apical dendrite retraction matches with the translaminar GABAergic connectivity, L6 Ntsr1+ neurons in V1 are only targeted by local GABAergic inputs, with a minority of L6 Ntsr1− cells receiving translaminar connections. The latter might include subpopulations of cortico-cortical L6 neurons that target higher-order visual cortices as well as cortico-claustral L6 neurons whose function is still poorly known (Cotel et al., 2018). It is still contentious what L6 excitatory neurons subtype are engaged by the thalamus, with a recent paper suggesting cortico-claustral L6 neurons are targeted by thalamic input directly and indirectly through L4 (Cotel et al., 2018). Further experiments are needed to reveal mature functions of L6 neuron subtypes as well as their connectivity patterns in the early brain.

The availability of a specific transgenic line to study L6 corticothalamic cells allowed to reveal how they are involved in the regulation of V1 functions. At the local level, they provide gain modulation through potent activation of local translaminar interneurons in L6 (Olsen et

al., 2012; Bortone et al., 2014). Through their corticothalamic projections, they can regulate information processing in the visual system through excitatory or inhibitory effect depending on the precise level of cortical activity (Crandall et al., 2015). Even during cortical development, corticothalamic projections are involved in the generation of spindle bursts events (Murata and Colonnese, 2016) and regulate retinogeniculate refinement (Seabrook et al., 2013; Thompson et al., 2016). My *in vivo* experiments using the *Ntsr1Cre-GN220* transgenic line showed that Ntsr1− L6 cells are recruited by visual stimulation before eye opening, whereas low sample size did not allow to understand the exact contribution of Ntsr1+ L6 cell. In the absence of a better way to discriminate L6 subtypes, Ntsr1− cells might also include subplate neurons, known targets of thalamocortical connections early in V1 development (Kanold et al., 2003; Zhao et al., 2009) and responding to sensory stimulation in early auditory cortex (Wess et al., 2017). Optogenetics experiments further showed that L6 Ntsr1+ corticothalamic cells attain their inhibitory effect on the cortical network only after eye opening, both concerning spontaneous and sensory-evoked activity. Before eye opening, optogenetic activation of Ntsr1+ cells led to a small reduction in responses of supragranular neurons during the slow phase of the sensory stimulation, in line with their role in supporting transmission of immature oscillatory activity in the thalamo-cortico-thalamic system (Murata and Colonnese, 2016).

6.5 – Conclusion

Throughout the thesis, I provided an extensive characterisation of networks and functions of GABAergic interneuron subtypes across developing primary sensory areas. The highlight of this work is the high degree of differences found at the network level between V1 and S1BF, with repercussions on the functional implication of GABAergic interneurons *in vivo*. Canonical cortical circuits have been reported as common features throughout the brain, at least concerning primary sensory areas (Harris and Shepherd, 2015). My thesis suggests that canonical cortical circuit motifs do not apply during early cortical development. This has translational relevance for human neuroscience, as impairment in GABAergic interneurons

underly several neurodevelopmental disorders (Marín, 2012). An understanding of the mechanisms underlying such conditions must start from functions and networks of interneurons in development and not inferred from their “canonical” role in the adult brain.

References

Ackman JB, Burbridge TJ, Crair MC (2012) Retinal waves coordinate patterned activity throughout the developing visual system. Nature 490:219–225.

Adesnik H, Bruns W, Taniguchi H, Huang ZJ, Scanziani M (2012) A neural circuit for spatial summation in visual cortex. Nature 490:226–230.

Akerman CJ, Smyth D, Thompson ID (2002) Visual Experience before Eye-Opening and the Development of the Retinogeniculate Pathway. Neuron 36:869–879.

Akhmetshina D, Nasretdinov A, Zakharov A, Valeeva G, Khazipov R (2016) The Nature of the Sensory Input to the Neonatal Rat Barrel Cortex. The Journal of Neuroscience 36:9922–9932.

Akrouh A, Kerschensteiner D (2013) Intersecting circuits generate precisely patterned retinal waves. Neuron 79:322–334.

Anastasiades PG, Butt SJB (2012) A Role for Silent Synapses in the Development of the Pathway from Layer 2/3 to 5 Pyramidal Cells in the Neocortex. The Journal of Neuroscience 32:13085–13099.

Anastasiades PG, Marques-Smith A, Butt SJB (2018) Studies of cortical connectivity using optical circuit mapping methods. Journal of Physiology 596:145–162.

Anastasiades PG, Marques-Smith A, Lyngholm D, Lickiss T, Raffiq S, Katzel D, Miesenbock G, Butt SJB (2016) GABAergic interneurons form transient layer-specific circuits in early postnatal neocortex. Nature Communications 7.

Arganda-Carreras I, Kaynig V, Rueden C, Eliceiri KW, Schindelin J, Cardona A, Seung HS (2017) Trainable Weka Segmentation: a machine learning tool for microscopy pixel classification. Bioinformatics 33:2424–2426.

Arshadi C, Günther U, Eddison M, Harrington KIS, Ferreira TA (2021) SNT: a unifying toolbox for quantification of neuronal anatomy. Nature Methods 18:374–377.

Attinger A, Wang B, Keller GB (2017) Visuomotor Coupling Shapes the Functional Development of Mouse Visual Cortex. Cell 169:1291-1302.e14.

Baruchin LJ, Ghezzi F, Kohl MM, Butt SJB (2021) Contribution of Interneuron Subtype-Specific GABAergic Signaling to Emergent Sensory Processing in Mouse Somatosensory Whisker Barrel Cortex. Cerebral Cortex 00:1–17.

Berens P (2009) CircStat: A MATLAB Toolbox for Circular Statistics. Journal of Statistical Software 31:1–21.

Blankenship AG, Feller MB (2010) Mechanisms underlying spontaneous patterned activity in developing neural circuits. Nature Reviews Neuroscience 11:18–29.

Blankenship AG, Hamby AM, Firl A, Vyas S, Maxeiner S, Willecke K, Feller MB (2011) The role of neuronal connexins 36 and 45 in shaping spontaneous firing patterns in the developing retina. The Journal of Neuroscience 31:9998–10008.

Bonifazi P, Goldin M, Picardo MA, Jorquera I, Cattani A, Bianconi G, Represa A, Ben-Ari Y, Cossart R (2009) GABAergic hub neurons orchestrate synchrony in developing hippocampal networks. Science (1979) 326:1419–1424.

Bortone DS, Olsen SR, Scanziani M (2014) Translaminar Inhibitory Cells Recruited by Layer 6 Corticothalamic Neurons Suppress Visual Cortex. Neuron 82:474–485.

Burbridge TJ, Xu HP, Ackman JB, Ge X, Zhang Y, Ye MJ, Zhou ZJ, Xu J, Contractor A, Crair MC (2014) Visual circuit development requires patterned activity mediated by retinal acetylcholine receptors. Neuron 84:1049–1064.

Butt SJ, Stacey JA, Teramoto Y, Vagnoni C (2017) A role for GABAergic interneuron diversity in circuit development and plasticity of the neonatal cerebral cortex. Current Opinion in Neurobiology 43:149–155.

Butts DA, Kanold PO (2010) The applicability of spike time dependent plasticity to development. Frontiers in Synaptic Neuroscience 2:30.

Butts DA, Kanold PO, Shatz CJ (2007) A burst-based "Hebbian" learning rule at retinogeniculate synapses links retinal waves to activity-dependent refinement. PLoS Biology 5:0651–0661.

Cang J, Rentería RC, Kaneko M, Liu X, Copenhagen DR, Stryker MP (2005) Development of precise maps in visual cortex requires patterned spontaneous activity in the retina. Neuron 48:797–809.

Chandrasekaran AR, Plas DT, Gonzalez E, Crair MC (2005) Evidence for an instructive role of retinal activity in retinotopic map refinement in the superior colliculus of the mouse. The Journal of Neuroscience 25:6929–6938.

Chattopadhyaya B, di Cristo G, Higashiyama H, Knott GW, Kuhlman SJ, Welker E, Huang ZJ (2004) Experience and activity-dependent maturation of perisomatic GABAergic innervation in primary visual cortex during a postnatal critical period. The Journal of Neuroscience 24:9598–9611.

Chen G, Zhang Y, Li X, Zhao X, Ye Q, Lin Y, Tao HW, Rasch MJ, Zhang X (2017) Distinct Inhibitory Circuits Orchestrate Cortical beta and gamma Band Oscillations. Neuron 96:1403-1418.e6.

Chini M, Gretenkord S, Kostka JK, Pöpplau JA, Cornelissen L, Berde CB, Hanganu-Opatz IL, Bitzenhofer SH (2019) Neural Correlates of Anesthesia in Newborn Mice and Humans. Front Neural Circuits 13.

Chubykin AA, Roach EB, Bear MF, Shuler MGH (2013) A cholinergic mechanism for reward timing within primary visual cortex. Neuron 77:723–735.

Clement EA, Richard A, Thwaites M, Ailon J, Peters S, Dickson CT (2008) Cyclic and Sleep-Like Spontaneous Alternations of Brain State Under Urethane Anaesthesia. PLOS ONE 3:e2004.

Colonnese MT (2014) Rapid developmental emergence of stable depolarization during wakefulness by inhibitory balancing of cortical network excitability. The Journal of Neuroscience 34:5477–5485.

Colonnese MT, Kaminska A, Minlebaev M, Milh M, Bloem B, Lescure S, Moriette G, Chiron C, Ben-Ari Y, Khazipov R (2010) A Conserved Switch in Sensory Processing Prepares Developing Neocortex for Vision. Neuron 67:480–498.

Colonnese MT, Khazipov R (2010) "Slow activity transients" in infant rat visual cortex: A spreading synchronous oscillation patterned by retinal waves. The Journal of Neuroscience 30:4325–4337.

Colonnese MT, Shen J, Murata Y (2017) Uncorrelated Neural Firing in Mouse Visual Cortex during Spontaneous Retinal Waves. Frontiers in Cellular Neuroscience 11:289.

Cotel F, Fletcher LN, Kalita-De Croft S, Apergis-Schoute J, Williams SR (2018) Cell Class-Dependent Intracortical Connectivity and Output Dynamics of Layer 6 Projection Neurons of the Rat Primary Visual Cortex. Cerebral Cortex 28:2340–2350.

Crair MC (1999) Neuronal activity during development: Permissive or instructive? Current Opinion in Neurobiology 9:88–93.

Crair MC, Malenka RC (1995) A critical period for long-term potentiation at thalamocortical synapses. Nature 375:325–328.

Crandall SR, Cruikshank SJ, Connors BW (2015) A Corticothalamic Switch: Controlling the Thalamus with Dynamic Synapses. Neuron 86:768–782.

Cruikshank SJ, Lewis TJ, Connors BW (2007) Synaptic basis for intense thalamocortical activation of feedforward inhibitory cells in neocortex. Nature Neuroscience 10:462–468.

Daw MI, Ashby MC, Isaac JTR (2007) Coordinated developmental recruitment of latent fast spiking interneurons in layer IV barrel cortex. Nature Neuroscience 10:453–461.

del Rio J, de Lecea L, Ferrer I, Soriano E (1994) The development of parvalbumin-immunoreactivity in the neocortex of the mouse. Brain Res Dev Brain Res 81:247–259.

Du T, Xu Q, Ocbina PJ, Anderson SA (2008) NKX2.1 specifies cortical interneuron fate by activating Lhx6. Development 135:1559–1567.

Duan ZRS, Che A, Chu P, Pisapia DJ, Cossart R, Duan ZRS, Che A, Chu P, Modol L, Bollmann Y, Babij R, Fetcho RN, Otsuka T, Fuccillo M v., Conor L, Pisapia DJ, Cossart R, de Marco Garcia N v. (2020) GABAergic Restriction of Network Dynamics Regulates Interneuron Survival in the Developing Cortex. Neuron 105:75–92.

Erzurumlu RS, Gaspar P (2012) Development and critical period plasticity of the barrel cortex. European Journal of Neuroscience 35:1540–1553.

Fagiolini M, Fritschy JM, Löw K, Möhler H, Rudolph U, Hensch TK (2004) Specific GABAA Circuits for Visual Cortical Plasticity. Science (1979) 303:1681–1683.

Feller MB, Scanziani M (2005) A precritical period for plasticity in visual cortex. Current Opinion in Neurobiology 15:94–100.

Frandolig JE, Matney CJ, Lee K, Kim J, Chevée M, Kim SJ, Bickert AA, Brown SP (2019) The Synaptic Organization of Layer 6 Circuits Reveals Inhibition as a Major Output of a Neocortical Sublamina. Cell Rep 28:3131-3143.e5.

Geiller T, Sadeh S, Rolotti S v., Blockus H, Vancura B, Negrean A, Murray AJ, Rózsa B, Polleux F, Clopath C, Losonczy A (2021) Local circuit amplification of spatial selectivity in the hippocampus. Nature:1–5.

Ghezzi F, Marques-Smith A, Anastasiades PG, Lyngholm D, Vagnoni C, Rowett A, Parameswaran G, Hoerder-Suabedissen A, Nakagawa Y, Molnar Z, Butt SJB (2021) Non-canonical role for lpar1-egfp subplate neurons in early postnatal mouse somatosensory cortex. Elife 10.

Gong S, Doughty M, Harbaugh CR, Cummins A, Hatten ME, Heintz N, Gerfen CR (2007) Targeting Cre recombinase to specific neuron populations with bacterial artificial chromosome constructs. The Journal of Neuroscience 27:9817–9823.

Gouwens NW et al. (2019) Classification of electrophysiological and morphological neuron types in the mouse visual cortex. Nature Neuroscience 22:1182–1195.

Greig LC, Woodworth MB, Galazo MJ, Padmanabhan H, Macklis JD (2013) Molecular logic of neocortical projection neuron specification, development and diversity. Nature Reviews Neuroscience 14:755–769.

Gribizis A, Ge X, Daigle TL, Ackman JB, Zeng H, Lee D, Crair MC (2019) Visual Cortex Gains Independence from Peripheral Drive before Eye Opening. Neuron 104:711-723.e3.

Gu Y, Cang J (2016) Binocular matching of thalamocortical and intracortical circuits in the mouse visual cortex. Elife 5.

Guan W, Cao J-W, Liu L-Y, Zhao Z-H, Fu Y, Yu Y-C (2017) Eye opening differentially modulates inhibitory synaptic transmission in the developing visual cortex. Elife 6.

Hagihara KM, Murakami T, Yoshida T, Tagawa Y, Ohki K (2015) Neuronal activity is not required for the initial formation and maturation of visual selectivity. Nature Neuroscience 18:1780–1788.

Hanganu IL, Ben-Ari Y, Khazipov R (2006) Retinal waves trigger spindle bursts in the neonatal rat visual cortex. The Journal of Neuroscience 26:6728–6736.

Harris KD, Shepherd GMG (2015) The neocortical circuit: Themes and variations. Nature Neuroscience 18:170–181.

Heintz TG, Hinojosa AJ, Lagnado L (2020) Opposing forms of adaptation in mouse visual cortex are controlled by distinct inhibitory microcircuits and gated by locomotion. bioRxiv:2020.01.16.909788.

Hensch TK (2005) Critical period plasticity in local cortical circuits. Nature Reviews Neuroscience 6:877–888.

Ho H, Fowle A, Coetzee M, Greger IH, Watson JF (2020) An inhalation anaesthesia approach for neonatal mice allowing streamlined stereotactic injection in the brain. Journal of Neuroscience Methods 342.

Hooks BM, Chen C (2006) Distinct roles for spontaneous and visual activity in remodeling of the retinogeniculate synapse. Neuron 52:281–291.

Hoy JL, Niell CM (2015) Layer-specific refinement of visual cortex function after eye opening in the awake mouse. The Journal of Neuroscience 35:3370–3383.

Hu H, Cavendish JZ, Agmon A (2013) Not all that glitters is gold: off-target recombination in the somatostatin-IRES-Cre mouse line labels a subset of fast-spiking interneurons. Front Neural Circuits 7:195.

Huberman AD, Feller MB, Chapman B (2008) Mechanisms Underlying Development of Visual Maps and Receptive Fields. Annual Review of Neuroscience 31:479–509.

Kanold PO, Kara P, Reid RC, Shatz CJ (2003) Role of subplate neurons in functional maturation of visual cortical columns. Science (1979) 301:521–525.

Kanold PO, Luhmann HJ (2010) The subplate and early cortical circuits. Annual Review of Neuroscience 33:23–48.

Kätzel D, Zemelman B v., Buetfering C, Wölfel M, Miesenböck G (2011) The columnar and laminar organization of inhibitory connections to neocortical excitatory cells. Nature Neuroscience 14:100–109.

Kerschensteiner D (2016) Glutamatergic Retinal Waves. Frontiers in Neural Circuits 10:38.

Kerschensteiner D, Wong ROL (2008) A Precisely Timed Asynchronous Pattern of ON and OFF Retinal Ganglion Cell Activity during Propagation of Retinal Waves. Neuron 58:851–858.

Khan AG, Poort J, Chadwick A, Blot A, Sahani M, Mrsic-Flogel TD, Hofer SB (2018) Distinct learning-induced changes in stimulus selectivity and interactions of GABAergic interneuron classes in visual cortex. Nature Neuroscience 21:851–859.

Khazipov R, Sirota A, Leinekugel X, Holmes GL, Ben-Ari Y, Buzsáki G (2004) Early motor activity drives spindle bursts in the developing somatosensory cortex. Nature 432:758–761.

Kirkby LA, Sack GS, Firl A, Feller MB (2013) A role for correlated spontaneous activity in the assembly of neural circuits. Neuron 80:1129–1144.

Kirmse K, Zhang C (2022) Principles of GABAergic signaling in developing cortical network dynamics. Cell Reports 38:110568.

Kloc M, Maffei A (2014) Target-specific properties of thalamocortical synapses onto layer 4 of mouse primary visual cortex. The Journal of Neuroscience 34:15455–15465.

Ko H, Cossell L, Baragli C, Antolik J, Clopath C, Hofer SB, Mrsic-Flogel TD (2013) The emergence of functional microcircuits in visual cortex. Nature 496:96–100.

Krug K, Akerman CJ, Thompson ID (2001) Responses of Neurons in Neonatal Cortex and Thalamus to Patterned Visual Stimulation Through the Naturally Closed Lids. Journal of Neurophysiology 85:1436–1443.

Kuhlman SJ, Olivas ND, Tring E, Ikrar T, Xu X, Trachtenberg JT (2013) A disinhibitory microcircuit initiates critical-period plasticity in the visual cortex. Nature 501:543–546.

Kuhlman SJ, Tring E, Trachtenberg JT (2011) Fast-spiking interneurons have an initial orientation bias that is lost with vision. Nature Neuroscience 14:1121–1133.

Kvitsiani D, Ranade S, Hangya B, Taniguchi H, Huang JZ, Kepecs A (2013) Distinct behavioural and network correlates of two interneuron types in prefrontal cortex. Nature 498:363–366.

Leighton AH, Cheyne JE, Houwen GJ, Maldonado PP, de Winter F, Levelt CN, Lohmann C (2021) Somatostatin interneurons restrict cell recruitment to retinally driven spontaneous activity in the developing cortex. Cell Reports 36:109316.

Lim L, Mi D, Llorca A, Marín O (2018) Development and Functional Diversification of Cortical Interneurons. Neuron 100:294–313.

Marín O (2012) Interneuron dysfunction in psychiatric disorders. Nature Reviews Neuroscience 13:107–120.

Marques-Smith A, Lyngholm D, Kaufmann AK, Stacey JA, Hoerder-Suabedissen A, Becker EBE, Wilson MC, Molnár Z, Butt SJB (2016) A Transient Translaminar GABAergic Interneuron Circuit Connects Thalamocortical Recipient Layers in Neonatal Somatosensory Cortex. Neuron 89:536–549.

McLaughlin T, Torborg CL, Feller MB, O'Leary DDM (2003) Retinotopic map refinement requires spontaneous retinal waves during a brief critical period of development. Neuron 40:1147–1160.

Miao Q, Yao L, Rasch MJ, Ye Q, Li X, Zhang X (2016) Selective Maturation of Temporal Dynamics of Intracortical Excitatory Transmission at the Critical Period Onset. Cell Reports 16:1677–1689.

Minlebaev M, Colonnese MT, Tsintsadze T, Sirota A, Khazipov R (2011) Early γ oscillations synchronize developing thalamus and cortex. Science (1979) 334:226–229.

Miyoshi G, Butt SJB, Takebayashi H, Fishell G (2007) Physiologically distinct temporal cohorts of cortical interneurons arise from telencephalic Olig2-expressing precursors. The Journal of Neuroscience 27:7786–7798.

Modol L, Bollmann Y, Tressard T, Babij R, Che A, Duan ZRS, Babij R, de Marco Garcia N v., Cossart R (2020) Assemblies of Perisomatic GABAergic Neurons in the Developing Barrel Cortex. Neuron 105:93–105.

Mrsic-Flogel TD, Hofer SB, Creutzfeldt C, Cloëz-Tayarani I, Changeux JP, Bonhoeffer T, Hubener M (2005) Altered map of visual space in the superior colliculus of mice lacking early retinal waves. The Journal of Neuroscience 25:6921–6928.

Murata Y, Colonnese MT (2016) An excitatory cortical feedback loop gates retinal wave transmission in rodent thalamus. Elife 5.

Murata Y, Colonnese MT (2018) Thalamus Controls Development and Expression of Arousal States in Visual Cortex. The Journal of Neuroscience 38:8772–8786.

Olsen SR, Bortone DS, Adesnik H, Scanziani M (2012) Gain control by layer six in cortical circuits of vision. Nature 483:47–52.

Pachitariu M, Steinmetz N, Kadir S, Carandini M, D. HK (2016) Kilosort: realtime spike-sorting for extracellular electrophysiology with hundreds of channels. bioRxiv:061481.

Packer AM, Yuste R (2011) Dense, Unspecific Connectivity of Neocortical Parvalbumin-Positive Interneurons: A Canonical Microcircuit for Inhibition? The Journal of Neuroscience 31:13260–13271.

Pakan JM, Francioni V, Rochefort NL (2018) Action and learning shape the activity of neuronal circuits in the visual cortex. Curr Opin Neurobiol 52:88–97.

Pan NC, Fang A, Shen C, Sun L, Wu Q, Wang X (2019) Early Excitatory Activity-Dependent Maturation of Somatostatin Interneurons in Cortical Layer 2/3 of Mice. Cerebral Cortex 29:4107–4118.

Penn AA, Riquelme PA, Feller MB, Shatz CJ (1998) Competition in Retinogeniculate Patterning Driven by Spontaneous Activity. Science (1979) 279:2108–2112.

Petreanu L, Huber D, Sobczyk A, Svoboda K (2007) Channelrhodopsin-2–assisted circuit mapping of long-range callosal projections. Nature Neuroscience 10:663–668.

Pfeffer CK, Xue M, He M, Huang ZJ, Scanziani M (2013) Inhibition of inhibition in visual cortex: the logic of connections between molecularly distinct interneurons. Nature Neuroscience 16:1068–1076.

Picardo MA, Guigue P, Bonifazi P, Batista-Brito R, Allene C, Ribas A, Fishell G, Baude A, Cossart R (2011) Pioneer GABA cells comprise a subpopulation of hub neurons in the developing hippocampus. Neuron 71:695–709.

Poort J, Wilmes KA, Blot A, Chadwick A, Sahani M, Clopath C, Mrsic-Flogel TD, Hofer SB, Khan AG (2021) Learning and attention increase visual response selectivity through distinct mechanisms. Neuron 0.

Rensing N, Moy B, Friedman JL, Galindo R, Wong M (2018) Longitudinal analysis of developmental changes in electroencephalography patterns and sleep-wake states of the neonatal mouse. PLOS ONE 13:e0207031.

Rochefort NL, Garaschuk O, Milos RI, Narushima M, Marandi N, Pichler B, Kovalchuk Y, Konnerth A (2009) Sparsification of neuronal activity in the visual cortex at eye-opening. Proc Natl Acad Sci U S A 106:15049–15054.

Rochefort NL, Narushima M, Grienberger C, Marandi N, Hill DN, Konnerth A (2011) Development of direction selectivity in mouse cortical neurons. Neuron 71:425–432.

Rossant C, Kadir SN, Goodman DFM, Schulman J, Hunter MLD, Saleem AB, Grosmark A, Belluscio M, Denfield GH, Ecker AS, Tolias AS, Solomon S, Buzsaki G, Carandini M, Harris KD (2016) Spike sorting for large, dense electrode arrays. Nature Neuroscience 19:634–641.

Rudy B, Fishell G, Lee S, Hjerling-Leffler J (2011) Three groups of interneurons account for nearly 100% of neocortical GABAergic neurons. Developmental Neurobiology 71:45–61.

Scala F, Kobak D, Shan S, Bernaerts Y, Laturnus S, Cadwell CR, Hartmanis L, Froudarakis E, Castro JR, Tan ZH, Papadopoulos S, Patel SS, Sandberg R, Berens P, Jiang X, Tolias AS (2019) Layer 4 of mouse neocortex differs in cell types and circuit organization between sensory areas. Nature Communications 10:1–12.

Seabrook TA, Burbridge TJ, Crair MC, Huberman AD (2017) Architecture, Function, and Assembly of the Mouse Visual System. Annual Review of Neuroscience 40:499–538.

Seabrook TA, El-Danaf RN, Krahe TE, Fox MA, Guido W (2013) Retinal input regulates the timing of corticogeniculate innervation. The Journal of Neuroscience 33:10085–10097.

Senzai Y, Fernandez-Ruiz A, Buzsáki G (2019) Layer-Specific Physiological Features and Interlaminar Interactions in the Primary Visual Cortex of the Mouse. Neuron 101:500-513.e5.

Shah RD, Crair MC (2008) Retinocollicular synapse maturation and plasticity are regulated by correlated retinal waves. The Journal of Neuroscience 28:292–303.

Shen J, Colonnese MT (2016) Development of Activity in the Mouse Visual Cortex. The Journal of Neuroscience 36:12259–12275.

Shen S, Jiang X, Scala F, Fu J, Fahey P, Kobak D, Tan Z, Reimer J, Sinz F, Tolias AS (2020) Distinct organization of two cortico-cortical feedback pathways. bioRxiv:2020.02.27.968792.

Siegel F, Heimel JA, Peters J, Lohmann C (2012) Peripheral and central inputs shape network dynamics in the developing visual cortex in vivo. Current Biology 22:253–258.

Smith SL, Trachtenberg JT (2007) Experience-dependent binocular competition in the visual cortex begins at eye opening. Nature Neuroscience 10:370–375.

Staiger JF, Petersen CCH (2021) Neuronal circuits in barrel cortex for whisker sensory perception. Physiological Reviews 101:353–415.

Sundberg SC, Lindström SH, Sanchez GM, Granseth B (2018) Cre-expressing neurons in visual cortex of Ntsr1-Cre GN220 mice are corticothalamic and are depolarized by acetylcholine. Journal of Comparative Neurology 526:120–132.

Taniguchi H, He M, Wu P, Kim S, Paik R, Sugino K, Kvitsani D, Fu Y, Lu J, Lin Y, Miyoshi G, Shima Y, Fishell G, Nelson SB, Huang ZJ (2011) A resource of Cre driver lines for genetic targeting of GABAergic neurons in cerebral cortex. Neuron 71:995–1013.

Tasic B et al. (2018) Shared and distinct transcriptomic cell types across neocortical areas. Nature 563:72–78.

Thompson AD, Picard N, Min L, Fagiolini M, Chen C (2016) Cortical Feedback Regulates Feedforward Retinogeniculate Refinement. Neuron 91:1021–1033.

Thomson AM (2010) Neocortical layer 6, a review. Frontiers in Neuroanatomy 4:13.

Tiriac A, Smith BE, Feller MB (2018) Light Prior to Eye Opening Promotes Retinal Waves and Eye-Specific Segregation. Neuron 100:1059-1065.e4.

Trachtenberg JT, Trepel C, Stryker MP (2000) Rapid extragranular plasticity in the absence of thalamocortical plasticity in the developing primary visual cortex. Science (1979) 287:2029–2032.

Tuncdemir SN, Wamsley B, Stam FJ, Osakada F, Goulding M, Callaway EM, Rudy B, Fishell G (2016) Early Somatostatin Interneuron Connectivity Mediates the Maturation of Deep Layer Cortical Circuits. Neuron 89:521–535.

Vagnoni C, Baruchin LJ, Ghezzi F, Ratti S, Molnar Z, Butt S (2020) Ontogeny of the VIP+ interneuron sensory-motor circuit prior to active whisking. bioRxiv:2020.07.01.182238.

Veit J, Hakim R, Jadi MP, Sejnowski TJ, Adesnik H (2017) Cortical gamma band synchronization through somatostatin interneurons. Nature Neuroscience 20:951–959.

Vélez-Fort M, Rousseau C v., Niedworok CJ, Wickersham IR, Rancz EA, Brown APY, Strom M, Margrie TW (2014) The stimulus selectivity and connectivity of layer six principal cells reveals cortical microcircuits underlying visual processing. Neuron 83:1431–1443.

Vinck M, van Wingerden M, Womelsdorf T, Fries P, Pennartz CMA (2010) The pairwise phase consistency: A bias-free measure of rhythmic neuronal synchronization. Neuroimage 51:112–122.

Wang Y, Toledo-Rodriguez M, Gupta A, Wu C, Silberberg G, Luo J, Markram H (2004) Anatomical, physiological and molecular properties of Martinotti cells in the somatosensory cortex of the juvenile rat. J Physiol 561:65–90.

Wen JA, Barth AL (2011) Input-specific critical periods for experience-dependent plasticity in layer 2/3 pyramidal neurons. The Journal of Neuroscience 31:4456–4465.

Wess JM, Isaiah A, Watkins P v, Kanold PO (2017) Subplate neurons are the first cortical neurons to respond to sensory stimuli. Proc Natl Acad Sci U S A 114:12602–12607.

Wiesel TN, Hubel DH (1963) Single-cell responses in striate cortex of kittens deprived of vision in one eye. Journal of Neurophysiology 26:1003–1017.

Wosniack ME, Kirchner JH, Chao LY, Zabouri N, Lohmann C, Gjorgjieva J (2021) Adaptation of spontaneous activity in the developing visual cortex. Elife 10.

Xu H, Jeong H-Y, Tremblay R, Rudy B (2013) Neocortical Somatostatin-Expressing GABAergic Interneurons Disinhibit the Thalamorecipient Layer 4. Neuron 77:155–167.

Xu HP, Burbridge TJ, Chen MG, Ge X, Zhang Y, Zhou ZJ, Crair MC (2015) Spatial pattern of spontaneous retinal waves instructs retinotopic map refinement more than activity frequency. Developmental Neurobiology 75:621–640.

Xu HP, Burbridge TJ, Ye M, Chen M, Ge X, Zhou ZJ, Crair MC (2016a) Retinal wave patterns are governed by mutual excitation among starburst amacrine cells and drive the refinement and maintenance of visual circuits. The Journal of Neuroscience 36:3871–3886.

Xu HP, Furman M, Mineur YS, Chen H, King SL, Zenisek D, Zhou ZJ, Butts DA, Tian N, Picciotto MR, Crair MC (2011) An Instructive Role for Patterned Spontaneous Retinal Activity in Mouse Visual Map Development. Neuron 70:1115–1127.

Xu Q, Tam M, Anderson SA (2008) Fate mapping Nkx2.1-lineage cells in the mouse telencephalon. J Comp Neurol 506:16–29.

Xu X, Olivas ND, Ikrar T, Peng T, Holmes TC, Nie Q, Shi Y (2016b) Primary visual cortex shows laminar-specific and balanced circuit organization of excitatory and inhibitory synaptic connectivity. The Journal of Physiology 594:1891–1910.

Yaeger CE, Ringach DL, Trachtenberg JT (2019) Neuromodulatory control of localized dendritic spiking in critical period cortex. Nature 567:100–104.

Yazaki-Sugiyama Y, Kang S, Cteau H, Fukai T, Hensch TK (2009) Bidirectional plasticity in fast-spiking GABA circuits by visual experience. Nature 462:218–221.

Zhang J, Ackman JB, Xu HP, Crair MC (2012) Visual map development depends on the temporal pattern of binocular activity in mice. Nature Neuroscience 15:298–307.

Zhao C, Kao JPY, Kanold PO (2009) Functional excitatory microcircuits in neonatal cortex connect thalamus and layer 4. The Journal of Neuroscience 29:15479–15488.